Taming Hadronic Effects at the Precision Frontier: From the Muon Anomaly to Rare Decays

Dissertation
zur
Erlangung des Doktorgrades (Dr. rer. nat.)
der
Mathematisch-Naturwissenschaftlichen Fakultät
der
Rheinischen Friedrich-Wilhelms-Universität Bonn

von
Long Bai (Bai-Long Hoid)
aus
der Inneren Mongolei, China

Bonn, 12.10.2020

Angefertigt mit Genehmigung der Mathematisch-Naturwissenschaftlichen Fakultät der Rheinischen Friedrich-Wilhelms-Universität Bonn

1. Gutachter:	PD Dr. Bastian Kubis
2. Gutachter:	Prof. Dr. Ulf-G. Meißner
Tag der Promotion:	26.11.2020
Erscheinungsjahr:	2021

To my father, Töbjirgal

ᠵᠠᠰᠠᠭᠴᠢ[1]

ᠵᠠᠰᠠᠭᠴᠢ ᠶᠡᠬᠡ ᠲᠤᠯᠠᠰᠤ ᠂ ᠵᠠᠰᠠᠭᠴᠢ ᠵᠤᠭᠤᠮ ᠲᠤᠯᠠᠰᠤ ᠂ ᠵᠠᠰᠠᠭᠴᠢ ᠵᠢᠷᠤᠭᠠᠨ ᠲᠤᠯᠠᠰᠤ ᠂ ᠵᠠᠰᠠᠭᠴᠢ ᠬᠠᠮᠤᠭ ᠵᠢᠷᠤᠭᠠᠨ ᠲᠤᠯᠠᠰᠤ ᠁

[1] Cumulative dust, big dust, tiny dust, very tiny dust ... .
— Agwangdander

Abstract

The strong interaction, one of the indispensable pillars of the Standard Model of particle physics, poses challenges at low energies because of the phase transition and the confinement nature of its underlying theory, quantum chromodynamics. Therefore, unveiling the emergent dynamics of its degrees of freedom at low energies, hadrons, and their interactions are of the essence at the low-energy precision frontier of the Standard Model.

In this thesis, we pursue a model-independent and high-precision description of the low-energy hadronic effects in the anomalous magnetic moment of the muon $(g-2)_\mu$ and the rare leptonic decay of the neutral pion $\pi^0 \to e^+e^-$. The approach is based on a synergy between general principles of the S-matrix, dispersion relations, low-energy theorems, and perturbative quantum chromodynamics.

In the first part, we investigate hadronic vacuum polarization in the muon $(g-2)_\mu$, including the contributions from the 3π and $\pi^0\gamma$ channels. The 3π channel, which constitutes the second-largest exclusive contribution to hadronic vacuum polarization and its uncertainty, is addressed using a dispersive representation of the $\gamma^* \to 3\pi$ amplitude. A global fit function using analyticity and unitarity of this amplitude and its normalization from a chiral low-energy theorem facilitates obtaining our best estimate $a_\mu^{3\pi}|_{\leq 1.8\,\mathrm{GeV}} = 46.16(82) \times 10^{-10}$, and providing a cross check for the compatibility of the different $e^+e^- \to 3\pi$ data sets. In a similar manner, we study the reaction $e^+e^- \to \pi^0\gamma$ based on a dispersive representation of the underlying $\pi^0 \to \gamma\gamma^*$ transition form factor. As a first application, we evaluate the contribution of the $\pi^0\gamma$ channel to the hadronic-vacuum-polarization correction to the anomalous magnetic moment of the muon. We find $a_\mu^{\pi^0\gamma}|_{\leq 1.35\,\mathrm{GeV}} = 4.38(6) \times 10^{-10}$, in line with evaluations from the direct integration of the data. Second, our fit determines the resonance parameters of ω and ϕ, which, in combination with the $e^+e^- \to 3\pi$ channel, are compared to the PDG average.

The more involved hadronic light-by-light scattering topology is discoursed in the second part. The pion pole, as the leading contribution in a dispersive approach to hadronic light-by-light scattering in the muon $(g-2)_\mu$, is unambiguously defined by the doubly-virtual pion transition form factor. In the absence of a complete measurement of this form factor covering all kinematic regions relevant for $(g-2)_\mu$, we report on a reconstruction from the available data for $\pi^0 \to \gamma\gamma$, $e^+e^- \to 3\pi$, and $e^+e^- \to e^+e^-\pi^0$, using a dispersive representation that accounts for all the low-lying singularities, reproduces the correct high- and low-energy limits, and proves suitable for the evaluation of the $(g-2)_\mu$ loop integral. Our final result, $a_\mu^{\pi^0\text{-pole}} = 63.0^{+2.7}_{-2.1} \times 10^{-11}$, provides a complete data-driven determination of the pion-pole contribution with fully controlled uncertainty estimates.

In the final part, we first consider the dominant decay modes of the neutral pion, which are all of electromagnetic nature. These decays are instrumental in disclosing the properties of the neutral pion, such as its quantum numbers. Second, we consider the dilepton decay $\pi^0 \to e^+e^-$ in detail. This loop- and helicity-suppressed decay not only maneuvers the dynamics of the Standard Model at low energies, but also raises potential sensitivity to physics beyond the Standard Model. Based upon a double-spectral representation of the pion transition form factor, we present a feasible formalism to reexamine this rare decay: the loop integral of the reduced amplitude is expressed in terms of the standard one-loop functions, yielding a two-dimensional integral representation suitable for the numerical treatment with the dispersively reconstructed pion transition form factor.

Parts of this thesis have been published in the following papers:

- M. Hoferichter, B.-L. Hoid, B. Kubis, S. Leupold and S. P. Schneider, *Pion-pole contribution to hadronic light-by-light scattering in the anomalous magnetic moment of the muon*, Phys. Rev. Lett. **121** (2018) 112002.
- M. Hoferichter, B.-L. Hoid, B. Kubis, S. Leupold and S. P. Schneider, *Dispersion relation for hadronic light-by-light scattering: pion pole*, JHEP **1810** (2018) 141.
- M. Hoferichter, B.-L. Hoid and B. Kubis, *Three-pion contribution to hadronic vacuum polarization*, JHEP **1908** (2019) 137.
- B.-L. Hoid, M. Hoferichter and B. Kubis, *Hadronic vacuum polarization and vector-meson resonance parameters from $e^+e^- \to \pi^0\gamma$*, Eur. Phys. J. C **80** (2020) 988.

The results from these publications enter the final compilation presented in the community report:

- T. Aoyama, ... , B.-L. Hoid et al., *The anomalous magnetic moment of the muon in the Standard Model*, Phys. Rept. **887** (2020) 1.

Excerpts of the above have also been published in the following proceedings contributions:

- B.-L. Hoid, M. Hoferichter, B. Kubis, S. Leupold and S. Schneider, *Pion-pole contribution to hadronic light-by-light scattering*, **CD2018** (2019) 052.
- B.-L. Hoid, M. Hoferichter and B. Kubis, *Hadronic vacuum polarization: three-pion channel*, EPJ Web Conf. **234** (2020) 01006.

Contents

Chapter 1

Introduction

Our modern knowledge of elementary particles is encoded in the Standard Model (SM) of particle physics. It depicts the electromagnetic, weak, and strong interactions between subatomic particles as a relativistic quantum field theory, a framework born as a marriage between special relativity and quantum mechanics. The astute idea of incorporating the interactions by imposing local gauge invariance traces back to Weyl's early work in 1919 [1], extended by Yang and Mills in 1954 [2] to the non-Abelian gauge theory of the $SU(2)$ isospin doublet proton and neutron. Although this theory can be easily obstructed by its unobserved would-be massless gauge bosons, it inspired Weinberg [3] to apply it together with another formidable idea of spontaneous symmetry breaking [4–8] via the Higgs mechanism [9–12] to the global $SU(2) \times U(1)$ electroweak theory proposed by Glashow [13]. Developed independently by Salam, it forms the $SU(2)_L \times U(1)_Y$ electroweak unified theory [14, 15]. About one decade later, the modern form of the strong interaction was formulated based on $SU(3)_c$ color gauge invariance [16, 17].

Elementary particles in the SM are classified into fermions and bosons, as listed in Table 1.1. The matter content of the SM consists of three generations of spin-1/2 quarks and leptons, with heavier higher generations exact replicas of the lowest. The spin-1 gauge bosons are the force mediators of the gauge interactions, whereas the spin-0 Higgs boson is responsible for the Yukawa interaction. The complete SM gauge group, $SU(3)_c \times SU(2)_L \times U(1)_Y$, is broken to $SU(3)_c \times U(1)_{\text{em}}$ by electroweak symmetry breaking, after which the masses of the fermions and gauge bosons are generated.

Quantum chromodynamics (QCD) built upon $SU(3)_c$ color gauge invariance is the underlying theory of the strong interaction between quarks and gluons forming hadrons. It possesses its own peculiarities and also challenges. In contrast to the one-loop beta function governing the energy-scale dependence of the fine structure constant α in quantum electrodynamics (QED) being positive [18],

$$\beta\left(\alpha(\mu)\right) = \mu \frac{\partial \alpha}{\partial \mu} = \frac{2\alpha^2}{3\pi}, \tag{1.1}$$

the running of the strong coupling constant α_s at one loop is predicted to be negative for

fermions	generations		
quarks	$\begin{pmatrix} u \\ d \end{pmatrix}$	$\begin{pmatrix} c \\ s \end{pmatrix}$	$\begin{pmatrix} t \\ b \end{pmatrix}$
leptons	$\begin{pmatrix} e \\ \nu_e \end{pmatrix}$	$\begin{pmatrix} \mu \\ \nu_\mu \end{pmatrix}$	$\begin{pmatrix} \tau \\ \nu_\tau \end{pmatrix}$

bosons	interactions
g (gluon)	strong
$W^{\pm}$, Z, γ	electroweak
H (Higgs)	Yukawa

Table 1.1: Elementary particles in the SM.

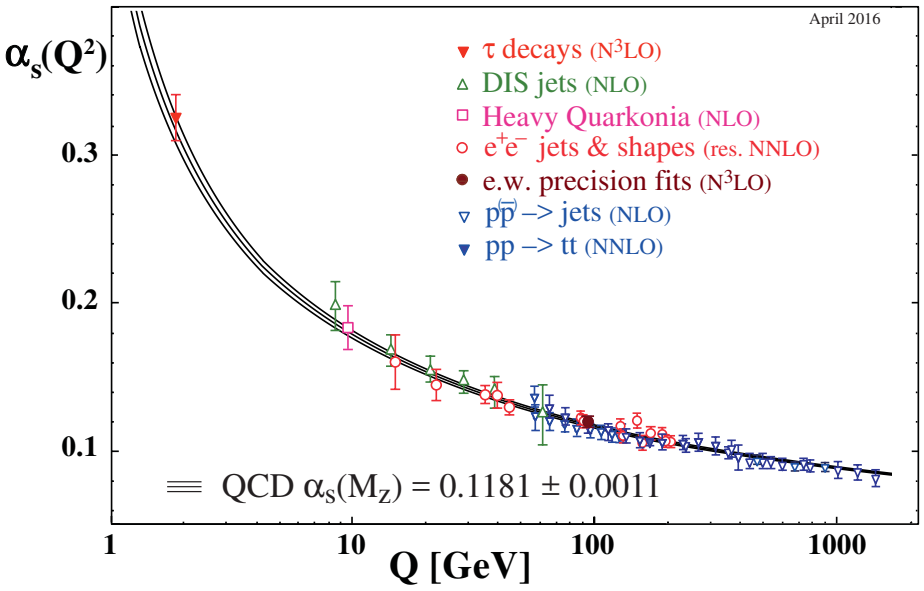

Figure 1.1: The summary of the measurements of the running coupling constant α_s versus the energy scale Q. The figure is taken from [19].

quark flavors $n_f \leq 16$,

$$\beta\left(\alpha_s(\mu)\right) = \mu\frac{\partial\alpha_s}{\partial\mu} = -\left(11 - \frac{2}{3}n_f\right)\frac{\alpha_s^2}{2\pi}\,. \tag{1.2}$$

Therefore, α_s tends to zero at high momentum transfer as shown in Figure 1.1, leading to the discovery of asymptotic freedom [20, 21]. This makes perturbative calculations in expansions of α_s feasible at high energies. Successful predictions by QCD in various processes, e.g., deep inelastic scattering, hard exclusive processes, and jet structures at hadron colliders, earn it confidence to become the true theory of the strong interaction. In particular, the world-average result of α_s determined at the scale of Z-boson mass from different measurements and lattice QCD calculations reads [22]

$$\alpha_s\left(M_Z\right) = 0.1179 \pm 0.0010\,. \tag{1.3}$$

On the other hand, perturbative calculations fail in the infrared domain due to the rise of α_s at low momentum transfer. This is the confining nature of the strong interaction in the non-perturbative domain of QCD: the fundamental degrees of freedom, quarks and gluons, have never been seen as asymptotic states in experiments; what were observed are color-singlet hadrons consisting of quarks and gluons. Although Wilson showed color confinement on the lattice in the strong coupling limit in his seminal work [23] as the birth of lattice gauge theory, the analytic proof of confinement is still one of the most intriguing challenges to date.

The symmetries of QCD are crucial to better understand the emergent mechanism of the structure and dynamics of hadrons at low energies. In this regard, the QCD Lagrangian exhibits additional chiral symmetry in the absence of the mass term of the light quarks (u, d, and s). Thus, the global symmetry group becomes

$$U(3)_L \times U(3)_R = SU(3)_L \times SU(3)_R \times U(1)_V \times U(1)_A \,. \tag{1.4}$$

The chiral part is spontaneously broken to its diagonal subgroup $SU(3)_V$, which is protected by the Vafa–Witten theorem [24],

$$SU(3)_L \times SU(3)_R \to SU(3)_V \,, \tag{1.5}$$

because of the non-zero quark condensate

$$\langle 0|\bar{q}_L q_R + \bar{q}_R q_L|0\rangle \neq 0 \tag{1.6}$$

in the non-trivial QCD vacuum. This gives rise to eight massless pseudoscalar Nambu–Goldstone bosons: $\pi^{\pm}$, π^0, $K^{\pm}$, K^0, $\bar{K}^0$, and η. In the real world, the light-quark masses are small compared to the non-perturbative scale $\Lambda_{\rm QCD} \sim 200\,\text{MeV}$. Therefore, the pseudoscalar-meson octet appears as the lightest particles in the QCD spectrum. The $U(1)_A$ symmetry is anomalous and is already broken by quantum corrections. This is why the η' mass is much higher than the other pseudoscalar mesons'. The theory developed further to describe the interactions of the octet mesons using systematic expansions in powers of momenta and quark masses is called chiral perturbation theory (ChPT) [25–27]. ChPT is a prototype of an effective-field-theory approach to tackle QCD at low energies. Besides, the toolkit concerns first-principle lattice QCD, dispersion relations, QCD sum rules, large-N_c expansion, hadronic models, and so on.

The SM has been a great triumph ever since its first inception owing to the excellent agreement between numerous theoretical predictions and experimental results. At the energy frontier, theoretically postulated elementary particles were subsequently discovered at particle colliders, e.g., $W^{\pm}$ and Z bosons [28, 29], t quark [30, 31], and the latest discovery of the Higgs boson in 2012 [32, 33]. Moreover, high-precision tests at the precision frontier revealed unprecedented consistencies with the SM. The discovery of the Lamb shift [34], the energy gap between the $2S_{1/2}$ and $2P_{1/2}$ energy levels of the hydrogen spectrum, and the first calculation performed by Bethe beyond the tree level [35] is one of the early examples, which laid the foundation of renormalization in QED.

Nonetheless, it is still distant for the SM to be the complete theory of the fundamental interactions, leaving gravity excluded and certain phenomena unexplained in its framework. There are experimental observations such as dark matter, dark energy, matter–antimatter asymmetry, and neutrino masses, which cannot be described by the SM and inevitably require beyond the Standard Model (BSM) physics for explanations. In the search for BSM signals, hadronic physics often plays an essential and connecting role. There are often both BSM physics and hadronic contributions to some low-energy observables for which one needs to consider the latter and control their uncertainties in a better way to filter the minute signals coming from the former. Therefore, commensurate precise description of hadronic effects is key to not only overcoming the crux of strong QCD dynamics, but also discovering the trail of BSM physics.

The anomalous magnetic moment of the muon witnesses the advancement of the SM all the way in a nutshell. It is one of the prime physical observables to monitor signals arising from BSM physics, which yet receives hadronic contributions at the same time. Its current tantalizing tension with the SM prediction is overshadowed by hadronic uncertainties.

The thesis was initiated under this background to study the hadronic effects at the precision frontier of the SM. The contents are formatted as follows: Sections 1.1, 1.2, and 1.3 cover a brief introduction to the anomalous magnetic moment of the muon, the theoretical tools used extensively throughout the contents, and anomalies playing an important role in the thesis. We begin by analyzing hadronic vacuum polarization (HVP) in the anomalous magnetic moment of the muon $(g-2)_\mu$ in Part I. In particular, the contributions from the 3π and $\pi^0\gamma$ channels are addressed in detail. Part II is devoted to the hadronic light-by-light (HLbL) scattering contribution to the muon $(g-2)_\mu$. In that, the pion-pole contribution to HLbL scattering is determined in a dispersive approach. In Part III, we review the neutral pion's main decay modes and investigate its rare leptonic decay $\pi^0 \to e^+e^-$; thereafter, a conclusion is drawn in Chapter 6.

1.1 The muon $(g-2)_\mu$

1.1.1 Introduction

The magnetic and electric dipole moments (MDM and EDM) of a particle are related to its *intrinsic* spin by

$$\boldsymbol{\mu} = g\left(\frac{Qe}{2m}\right)\boldsymbol{S} \quad \text{and} \quad \boldsymbol{d} = \eta\left(\frac{Qe}{2m}\right)\boldsymbol{S}\,, \tag{1.7}$$

where m is the mass of the particle and Q is the charge in units of e. The gyromagnetic ratio (g-factor) is label by g, and η is the electric pendant. The MDM and EDM induce an interaction Hamiltonian with magnetic and electric fields

$$\mathcal{H} = -\boldsymbol{\mu}\cdot\boldsymbol{B} - \boldsymbol{d}\cdot\boldsymbol{E}\,, \tag{1.8}$$

from which it is evident that the MDM interaction is allowed by the separate discrete symmetries, while the EDM term violates parity and time reversal, hence equivalently charge conjugation and parity CP. In the SM, non-vanishing contributions to the EDMs of leptons only appear at four-loop level [36] via the CP-violating phase of the Cabbibo–Kobayashi–Maskawa mechanism [37]. Permanent EDMs not only serve as a probe of new physics, but also play an important role in the extraction of MDMs from experiments.

The Dirac equation universally predicts $g = 2$ as a tree-level upshot for charged leptons [38, 39], in contrast to $g = 1$ for the ordinary orbital angular momentum. Furthermore, quantum loop corrections lead to a gyromagnetic ratio that deviates from the classical Dirac value 2. So we define the anomalous magnetic moment of a lepton or lepton anomaly as

$$a_\ell = \frac{(g-2)_\ell}{2}\,, \tag{1.9}$$

where $\ell = e$, μ, or τ.

Our interest is the interaction of a lepton with a *classical external* electromagnetic field $A^{\mathrm{cl}}_\mu(x)$. To lowest order in the external field, the matrix element reads

$$i\mathcal{M} = -ie\,\langle p', s'\,|j^\mu(0)|\,p, s\rangle \tilde{A}^{\mathrm{cl}}_\mu(q) = -ie\,\bar{u}(p', s')\Gamma^\mu(p', p)u(p, s)\,\tilde{A}^{\mathrm{cl}}_\mu(q)\,, \tag{1.10}$$

where $q = p' - p$ and the incoming and outgoing spinors of the lepton are labeled by $u(p, s)$ and $\bar{u}(p', s')$ respectively. Owing to current and parity conservation in QED, the general structure of Γ^μ can be decomposed as [40]

$$\Gamma^\mu(p', p) = \gamma^\mu F_1(q^2) + \frac{i\sigma^{\mu\nu}q_\nu}{2m}F_2(q^2)\,, \tag{1.11}$$

where $\sigma^{\mu\nu} = \frac{i}{2}\,[\gamma^\mu, \gamma^\nu]$. F_1 and F_2 are called the Dirac and Pauli form factors; to lowest order, $F_1 = 1$ and $F_2 = 0$. These form factors contain the complete information about the electromagnetic couplings of the lepton. Especially, we find for static electric and magnetic fields in the non-relativistic limit ($q \to 0$)

$$F_1(0) = 1\,, \quad \text{and} \quad g = 2\,[F_1(0) + F_2(0)] = 2 + 2F_2(0)\,, \tag{1.12}$$

where the first relation is exact to all orders as a consequence of the charge-renormalization condition, and loop corrections to $F_2(0)$ give rise to the lepton anomaly

$$a_\ell = F_2(0)\,. \tag{1.13}$$

The anomalous magnetic moment of a lepton is a finite dimensionless number that can be unambiguously calculated in a renormalizable local relativistic quantum field theory. This is due to the fact that there is no corresponding tree-level operator present in QED, of which we can adjust its coupling in an ambiguous way. In fact, it can be generated by an effective dimension-5 operator

$$\bar{\psi}_L F_{\mu\nu}\sigma^{\mu\nu}\psi_R + \bar{\psi}_R F_{\mu\nu}\sigma^{\mu\nu}\psi_L\,, \tag{1.14}$$

where $F_{\mu\nu} = \partial_\mu A_\nu - \partial_\nu A_\mu$. This operator is forbidden in a renormalizable theory.

In general, anomalous magnetic moments receive contributions from different particles with hierarchical masses. Therefore, we first discuss the general properties of the loop contribution of a particle with the mass M to the anomalous magnetic moment. For the case $M \ll m$, the contribution reads

$$\delta a_\ell \sim \left(\frac{\alpha}{\pi}\right)^n \ln^k \frac{m}{M}\,, \tag{1.15}$$

where n is the corresponding order in the fine structure constant α and the power of the logarithm $k < n$. In the inverse case $M \geq m$,

$$\delta a_\ell \sim \left(\frac{\alpha}{\pi}\right)^n \frac{m^2}{M^2} \ln^k \frac{M}{m}\,. \tag{1.16}$$

This is the important property of the lepton anomaly pointed out in [41, 42] that it is induced by *chirality-flip* interactions (see also (1.14)): the contribution from a heavier particle decouples quadratically with the mass M.[1] The consequence of this observation is two-fold: firstly, the reduced sensitivity of the electron anomaly to any contributions beyond QED and its extremely precise determination [48, 49],

$$a_e^{\text{exp}} = 1159652180.73(28) \times 10^{-12}\ (0.24\,\text{ppb})\,, \tag{1.17}$$

rendered us the most precise determination of the fine structure constant,[2] which in turn is an important input for determinations of other physical quantities. Secondly, the τ lepton anomaly should be the most sensitive quantity to probe new physics. But τ is so shortly lived with a lifetime of 2.906×10^{-13} s that it is impossible to measure its anomalous magnetic moment under current experimental conditions. For the lighter generation, the muon anomaly is more sensitive to the ultraviolet scale than the electron's by a factor of $m_\mu^2/m_e^2 \sim 4 \times 10^4$, thus becoming the next prime candidate for exploring new physics, see [53–61] for recent reviews.

The SM contributions to the muon $(g-2)_\mu$ are typically divided into three parts:

$$a_\mu^{\text{SM}} = a_\mu^{\text{QED}} + a_\mu^{\text{EW}} + a_\mu^{\text{Had}}\,, \tag{1.18}$$

where a_μ^{QED}, a_μ^{EW}, and a_μ^{Had} refer to the QED, electroweak, and hadronic contributions, respectively. We sketch the experimental measurements of the muon $(g-2)_\mu$ before introducing the different SM contributions.

[1] This feature is possible to change for BSM scenarios as non-trivial enhancement mechanism (such as chiral enhancement for leptoquarks) could show up in specific models [43–47].

[2] The situation has changed after the Cs interferometry measurement of the fine structure constant (0.20 ppb) [50], which hints at a deviation from the SM emerging in the anomalous magnetic moment of the electron, $(g-2)_e$, albeit presently only at the level of $2.5\,\sigma$ [45, 46, 51, 52].

1.1.2 Measurements

The measurements of the muon anomalous magnetic moment depend primarily on two weak processes that happen successively. First of all, the parity-violating decay $\pi^\pm \to \mu^\pm + \nu_\mu(\bar{\nu}_\mu)$ produces polarized muons. Later, its spin direction at the time of decay can be inferred from the final-state electron emitted from its predominant three-body decay mode $\mu^\pm \to e^\pm + \nu_e(\bar{\nu}_e) + \bar{\nu}_\mu(\nu_\mu)$.

In detail, the polarized muon beam is injected into a cyclotron with a constant magnetic field $\boldsymbol{B}$. Provided that $\boldsymbol{v} \cdot \boldsymbol{B} = 0$, where $\boldsymbol{v}$ is the velocity of the muon, the cyclotron frequency of the circular motion of the muon is given as

$$\boldsymbol{\omega}_c = -\frac{e}{m_\mu \gamma}\boldsymbol{B}\,, \tag{1.19}$$

where $\gamma = 1/\sqrt{1-v^2}$ is the relativistic Lorentz factor. Inside the magnetic field, the muon spin precesses around the direction of the magnetic field. The Larmor precession frequency of the spin equals to

$$\boldsymbol{\omega}_s = -\frac{e}{m_\mu \gamma}\boldsymbol{B} - a_\mu \frac{e}{m_\mu}\boldsymbol{B}\,. \tag{1.20}$$

Thus, it was observed already in [62, 63] that the spin-precession frequency of the muon would coincide with the cyclotron frequency if the anomalous magnetic moment vanished. To this end, the angular frequency of the muon spin precession around its momentum, the difference between the two frequencies provides a *direct* measurement of a_μ:

$$\boldsymbol{\omega}_a = \boldsymbol{\omega}_s - \boldsymbol{\omega}_c = -a_\mu \frac{e}{m_\mu}\boldsymbol{B}\,. \tag{1.21}$$

In order to sustain the muons' motion inside the cyclotron, a focusing quadrupole electric field $\boldsymbol{E}$ is applied. This electric field modifies the angular frequency according to

$$\boldsymbol{\omega}_a = -\frac{e}{m_\mu}\left[a_\mu \boldsymbol{B} + \left(\frac{1}{\gamma^2-1} - a_\mu\right)\boldsymbol{v}\times\boldsymbol{E}\right]\,, \tag{1.22}$$

which requires an additional impossibly precise measurement of the electric field. Fortunately, we can dodge the problem observing that a special choice of a "magic" γ, $\left(\gamma^2-1\right)^{-1} = a_\mu$, can eliminate the effect of the electric field [64]. Accordingly, the muon beam energy should be tuned to

$$E_\mu = m_\mu \gamma = m_\mu \sqrt{1+\frac{1}{a_\mu}} \approx 3.1\,\text{GeV}\,. \tag{1.23}$$

A possible correction to the muon spin precession could arise from a non-zero EDM of the muon. It would induce an extra spin-precession frequency

$$\boldsymbol{\omega}_\eta = -\eta\frac{e}{2m_\mu}\left(\boldsymbol{E} + \boldsymbol{\beta}\times\boldsymbol{B}\right)\,, \tag{1.24}$$

which would cause an additional vertical precession of the spin and tilt the spin-precession plane of the muon. As a consequence, it is possible to set a new limit on the muon EDM from the muon $(g-2)_\mu$ experiment, $\left|d_\mu\right| < 1.9 \times 10^{-19} e \cdot \text{cm}$ [65].

It is clear from (1.21) that the angular frequency and the magnetic field need to be measured in experiments to determine a_μ. The charge-to-mass ratio of the muon is usually convoluted with the measurement of the magnetic field to reduce further uncertainties. The magnitude ω_a of the angular frequency is extracted from the pattern of the detected electrons, which prefer to decay opposite to the spin directions of the muons owing to the $V-A$ structure of the weak interaction. In that, the number of the detected electrons follows

$$N(t) = N_0 e^{-t/(\tau_\mu \gamma)} \left[1 + A\cos\left(\omega_a t + \phi\right)\right] , \tag{1.25}$$

where τ_μ is the muon lifetime and the oscillation pattern gives access to the determination of ω_a. The magnetic field is measured by the nuclear magnetic resonance of the free proton calibrated to its Larmor precession frequency ω_p and the ratio of the muon-to-proton magnetic moments μ_μ/μ_p from the hyperfine splitting of muonium [66]. In the end, the anomalous magnetic moment is extracted from

$$a_\mu = \frac{R}{\lambda - R} , \tag{1.26}$$

where $R = \omega_a/\omega_p$ and $\lambda = \mu_\mu/\mu_p$.

The recent E821 experiment conducted at Brookhaven National Laboratory (BNL) measured a_μ to be [67, 68]

$$a_\mu^{\text{exp}} = 116592089(54)(33)(63) \times 10^{-11} \, (0.54\,\text{ppm}) , \tag{1.27}$$

achieving a 14-fold improvement in precision over the old classical experiments at Conseil Européen pour la Recherche Nucléaire (CERN) [69]. The first and second errors in the brackets are statistical and systematic; the total error in the last brackets is obtained by adding the statistical and systematic errors in quadrature. There is a (3–4) σ discrepancy between the theoretical calculations and experiments after the release of the BNL results. For this reason, two new ambitious muon $(g-2)_\mu$ experiments have been planned at Fermi National Accelerator Laboratory (Fermilab) [70] aiming for a precision of $\delta a_\mu \approx 16 \times 10^{-11}$ and at Japan Proton Accelerator Research Complex (J-PARC) [71] using a very different technique. As the current theoretical uncertainties are comparable to current experimental errors, progresses on the SM calculation concurrent with advents of the new measurements are expected to provide more precise control of theoretical uncertainties for the comparison to the new results of planned experiments.

1.1.3 QED contributions

Quantum loops involving photons and all charged leptons (e, μ, and τ) are conventionally collected in the QED contributions. The corrections from quarks and electroweak gauge

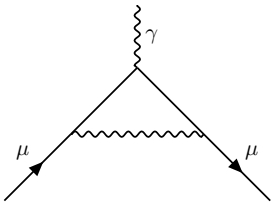

Figure 1.2: One-loop QED contribution to the muon $(g-2)_\mu$.

bosons are mandated to the hadronic and electroweak contributions. In QED, the anomalous magnetic moment is calculated in an expansion in the fine structure constant α,

$$a_\mu^{\text{QED}} = \sum_{n=1}^{\infty} a_\mu^{\text{QED}\,(n)} = \sum_{n=1}^{\infty} c_n \left(\frac{\alpha}{\pi}\right)^n . \tag{1.28}$$

They have been calculated to five loops, starting with the famous Schwinger contribution [72],

$$\begin{aligned} a_\mu^{\text{QED}} = {} & \frac{\alpha}{2\pi} + 0.765857420(13) \left(\frac{\alpha}{\pi}\right)^2 + 24.05050984(26) \left(\frac{\alpha}{\pi}\right)^3 \\ & + 130.8783(58) \left(\frac{\alpha}{\pi}\right)^4 + 751.00(87) \left(\frac{\alpha}{\pi}\right)^5 . \end{aligned} \tag{1.29}$$

Using the most up-to-date a_e-independent determination of the fine structure constant α [50] in (1.29) leads to [61, 73, 74]

$$a_\mu^{\text{QED}} = 116584718.931(104) \times 10^{-11} . \tag{1.30}$$

One-loop result

The one-loop contribution illustrated in Figure 1.2 was first calculated by Schwinger in 1948 [72],

$$a_\mu^{\text{QED}\,(1)} = \frac{\alpha}{2\pi} . \tag{1.31}$$

This calculation was done for the electron almost at the same time when the first precise measurement of its anomalous magnetic moment [75, 76] was performed, but it is universal for all charged leptons. Since it has become a standard quantum field theory textbook calculation nowadays [77–79], we will not repeat its derivation here. This celebrated result made another electrifying success in higher-order QED predictions besides the aforementioned Lamb shift [35].

Two-loop result

The full two-loop diagrams are collected in Figure 1.3, which were firstly calculated in [80–85]. The first seven diagrams contribute to the *universal* term, while the results of

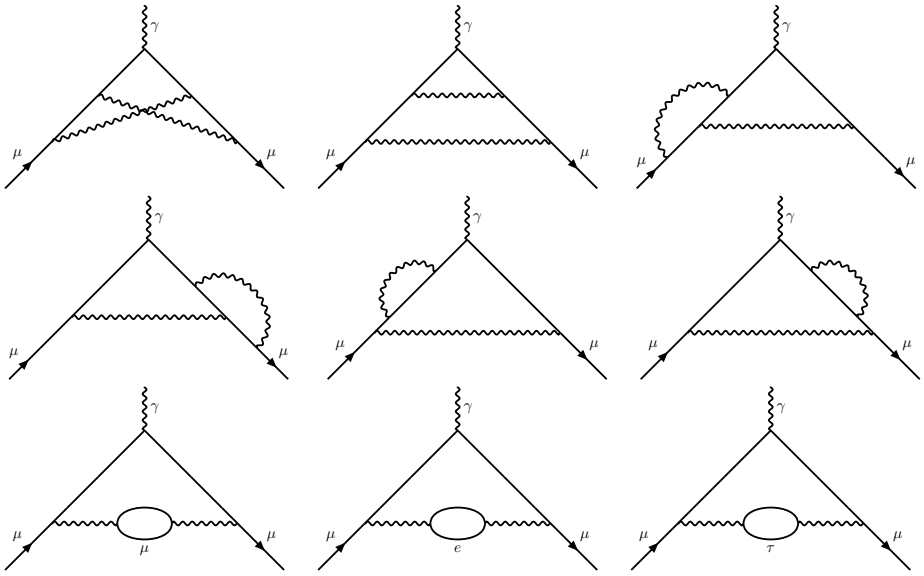

Figure 1.3: Two-loop QED diagrams contributing to the muon $(g-2)_\mu$.

the last two diagrams turn out to be *mass dependent*. A new feature appears at this order of expansion: the universality of lepton anomalies is violated by the mass dependence of the vacuum polarization (VP) diagrams. To this end, we write the two-loop contributions as

$$a_\mu^{\mathrm{QED}\,(2)} = \left[c_2^{\mathrm{uni}} + c_2^{\mathrm{vap}\,(e)} + c_2^{\mathrm{vap}\,(\tau)}\right]\left(\frac{\alpha}{\pi}\right)^2, \tag{1.32}$$

where c_2^{uni}, $c_2^{\mathrm{vap}\,(e)}$, and $c_2^{\mathrm{vap}\,(\tau)}$ represent the universal, electron VP, and τ VP contributions. Adding the counterterms and performing renormalization, the universal part leads to [82–85]

$$c_2^{\mathrm{uni}} = \frac{197}{144} + \frac{3}{4}\zeta(3) - \frac{\pi^2}{2}\ln 2 + \frac{\pi^2}{12}, \tag{1.33}$$

where $\zeta(s) = \sum_{n=1}^{\infty} 1/n^s$ is the Riemann zeta function.

The calculation of the mass-dependent VP diagrams requires insertions of photon self-energies from electron and τ loops. In a gauge-invariant form, it reads

$$\Pi^{\mu\nu}(k) = \left(k^2 g^{\mu\nu} - k^\mu k^\nu\right)\Pi(k^2), \tag{1.34}$$

in which the renormalized self-energy function

$$\Pi^{\mathrm{ren}}(s) = \Pi(s) - \Pi(0) \tag{1.35}$$

satisfies a subtracted dispersion relation

$$\Pi^{\mathrm{ren}}(s) = \frac{s}{\pi}\int_{4m_\ell^2}^{\infty} \mathrm{d}s' \frac{\mathrm{Im}\,\Pi(s')}{s'(s'-s)}. \tag{1.36}$$

The optical theorem links the imaginary part of $\Pi(s)$ to the e^+e^- annihilation cross section into a lepton pair via

$$\operatorname{Im}\Pi(s) = \frac{\alpha}{3} R_{\rm lep}(s)\,, \tag{1.37}$$

and

$$R_{\rm lep}(s) = \frac{\sigma_{\rm lep}(s)}{\sigma_{\rm point}(s)} = \sqrt{1-\frac{4m_\ell^2}{s}}\left(1+\frac{2m_\ell^2}{s}\right), \tag{1.38}$$

where $\sigma_{\rm point}(s) = 4\pi\alpha^2/(3s)$ is the point cross section in the limit $s \gg 4m_\ell^2$. With the input self-energy function $\Pi^{\rm ren}$, the remaining one-loop integral can be evaluated with a modified photon propagator, leading to nothing but the contribution from a massive photon with effective mass $\sqrt{s}$. Accordingly, the entire VP contribution is a convolution of the renormalized self-energy spectral function with the one-loop massive-photon contribution,

$$c_2^{{\rm vap}\,(\ell)} = \frac{\pi}{3\alpha}\int_{4m_\ell^2}^{\infty}\frac{{\rm d}s}{s} R_{\rm lep}(s)\, a_\mu^{{\rm QED}\,(1)\,({\rm massive}\,\gamma)}(s)\,, \tag{1.39}$$

where

$$a_\mu^{{\rm QED}\,(1)\,({\rm massive}\,\gamma)}(s) \equiv \frac{\alpha}{\pi}K(s) = \frac{\alpha}{\pi}\int_0^1 {\rm d}x \frac{x^2(1-x)}{x^2+\left(s/m_\mu^2\right)(1-x)} \tag{1.40}$$

is the one-loop contribution from a massive photon. As a cross-check, we reproduce the Schwinger value (1.31) for $s=0$. Its Feynman-parameter integral can be performed and the result reads [86, 87]

$$K(s) = \frac{x^2}{2}(2-x^2) + \frac{(1+x^2)(1+x)^2}{x^2}\left[\ln(1+x) - x + \frac{x^2}{2}\right] + \frac{1+x}{1-x}x^2\ln x\,, \tag{1.41}$$

where

$$x = \frac{1-\sigma_\mu}{1+\sigma_\mu}\,, \quad \text{and} \quad \sigma_\mu = \sqrt{1-\frac{4m_\mu^2}{s}}\,. \tag{1.42}$$

The integral of (1.39) can be further evaluated analytically resorting to the explicit expression of $K(s)$. Its approximate value was firstly obtained in [80, 81], while the full analytic result was derived in [88] and later given in a compact form as [89]

$$\begin{aligned} c_2^{{\rm vap}\,(\ell)} = &-\frac{25}{36} - \frac{\ln r}{3} + r^2(4+3\ln r) + r^4\left[\frac{\pi^2}{3} - 2\ln r\ln\left(\frac{1}{r}-r\right) - {\rm Li}_2\left(r^2\right)\right] \\ &+ \frac{r}{2}\left(1-5r^2\right)\left[\frac{\pi^2}{2} - \ln r\ln\left(\frac{1-r}{1+r}\right) - {\rm Li}_2(r) + {\rm Li}_2(-r)\right], \end{aligned} \tag{1.43}$$

where $r = m_\ell/m_\mu$ and ${\rm Li}_2(r) = -\int_0^r {\rm d}t\ \ln(1-t)/t$ is the dilogarithmic function.

The VP contributions of electron and τ loops differ drastically due to the mass hierarchy. In order to find their features in a simpler manner, we employ approximations for the massive-photon contribution (1.40). For the electron loop, a logarithmically enhanced term arises for $m_e^2 \ll s \ll m_\mu^2$. In this limit, $a_\mu^{\mathrm{QED}\,(1)\,(\mathrm{massive}\,\gamma)}(s) \approx \alpha/(2\pi)$ and $R_{\mathrm{lep}}(s) \approx 1$. Equation (1.39) reduces to

$$c_2^{\mathrm{vap}\,(e)} \approx \frac{1}{6}\int_{4m_e^2}^{4m_\mu^2} \frac{\mathrm{d}s}{s} = \frac{1}{3}\ln\frac{m_\mu}{m_e}\,. \tag{1.44}$$

This upshot can be understood on more general grounds from the renormalization group evolution of the fine structure constant α under leading-log approximation (1.1). That is, $\alpha(\mu)$ should be evolved to the relevant momentum scale of the physical process, the muon mass m_μ [90],

$$\frac{\alpha(m_\mu)}{\alpha} = 1 + \frac{2\alpha}{3\pi}\ln\frac{m_\mu}{m_e}\,, \tag{1.45}$$

where $\alpha = \alpha(m_e)$ is the fine structure constant in the Thomson limit $\mu \to 0$. If we replace α by $\alpha(m_\mu)$ in (1.31), the leading logarithmic term of VP is reproduced exactly.

On the contrary, for $m_\tau \gg m_\mu$, the dominant contribution arises from the region $s \gg m_\mu^2$. Using the approximation

$$a_\mu^{\mathrm{QED}\,(1)\,(\mathrm{massive}\,\gamma)}(s) \approx \left(\frac{\alpha}{\pi}\right)\frac{m_\mu^2}{3s}\,, \tag{1.46}$$

the contribution becomes

$$c_2^{\mathrm{vap}\,(\tau)} \approx \frac{m_\mu^2}{9}\int_{4m_\tau^2}^{\infty}\frac{\mathrm{d}s}{s^2}\sqrt{1-\frac{4m_\tau^2}{s}}\left(1+\frac{2m_\tau^2}{s}\right) = \frac{m_\mu^2}{45m_\tau^2}\,. \tag{1.47}$$

We find the expected quadratic power suppression of heavy-scale contributions.

Three- to five-loop results

At three-loop order another new topology shows up apart from higher-order VP insertions, light-by-light (LbL) scattering illustrated in the left diagram of Figure 1.4. We divide the three-loop contributions into the following parts:

$$a_\mu^{\mathrm{QED}\,(3)} = \left[c_3^{\mathrm{uni}} + c_3^{\mathrm{vap}\,(e)} + c_3^{\mathrm{vap}\,(\tau)} + c_3^{\mathrm{vap}\,(e\,\tau)} + c_3^{\mathrm{lbl}\,(e)} + c_3^{\mathrm{lbl}\,(\tau)}\right]\left(\frac{\alpha}{\pi}\right)^3\,. \tag{1.48}$$

where $c_3^{\mathrm{lbl}\,(e)}$ and $c_3^{\mathrm{lbl}\,(\tau)}$ label the LbL scattering contributions of electron and τ loops. $c_3^{\mathrm{vap}\,(\ell)}$ contains at least one insertion of VP from lepton ℓ, while $c_3^{\mathrm{vap}\,(e\,\tau)}$ collects contributions

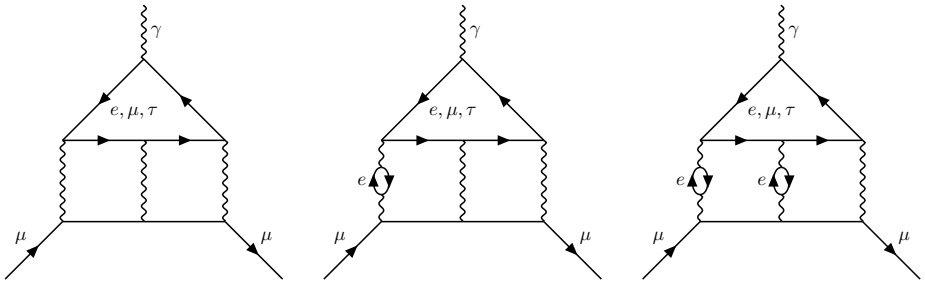

Figure 1.4: The LbL scattering diagrams at three loops and with enhanced electron loops at four and five loops.

from both electron and τ VP loops. The mass-independent contributions have been worked out in a compact form [91],

$$c_3^{\text{uni}} = \frac{28259}{5184} + \frac{17101}{810}\pi^2 - \frac{298}{9}\pi^2 \ln 2 + \frac{139}{18}\zeta(3) + \frac{100}{3}\left[\text{Li}_4\left(\frac{1}{2}\right) + \frac{1}{24}\ln^4 2 - \frac{1}{24}\pi^2 \ln^2 2\right] - \frac{239}{2160}\pi^4 + \frac{83}{72}\pi^2\zeta(3) - \frac{215}{24}\zeta(5)\,, \tag{1.49}$$

where $\text{Li}_4\left(\frac{1}{2}\right) = \sum_{n=1}^{\infty} 1/\left(2^n n^4\right)$ is the polylogarithm.

The electron LbL scattering is enhanced by $\ln\left(m_\mu/m_e\right)$ and also a large prefactor π^2. In comparison, LbL scattering from the τ loop appears to be small. The complete analytic result of mass-dependent contributions at three loops has been made available by thrilling efforts [92–94] and therefore can be expanded in terms of mass ratios to the desired precision.

Calculations of four and five loops could be done along the same path, but the level of difficulties increases enormously. Two of the electron-loop-enhanced diagrams are shown in Figure 1.4. The four-loop universal term c_4^{uni} was almost analytically evaluated [95]. There are some analytic cross-checks in the framework of asymptotic expansions for mass-dependent contributions at four and five loops [96–98], complementary to numerical approaches. The latest four- and five-loop numerical calculations were carried out in [73, 74, 99, 100]. Adding these contributions up to and including five loops, we get the complete QED contributions given in (1.29).

1.1.4 Electroweak contributions

The electroweak contributions include massive gauge and Higgs bosons' loop corrections. They are suppressed at least by a factor of $(\alpha/\pi)(m_\mu^2/M_W^2) \simeq 4 \times 10^{-9}$ and the updated numerical result computed to the two-loop order reads [61, 101, 102]

$$a_\mu^{\text{EW}} = 153.6(1.0) \times 10^{-11}\,. \tag{1.50}$$

Its first one-loop calculations were carried out by five independent groups [103–107] shortly after 't Hooft had proven the renormalizability of the electroweak sector in his PhD

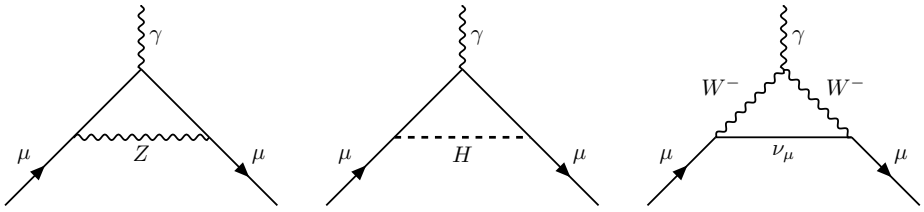

Figure 1.5: Electroweak contributions to a_μ at one loop in the unitary gauge.

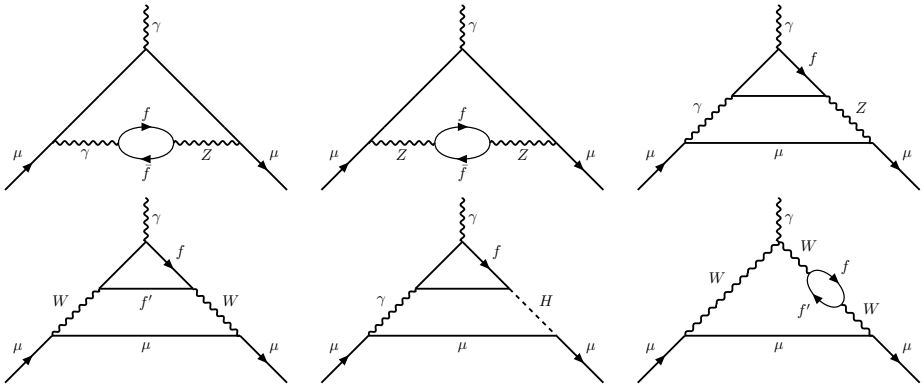

Figure 1.6: Two-loop electroweak contributions to a_μ with fermion loops in the unitary gauge. f and f' represent the $SU(2)_L$-doublet partners. The neutrinos are excluded in f in the triangle subgraphs as they do not couple to the photon.

work [108–110]. The pertinent one-loop diagrams in the physical unitary gauge are depicted in Figure 1.5 and their contributions are collected to

$$a_\mu^{\mathrm{EW}\,(1)} = \frac{G_F m_\mu^2}{8\sqrt{2}\pi^2}\Bigg[\underbrace{\frac{10}{3}}_{W} + \underbrace{\frac{1}{3}\left(1-4\sin^2\theta_W\right)^2 - \frac{5}{3}}_{Z} + O\left(\frac{m_\mu^2}{M_W^2}\right) + O\left(\frac{m_\mu^2}{M_H^2}\right)\Bigg], \tag{1.51}$$

where G_F is the Fermi coupling constant and the weak mixing angle $\sin^2\theta_W = 1 - M_W^2/M_Z^2$. The W and Z boson contribute with different signs. The Higgs contribution is further suppressed by a factor m_μ^2/M_H^2 due to the smallness of its Yukawa coupling to the muon.

The two-loop corrections are usually divided into the fermionic- and bosonic-loop contributions, with the fermionic-loop effects illustrated in Figure 1.6. These two-loop contributions are typically enhanced by large logarithms of $\ln\left(M_Z/m_f\right)$, where f is the fermion inside the fermionic loop. Moreover, they coherently add up to a sizable negative value $-41.2(1.0)10^{-11}$ even comparable to the one-loop corrections $194.8(0.0)\times10^{-11}$ [101, 102]. The top-left and top-right diagrams of Figure 1.6 are logarithmically dominant compared to the rest. However, the top-left γZ-mixing diagram is suppressed by the vector coupling $1-4\sin^2\theta_W \sim 0.1$ compared to the top-right $\gamma\gamma Z$-vertex diagram. The most prominent features at this order are the occurrences of the non-perturbative hadronic effects

symbolically represented inside the light-quark (u, d, and s) loops and the vector–vector–axialvector (VVA) anomaly [111–113] (see Section 1.3 for more details) in the triangle fermionic loops.

The first calculation of these logarithmic corrections was performed in 1992 [114], which however only included the leptons in the triangle loops. Obviously, the anomaly cancellation in the SM [115–117] demands each full fermion generation to be involved. These refined analyses were provided by [118–121], which indeed showed that the coefficient of the leading $\ln\left(M_Z/m_f\right)$ term vanishes for the first and second generations because of the anomaly-cancellation condition

$$\sum_f N_f I_3^f Q_f^2 = 0\,, \tag{1.52}$$

where $N_f = 1(3)$ for leptons (quarks), I_3^f is the third component of the weak isospin, and Q_f is the electric charge. For the third generation, there is an imbalance because of the mass hierarchy. The account of hadronic effects inside the fermion loops was pioneered in [118] and later improved in [101, 122]. Closely following [101], the $\gamma\gamma Z$ anomalous amplitude exhibits the longitudinal and transversal structure functions $w_{L,T}(q^2)$. Because of the topological nature of anomalies, the longitudinal structure function w_L is not renormalized in higher-order perturbative QCD (pQCD). Furthermore, non-perturbative corrections to w_L are absent thanks to the 't Hooft anomaly matching condition [123]. This behavior was carried forward to the transversal function by Vainshtein [124], who showed that

$$w_L(q^2)|_{m_f=0} = 2w_T(q^2)|_{m_f=0} = \frac{-2N_f Q_f^2}{q^2} \tag{1.53}$$

is valid in pQCD to all orders in the chiral limit. Therefore, corrections to w_T must be of non-perturbative origin. These features should be and have been consistently accounted for when considering perturbative and non-perturbative effects in the triangle amplitude.

The bosonic contributions were calculated resorting to asymptotic expansions in masses [120], and were refined later by [125, 126]. The theoretical prediction for the QED and electroweak contributions is determined with small well-controlled uncertainties.

1.1.5 Hadronic contributions

The hadronic contributions in particular refer to those corrections with hadronic effects among the electromagnetic (QED) interaction. The electroweak corrections with insertions of hadronic loops are already included in the electroweak contributions a_μ^{EW} as explained in Section 1.1.4, with a result found to be of the order of the experimental error. The hadronic contributions are hard to tackle in first-principles calculations and thus dominate the uncertainties of the theoretical prediction for the muon $(g-2)_\mu$. They fall into two different categories: HVP and HLbL scattering, as shown in Figure 1.7. Although these

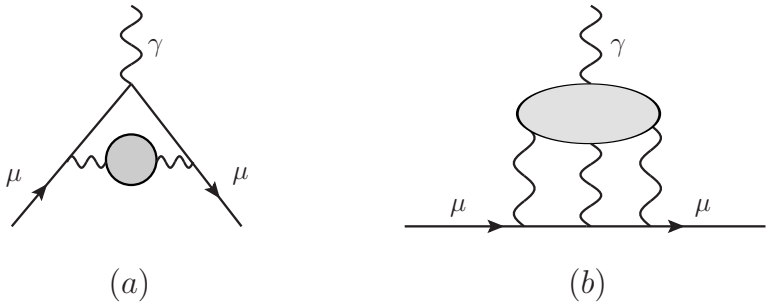

Figure 1.7: Diagrammatic representation of (a) HVP and (b) HLbL.

two contributions are of non-perturbative nature, it is possible to make estimates of them utilizing a data-driven approach or a lattice QCD simulation. We only review some general aspects of these two contributions here, more details are relegated to the main parts of the thesis.

Hadronic vacuum polarization

HVP turns out to be the leading hadronic contribution entering at $O(\alpha^2)$ in the expansion of the fine structure constant. A coarse estimate of the total contribution can be made based on the previous observations that

$$a_\mu^{\text{HVP}} \sim \left(\frac{\alpha}{\pi}\right)^2 \frac{m_\mu^2}{M_{\text{had}}^2} \sim 6000 \times 10^{-11} \,, \tag{1.54}$$

when the hadronic scale M_{had} is chosen to be 1 GeV. Given the scale of the muon mass, non-perturbative effects of the strong interaction cannot be eluded at all. We take dispersion relations to rescue: HVP can be related to the total cross section of $e^+e^- \to$ hadrons using the optical theorem. In analogy to the lepton VP contributions, the leading-order (LO) HVP contribution in diagram (a) of Figure 1.7 can be represented as [86, 87]

$$a_\mu^{\text{HVP}} = \left(\frac{\alpha m_\mu}{3\pi}\right)^2 \int_{s_{\text{th}}}^{\infty} \mathrm{d}s \frac{\hat{K}(s)}{s^2} R_{\text{had}}(s) \,, \tag{1.55}$$

with the kernel function

$$\hat{K}(s) = \frac{3s}{m_\mu^2} K(s) \,, \tag{1.56}$$

where $K(s)$ is given in (1.41), and the hadronic *bare* cross section

$$R_{\text{had}}(s) = \frac{\sqrt{1 - 4m_e^2/s}}{1 + 2m_e^2/s} \frac{\sigma^0\left(e^+e^- \to \text{hadrons}\right)}{4\pi\alpha^2/(3s)} \,. \tag{1.57}$$

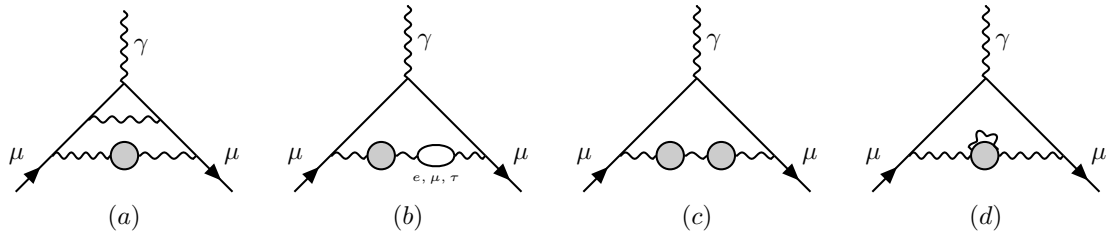

Figure 1.8: Next-to-leading order HVP contributions.

Note that $R_{\text{had}}(s)$ is not exactly the usual R ratio defined as $\sigma^0(e^+e^- \to \text{hadrons})/\sigma_{\text{point}}$, but coincides for a tree-level muonic cross section and in the limit $s \gg m_\mu^2$.

The kernel function $\hat{K}(s)$ in (1.55) monotonically increases from 0.63... to 1 from the 2π threshold to infinity. Therefore, the integrand of (1.55) is weighted by a factor of $1/s^2$ such that the low-energy region is enhanced and a rapid convergence of the integral is expected. The hadronic cross sections are measured by either energy-scan or radiative-return methods. At low energies, data of exclusive channels are available. The main subtlety turns out to be the combination of different data sets in a statistically consistent manner. Inclusive data can be used in the intermediate energy range. Beyond the resonance region, pQCD is exploited to estimate $R_{\text{had}}(s)$ (see Section 1.2.4). Although the use of hadronic τ-decay data was advocated in [127], unexpected caveats in the theoretical treatment prevent it from making a prediction at a commensurate level as the e^+e^- data.

The next-to-leading-order (NLO) HVP contributions are shown in Figure 1.8. The diagrams (a)–(c) are convoluted with new kernel functions [128, 129],

$$
\begin{aligned}
a_\mu^{\text{HVP}\,(2),\,(i)} &= \left(\frac{\alpha}{\pi}\right)^3 \frac{2}{3} \int_{s_{\text{th}}}^{\infty} \frac{\mathrm{d}s}{s} R_{\text{had}}(s) K^{(i)}(s)\,, \quad i = a, b\,; \\
a_\mu^{\text{HVP}\,(2),\,(c)} &= \left(\frac{\alpha}{\pi}\right)^3 \frac{1}{9} \int_{s_{\text{th}}}^{\infty} \int_{s_{\text{th}}}^{\infty} \frac{\mathrm{d}s}{s} \frac{\mathrm{d}s'}{s'} R_{\text{had}}(s) R_{\text{had}}(s') K^{(c)}(s, s')\,,
\end{aligned}
\tag{1.58}
$$

whilst the (d)-type contributions are allowed for by including the final-state radiation (FSR) into the hadronic cross section $\sigma^0(e^+e^- \to \text{hadrons})$.

HVP has been evaluated to the next-to-next-to-leading order (NNLO) [130] ($12.4(0.1) \times 10^{-11}$) and the most recent representative total estimate based on e^+e^- data is given as [61, 130–136]

$$
a_\mu^{\text{HVP}} = 6845(40) \times 10^{-11}\,. \tag{1.59}
$$

Hadronic light-by-light scattering

At $O(\alpha^3)$, a new topology, the lowest-order HLbL scattering shows up. Unlike the HVP effects, the four-point HLbL tensor involves complex insertions of hadronic subgraphs in contrast to the two-point HVP function, such that its total contribution cannot be related to *one simple* observable in dispersion relations. Instead, different long- and short-distance

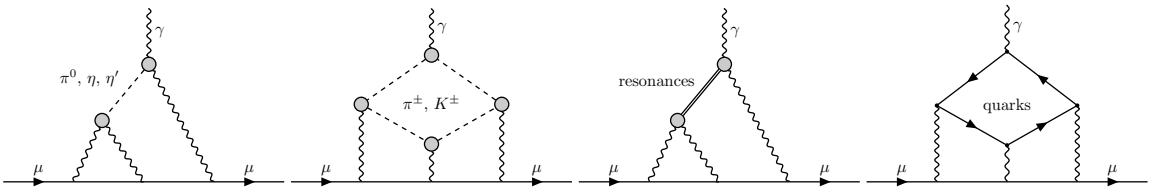

Figure 1.9: Decomposition of HLbL contributions in model calculations.

contributions	large-N_c expansion	chiral expansion
pseudoscalar poles $\pi^0,\ \eta,\ \eta'$	N_c	p^8
meson loops $\pi^\pm,\ K^\pm$	1	p^6
resonances $f_0,\ a_1,\ f_2$	N_c	p^{10}
quark loops	N_c	p^{10}

Table 1.2: Orders of leading contributions in large-N_c and chiral expansions.

contributions have to be taken into account separately in early model calculations following QCD and respecting its symmetries, as depicted in Figure 1.9.

The low- and high-energy constraints of the HLbL scattering amplitude can be derived from certain limits of QCD: large-N_c expansion, chiral expansion, or perturbative expansion in terms of α_s. A classification of the different contributions coming from the dominant intermediate hadronic states appealing to the large-N_c and chiral power countings [137] is shown in Table 1.2. In the framework of the operator product expansion (OPE), the HLbL scattering amplitude in a specific kinematic configuration can be related to the VVA triangle amplitude [138], of which we know the asymptotic behavior better. These expansion methods not only play an important role in identifying the properties of the HLbL scattering amplitude itself, but also in each individual contribution where relevant form factors and scattering amplitudes enter. Therefore, some of these theoretical tools will be explained in Section 1.2.

The complication of HLbL scattering is also reflected in the fact that it is difficult to make a prior estimate for it. Only after realizing that the N_c-enhanced contributions prevail over the chirally enhanced ones, we may arrive at an estimate:

$$a_\mu^{\mathrm{HLbL}} \sim \left(\frac{\alpha}{\pi}\right)^3 \left(N_c \frac{m_\mu}{M_{\mathrm{had}}}\right)^2 \sim 100 \times 10^{-11} \ . \tag{1.60}$$

In particular, for the numerically dominant pseudoscalar-pole contributions, we can make use of the Wess–Zumino–Witten effective Lagrangian [139, 140],

$$\mathcal{L}_{\mathrm{WZW}} = -\frac{\alpha N_c}{24\pi F_\pi} F_{\mu\nu}\tilde{F}^{\mu\nu}\left(\pi^0 + \frac{1}{\sqrt{3}}\eta_8 + \frac{2\sqrt{2}}{\sqrt{3}}\eta_0\right), \tag{1.61}$$

where F_π is the pion decay constant and $\tilde{F}^{\mu\nu} = \varepsilon^{\mu\nu\alpha\beta}F_{\alpha\beta}$. η_8 and η_0 are mixtures of the physical states η and η'. Furthermore, the charged-pion loop at low energies can be derived from scalar QED

$$\mathcal{L}_{\text{sQED}} = |D_\mu \boldsymbol{\pi}|^2 - M_\pi^2|\boldsymbol{\pi}|^2 - \frac{1}{4}F_{\mu\nu}F^{\mu\nu} \,. \tag{1.62}$$

However, low-energy theories are not adequate to describe the entire contributions as, for instance, we would find a divergent result for the pion pole unless we impose a physical ultraviolet cut-off at the scale of vector mesons. This is related to the involvement of very different soft and hard scales in the integrand of HLbL scattering. Consequently, as stressed in [141], previous calculations of the HLbL contributions are mainly based on hadronic models with guessed uncertainties, which were built at most in line with the QCD chiral and short-distance constraints.

In this regard, a dispersive framework for a *model-independent* evaluation of HLbL scattering based on the general principles of analyticity, unitarity, and crossing symmetry has been recently developed [142–146]. Such a framework, based on the analytic structure of the HLbL four-point amplitude and reconstruction of it from dispersion relations, directly attributes a_μ^{HLbL} to experimentally accessible observables like form factors and scattering amplitudes. Following this spirit in a fully data-driven determination of HLbL scattering, dedicated efforts have completed the evaluations of the $\pi\pi$ contribution [147, 148], pion-pole contribution [149, 150], and short-distance constraints [151, 152][3].

Since a complete dispersive evaluation of HLbL scattering is not yet available, we will adopt one representative phenomenology + lattice QCD combined estimate [61, 138, 147–153, 159–161], including the NLO HLbL contribution [162]:

$$a_\mu^{\text{HLbL}} = 92(18) \times 10^{-11}. \tag{1.63}$$

1.1.6 Standard Model and beyond the Standard Model predictions

Adding up the QED, electroweak, and hadronic contributions discussed in the previous Sections, the total prediction for the muon $(g-2)_\mu$ in the SM amounts to [61]

$$a_\mu^{\text{SM}} = 116591810(43) \times 10^{-11} \,. \tag{1.64}$$

In comparison to the experiment,

$$\Delta a_\mu = a_\mu^{\text{exp}} - a_\mu^{\text{SM}} = 279(76) \times 10^{-11} \,, \tag{1.65}$$

this shows a discrepancy of $3.7\,\sigma$ standard deviation. Notwithstanding the fact that it may be induced by imprecise SM calculations or statistical fluctuations in experiment, the discrepancy could also stem from potential BSM contributions. Accordingly, we will discuss general parameterizations of new-physics contributions closely following [55] and introduce some of the specific models thereafter.

[3] See also [153–158].

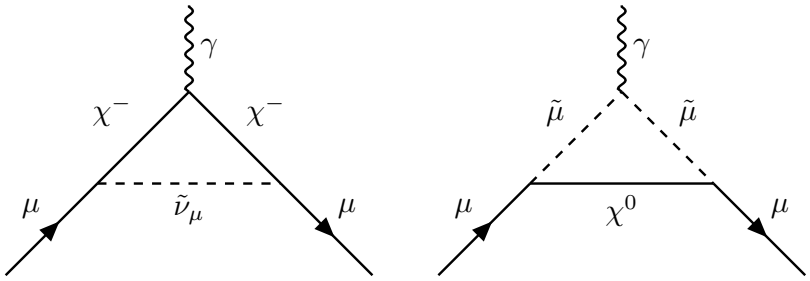

Figure 1.10: Lowest-order SUSY contributions to the muon $(g-2)_\mu$.

We assume a Dirac fermion with mass M and an exotic boson with mass M_0 for the general new interaction. The coupling strength of this interaction is f. For a general one-loop contribution from an neutral exotic boson exchange,

$$a_\mu^{\mathrm{NP}} = \frac{f^2}{4\pi^2}\frac{m_\mu^2}{M_0^2}L\,, \quad L = \frac{1}{2}\int_0^1 \mathrm{d}x \frac{Q(x)}{(1-x)\left(1-\lambda^2 x\right)+(\epsilon\lambda)^2 x}\,, \tag{1.66}$$

where $\epsilon = M/m_\mu$ and $\lambda = m_\mu/M_0$. The explicit form of $Q(x)$ depends on different types of interactions. For a charged boson, the contribution reads

$$a_\mu^{\mathrm{NP}} = \frac{f^2}{4\pi^2}\frac{m_\mu^2}{M_0^2}L\,, \quad L = \frac{1}{2}\int_0^1 \mathrm{d}x \frac{Q(x)}{\lambda^2(1-x)\left(\epsilon^2-x\right)+x}\,, \tag{1.67}$$

where $Q(x)$ is again dependent on interaction types.

Supersymmetry

Supersymmetry (SUSY) extends the space-time symmetry to include the symmetry mapping between bosons and fermions [163]. Each particle is conjectured to present a superpartner, which has the same mass but the spin differing by one-half unit. As these addenda to the particle spectrum have not been observed yet, the symmetry should be broken in a way to generate heavier superpartners. As pointed out in [164], the anomalous magnetic moment of the matter fermion vanishes in the originally proposed exact supersymmetric model [163]. Nevertheless, in the broken minimal supersymmetric extension of the SM, the contributing one-loop chargino–sneutrino and neutralino–smuon diagrams are shown in Figure 1.10. The contributions in a simplified form read [165]

$$a_\mu^{\mathrm{SUSY}\,(\chi^\pm)} = \frac{\tan\beta}{32\pi^2}\frac{m_\mu^2}{M_{\mathrm{SUSY}}^2}g_2^2\,, \quad a_\mu^{\mathrm{SUSY}\,(\chi^0)} = \frac{\tan\beta}{192\pi^2}\frac{m_\mu^2}{M_{\mathrm{SUSY}}^2}\left(g_1^2-g_2^2\right)\,, \tag{1.68}$$

where $\tan\beta$ is the ratio of the vacuum expectation values of the two Higgs doublets, and M_{SUSY} is the mass of the superpartners. The g_1 and g_2 are the $U(1)_Y$ and $SU(2)_L$ gauge couplings. The dominant contribution is from the chargino–sneutrino diagram.

Technicolor and compositeness

In contrast to the standard Higgs mechanism, technicolor models are speculated to *dynamically* generate masses for the gauge bosons via broken new strong interactions. Inspired by technicolor, in the composite Higgs model [166], the Higgs particle is envisaged as a pseudo-Goldstone boson of a spontaneously broken new strongly interacting sector. In these models, the gauge bosons could have an anomalous coupling departing from the SM, and in view of the γW^+W^- effective Lagrangian with two parameters κ and λ, the one-loop correction is given as

$$a_\mu^{\mathrm{TEC}\,(W^\pm)} = \frac{G_F m_\mu^2}{4\sqrt{2}\pi^2}\Big[(\kappa-1)\ln\frac{\Lambda^2}{M_W^2} - \frac{\lambda}{3}\Big], \tag{1.69}$$

where the cut-off Λ is the compositeness scale.

Extra dimensions

In extra dimensions, our four-dimensional space-time is embedded into a higher-dimensional space-time. The extra spatial dimensions are called compactified, with a characteristic length scale R. Extra dimensions are required in string theory, and extra-dimensional theories can explain the observed hierarchy between the electroweak scale and the Plank scale. Usually in this type of theories, the corrections to a_μ enter with a minus sign, hence it is difficult to explain the persistent discrepancy.

1.2 Theoretical tools

1.2.1 Theory of scattering processes

S-matrix theory

S-matrix theory is the general theory of scattering and decay of particles in quantum mechanics and quantum field theory, focusing on the direct study of the properties of the scattering amplitudes. It can be defined without the underlying quantum fields, and was once proposed to replace the local quantum field theory when perturbative calculations of the strong interaction were plagued with proliferated numbers of observed hadrons and convergence issues because of the strong coupling. It flourished in the 1960s, culminated in the so called "*S*-matrix school." In a textbook from that time [167], the authors state: "For both electromagnetic and weak interactions one normally works inside the framework of quantum filed theory[†][...]. The interaction is described in terms of an interaction Hamiltonian (or Lagrangian) constructed from field operators. On the other hand, the approach which so far has been most successful for describing strong interactions is based on the unitarity, analyticity and crossing properties of the so-called *S*-matrix elements." After the advent of QCD and its triumph in the description of the strong interaction, the

S-matrix approach faded out from the mainstream theories. Interestingly, it was revived from the 1990s on in phenomenological applications in combination with effective field theories and in multi-loop calculations. This comeback is clearly reflected in a more recent textbook [79]: "Again, in closing words I mumble something (from steepest descent to integral to what?) about modifying the form of the path integral. The recursion program and the resuscitated S-matrix approach might be a step in this direction, formulating field theory while avoiding mention of a local Lagrangian. But we need analyticity, and of course analyticity follows from locality and causality, as far as we understand."

In scattering processes of short-range interacting particles, incoming particles in the remote past $t \to -\infty$ are well separated in spatial configuration such that they can be approximately treated as free particles. These particles undergo interactions in a finite time interval when they approach each other and evolve into the asymptotic final states of outgoing free particles in the remote future $t \to +\infty$. These asymptotic incoming and outgoing states are called $|\text{in}\rangle$ and $|\text{out}\rangle$ states. Since the incoming and outgoing particles are well separated from each other, $|\text{in}\rangle$ and $|\text{out}\rangle$ states are eigenstates of the full 4-momentum operator of the system, containing the interaction term as well.

For simplicity, we consider scattering of spinless particles of identical mass. Let $|p_1, \ldots, p_n; \text{in}\rangle$ denote the initial state consisting of n incoming particles and $|q_1, \ldots, q_m; \text{out}\rangle$ denote the final state consisting of m outgoing particles. The evolution from the asymptotic $|\text{in}\rangle$ state to asymptotic $|\text{out}\rangle$ state is given by the S-matrix,

$$|q_1, \ldots, q_m; \text{out}\rangle = S^\dagger \, |q_1, \ldots, q_m; \text{in}\rangle \ . \tag{1.70}$$

It contains all the dynamical information of the evolution of the physical states in time. The $|\text{in}\rangle$ and $|\text{out}\rangle$ states are constructed to fulfill the orthonormality condition separately and are postulated to form two complete bases of the Fock space of the interacting theory. The completeness relations for these two bases read

$$\begin{aligned} \mathbb{1} &= |0\rangle\langle 0| + \sum_{n=1}^{\infty} \frac{1}{n!} \int \frac{\mathrm{d}^3 \boldsymbol{p}_1}{(2\pi)^3 2E_{\boldsymbol{p}_1}} \cdots \frac{\mathrm{d}^3 \boldsymbol{p}_n}{(2\pi)^3 2E_{\boldsymbol{p}_n}} \, |p_1, \ldots, p_n; \text{in}\rangle \langle p_1, \ldots, p_n; \text{in}| \\ &= |0\rangle\langle 0| + \sum_{m=1}^{\infty} \frac{1}{m!} \int \frac{\mathrm{d}^3 \boldsymbol{q}_1}{(2\pi)^3 2E_{\boldsymbol{q}_1}} \cdots \frac{\mathrm{d}^3 \boldsymbol{q}_m}{(2\pi)^3 2E_{\boldsymbol{q}_m}} \, |q_1, \ldots, q_m; \text{out}\rangle \langle q_1, \ldots, q_m; \text{out}| \ , \end{aligned} \tag{1.71}$$

where $|0\rangle$ is the vacuum state of the theory and $E_{\boldsymbol{p}}$ is the energy of the particle. Since the S-matrix transforms these two complete bases into each other, it fulfills the unitarity relation

$$S S^\dagger = S^\dagger S = \mathbb{1} \ , \tag{1.72}$$

which is also the requirement of probability conservation. Using the unitarity relation (1.72), one can derive another three similar relations from (1.70),

$$\begin{aligned} &\langle q_1, \ldots, q_m; \text{in}| = \langle q_1, \ldots, q_m; \text{out}| \, S^\dagger, \quad |q_1, \ldots, q_m; \text{in}\rangle = S \, |q_1, \ldots, q_m; \text{out}\rangle \ , \\ &\langle q_1, \ldots, q_m; \text{out}| = \langle q_1, \ldots, q_m; \text{in}| \, S \ , \end{aligned} \tag{1.73}$$

and express the S-matrix as

$$S = \sum_m |q_1, \ldots, q_m; \text{in}\rangle \langle q_1, \ldots, q_m; \text{out}| \ ,$$
$$S^\dagger = \sum_m |q_1, \ldots, q_m; \text{out}\rangle \langle q_1, \ldots, q_m; \text{in}| \ , \tag{1.74}$$

using orthonormality condition and completeness relation.

The probability amplitude for the transition from initial state to final state is given by the S-matrix element,

$$\begin{aligned}\langle q_1, \ldots, q_m; \text{out}|p_1, \ldots, p_n; \text{in}\rangle &= \langle q_1, \ldots, q_m; \text{in}|S|p_1, \ldots, p_n; \text{in}\rangle \\ &= \langle q_1, \ldots, q_m; \text{out}|S|p_1, \ldots, p_n; \text{out}\rangle \ ,\end{aligned} \tag{1.75}$$

such that the $|\text{in}\rangle$ or the $|\text{out}\rangle$ state labels can be safely omitted. Any scattering experiments can be predicted once the S-matrix elements are known since the square of the matrix elements produces the probability for the processes to happen.

Another general property of the S-matrix comes from the consequences of translation and Lorentz invariance of the theory. For an arbitrary translation and proper orthochronous Lorentz transformation

$$x \mapsto \Lambda x + a \ , \tag{1.76}$$

the group representation of the transformation on the Hilbert space of quantum states can be implemented as a unitary operator $U(\Lambda, a)$ given that the states are relativistically normalized. The requirement of relativistic invariance leads to the constraint for the S-matrix,

$$U(\Lambda, a) S U^\dagger(\Lambda, a) = S \ . \tag{1.77}$$

Unitarity and analyticity

In scattering experiments, particles may collide with each other to produce some other particles. But it is also possible that final-state particles remain exactly the same as initial-state particles with the same outgoing momenta as incoming momenta. In order to separate the interesting interaction part from the trivial non-interaction part, one often divides the S-matrix into unity and the T-matrix,

$$S = \mathbb{1} + iT \ , \tag{1.78}$$

where the T-matrix contains the non-trivial interaction part. T-matrix elements can be obtained from the T-matrix,

$$\langle q_1, \ldots, q_m|T|p_1, \ldots, p_n\rangle = (2\pi)^4 \delta^4(p_f - p_i) M_{fi} \ , \tag{1.79}$$

which also defines the transition amplitude M_{fi} and i and f are shorthand notations for the initial and final states. $p_i = p_1 + \cdots + p_n$ and $p_f = q_1 + \cdots + q_m$ are the total 4-momenta of

incoming and outgoing particles, respectively. The momentum conserving delta function is the direct consequence of translation invariance of the system and is explicitly separated out from the transition amplitude. Since the left-hand side of (1.79) and the delta function $\delta^4(p_f - p_i)$ are Lorentz invariant, the transition amplitude M_{fi} must also be Lorentz invariant.

The relation (1.72) implies a unitarity condition for the T-matrix,

$$-i(T - T^\dagger) = T^\dagger T = TT^\dagger \,. \tag{1.80}$$

Taking the matrix element gives

$$-i\,\langle q_1, \ldots, q_m|(T - T^\dagger)|p_1, \ldots, p_n\rangle = \langle q_1, \ldots, q_m|T^\dagger T|p_1, \ldots, p_n\rangle \,. \tag{1.81}$$

According to (1.79), the left-hand side of (1.81) becomes

$$-i\,\langle q_1, \ldots, q_m|(T - T^\dagger)|p_1, \ldots, p_n\rangle = -i(2\pi)^4\delta^4(p_f - p_i)(M_{fi} - M_{if}^*) \,. \tag{1.82}$$

As the next step, one needs to insert complete sets of intermediate states in the right-hand side of (1.81),

$$\begin{aligned}\langle q_1, \ldots, q_m|T^\dagger T|p_1, \ldots, p_n\rangle = \sum_j \frac{1}{j!}\int \frac{\mathrm{d}^3\boldsymbol{k}_1}{(2\pi)^3 2E_{\boldsymbol{k}_1}} \cdots \frac{\mathrm{d}^3\boldsymbol{k}_j}{(2\pi)^3 2E_{\boldsymbol{k}_j}} \\ \times \left\langle q_1, \ldots, q_m\middle|T^\dagger\middle|k_1, \ldots, k_j\right\rangle \left\langle k_1, \ldots, k_j\middle|T\middle|p_1, \ldots, p_n\right\rangle \,.\end{aligned} \tag{1.83}$$

Using (1.79), one finds in the end for the transition amplitude,

$$\begin{aligned}-i(M_{fi} - M_{if}^*) = \sum_j \frac{1}{j!}\int \frac{\mathrm{d}^3\boldsymbol{k}_1}{(2\pi)^3 2E_{\boldsymbol{k}_1}} \cdots \frac{\mathrm{d}^3\boldsymbol{k}_j}{(2\pi)^3 2E_{\boldsymbol{k}_j}} (2\pi)^4\delta^4\Big(p_i - \sum_{l=1}^{j} k_l\Big) \\ \times M^*(q_1, \ldots, q_m \to \{k_j\}) M(p_1, \ldots, p_n \to \{k_j\}) \,,\end{aligned} \tag{1.84}$$

times an overall delta function $(2\pi)^4\delta^4(p_f - p_i)$. The set $\{k_j\}$ represents the intermediate states labels $k_1, \ldots, k_j$. For parity and time-reversal symmetric processes, as it is the case for the strong interaction, we have

$$\begin{aligned}\langle q_1, \ldots, q_m|T|p_1, \ldots, p_n\rangle &= \langle \tilde{q}_1, \ldots, \tilde{q}_m|(\hat{P}\hat{T})^{-1}(\hat{P}\hat{T})T(\hat{P}\hat{T})^{-1}(\hat{P}\hat{T})|\tilde{p}_1, \ldots, \tilde{p}_n\rangle^* \\ &= \langle p_1, \ldots, p_n|T|q_1, \ldots, q_m\rangle \,,\end{aligned} \tag{1.85}$$

which leads to the relation $M_{fi} = M_{if}$ for the transition amplitude. Consequently, the left-hand side of (1.84) becomes exactly $2\mathrm{Im}\, M_{fi}$. Noting that the first line on the right-hand side of (1.84) is nothing but the j-body phase space, we find

$$2\mathrm{Im}\, M_{fi} = \sum_j \int \mathrm{d}\Pi_j\, M_{fj}^*\, M_{ij} \,, \tag{1.86}$$

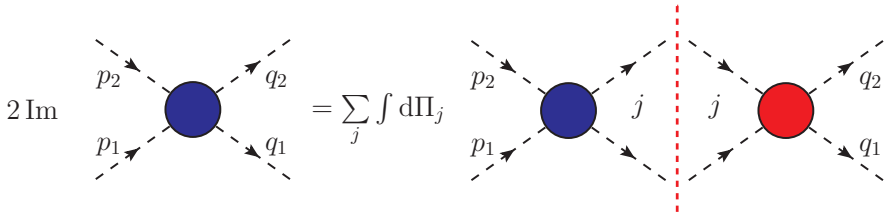

Figure 1.11: Graphical representation of (1.86) in the case of $2 \to 2$ scattering. The imaginary part of the scattering amplitude gets contributions from all possible intermediate states.

where $\mathrm{d}\Pi_j$ is the abbreviation for the Lorentz-invariant j-body phase space. Equation (1.86) relates the imaginary part of the transition amplitude to the sum of the products of transition amplitudes of scattering processes from initial and final states to intermediate states. The Graphical form of (1.86) for a $2 \to 2$ scattering process is shown in Figure 1.11, from which one can see the physical image clearly.

The master formula (1.86) yields stringent constraints on the imaginary parts of the transition amplitudes, hence on the transition amplitudes themselves, and especially on their analytic properties. For a two-particle scattering process, the two-particle intermediate state is called elastic and other heavier intermediate channels are referred to as inelastic. When the total energy is above the elastic intermediate-state threshold and below the first inelastic threshold, the imaginary part of the transition amplitude is solely determined by the elastic scattering amplitude. Above the inelastic scattering threshold, one new term must be added to the right-hand side of the master formula (1.86) once a new physical scattering process is allowed to happen. It means that the imaginary part of the transition amplitude has a singularity structure at each energy threshold of a new physical scattering process. As the consequence, the thresholds become branch points of transition amplitudes regarded as functions of complex energy-squared and physical scattering amplitudes are given by the real-boundary values of analytic functions of complex variables [168].

More explicitly, the elastic scattering amplitude M is a function of total energy-squared s and transfer momentum-squared t defined in (1.96) for a general $2 \to 2$ scattering process. For the moment we will keep t fixed and consider the scattering amplitude $M(s)$ as a function of s only. We assume that no selection rule forbids the creation of any specific number of particles from the two-particle state. As discussed in the previous paragraph, $M(s)$ exhibits branch points at $s = 4m^2,\ 9m^2,\ 16m^2, \ldots$, which are the production thresholds of multi-particle intermediate states. These thresholds are called normal thresholds and s must be at least $4m^2$ to ensure the physical scattering to happen. The elastic scattering can also be mediated by a single-particle state as shown in Figure 1.12. Perturbation theory shows that this single-particle state contributes as a simple pole but not a branch point for the scattering amplitude at the unphysical energy-squared value

$$s = m^2 \ . \tag{1.87}$$

The singularity structure of the scattering amplitude due to the pole and branch points in

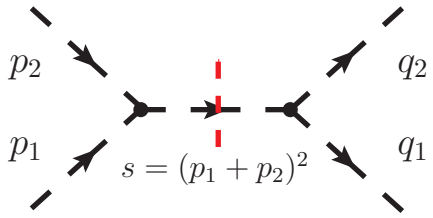

Figure 1.12: Elastic $2 \to 2$ scattering by a single-particle intermediate state.

the complex s-plane is plotted in Figure 1.13. For each branch point, the branch cut runs along the real axis from the branch point to infinity. The branch-cut structure suggests that there exist several Riemann sheets for the analytic scattering amplitude. On each Riemann sheet, the scattering amplitude takes the value of one single analytic branch. The sheet on which the physical scattering amplitude is obtained along the real-boundary cut is called the physical sheet and other sheets are known as unphysical sheets.

Going one step backwards, the analyticity of the S-matrix is often claimed as the outcome of micro-causality. On the field-theoretical level, causality demands that scalar fields commute with each other

$$[\phi(x_1),\, \phi(x_2)] = 0\,, \tag{1.88}$$

and fermionic fields anticommute with each other

$$\{\psi(x_1),\, \psi(x_2)\} = 0\,, \tag{1.89}$$

outside the light-cone where the space-time arguments x_1 and x_2 fulfill $(x_1 - x_2)^2 < 0$. Nevertheless, very few analytic properties of the S-matrix can be rigorously proven in the framework of quantum field theory without relying on perturbative expansions, even though analytic properties of the transition amplitudes were shown to emerge in perturbation series order by order. Thus in the following we will relate causality to analyticity by taking a simple example in classical physics into account: a single-variable transition amplitude $A(\omega)$ as a function of energy ω can be expressed by the Fourier transform as

$$A(\omega) = \frac{1}{2\pi} \int_{-\infty}^{+\infty} A(t) e^{i\omega t}\, \mathrm{d}t\,, \tag{1.90}$$

where $A(t)$ is the Fourier transformed pair function in the time domain t. Because of causality, $A(t)$ should be a retarded function that fulfills $A(t) = 0$ for $t < 0$. $A(\omega)$ then reads

$$A(\omega) = \frac{1}{2\pi} \int_{0}^{+\infty} A(t) e^{i\omega t}\, \mathrm{d}t\,. \tag{1.91}$$

This integral is absolutely convergent for $\mathrm{Im}\,\omega > 0$ as long as $A(t)$ increases slower than κt^N for some fixed N when $t \to +\infty$. Since $e^{i\omega t}$ is an entire function of ω, $A(\omega)$ is analytic

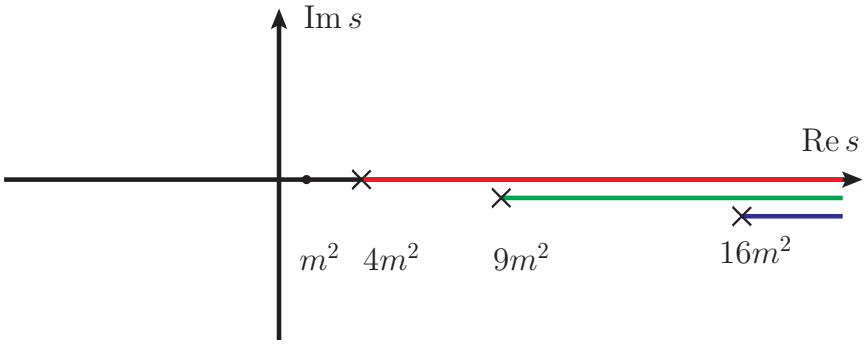

Figure 1.13: A simple pole and branch cuts for the scattering amplitude $M(s)$ in the complex s-plane.

in the upper half plane of complex variable ω. Furthermore, we assume that $A(\omega)$ takes real values along the real axis and use the Schwarz reflection principle

$$A(\omega^*) = A^*(\omega) \,, \tag{1.92}$$

to analytically continue $A(\omega)$ into the lower half complex plane, thus obtaining an analytic function $A(\omega)$ in the whole complex plane.

Physical scattering amplitudes were shown to fulfill a very important property called *hermitian analyticity*[4] [169]

$$M(s^*) = M^*(s) \,. \tag{1.93}$$

Since the Schwarz reflection principle can be extended to meromorphic functions, we can analytically continue $M(s)$ to the whole complex plane by virtue of hermitian analyticity (1.93). $M(s)$ takes real values when s is real and smaller than the lightest intermediate state threshold $4m^2$ since no intermediate states can go on shell. Near the real axis for $s > 4m^2$, the Schwarz reflection principle implies

$$\begin{aligned} \mathrm{Re}\, M(s + i\epsilon) &= \mathrm{Re}\, M(s - i\epsilon) \,, \\ \mathrm{Im}\, M(s + i\epsilon) &= -\mathrm{Im}\, M(s - i\epsilon) \,. \end{aligned} \tag{1.94}$$

The $+i\epsilon$ prescription in the Feynman calculation of perturbation theory implies that the physical scattering amplitude is obtained by approaching the cuts along the real axis from above, as $M(s + i\epsilon)$. The cut structure caused by multi-particle intermediate-state contributions together with other analytic properties of the transition amplitude are essential ingredients for constructing dispersion relations for form factors and scattering amplitudes in Section 1.2.2.

[4] This relation does not hold for decay amplitudes any longer.

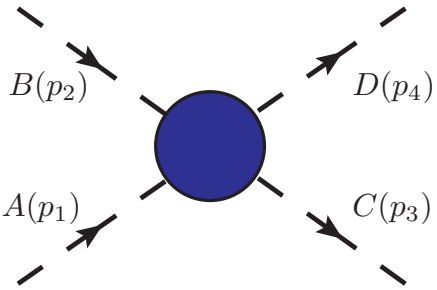

Figure 1.14: Scattering process of $A(p_1) + B(p_2) \to C(p_3) + D(p_4)$.

Kinematics and crossing symmetry

It was mentioned before that $2 \to 2$ scattering amplitudes are generally functions of two kinematic variables. This can be found by counting the degrees of freedom of the system. In total ten Lorentz invariant quantities can be built from four different momenta of the particles, of which four are fixed by the on-mass-shell condition and another four are determined by energy-momentum conservation, leaving only two invariant variables. We will continue the investigation thoroughly by considering the generic process $A(p_1)+B(p_2) \to C(p_3)+D(p_4)$ shown in Figure 1.14 as $2 \to 2$ scattering is the most relevant process in this thesis. Moreover, it is related to the decay of a particle to three final-state particles by analytic continuation, despite the complication of the analytic structures of the decay. We consider scalar particles with different masses. The momenta of the particles are labeled by $p_i = (p_i^0, \boldsymbol{p}_i)$, where

$$p_i^0 = E_i = \sqrt{m_i^2 + |\boldsymbol{p}_i|^2} \,. \tag{1.95}$$

It is customary to define Lorentz-invariant Mandelstam variables

$$\begin{aligned} s &= (p_1 + p_2)^2 = (p_3 + p_4)^2 \,, \\ t &= (p_1 - p_3)^2 = (p_2 - p_4)^2 \,, \\ u &= (p_1 - p_4)^2 = (p_2 - p_3)^2 \,, \end{aligned} \tag{1.96}$$

where the variables s, t, and u satisfy

$$s + t + u = \sum_{i=1}^{4} m_i^2 \,. \tag{1.97}$$

Hence only two kinematic variables are independent as stated. It is convenient to choose the center-of-mass frame to evaluate the Mandelstam variables where $\boldsymbol{p}_1 + \boldsymbol{p}_2 = 0$ and thus $\boldsymbol{p}_3 + \boldsymbol{p}_4 = 0$. Apparently, s becomes the square of the total energies of the scattering particles

$$s = (E_1 + E_2)^2 = (E_3 + E_4)^2 \,. \tag{1.98}$$

The invariants t and u can be represented as

$$\begin{aligned} t &= m_1^2 + m_3^2 - 2E_1E_3 + 2|\boldsymbol{p}_1||\boldsymbol{p}_3|\cos\theta \\ &= m_2^2 + m_4^2 - 2E_2E_4 + 2|\boldsymbol{p}_1||\boldsymbol{p}_3|\cos\theta\,, \\ u &= m_1^2 + m_4^2 - 2E_1E_4 - 2|\boldsymbol{p}_1||\boldsymbol{p}_3|\cos\theta \\ &= m_2^2 + m_3^2 - 2E_2E_3 - 2|\boldsymbol{p}_1||\boldsymbol{p}_3|\cos\theta\,, \end{aligned} \tag{1.99}$$

where the scattering angle θ between particles A and C is given by

$$\cos\theta = \frac{\boldsymbol{p}_1 \cdot \boldsymbol{p}_3}{|\boldsymbol{p}_1||\boldsymbol{p}_3|}\,. \tag{1.100}$$

Applying the mass-shell relation (1.95) to Equation (1.98), one finds the solution for the three-momenta of the particles:

$$|\boldsymbol{p}_1| = |\boldsymbol{p}_2| = \frac{\lambda^{1/2}(s, m_1^2, m_2^2)}{2\sqrt{s}}\,, \qquad |\boldsymbol{p}_3| = |\boldsymbol{p}_4| = \frac{\lambda^{1/2}(s, m_3^2, m_4^2)}{2\sqrt{s}}\,, \tag{1.101}$$

where λ is the Källén triangle function defined as

$$\lambda(x, y, z) = x^2 + y^2 + z^2 - 2xy - 2xz - 2yz\,. \tag{1.102}$$

Using the expressions of the three-momenta (1.101) and the mass-shell relation (1.95), the energies of the particles are obtained:

$$E_1 = \frac{s + \Delta_{12}}{2\sqrt{s}}\,, \qquad E_2 = \frac{s + \Delta_{21}}{2\sqrt{s}}\,, \qquad E_3 = \frac{s + \Delta_{34}}{2\sqrt{s}}\,, \qquad E_4 = \frac{s + \Delta_{43}}{2\sqrt{s}}\,, \tag{1.103}$$

where $\Delta_{ij} = m_i^2 - m_j^2$. It is obvious that s is required to be at least the square of the largest sum of the masses of the colliding particles. So the physically allowed range for s is given by

$$s \geq \max\left((m_1 + m_2)^2, (m_3 + m_4)^2\right). \tag{1.104}$$

The physical ranges of t and u can be found from the condition $-1 \leq \cos\theta \leq 1$ together with the range of the variable s. For particles with equal mass m, we find simple expressions for the Mandelstam variables

$$s = 4(m^2 + |\boldsymbol{p}_1|^2)\,, \quad t = -2|\boldsymbol{p}_1|^2(1 - \cos\theta)\,, \quad u = -2|\boldsymbol{p}_1|^2(1 + \cos\theta)\,, \tag{1.105}$$

from which the physical region of the Mandelstam variables is worked out as

$$s \geq 4m^2\,, \qquad t \leq 0\,, \qquad u \leq 0\,. \tag{1.106}$$

In quantum field theory, antiparticles moving forward in time are equivalent to negative energy particles moving backward in time based on the Feynman–Stueckelberg interpretation.

This property translates to a crucial corollary called the crossing transformation of scattering amplitudes in scattering theory.

In general, the scattering amplitude of a process that contains an incoming scalar particle with momentum p labeled by $\phi(p)$ is equal to the scattering amplitude of the otherwise same process where the incoming particle is replaced by the outgoing antiparticle with momentum $-p$, that is

$$M(\phi(p) + \cdots \to \cdots) = M(\cdots \to \bar{\phi}(-p) + \cdots)\,, \tag{1.107}$$

where $\bar{\phi}(-p)$ is the antiparticle of $\phi(p)$ with momentum $-p$. This relation can be easily proven in perturbation theory for scalar particles where there are no external leg factors, while special care needs to be taken for fermions because of the relative phases between them [78]. It means that the same scattering amplitude $M(s,t,u)$ of the process $A(p_1)+B(p_2) \to C(p_3)+D(p_4)$ can also describe the so-called crossed-channel processes

$$\begin{aligned} &A(p_1) + \bar{C}(-p_3) \to \bar{B}(-p_2) + D(p_4)\,, \\ &A(p_1) + \bar{D}(-p_4) \to \bar{B}(-p_2) + C(p_3)\,, \end{aligned} \tag{1.108}$$

where $\bar{B}$, $\bar{C}$ and $\bar{D}$ denote the antiparticles of the corresponding particles. These two channels are conventionally referred to as t- and u-channels in contrast to the original s-channel process, since they induce equivalent replacements $s \leftrightarrow t$ and $s \leftrightarrow u$ for the kinematic variables. So for equal-mass particles, the physical region for the t-channel process is given by

$$t \geq 4m^2\,, \qquad s \leq 0\,, \qquad u \leq 0\,, \tag{1.109}$$

so that the scattering amplitude $M(s,t,u)$ can be analytically continued to the t-channel physical region (1.109) to describe the t-channel process. Similarly $M(s,t,u)$ evaluated in the u-channel kinematic region

$$u \geq 4m^2\,, \qquad s \leq 0\,, \qquad t \leq 0\,, \tag{1.110}$$

gives exactly the corresponding u-channel scattering amplitude. All in all, one single analytic function $M(s,t,u)$ can be used to describe all three channels by choosing the appropriate physical regions for the Mandelstam variables. Since different physical regions are separated from each other, this only makes sense if scattering amplitudes are analytically continued from the physical region of one channel through the unphysical region to the physical regions of the other channels.

The kinematic regions of the different channels for equal-mass particles are plotted in the Mandelstam plane in Figure 1.15. In the Mandelstam plane, each side of the equilateral triangle is chosen as the coordinate axis for the variables s, t, and u since the sum of the perpendicular distances from one point in the plane to the triangle's sides is fixed to the triangle height, conveniently representing the relation (1.97) provided that the height of the triangle is equal to $\sum_i m_i^2$. Shaded regions in the figure indicate the kinematic regions of the

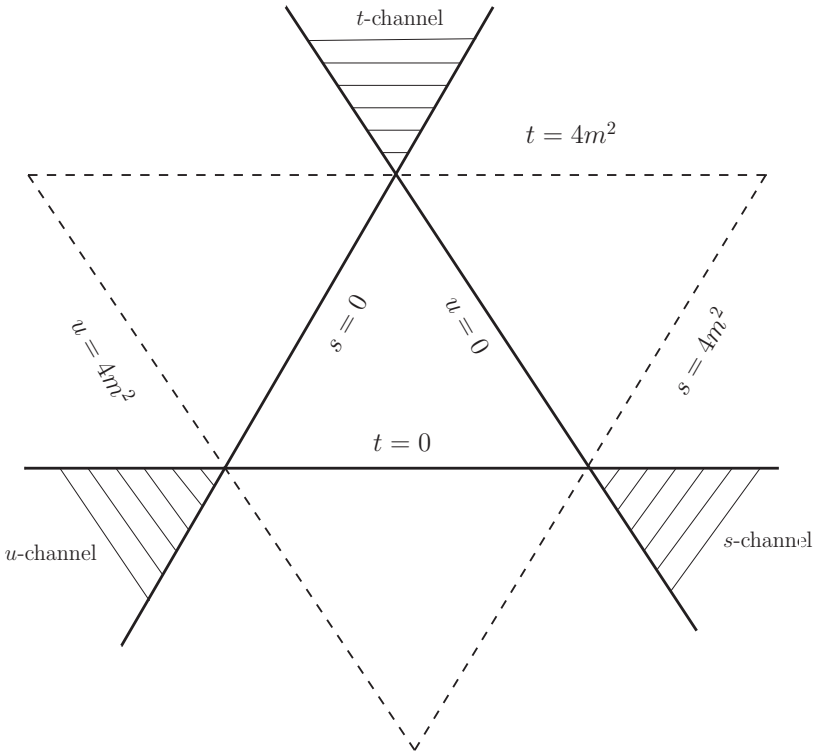

Figure 1.15: The Mandelstam plane for $2 \to 2$ scattering of particles with equal mass m. The shaded regions represent the s-, t-, and u- channel physical regions, respectively. The boundaries of the regions are given in the plot.

different channels. Furthermore if one of the particles is heavy enough to decay into three other particles, there appears a decay region in the center of the Mandelstam plane.

If one of the crossed channels is identical to the original channel after crossing transformation, the scattering amplitude exhibits a *crossing symmetry*. For instance, we consider Bhabha scattering $e^-(p_1)e^+(p_2) \to e^-(p_3)e^+(p_4)$. This process is obviously crossing symmetric in s- and t-channels. Therefore the spin averaged scattering amplitude squared possesses the property

$$\overline{|M|^2}(s,t,u) = \overline{|M|^2}(t,s,u) \ . \tag{1.111}$$

Crossing generates additional singularities for scattering amplitudes that arise from crossed-channel processes. Just as in the case of the s-channel, the normal thresholds of t- and u- channels for identical mass particles appear at

$$\begin{aligned} t &= 4m^2 \ , \quad 9m^2 \ , \quad 16m^2 \ , \quad \dots \ , \\ u &= 4m^2 \ , \quad 9m^2 \ , \quad 16m^2 \ , \quad \dots \ . \end{aligned} \tag{1.112}$$

Because of the relation (1.97), if we fix one of the kinematic variables like u, scattering amplitudes can be treated as functions of only one variable s or t. For fixed $u = u_0$, the pole

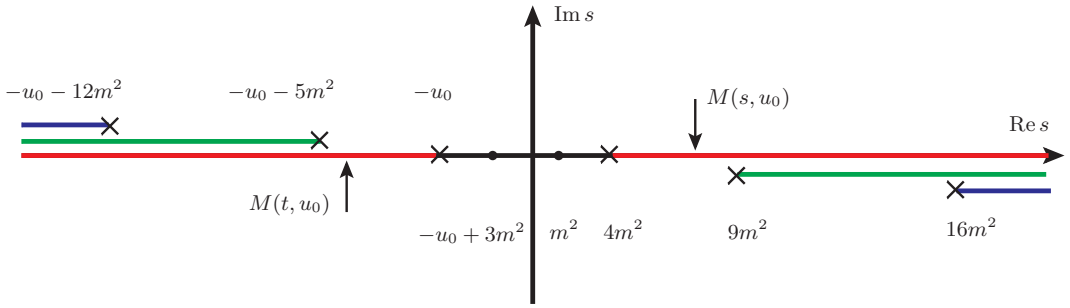

Figure 1.16: Simple poles and branch cuts of the scattering amplitude $M(s, u_0)$ in the complex s-plane arising from singularities in the s-channel and in the t-channel and physical limits of scattering amplitudes for s- and t-channels.

$t = m^2$ in the t-channel will appear in the s-plane at

$$s = -u_0 + 3m^2 \,, \tag{1.113}$$

and branch points in the t-channel emerge at

$$s = -u_0 \,, \quad -u_0 - 5m^2 \,, \quad -u_0 - 12m^2 \,, \quad \dots \,, \tag{1.114}$$

causing additional branch cuts for the s variable starting from branch points given in Equation (1.113) and extending to minus infinity. These cuts due to crossed-channel processes are called *left-hand* cuts, while the aforementioned normal threshold cuts are called *right-hand* cuts.

Since for the t-channel process, the physical scattering amplitude $M(t, u_0)$ should be evaluated at $t + i\epsilon$ for the variable t, it should be evaluated in the s-plane as $M(s - i\epsilon, u_0)$, approaching the left-hand cuts from the lower rim owing to the relation (1.97). In the end, the whole singularity structure of the scattering amplitude $M(s, u_0)$ for fixed $u = u_0$ is shown in Figure 1.16, where the physical scattering amplitudes are also defined.

1.2.2 Dispersion relations

We have extensively discussed general properties of scattering amplitudes, unitarity, analyticity, and crossing symmetry in Section 1.2.1. These properties of scattering amplitudes can be accumulated into the dispersion relation, an integral representation of scattering amplitudes with their imaginary parts as input. Credited with the power of complex analysis, the dispersion relation was very popular before the advent of gauge theory, while it is still a useful contemporary toolkit for theorists.

Before developing dispersion relations, we first summarize singularities of scattering amplitudes, including those which have not been covered in the previous discussions. We list these singularities without providing further detailed proof. Dynamical singularities of scattering amplitudes come from particle production thresholds, which are:

- bound states and one-particle simple poles on the physical sheet;
- branch cuts associated with multi-particle intermediate states;
- resonances and virtual-state poles on unphysical sheets;
- singularities at infinity.

One needs to take these singularities into account when constructing dispersion relations using the Cauchy integral formula.

Dispersion relations for single-variable functions

We first consider dispersion relations for a general single-variable function $f(s)$, which fulfills analytic properties of scattering amplitudes. Typical physical examples are the photon self-energy in QED and the pion vector form factor in hadron physics.

Suppose $f(s)$ has a branch cut starting from the threshold s_{th} to infinity and is real on the real axis below the threshold. It is analytic in the whole complex plane except for the branch cut and fulfills the Schwarz reflection principle,

$$f(s^*) = f^*(s) \,. \tag{1.115}$$

The analytic continuation of $f(s)$ is provided by dispersion relations. Using Cauchy's integral formula, we can express the analytic function $f(s)$ as

$$f(s) = \frac{1}{2\pi i} \oint_\Omega \frac{f(s')}{s'-s} \, \mathrm{d}s' \,, \tag{1.116}$$

where s is a point in the interior of the closed counter-clockwise contour Ω, provided that $f(s)$ is analytic inside Ω and no singularities are included in the contour. Thus we inflate the integration contour for $f(s)$ skirting the cut as shown in Figure 1.17 so that Cauchy's integral formula (1.116) applies to any s in the complex plane except for the cut. We separate the integration path into three pieces as

$$f(s \pm i\epsilon) = \frac{1}{2\pi i} \int_{s_{\text{th}}}^{\Lambda^2} \frac{\operatorname{disc} f(s')}{s' - s \mp i\epsilon} \, \mathrm{d}s' + \frac{1}{2\pi i} \int_\gamma \frac{f(s')}{s'-s} \, \mathrm{d}s' + \frac{1}{2\pi i} \int_{|s'|=\Lambda^2} \frac{f(s')}{s'-s} \, \mathrm{d}s' \,, \tag{1.117}$$

where the discontinuity of $f(s)$ is defined as

$$\operatorname{disc} f(s) = f(s + i\epsilon) - f(s - i\epsilon) \,, \tag{1.118}$$

and γ is a small semicircle path surrounding the threshold s_{th}. The integral along γ vanishes with the length of the integration path as long as s_{th} is not a pole of $f(s)$. Since $f(s)$ satisfies the Schwarz reflection principle, the discontinuity can be replaced by its imaginary part,

$$\operatorname{disc} f(s) = f(s + i\epsilon) - f^*(s + i\epsilon) = 2i \operatorname{Im} f(s + i\epsilon) = 2i \operatorname{Im} f(s) \,. \tag{1.119}$$

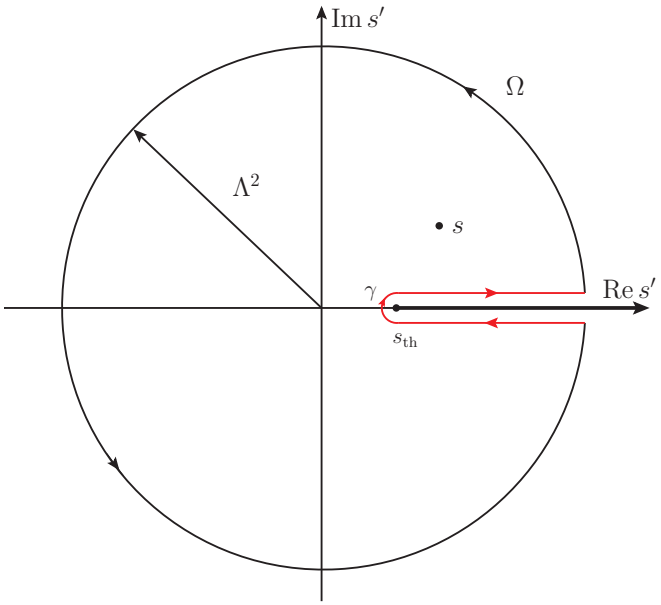

Figure 1.17: The integration contour Ω of Cauchy integral (1.116) for $f(s)$.

Assuming $f(s)$ tends to zero when $|s| \to \infty$, we find that the third integral in (1.117) along the circle vanishes in the limit $\Lambda^2 \to \infty$ and we are left with a convergent integral along the cut,

$$f(s \pm i\epsilon) = \frac{1}{\pi} \int_{s_{\text{th}}}^{\infty} \frac{\operatorname{Im} f(s')}{s' - s \mp i\epsilon} \, \mathrm{d}s' \,. \tag{1.120}$$

This is an example of the so-called *unsubtracted* dispersion relations. Referred to as the Hilbert transform in mathematics, it restores an analytic function using its imaginary part as input, which is due to the propagation of on-shell intermediate states. The $\pm i\epsilon$ prescription is included in order to avoid the cut singularity at $s' = s$ if s sits on the cut. We will drop the $\pm i\epsilon$ prescription in the following as physical functions always take the limit $f(s + i\epsilon)$.

Owing to a theorem derived by Sugawara and Kanazawa [170], unsubtracted dispersion relations can be applied to any function $f(s)$ that is bounded by some finite power of $|s|$ when $|s| \to \infty$ and vanishes along the cut as $s \to \infty$. But if $f(s)$ does not go to zero along the cut when $s \to \infty$, we cannot represent $f(s)$ using unsubtracted dispersion relations. In this situation, dispersion relations can be remedied by performing subtractions. Assuming $f(s)$ to go to a constant for large $|s|$, we can write an unsubtracted dispersion relation for $(f(s) - f(0))/s$,

$$\frac{f(s) - f(0)}{s} = \frac{1}{\pi} \int_{s_{\text{th}}}^{\infty} \frac{\mathrm{d}s'}{s' - s} \operatorname{Im} \left[\frac{f(s') - f(0)}{s'} \right] , \tag{1.121}$$

as this function does not introduce singularities in the contour Ω and vanishes for $|s| \to \infty$.

Given that $\mathrm{Im}\, f(0) = 0$, we end up with a *once-subtracted* dispersion relation for $f(s)$,

$$f(s) = f(0) + \frac{s}{\pi} \int_{s_{\mathrm{th}}}^{\infty} \frac{\mathrm{Im}\, f(s')}{s'(s'-s)}\, \mathrm{d}s' \,, \tag{1.122}$$

where $f(0)$ is called the subtraction constant, which cannot be determined by dispersion relations and needs to be fixed by some other means. These subtraction constants are closely related to singularities at infinity and are equivalent to low-energy parameters in effective field theories, which reveal our lack of knowledge in the high-energy regime.

Now consider a more general case where $f(s)$ shows a behavior $|f(s)| \sim |s|^{N-1}$ for $|s| \to \infty$, with N a positive integer. Then we can still obtain a dispersion relation for $f(s)$ if it is analytic in the cut s-plane by considering the function

$$\frac{f(s)}{(s-s_1)\cdots(s-s_N)} \,, \tag{1.123}$$

which has N poles at fixed subtraction points $s_1, \ldots, s_N$ chosen below s_{th}. The unsubtracted dispersion relation now applies to the function (1.123) since it vanishes at the circle boundary. Applying Cauchy's integral formula, we collect residues of poles and find a dispersion relation of the form

$$f(s) = P_{N-1}(s) + \frac{(s-s_1)\cdots(s-s_N)}{\pi} \int_{s_{\mathrm{th}}}^{\infty} \frac{\mathrm{Im}\, f(s')}{(s'-s_1)\cdots(s'-s_N)(s'-s)}\, \mathrm{d}s' \,, \tag{1.124}$$

where $P_{N-1}(s)$ is a polynomial of degree $N-1$ in s. This is an example of dispersion relations with N subtractions. The N subtraction constants can only be fixed once we know the values of $f(s)$ at N points s_i. The predictive power of dispersion relations is obvious: we can reconstruct $f(s)$ itself in the whole complex plane up to a polynomial once we know the imaginary part of $f(s)$ up to infinity.

The pion vector form factor and the Omnès function

Form factors are basic observables of composite particles that contain information about their internal structures and interaction properties, for which complete calculations based on the underlying physics are mostly impossible. We study the pion vector form factor using dispersion relations, which appears in the photon–pion–pion vertex $\gamma^*\pi^+\pi^-$ in the pion production process $e^+(k_1)e^-(k_2) \to \pi^+(p_1)\pi^-(p_2)$ as shown in Figure 1.18. This process is related to the scattering process $e^-(k_2)\pi^-(-p_1) \to e^-(-k_1)\pi^-(p_2)$ by crossing. QED does not determine the $\gamma^*\pi^+\pi^-$ vertex as pions are strongly interacting particles. The most general form of the matrix element of this vertex fulfilling Lorentz and gauge invariance is given as

$$\left\langle \pi^+(p_1)\pi^-(p_2) \middle| j^\mu(0) \middle| 0 \right\rangle = e(p_1-p_2)^\mu F_\pi^V(s) \,, \tag{1.125}$$

where $j^\mu(x)$ is the electromagnetic current operator and e is the electric charge in units of the proton charge. Separating out the Lorentz four-vector structure, the remaining Lorentz

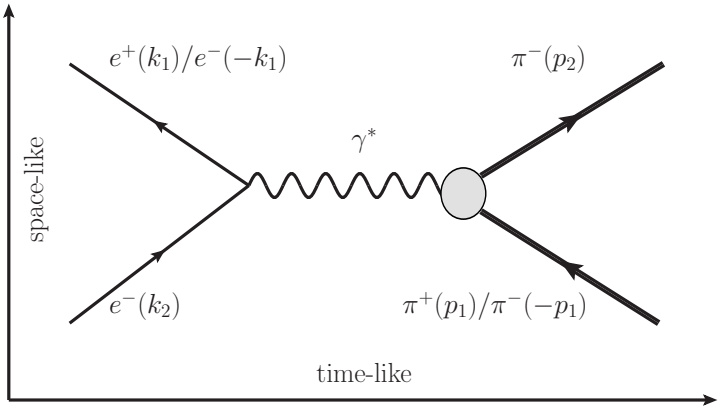

Figure 1.18: Feynman diagram of the production process $e^+e^- \to \pi^+\pi^-$ and the scattering $e^-\pi^- \to e^-\pi^-$. The gray blob represents the vertex described by the pion vector form factor.

scalar degree of freedom is described by the pion vector form factor $F_\pi^V(s)$, which is a function of the only non-constant scalar variable, the total energy-squared $s = (p_1 + p_2)^2$. $F_\pi^V(s)$ exhibits the electromagnetic structure of the pion and simply reduces to the Fourier transform of the charge distribution of the pion in the Breit frame.

The kinematic region of the production process is given by $s \geq 4M_\pi^2$, where M_π is the mass of the pion. The $\gamma^*\pi^-\pi^-$ vertex in the scattering process is also described by $F_\pi^V(s)$ because of crossing, even though the form factor is evaluated in a different kinematic domain $s \leq 0$. $F_\pi^V(s)$ only shows right-hand cuts since there are no possible on-shell intermediate states in the region $s \leq 0$. The analytic continuation relating $F_\pi^V(s)$ in two non-overlapping regions is done by dispersion relations, which need the discontinuity of the form factor as input. To this end, the intermediate states coupling to 2π through strong interaction allowed by conservation laws in the isospin limit are $2\pi, 4\pi, \ldots$, as presented in Figure 1.19. Only considering elastic scattering, the discontinuity from the 2π intermediate state reads [171]

$$\begin{aligned}&(p_1 - p_2)^\mu \operatorname{disc} F_\pi^V(s)\\ &\quad = \frac{i}{2}\int \frac{\mathrm{d}^4 l}{(2\pi)^4}(2\pi)\delta(l^2 - M_\pi^2)(2\pi)\delta((p_s - l)^2 - M_\pi^2)T_I^*(s, z_l)(p_s - 2l)^\mu F_\pi^V(s)\,,\end{aligned} \tag{1.126}$$

where l is the loop momentum, $z_l = \cos\theta_l$ gives the cosine of the center-of-mass scattering angle θ_l, $T_I(s, z_l)$ represents the $\pi\pi$ scattering amplitude with isospin I and $p_s = p_1 + p_2$ denotes the center-of-mass momentum. Integrating out the delta functions yields

$$(p_1 - p_2)^\mu \operatorname{disc} F_\pi^V(s) = \frac{i}{64\pi^2}\sigma_\pi(s)F_\pi^V(s)\int \mathrm{d}\Omega_l T_I^*(s, z_l)(p_s - 2l)^\mu\,, \tag{1.127}$$

where $\sigma_\pi(s) = \sqrt{1 - 4M_\pi^2/s}$ and Ω_l are the phase space and the solid angle of the $\pi\pi$ subsystem respectively. Recall that the partial-wave expansion of the $\pi\pi$-scattering amplitude

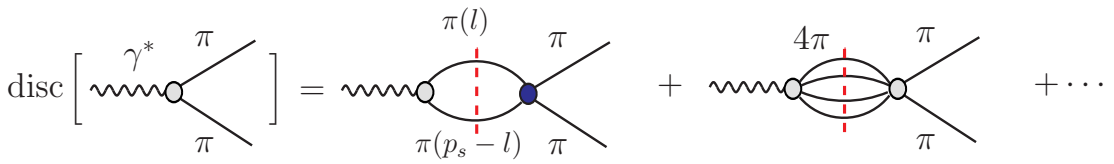

Figure 1.19: Intermediate states contributing to the discontinuity of the pion vector form factor. For the two-pion intermediate state, the gray blob represents the pion vector form factor and the blue blob represents the $\pi\pi$-scattering amplitude.

reads

$$T_I(s,z) = 32\pi \sum_{\ell=0}^{\infty} (2\ell+1) P_\ell(z) t_\ell^I(s)\,, \tag{1.128}$$

where $P_\ell(z)$ are the Legendre polynomials and $t_\ell^I(s)$ is the partial-wave amplitude with angular momentum ℓ and isospin I. By virtue of the orthogonality condition of the Legendre polynomials, only the $\ell = 1$ partial wave in the partial-wave expansion is projected out in (1.127), which is also the consequence of angular momentum conservation. Furthermore, only the isospin $I = 1$ partial wave $t_1^1(s)$ contributes due to Bose symmetry. Parameterizing the partial-wave amplitude by the phase shift as

$$t_1^1(s) = \frac{\sin\delta_1^1(s)\, e^{i\delta_1^1(s)}}{\sigma_\pi(s)}\,, \tag{1.129}$$

we find after some simple calculations,

$$\text{disc}\, F_\pi^V(s) = 2iF_\pi^V(s) \sin\delta_1^1(s)\, e^{-i\delta_1^1(s)} \theta(s - 4M_\pi^2)\,. \tag{1.130}$$

Equation (1.130) is the manifestation of Watson's final-state theorem [172], which states that the phase of the form factor below inelastic thresholds is given by the two-particle scattering phase shift. A solution of $F_\pi^V(s)$ can be constructed analytically by parameterizing it as

$$F_\pi^V(s) = P(s)\Omega(s)\,, \tag{1.131}$$

where $P(s)$ is a real function free of cuts below inelastic thresholds and $\Omega(s)$ is a special solution free of zeros. Then the discontinuity equation (1.130) for the form factor translates to

$$\text{disc}\, \log\Omega(s) = 2i\delta_1^1(s)\,, \tag{1.132}$$

from which we can write a dispersion relation for $\log\Omega(s)$,

$$\log\Omega(s) = \frac{1}{2\pi i} \int_{4M_\pi^2}^{\infty} \mathrm{d}s' \frac{\text{disc}\, \log\Omega(s')}{s' - s}\,. \tag{1.133}$$

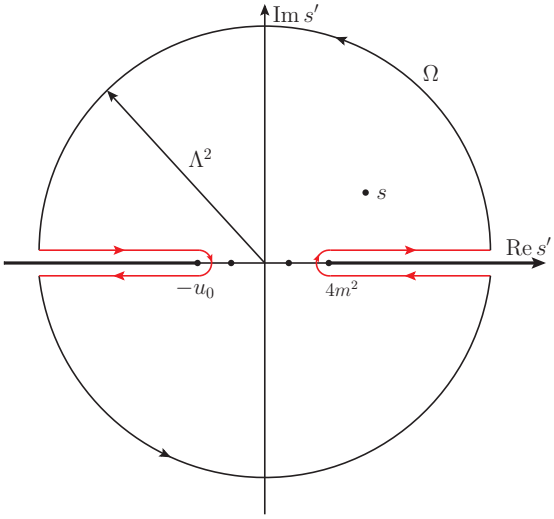

Figure 1.20: The integration contour Ω for deriving dispersion relations for $M(s, u_0)$.

Taking into account the necessary subtraction and the normalization $\Omega(0) = 1$, we end up with a once-subtracted dispersion integral for $\Omega(s)$,

$$\Omega(s) = \exp\left\{\frac{s}{\pi}\int_{4M_\pi^2}^{\infty} \mathrm{d}s' \frac{\delta_1^1(s')}{s'(s'-s)}\right\}. \tag{1.134}$$

The above solution to the discontinuity equation of the form factor is known as the Omnès function [173]. It takes into account the final-state interaction of the 2π system, representing the iteration of bubble diagrams of the elastic scattering. The Omnès function is entirely determined by the $\pi\pi$ P-wave scattering phase shift up to inelastic contributions.

Dispersion relations for scattering amplitudes

The basic strategies to the dispersive formalism of scattering amplitudes are similar to those of form factors, albeit with complications of analytic structures arising from left-hand cuts due to crossed-channel processes.

Let us consider dispersion relations for a $2 \to 2$ scattering amplitude $M(s, t, u)$, where s, t, and u are the Mandelstam variables of respective channels. In the equal-mass case, the singularity structure of the scattering amplitude $M(s, u_0)$ for fixed $u = u_0$ is shown in Figure 1.20, which is of direct relevance to the choice of the integration contour of the Cauchy integral for dispersion relations. These are two simple poles related to one-particle exchanges and right- and left-hand cuts due to elastic s-channel and crossed-channel scatterings. Ignoring branch cuts from inelastic contributions for simplicity, the integration contour should be chosen as in Figure 1.20 to avoid the elastic scattering cuts. Assuming the integral along the arc to vanish in the $\Lambda^2 \to \infty$ limit, we find an unsubtracted *fixed-u*

dispersion relation for $M(s,u_0)$ in the Mandelstam variable s,

$$M(s,u_0) = P + \frac{1}{\pi}\int_{-\infty}^{-u_0} \mathrm{d}s' \frac{\mathrm{Im}\, M_t(s',u_0)}{s'-s} + \frac{1}{\pi}\int_{4m^2}^{\infty} \mathrm{d}s' \frac{\mathrm{Im}\, M_s(s',u_0)}{s'-s}\,, \tag{1.135}$$

where $\mathrm{Im}\, M_s$ and $\mathrm{Im}\, M_t$ are respectively imaginary parts of M both evaluated at the upper rim of the right-hand and the left-hand cuts, while P represents contributions from the two simple poles located in the contour,

$$P = \frac{R_s}{s-m^2} + \frac{R_t}{s+u_0-3m^2}\,, \tag{1.136}$$

where R_s and R_t are the residues of the two poles. One can also write down a fixed-u dispersion relation in the Mandelstam variable t in a similar way.

We recall that the pole at $s = -u_0 + 3m^2$ and the left-hand cut in the s-channel originate from the t-channel pole at position $t = m^2$ and the right-hand cut in t. So making use of the relation $s' + t' + u_0 = 4m^2$, we can write (1.135) in a more elegant form

$$M(s,t,u_0) = \frac{R_s}{s-m^2} + \frac{R_t}{t-m^2} + \frac{1}{\pi}\int_{4m^2}^{\infty} \mathrm{d}s' \frac{\mathrm{Im}\, M_s(s',u_0)}{s'-s} + \frac{1}{\pi}\int_{4m^2}^{\infty} \mathrm{d}t' \frac{\mathrm{Im}\, M_t(t',u_0)}{t'-t}\,. \tag{1.137}$$

In addition, fixed-t and fixed-s dispersion relations can be written down in a similar manner.

Discontinuities or imaginary parts entering (1.137) are easily accessible in physical regions, e.g., $\mathrm{Im}\, M_s$ when u_0 takes some negative values. But if this is not the case, analytic continuations are demanded even for the discontinuities themselves from the physical regions. Mandelstam [174] proposed a representation with possible analytic continuations of the discontinuities based on his famous Mandelstam hypothesis, which reads

$$\begin{aligned} M(s,t,u) = P &+ \frac{1}{\pi^2}\int_{s_\mathrm{th}}^{\infty}\int_{t_\mathrm{th}}^{\infty} \frac{\rho_{st}(s',t')}{(s'-s)(t'-t)}\mathrm{d}s'\mathrm{d}t' + \frac{1}{\pi^2}\int_{t_\mathrm{th}}^{\infty}\int_{u_\mathrm{th}}^{\infty} \frac{\rho_{tu}(t',u')}{(t'-t)(u'-u)}\mathrm{d}t'\mathrm{d}u' \\ &+ \frac{1}{\pi^2}\int_{u_\mathrm{th}}^{\infty}\int_{s_\mathrm{th}}^{\infty} \frac{\rho_{us}(u',s')}{(u'-u)(s'-s)}\mathrm{d}u'\mathrm{d}s', \end{aligned} \tag{1.138}$$

where the integrations are over real regions starting from the respective threshold in each channel and the constraint $s' + t' + u' = 4m^2$ is implied. This is called the Mandelstam representation or the double dispersion relation. The spectral function ρ_{st} gives the double discontinuity across cuts in the s-channel and the t-channel simultaneously, and the same holds for ρ_{tu} and ρ_{us} in the respective channels.

So far we have not discussed subtractions in dispersion relations for scattering amplitudes. The approach is similar to the one which is applied for single-variable functions. The necessary number of subtractions can be determined referring to Regge theory [175] or

the Froissart–Martin bound [176, 177], which states that the absolute value of the forward scattering amplitude behaves like

$$|M(s, \cos\theta = 1)| < \text{const.}\, s(\ln s)^2 \,, \tag{1.139}$$

when $s \to \infty$.

In practice, the inputs of dispersion relations such as phase shifts or discontinuities extracted from experiments are not available to arbitrarily high energies. In this sense, subtractions are preferred in order to lessen the influences coming from the high-energy region provided that we are able to precisely determine the subtraction constants.

1.2.3 Operator product expansion

Proposed by Wilson in 1969 [178], the essential idea of the OPE is to expand the time-ordered product of two (or more) local operators $A(x)$ and $B(y)$ as a sum of other *renormalized* composite local operators evaluated at x or y, with coefficients depending on the space-time difference $x - y$,

$$T\{A(x)B(y)\} = \sum_n C_n(x-y)O_n(y) \,, \tag{1.140}$$

where C_n are called the Wilson coefficients. The OPE is very useful under the circumstances when $x \to y$, for which only a few singular or non-suppressed terms of the expansion are relevant. Consider a free massless scalar field as an instance, whose expansion looks like

$$T\{\phi(x)\phi(0)\} = -\frac{1}{4\pi^2}\frac{1}{x^2 - i\epsilon} + \Big(1 + \frac{1}{2}x^\mu\partial_\mu\Big)\phi(0)^2 + O(x^2) \,. \tag{1.141}$$

The importance of present operators in the OPE is categorized by their *twists*, which are defined as the difference between the dimension and spin of the pertinent term. The identity operator has twist 0 and ϕ^2 has dimension 2 spin 0 and thus twist 2. It is clear from the above expansion that lower-twist operators dominate in the OPE and higher-twist operators are suppressed.

What concerns us here are hadronic correlation functions. In this aspect, a general hadronic current is written in terms of quark bilinear as $j_\Gamma(x) = \bar{q}_i(x)\Gamma q_j(x)$, where i and j are flavor labels and the tensor structure resides in Γ. A practical form of the OPE in this application reads

$$i\int \mathrm{d}^4x\, e^{iq\cdot x}\, T\{j_\Gamma(x)j_\Gamma(0)\} = \sum_n C_n^\Gamma(q)O_n(0) \tag{1.142}$$

at short distances $Q^2 = -q^2 \gg \Lambda^2_{\text{QCD}}$. The Wilson coefficients are given in momentum space and the operators in position space. Constructed in this way, the OPE factorizes the short-distance and long-distance contributions to treat them separately. The short-distance part can be calculated in pQCD expansion in terms of α_s,

$$C_n^\Gamma(q) = A_n^\Gamma(q) + B_n^\Gamma(q)\alpha_s + O(\alpha_s^2) \,. \tag{1.143}$$

The long-distance dynamics are usually absorbed into universal hadronic matrix elements like vacuum condensates, light-cone distribution amplitudes, or parton distribution functions. The unambiguous separation of two contributions defines a normalization (factorization) scale μ. Required by the μ-independence of physical processes, the μ-dependence of Wilson coefficients is canceled by the μ-dependence of hadronic matrix elements. OPEs are widely used in combination with QCD and light-cone sum rules in hadron phenomenology.

1.2.4 QCD and light-cone sum rules

QCD sum rules [179] interrelate the perturbative and non-perturbative regimes of QCD via OPEs and dispersion relations. Hadrons are represented by their interpolating quark currents with correct quantum numbers, the vacuum-to-vacuum correlation function $\Pi_\Gamma(q^2)$ of which is calculated in the framework of the OPE at large virtualities firstly. The non-perturbative effects stemming from the non-trivial QCD vacuum are later absorbed in the non-vanishing vacuum expectation values like quark and gluon condensates

$$\langle 0|\bar{q}q|0\rangle\,, \quad \langle 0|G^a_{\mu\nu}G^{a\,\mu\nu}|0\rangle\,. \tag{1.144}$$

In the meantime, the same correlation function $\Pi_\Gamma(q^2)$ can be evaluated as a sum over hadronic states using dispersion relations up to subtraction constants, assuming quark-hadron duality [180]. The key equation of QCD sum rules is then obtained by equating the two approaches:

$$\sum_n C_n^\Gamma(q)\langle 0|O_n|0\rangle = \frac{(q^2)^n}{\pi}\int_{s_{\text{th}}}^\infty \mathrm{d}s\frac{\operatorname{Im}\Pi_\Gamma(s)}{s^n(s-q^2)} + \sum_{k=0}^{n-1} a_k(q^2)^k\,. \tag{1.145}$$

The bond of the two equips us to either extract information of hadrons like decay constants from QCD calculations or determine QCD parameters such as quark masses with the aid of experimental inputs into dispersion relations [181, 182]. We discuss one example in more detail.

The Adler function is defined via the VP function $\Pi(q^2)$ of quark currents,

$$D(q^2) = q^2\frac{\mathrm{d}\Pi(q^2)}{\mathrm{d}q^2}\,. \tag{1.146}$$

Its calculation in pQCD simplifies to

$$D(q^2) = -\frac{1}{4\pi^2}\sum_q^{n_f} Q_q^2\Big[1+\frac{\alpha_s}{\pi}+O(\alpha_s^2)\Big]\,, \tag{1.147}$$

for $Q^2 = -q^2 \gg m_q^2$, where m_q is the quark mass. n_f is the number of involved active quark flavors and Q_q their charges. With guaranteed convergence, we write down a dispersion

relation for the Adler function:

$$D(q^2) = \frac{q^2}{\pi}\int_{s_{\rm th}}^{\infty} \mathrm{d}s \frac{\mathrm{Im}\,\Pi(s)}{(s-q^2)^2} = \frac{q^2}{12\pi^2}\int_{s_{\rm th}}^{\infty} \mathrm{d}s \frac{R_{\rm had}(s)}{(s-q^2)^2}\,, \tag{1.148}$$

where $R_{\rm had}(s)$ is the hadronic ratio defined in Section 1.1. Equating the two results gives

$$-\frac{1}{4\pi^2}\sum_q^{n_f} Q_q^2\Big[1+\frac{\alpha_s}{\pi}+O(\alpha_s^2)\Big] = \frac{q^2}{12\pi^2}\int_{s_{\rm th}}^{\infty} \mathrm{d}s \frac{R_{\rm had}(s)}{(s-q^2)^2}\,. \tag{1.149}$$

Driven by the validity of (1.149) in the deep Euclidean domain $Q^2 = -q^2 \to \infty$, we find

$$R_{\rm had}(s) \to 3\sum_q^{n_f} Q_q^2\,, \tag{1.150}$$

which shows that the hadronic R ratio is determined by pQCD. This result is used as the HVP contribution to a_μ from the perturbative region.

We studied the Adler function (1.146) instead of the VP function itself to guarantee the convergence of the dispersion integral. In practical applications, in order to validate the dominance of low-lying resonances, moments or Borel transforms are often applied to suppress the higher-resonance contributions.

An important variant of QCD sum rules, the light-cone sum rule (LCSR) method [183–185], is favorably applied to hard exclusive processes in QCD. Contrasted with QCD sum rules dealing with vacuum-to-vacuum correlation functions, the LCSRs start with time-ordered product of two hadronic currents sandwiched between the vacuum and one external hadronic state. We consider one application to the $B \to \pi$ form factor in $B \to \pi l \bar{\nu}_l$ weak decays closely following [182, 186]. The relevant matrix element reads

$$\langle \pi^+(p)|\bar{u}\gamma_\mu b|B(p+q)\rangle = 2f_+^{B\to\pi}(q^2)p_\mu + \Big[f_+^{B\to\pi}(q^2)+f_-^{B\to\pi}(q^2)\Big]q_\mu\,, \tag{1.151}$$

where $p^2 = M_\pi^2$ and $(p+q)^2 = m_B^2$. Among the two form factors only $f_+^{B\to\pi}$ is relevant, for $f_-^{B\to\pi}$ is kinematically suppressed. In the LCSR approach, we use the interpolating current for the B meson to study a particular hadronic matrix element

$$\begin{aligned} F_\mu(q,p) &= i\int \mathrm{d}^4x\, e^{iqx}\langle \pi^+(p)|\,T\,\{\bar{u}(x)\gamma_\mu b(x)\, m_b\bar{b}(0)i\gamma_5 d(0)\}|0\rangle \\ &= F(q^2,(p+q)^2)p_\mu + \tilde{F}(q^2,(p+q)^2)q_\mu\,, \end{aligned} \tag{1.152}$$

where it is sufficient to study only F.

For $Q^2 = -q^2$, $|p+q|^2 \gg \Lambda_{\rm QCD}^2$, the main contribution to the integral (1.152) arises from the light-cone region $x^2 = 0$. A quark and an antiquark are created at space-time points x and 0 to form one pion final state. In this context, the leading-twist OPE expansion

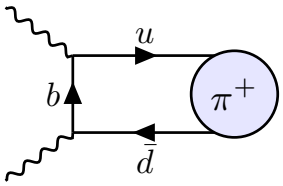

Figure 1.21: The leading diagram contributing to (1.152), with the pion distribution amplitude represented by the blob.

of the currents near the light-cone defines the short-distance b-quark propagator and the long-distance light-cone distribution amplitude of the pion $\phi_\pi(u,\mu)$, as diagrammatically represented in Figure 1.21:

$$\langle \pi^+(p)|\bar{u}(x)\gamma_\mu\gamma_5 d(0)|0\rangle = -ip_\mu F_\pi \int_0^1 \mathrm{d}u\, e^{iup\cdot x}\phi_\pi(u,\mu)\,, \tag{1.153}$$

where F_π is the pion decay constant and μ is the normalization scale. The pion distribution amplitude embodies the longitudinal-momentum sharing of valance quark and antiquark inside the pion and serves the role of non-perturbative vacuum condensates in QCD sum rules. With the universal long-distance part defined, the LO result for the invariant amplitude F reads

$$F(q^2,(p+q)^2) = m_b F_\pi \int_0^1 \frac{\mathrm{d}u\,\phi_\pi(u,\mu)}{m_b^2-(q+up)^2}\,. \tag{1.154}$$

The form factor $f_+^{B\to\pi}$ is then determined by writing down a dispersion relation for the invariant amplitude F.

1.2.5 Large-N_c expansion

There exists a systematic expansion for QCD when we take the number of quark colors $N_c \to \infty$ while keeping the $\alpha_s N_c$ limit fixed [187, 188]. This is called the large-N_c or $1/N_c$ expansion, which makes the physics of the strong interaction simpler while keeping its essential features in the real world $N_c = 3$. Contrasted with the perturbative expansion in α_s, which is limited in the asymptotic-free domain, the $1/N_c$ expansion is the only expansion in QCD that is valid at arbitrary energy scales.

In a general $SU(N_c)$ color gauge theory, quarks reside in the fundamental representation carrying one color index, while antiquarks in the conjugate representation carry another color index. Gluons are in the adjoint representation, labeled by traceless $N_c \times N_c$ matrices $(A_\mu)^\alpha_\beta$. Based on this group-theory analysis, it is convenient to introduce the 't Hooft double-line notation: quarks and antiquarks are drawn by arrowed lines with opposite color flows; gluons are represented by double lines with two opposite arrows. The QCD interaction vertices are shown in Figure 1.22 for a clarification.

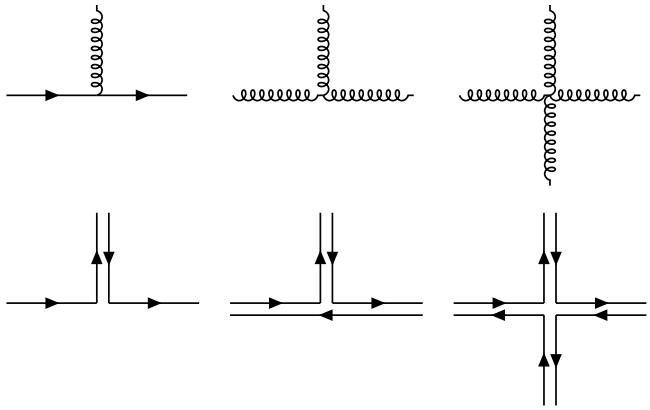

Figure 1.22: QCD interaction vertices and their double-line notations.

With the double-line notation, we are ready to formulate the large-N_c powering counting. The main upshots are: the *planar* diagrams, which can be drawn in a plane with the double-line notation without crossing the lines, prevail over the non-planar ones, for non-planar diagrams are suppressed by an additional factor $1/N_c^2$; in addition, internal quark-loops are suppressed by a factor of $1/N_c$. In formal studies, the large-N_c counting is determined by the topological invariants of the given diagrams.

The evidence of $N_c = 3$ is reflected in the hadronic R ratio defined in Section 1.1. For general N_c, the anomaly cancellation in the SM is achieved by changing the quark charges to be multiples of $1/N_c$, with more details given in Appendix B.1 of Part II. In reality, one may doubt the expansion parameter $1/N_c = 1/3$ being not too small. This argument can be revoked by the Witten's "wisecrack" [189] that in the QED expansion $\alpha = e^2/4\pi \approx 1/137$ gives $e \approx 0.3$, which does not deviate that much from $1/3$, so that the expansion should not be rejected a priori. More practically, the large-N_c analysis on one hand gives simple rationales for phenomenology of mesons: mesons become narrow, free, and non-interacting and the QCD spectrum boils down to infinite towers of one-meson states. On the other hand, it provides quantitative descriptions for baryons, see the reviews [189–191] for more details.

1.3 Anomalies

1.3.1 Chiral anomaly

Noether's theorem states that for every classical (internal or space-time) symmetry of the action, there exists a conserved current j^μ such that $\partial_\mu j^\mu = 0$. But a classical symmetry is not guaranteed to hold at the quantum level. If such a classical symmetry is broken by quantum effects, it is called *anomalous*. The most crucial of this type includes chiral symmetries of theories with massless fermions.

We review the chiral anomaly [111–113] by studying a massless QED theory with chiral fermions ψ. The Lagrangian is invariant under separate left- and right-chiral transformations.

The associated vector and axial-vector currents are conserved classically,

$$\partial_\mu j^\mu = 0\,,\ \partial_\mu j_5^\mu = 0\,; \quad j^\mu = \bar\psi\gamma^\mu\psi\,,\ j_5^\mu = \bar\psi\gamma^\mu\gamma^5\psi\,. \tag{1.155}$$

However, the axial-vector current turns out to be anomalous,

$$\partial_\mu j_5^\mu = -\frac{e^2}{16\pi^2}\varepsilon^{\mu\nu\rho\sigma}F_{\mu\nu}F_{\rho\sigma}\,. \tag{1.156}$$

We investigate this anomalous symmetry using the path-integral treatment first derived in [192], with the upshot that anomalies dwell in the non-trivial transformation laws of integration measures. The fermionic functional integral of the theory is given by [78]

$$\mathcal{Z} = \int \mathcal{D}\psi\mathcal{D}\bar\psi\exp\Big[i\int \mathrm{d}^4x\,\bar\psi(i\not{D})\psi\Big]\,, \tag{1.157}$$

where $\not{D} = \not{\partial} + ie\not{A}$. Under a local chiral gauge transformation,

$$\psi(x)\to\psi'(x) = e^{i\alpha(x)\gamma^5}\psi(x)\,, \quad \bar\psi(x)\to\bar\psi'(x) = \bar\psi e^{i\alpha(x)\gamma^5}\,, \tag{1.158}$$

the resulting transformation of the action reads

$$\int \mathrm{d}^4x\,\bar\psi(i\not{D})\psi \to \int \mathrm{d}^4x\Big[\bar\psi(i\not{D})\psi + \alpha(x)\partial_\mu j_5^\mu\Big]\,. \tag{1.159}$$

Formally, the integration measure changes to

$$\mathcal{D}\psi\mathcal{D}\bar\psi \to \mathcal{J}^{-1}\mathcal{D}\psi\mathcal{D}\bar\psi\,, \tag{1.160}$$

with the Jacobian

$$\mathcal{J} = \det\left(e^{2i\alpha(x)\gamma^5}\right) = \exp\Big[2i\,\mathrm{tr}\,\alpha(x)\gamma^5\Big]\,. \tag{1.161}$$

Naive implementation of the trace would result in a trivial transformation and vanishing of the anomaly. The caveat is that the determinant is divergent, for which we need a regularization prescription. It is this regularization prescription that generates the correct anomaly. To this end, we take the trace over the complete eigenstates of the operator $i\not{D}$ and introduce the regulator for the high-energy modes,

$$\mathcal{J} = \lim_{M\to\infty}\exp\Big[2i\int \mathrm{d}^4x\,\alpha(x)\langle x|\,\mathrm{tr}\,[\gamma^5 e^{(i\not{D})^2/M^2}]|x\rangle\Big]\,. \tag{1.162}$$

With the identity

$$\not{D}^2 = D^2 + \frac{ie}{4}[\gamma^\mu,\gamma^\nu]F_{\mu\nu}\,, \tag{1.163}$$

we find

$$\begin{aligned}
&\lim_{M\to\infty}\langle x|\,\mathrm{tr}\left[\gamma^5 e^{-\left(D^2+\frac{ie}{4}[\gamma^\mu,\gamma^\nu]F_{\mu\nu}\right)/M^2}\right]|x\rangle \\
&\quad=\lim_{M\to\infty}\frac{1}{2!}\,\mathrm{tr}\left[\gamma^5\left(\frac{ie}{4M^2}[\gamma^\mu,\gamma^\nu]F_{\mu\nu}\right)^2\right]\langle x|e^{-\partial^2/M^2}|x\rangle \\
&\quad=-\frac{e^2}{32\pi^2}\varepsilon^{\mu\nu\rho\sigma}F_{\mu\nu}F_{\rho\sigma}\,,
\end{aligned}\tag{1.164}$$

where the following equality is used:

$$\begin{aligned}
\langle x|e^{-\partial^2/M^2}|x\rangle&=\lim_{x\to y}\int\frac{\mathrm{d}^4k}{(2\pi)^4}e^{-ik\cdot(x-y)}e^{k^2/M^2} \\
&=i\int\frac{\mathrm{d}^4k_E}{(2\pi)^4}e^{-k_E^2/M^2}=i\frac{M^4}{16\pi^2}\,.
\end{aligned}\tag{1.165}$$

Combining the variation of the action and the measure,

$$\mathcal{Z}=\int\mathcal{D}\psi\mathcal{D}\bar\psi\exp\left\{i\int\mathrm{d}^4x\left[\bar\psi(i\not{D})\psi+\alpha(x)\left(\partial_\mu j_5^\mu+\frac{e^2}{16\pi^2}\varepsilon^{\mu\nu\rho\sigma}F_{\mu\nu}F_{\rho\sigma}\right)\right]\right\}.\tag{1.166}$$

The invariance of the functional gives the chiral anomaly (1.156). One may doubt that the above derivation would be subject to a special choice of the regulator, but the chiral anomaly is general for all different choices of regulators provided that they preserve the vector gauge invariance.

1.3.2 't Hooft anomaly matching

The chiral anomaly is a type of anomaly that pertains to global symmetries. Its generalization to non-Abelian theories is straightforward: we should take the trace over the additional group indices. For massless two-flavor QCD ($m_u=m_d=0$) of interest to us, the chiral anomaly for the iso-triplet current from the QED interaction reads

$$\begin{aligned}
\partial_\mu j_5^{\mu\,a}&=-\frac{e^2}{16\pi^2}\varepsilon^{\mu\nu\rho\sigma}F_{\mu\nu}F_{\rho\sigma}\,\mathrm{tr}\left(\frac{\sigma^a}{2}Q^2\right)\cdot\mathrm{tr}\,1_3 \\
&=-\frac{N_c e^2}{16\pi^2}\varepsilon^{\mu\nu\rho\sigma}F_{\mu\nu}F_{\rho\sigma}\,\mathrm{tr}\left(\frac{\sigma^a}{2}Q^2\right),
\end{aligned}\tag{1.167}$$

where the quark charge matrix is

$$Q=\begin{pmatrix}2/3 & 0\\ 0 & -1/3\end{pmatrix}.\tag{1.168}$$

This gives a non-zero result only for $a = 3$ and drives π^0 predominantly decaying into two photons.

Apart from anomalies in global symmetries, the second type of anomalies appears in gauge theories. These gauge anomalies are fatal as they violate Ward identities, which are indispensable for renormalizability and unitarity of the theory. Therefore, gauge anomalies must be canceled in chiral gauge theories. This leads to the anomaly cancellation condition (1.52) in the SM.

Like QCD, an asymptotically free gauge theory can be strongly coupled at short distances. This scenario indicates new relevant degrees of freedom at low energies and a new effective field theory for its description. What is the fate of possible global anomalies arising from the fundamental degrees of freedom at high energies? 't Hooft [193] discovered that the anomaly should be present and exact in both theories with relevant degrees of freedom regardless of the coupling strength. In the infrared domain, the anomaly should be restored by massless fermion bound states or Nambu–Goldstone bosons if the symmetry is spontaneously broken. In the case of QCD, the Wess–Zumino–Witten effective action [139, 140] of the pseudoscalar octet generates the anomaly after chiral symmetry breaking.

1.3.3 Wess–Zumino–Witten action

The ChPT Lagrangian is constructed from the Goldstone-boson fields collected in a unitary matrix representation $U(\phi(x))$ respecting chiral symmetry,

$$U(\phi(x)) = \exp\left(i\frac{\phi(x)}{F_0}\right), \tag{1.169}$$

where

$$\phi(x) = \sum_{a=1}^{8} \lambda_a \phi_a(x) = \sqrt{2}\begin{pmatrix} \frac{\pi^0}{\sqrt{2}} + \frac{\eta_8}{\sqrt{6}} & \pi^+ & K^+ \\ \pi^- & -\frac{\pi^0}{\sqrt{2}} + \frac{\eta_8}{\sqrt{6}} & K^0 \\ K^- & \bar{K}^0 & -\frac{2\eta_8}{\sqrt{6}} \end{pmatrix}. \tag{1.170}$$

The dimensionful constant F_0 is identified with the meson decay constant in the chiral limit. This construction contains a larger symmetry than QCD itself: the Lagrangian is invariant under $\phi(x) \to -\phi(x)$. Consequently, this usual construction is only capable of describing interactions involving even numbers of Goldstone bosons. The reactions driven by the anomaly in the odd-intrinsic-parity sector, like $\pi^0 \to \gamma\gamma$ and $\gamma \to 3\pi$, are relentlessly ruled out. Since the chiral symmetry is violated at a fundamental level by the fermionic determinant, the anomalous term should be added into the effective Lagrangian consistently. Wess and Zumino [139] worked out the result as a Taylor expansion of the explicit Goldstone-boson fields, as it cannot be expressed using $U(\phi(x))$ as a single local effective Lagrangian in a gauge-invariant form. Witten [140] later reformulated the effective action into an elegant representation as a five-dimensional Chern–Simons term, whose

boundary is the four-dimensional Minkowski space. To be more specific, it reads

$$S[U,\ell,r]_{\mathrm{WZW}} = -\frac{iN_c}{240\pi^2}\int_{B_5} \mathrm{d}^5x\,\epsilon^{ijklm}\,\mathrm{tr}\left(\Sigma_i^L\Sigma_j^L\Sigma_k^L\Sigma_l^L\Sigma_m^L\right) - \frac{iN_c}{48\pi^2}\int_{M_4}\mathrm{d}^4x\,\varepsilon_{\mu\nu\rho\sigma}\Big(W(U,\ell,r)^{\mu\nu\rho\sigma} - W(\mathbb{1},\ell,r)^{\mu\nu\rho\sigma}\Big)\,, \tag{1.171}$$

where the indices $i,\ldots,m$ run from 0 to 4, with the antisymmetric tensor $\epsilon_{01234} = -\epsilon^{01234} = 1$, and

$$\begin{aligned} W(U,\ell,r)_{\mu\nu\rho\sigma} = \mathrm{tr}\Big(&U\ell_\mu\ell_\nu\ell_\rho U^\dagger r_\sigma + \frac{1}{4}U\ell_\mu U^\dagger r_\nu U\ell_\rho U^\dagger r_\sigma + iU\partial_\mu\ell_\nu\ell_\rho U^\dagger r_\sigma \\ &+ i\partial_\mu r_\nu U\ell_\rho U^\dagger r_\sigma - i\Sigma_\mu^L\ell_\nu U^\dagger r_\rho U\ell_\sigma + \Sigma_\mu^L U^\dagger\partial_\nu r_\rho U\ell_\sigma \\ &- \Sigma_\mu^L\Sigma_\nu^L U^\dagger r_\rho U\ell_\sigma + \Sigma_\mu^L\ell_\nu\partial_\rho\ell_\sigma + \Sigma_\mu^L\partial_\nu\ell_\rho\ell_\sigma - i\Sigma_\mu^L\ell_\nu\ell_\rho\ell_\sigma \\ &+ \frac{1}{2}\Sigma_\mu^L\ell_\nu\Sigma_\rho^L\ell_\sigma - i\Sigma_\mu^L\Sigma_\nu^L\Sigma_\rho^L\ell_\sigma\Big) - (L\leftrightarrow R)\,, \end{aligned} \tag{1.172}$$

where

$$\Sigma_\mu^L = U^\dagger\partial_\mu U, \quad \Sigma_\mu^R = U\partial_\mu U^\dagger\,. \tag{1.173}$$

$L\leftrightarrow R$ stands for the interchanges $U\leftrightarrow U^\dagger$, $\ell_\mu\leftrightarrow r_\mu$, and $\Sigma_\mu^L\leftrightarrow\Sigma_\mu^R$. The first integral in (1.171) is over the boundary of a five-dimensional sphere B_5 and the second over the four-dimensional Minkowski space. Despite the complexity, the effective action (1.171) has no free parameters apart from the number of colors due to the anomaly matching. Inserting $\ell_\mu = r_\mu = eQA_\mu$ for the external currents and evaluating the traces render us the tree-level Lagrangian (1.61) for the pseudoscalar–photon–photon interactions.

Part I

Hadronic vacuum polarization

Chapter 2

Hadronic vacuum polarization: 3π[1]

2.1 Introduction

Three-particle decays subject to strong final-state interactions are notoriously difficult to describe in a fully model-independent way, i.e., without assumptions on intermediate states of the decay or other approximations of the hadron dynamics. One of the simplest examples is the three-pion decay of vector mesons, $V = \omega, \phi$, which phenomenologically is dominated by the $\rho(770)$ resonance formed in the final-state rescattering of the pions. However, a description beyond a simple isobar model is challenging, especially given that the decay is out of reach for low-energy effective field theories. A strategy to control the pion final-state interactions based on analyticity and unitarity was first developed in the context of $K \to 3\pi$ [195] and applied to $\omega \to 3\pi$ as early as [196]. These Khuri–Treiman (KT) equations have since become a standard tool in three-particle decays, with recent applications specifically to $\omega, \phi \to 3\pi$ decays in [197–200], in part triggered by significant progress in the determination of the $\pi\pi$ phase shifts that are required as crucial input in the solution [201, 202].

A detailed, model-independent understanding of hadronic amplitudes can have significant impact beyond low-energy QCD itself, most notably in low-energy searches for physics beyond the SM such as the muon $(g-2)_\mu$, whose SM prediction (1.64) currently disagrees with experiment (1.27) at the level of $3.7\,\sigma$. To confront the SM with upcoming experiments at Fermilab [70] and J-PARC [71], one needs to be able to control the theoretical uncertainties at a commensurate level. In this context, the issue of hadronic modeling is most severe in the HLbL contribution, for which a data-driven dispersive approach has only been recently developed [142–152].[2] In contrast, the leading hadronic contribution, HVP, is, in principle, fully determined by the cross section for $e^+e^- \to$ hadrons [86, 87], and indeed a combination of the analysis of exclusive channels, inclusive data, and pQCD constraints are used for current estimates of the HVP contribution [131, 132, 135, 136, 206, 207].[3] However, only the compilations from [131, 132, 135, 136] are exclusively based on the direct integration

[1] This Chapter's contents including Appendix A have been published in [134, 194].

[2] See [160, 161, 203–205] for recent progress in lattice-QCD calculations of HLbL scattering.

[3] This does not apply to space-like approaches, as in lattice QCD [208–216] or the MUonE proposal [217], which are complementary to but not yet competitive with the time-like approach.

of the data, while [206, 207] do involve some model assumptions, in particular for the ω and ϕ contributions. In general, tensions among data sets are typically taken into account by a local error inflation.

For the lowest-multiplicity channels that dominate HVP at low energies the available constraints from analyticity and unitarity (as well as low-energy theorems) are powerful enough to define a global fit function that the data need to follow if consistent with all QCD constraints. Such an approach to the 2π channel below 1 GeV has recently been completed in [133], relying on a close relation between $\pi\pi$ scattering, the pion vector form factor, and the HVP integral [218–222]. As a result, it was found that despite the known tension between BaBar [223, 224] and KLOE [225–228], each data set by itself is consistent with QCD constraints, and a global fit then defines an average that only uses as additional input information on the covariance matrices as provided by experiment.

Here, we extend this strategy to the 3π channel, which produces both the second-largest contribution to the total HVP value and its uncertainty. Instead of the pion vector form factor, the underlying hadronic amplitude becomes $\gamma^* \to 3\pi$, which will be discussed in Section 2.2.[4] It further emerges in the two-pion contributions via the left-hand cut in $\gamma^*\gamma^* \to \pi\pi$ [233–238]. For an isoscalar-photon virtuality $q^2 = M_\omega^2, M_\phi^2$, this amplitude is directly related to the three-particle decays of ω and ϕ, and indeed the KT approach can be generalized to obtain a dispersive representation of the $e^+e^- \to 3\pi$ cross section, see Section 2.2 for a short review. The ω and ϕ resonance peaks thus constitute the most conspicuous features of the cross section, but for the HVP integral also the off-peak regions need to be controlled, with QCD determining, via the Wess–Zumino–Witten anomaly [139, 140], the normalization in terms of the pion decay constant F_π [239–241], and, in terms of the KT equations, the $\pi\pi$ rescattering among the final-state pions.

In the 2π channel the average is dominated by experiments using the initial-state-radiation (ISR) technique, while data from energy-scan experiments [242–247] are consistent but currently less precise. For the 3π channel this situation is reversed, with only a single ISR data set, which, in addition, only covers the energy region above the ϕ [248]. Instead, the low-energy region including the ω and ϕ resonances has been most precisely measured by the Novosibirsk experiments SND [249–252] and CMD-2 [243, 253–255]. For completeness, we will also consider earlier data from DM1 [256], DM2 [257], and ND [258]. The main part of this Chapter is then devoted to the fit systematics to the various data sets, as detailed in Section 2.3, before working out the consequences for HVP in Section 2.4 and summarizing our findings in Section 2.5.

[4] This representation for the $\gamma^* \to 3\pi$ amplitude was first developed in the context of the pion-pole contribution to HLbL scattering [149, 150, 229–232] that will be discussed in Chapter 4, and later applied to the HVP contributions from the 3π and $\pi^0\gamma$ channels (Chapters 2 and 3). In this thesis, we discuss the results in reversed order to enhance the coherence of the presentation.

2.2 Dispersive representation of the $\gamma^* \to 3\pi$ amplitude

Neglecting the mass of the electron, the HVP contribution to $(g-2)_\mu$ can be expressed as (1.55), with the kernel function

$$\hat{K}(s) = \frac{3s}{m_\mu^2} \int_0^1 \mathrm{d}x \frac{x^2(1-x)}{x^2 + s/m_\mu^2(1-x)}\,, \tag{2.1}$$

which can be further expressed in terms of $K(s)$ in (1.41). Since higher-order iterations of HVP do become relevant [130, 259] (at NLO, this issue arises, at least in principle, even for HLbL [162]), conventions for the radiative corrections need to be specified. The hadronic cross section is to be understood including FSR, but with ISR and VP removed (*bare* cross section). This issue of radiative corrections is most severe for the 2π channel, and therein for the ISR data sets, but as demonstrated in [260] the corrections are now known sufficiently accurately that they cannot account for the $(g-2)_\mu$ anomaly.

For the 3π channel, we have $s_{\mathrm{th}} = 9M_\pi^2$ in (1.55) and the radiative corrections to the cross section are mainly of conceptual nature. Strictly speaking, a dispersive representation of the $\gamma^* \to 3\pi$ amplitude is only valid in pure QCD, so that, in principle, all photon contributions including FSR should be removed before the fit and only afterwards added again in a perturbative way. In the case of the 2π channel [133], this strategy was indeed carried through in the context of a scalar-QED approximation. For the 3π channel, the full HVP contribution is more than an order of magnitude smaller, so that the total size of the $3\pi\gamma$ final state would be naively estimated at the level $\lesssim 0.3 \times 10^{-10}$, which by itself is borderline relevant at the current level of accuracy. However, since FSR is automatically included in the cross sections provided by experiment, the actual effect only concerns a possible distortion of the fit due to subtracting and adding the FSR contribution, which will be even smaller and therefore neglected here. In contrast, the VP removal does become relevant at the current level of accuracy, mainly because of the resonance enhancement in the vicinity of ρ, ω, and ϕ, which shifts the pole position, see Section 2.3.5, and modifies the spectral function. When provided by experiment, we use the bare cross section directly, otherwise we apply the VP routine from [132]. To check the sensitivity to this correction, we also constructed an independent VP function based on the 2π fit from [133] as well as the 3π cross section from the present Chapter, so that major deviations to the full VP only start in the vicinity of the ϕ, where the $K\bar{K}$ channels become relevant. We can therefore check the 3π contribution self-consistently up-to-and-including the ω peak, producing a difference of less than 0.1×10^{-10} in the HVP integral. Accordingly, we conclude that the details of the VP routine lead to a negligible effect as well.

The dispersive representation that we fit to the bare cross section is constructed along the following lines. First, the cross section is given in terms of the $\gamma^* \to 3\pi$ amplitude

$\mathcal{F}(s,t,u;q^2)$ according to

$$\sigma_{e^+e^-\to 3\pi}(q^2) = \alpha^2 \int_{s_{\min}}^{s_{\max}} \mathrm{d}s \int_{t_{\min}}^{t_{\max}} \mathrm{d}t \, \frac{(s-4M_\pi^2)\,\lambda(q^2,M_\pi^2,s)\sin^2\theta_s}{768\,\pi\,q^6} \,|\mathcal{F}(s,t,u;q^2)|^2 \,, \tag{2.2}$$

with integration boundaries

$$\begin{aligned} s_{\min} &= 4M_\pi^2 \,, & s_{\max} &= \left(\sqrt{q^2}-M_\pi\right)^2 \,, \\ t_{\min/\max} &= (E_-^* + E_0^*)^2 - \left(\sqrt{E_-^{*2}-M_\pi^2} \pm \sqrt{E_0^{*2}-M_\pi^2}\right)^2 \,, \end{aligned} \tag{2.3}$$

and

$$E_-^* = \frac{\sqrt{s}}{2} \,, \qquad E_0^* = \frac{q^2-s-M_\pi^2}{2\sqrt{s}} \,. \tag{2.4}$$

The amplitude itself is defined by the matrix element of the electromagnetic current j_μ

$$\langle 0|j_\mu(0)|\pi^+(p_+)\pi^-(p_-)\pi^0(p_0)\rangle = -\varepsilon_{\mu\nu\rho\sigma}\,p_+^\nu p_-^\rho p_0^\sigma \mathcal{F}(s,t,u;q^2) \,, \tag{2.5}$$

with $q = p_+ + p_- + p_0$ and kinematics

$$\begin{aligned} &s = (q-p_0)^2, \qquad t = (q-p_+)^2 \,, \qquad u = (q-p_-)^2 \,, \qquad s+t+u = 3M_\pi^2 + q^2 \,, \\ &z_s = \cos\theta_s = \frac{t-u}{\sigma_\pi(s)\lambda^{1/2}(q^2,M_\pi^2,s)} \,, \\ &\sigma_\pi(s) = \sqrt{1-\frac{4M_\pi^2}{s}} \,, \qquad \lambda(a,b,c) = a^2+b^2+c^2-2(ab+ac+bc) \,. \end{aligned} \tag{2.6}$$

At low energy, the Wess–Zumino–Witten anomaly [139, 140] provides a normalization for $\mathcal{F}$ in the chiral limit [239–241], which reads

$$\mathcal{F}(0,0,0;0) = \frac{1}{4\pi^2 F_\pi^3} \equiv F_{3\pi} \,, \tag{2.7}$$

where $F_\pi = 92.28(10)$ MeV [22] is the pion decay constant. So far, this normalization has been tested only at the 10% level both in the extraction from Primakoff measurements [261] and from the reaction $\pi^- e^- \to \pi^- e^- \pi^0$ [262]. Therefore, a dispersive framework was proposed in [230, 232] to extract the chiral anomaly from the $\gamma\pi \to \pi\pi$ cross section up to 1 GeV, using forthcoming data on $\gamma\pi^- \to \pi^-\pi^0$ taken in the COMPASS Primakoff program [263].

The constraints from analyticity and unitarity are most conveniently formulated in terms of the partial-wave amplitudes [264]

$$\mathcal{F}(s,t,u;q^2) = \sum_{l\ \mathrm{odd}} f_l(s,q^2) P_l'(z_s) \,, \tag{2.8}$$

with derivatives of the Legendre polynomials $P_l'(z_s)$, and the dominant P-wave is projected out by

$$f_1(s,q^2) = \frac{3}{4}\int_{-1}^{1} \mathrm{d}z_s\,(1-z_s^2)\,\mathcal{F}(s,t,u;q^2)\,. \tag{2.9}$$

Since higher partial waves are completely irrelevant below the $\rho_3(1690)$ resonance [197, 232] (see Appendix A.1 for an estimate of the F-wave contribution), $\mathcal{F}$ can be decomposed into single-variable functions based on the reconstruction theorem [265, 266],

$$\mathcal{F}(s,t,u;q^2) = \mathcal{F}(s,q^2) + \mathcal{F}(t,q^2) + \mathcal{F}(u,q^2)\,. \tag{2.10}$$

$\mathcal{F}(s,q^2)$ is related to the $l=1$ partial wave according to

$$\begin{aligned} f_1(s,q^2) &= \mathcal{F}(s,q^2) + \hat{\mathcal{F}}(s,q^2)\,,\\ \hat{\mathcal{F}}(s,q^2) &= \frac{3}{2}\int_{-1}^{1} \mathrm{d}z_s\,(1-z_s^2)\,\mathcal{F}(t(s,q^2,z_s),q^2)\,, \end{aligned} \tag{2.11}$$

where

$$t(s,q^2,z_s) = \frac{1}{2}\,(3M_\pi^2 + q^2 - s) + \frac{1}{2}\,\sigma_\pi(s)\,\lambda^{1/2}(q^2,M_\pi^2,s)\,z_s\,. \tag{2.12}$$

$\hat{\mathcal{F}}(s,q^2)$ contains the left-hand-cut contribution to the partial wave $f_1(s,q^2)$ arising from the crossed-channel singularities. Furthermore, the angular integration in $\hat{\mathcal{F}}(s,q^2)$ imposes a complex analytic structure in the decay region $q^2 > 9M_\pi^2$, which is explained in detail in [197]. The discontinuity equation for $\mathcal{F}(s,q^2)$ reads

$$\mathrm{disc}\,\mathcal{F}(s,q^2) = 2i\,(\mathcal{F}(s,q^2) + \hat{\mathcal{F}}(s,q^2))\,\theta(s-4M_\pi^2)\sin\delta(s)\,e^{-i\delta(s)}\,, \tag{2.13}$$

where $\delta(s)$ refers to the $\pi\pi$ P-wave phase shift. This is where, in a model-independent way, the information about the $\rho(770)$ enters. The solution is given by a once-subtracted dispersive representation [197]:

$$\mathcal{F}(s,q^2) = \Omega(s)\left\{a(q^2) + \frac{s}{\pi}\int_{4M_\pi^2}^{\infty}\mathrm{d}s'\,\frac{\hat{\mathcal{F}}(s',q^2)\sin\delta(s')}{s'(s'-s)|\Omega(s')|}\right\}, \tag{2.14}$$

with the Omnès function [173]

$$\Omega(s) = \exp\left\{\frac{s}{\pi}\int_{4M_\pi^2}^{\infty}\mathrm{d}s'\,\frac{\delta(s')}{s'(s'-s)}\right\}, \tag{2.15}$$

The numerical calculation of the integral equation (2.14) relies on the iterative solution of the KT equations based on the observation that $\hat{\mathcal{F}}$ is linear in $\mathcal{F}$. In practice, we solve (2.14) with the $\pi\pi$ phase shift recently extracted from the $e^+e^- \to \pi^+\pi^-$ channel [133] and a cutoff parameter $\Lambda_{3\pi} = 2.5\,\mathrm{GeV}$ for $a(q^2) \to 1$ and restore the full dependence as an overall normalization of the iterative solution. Variations of these input quantities prove irrelevant compared to other sources of systematic uncertainties.

For a given q^2, the KT equations determine the s-dependence of the partial-wave amplitude $f_1(s, q^2)$, but the overall normalization $a(q^2)$ is not predicted. At $q^2 = 0$ it is determined by the low-energy theorem, at $q^2 = M_\omega^2, M_\phi^2$ it is related to the $\omega, \phi \to 3\pi$ decay widths, and in general it can be extracted from a fit to the $e^+e^- \to 3\pi$ cross section. We take essentially the same parameterization as in [149, 150]

$$a(q^2) = \alpha_A + \frac{q^2}{\pi} \int_{s_{\text{th}}}^{\infty} \mathrm{d}s' \, \frac{\operatorname{Im} \mathcal{A}(s')}{s'(s' - q^2)} + C_p(q^2) \,, \tag{2.16}$$

constructed in such a way as to fulfill the low-energy constraint from the chiral anomaly, preserve analyticity of $\mathcal{F}(s, t, u; q^2)$, and be flexible enough to describe the data up to 1.8 GeV. The significance of the individual terms is as follows: the subtraction constant α_A is determined by the chiral anomaly (corrected by quark-mass renormalization) [230, 267],

$$\alpha_A = \frac{F_{3\pi}}{3} \times 1.066(10) \,. \tag{2.17}$$

The function $\mathcal{A}$ is given by the sum of Breit–Wigner parameterizations

$$\mathcal{A}(q^2) = \sum_V \frac{c_V}{M_V^2 - q^2 - i\sqrt{q^2}\, \Gamma_V(q^2)} \,, \tag{2.18}$$

where V represents ω and ϕ and as well as $\omega'(1420)$ and $\omega''(1650)$ as the description of the $e^+e^- \to 3\pi$ cross section extends to 1.8 GeV. The energy-dependent widths $\Gamma_{\omega/\phi}(q^2)$ of the ω/ϕ mesons derive from their main decay channels according to

$$\begin{aligned}
\Gamma_\omega(q^2) &= \frac{\gamma_{\omega\to 3\pi}(q^2)}{\gamma_{\omega\to 3\pi}(M_\omega^2)} \Gamma_{\omega\to 3\pi} + \frac{\gamma_{\omega\to \pi^0\gamma}(q^2)}{\gamma_{\omega\to \pi^0\gamma}(M_\omega^2)} \Gamma_{\omega\to \pi^0\gamma} \,, \\
\Gamma_\phi(q^2) &= \frac{\gamma_{\phi\to 3\pi}(q^2)}{\gamma_{\phi\to 3\pi}(M_\phi^2)} \Gamma_{\phi\to 3\pi} + \sum_{K=K^+,K^0} \frac{\gamma_{\phi\to K\bar{K}}(q^2)}{\gamma_{\phi\to K\bar{K}}(M_\phi^2)} \Gamma_{\phi\to K\bar{K}} \,,
\end{aligned} \tag{2.19}$$

with Γ_i the measured partial decay width for the decay i and the energy-dependent coefficients

$$\gamma_{\omega\to\pi^0\gamma}(q^2) = \frac{(q^2 - M_\pi^2)^3}{(q^2)^{3/2}} \,, \qquad \gamma_{\phi\to K\bar{K}}(q^2) = \frac{(q^2 - 4M_K^2)^{3/2}}{q^2} \,. \tag{2.20}$$

The phase space $\gamma_{\omega/\phi\to 3\pi}(q^2)$ is calculated as described in [197]. These main channels amount to about 98% of the ω and ϕ total widths, while the missing 2% are remedied by rescaling all partial widths accordingly. We also considered adding the leading missing channels $\omega \to \pi^+\pi^-$ and $\phi \to \eta\gamma$ explicitly to the parameterization, but this yields an almost identical effect compared to the simple rescaling of the partial widths. Due to

the $\pi^0\gamma$ channel, the integration starts at $s_{\text{th}} = M_{\pi^0}^2$. The parameters for ω' and ω'' are taken from [22], assuming a 100% branching ratio to 3π, but for ω and ϕ we now allow mass and width to vary: with VP removed, noticeable differences to the PDG emerge, see Section 2.3.5, which is expected since the PDG parameters subsume radiative effects.

Finally, the conformal polynomial in (2.16)

$$C_p(q^2) = \sum_{i=1}^{p} c_i (z(q^2)^i - z(0)^i)\,, \qquad z(q^2) = \frac{\sqrt{s_{\text{inel}} - s_1} - \sqrt{s_{\text{inel}} - q^2}}{\sqrt{s_{\text{inel}} - s_1} + \sqrt{s_{\text{inel}} - q^2}}\,, \tag{2.21}$$

accounts for non-resonant effects. The inelastic threshold s_{inel} is set to $1\,\text{GeV}^2$. motivated by the nearby $K\bar{K}$ threshold, the second parameter to $s_1 = -1\,\text{GeV}^2$. Further constraints are implemented to remove the S-wave cusp in the polynomial and to ensure that the sum rule

$$\alpha_A = \frac{1}{\pi}\int_{s_{\text{th}}}^{\infty} \mathrm{d}s' \frac{\operatorname{Im} a(s')}{s'} = \frac{1}{\pi}\int_{s_{\text{th}}}^{\infty} \mathrm{d}s' \frac{\operatorname{Im} \mathcal{A}(s')}{s'} + \frac{1}{\pi}\int_{s_{\text{inel}}}^{\infty} \mathrm{d}s' \frac{\operatorname{Im} C_p(s')}{s'} \tag{2.22}$$

is fulfilled exactly. In [149, 150] we also introduced further parameters to be able to impose a faster asymptotic behavior of the imaginary part as required for the dispersive description of the pion transition form factor (TFF), but since this impaired to some extent the description of the cross section, here, we only consider these additional constraints to estimate systematic uncertainties.

2.3 Fits to e^+e^- data

2.3.1 Data sets and unbiased fitting

We start with a brief summary of the data sets that we will include in our analysis, see Table 2.1. For all data sets the statistical errors are given in diagonal form, with the implication that correlations are negligible at least at the quoted level of uncertainty. In contrast, the treatment of the systematic uncertainties is more ambiguous, since assumptions need to be made on the correlations between data points. Some sources of systematic uncertainty are, by definition, 100% correlated, these are normalization uncertainties for instance due to the luminosity measurement and the detection efficiency, but other systematic effects may well be localized in certain energy regions and therefore should not be considered fully correlated. To follow the experimental documentation as closely as possible, we consider a systematic error of normalization-type origin whenever given as a percentage, otherwise, we treat that uncertainty as a diagonal error. Note that this distinction mainly affects the SND data sets, while for the other energy-scan experiments all systematic errors are given as a percentage. The exception is the ISR data set from BaBar, but [248] states explicitly that the systematic errors for different mass bins are fully correlated.

Experiment	Region of $\sqrt{s}$ [GeV]	# data points	Normalization uncertainty
SND 2002 [249, 250]	[0.98, 1.38]	67	5.0% (data from [249]) 5.4% (otherwise)
SND 2003 [251]	[0.66, 0.97]	49	3.4% for $\sqrt{s} < 0.9\,\text{GeV}$ 4.5% for $\sqrt{s} > 0.9\,\text{GeV}$
SND 2015 [252]	[1.05, 1.80]	31	3.7%
CMD-2 1995 [253]	[0.99, 1.03]	16	4.6%
CMD-2 1998 [254]	[0.99, 1.03]	13	2.3%
CMD-2 2004 [243]	[0.76, 0.81]	13	1.3%
CMD-2 2006 [255]	[0.98, 1.06]	54	2.5%
DM1 1980 [256]	[0.75, 1.10]	26	3.2%
ND 1991 [258]	[0.81, 1.39]	28	10% for $\sqrt{s} < 1.0\,\text{GeV}$ 20% for $\sqrt{s} > 1.0\,\text{GeV}$
DM2 1992 [257]	[1.34, 1.80]	10	8.7%
BaBar 2004 [248]	[1.06, 1.80]	30	all systematics

Table 2.1: Summary of data sets for $e^+e^- \to 3\pi$. For [248, 252, 257] only data points for $\sqrt{s} \leq 1.8\,\text{GeV}$ are included. In the last column we indicate the size of the systematic errors that we interpret as a normalization-type uncertainty and therefore assume to be 100% correlated.

These details are important to monitor a potential bias in the fit. Most importantly, a χ^2-minimization with an empirical full covariance matrix $\mathrm{V}(i,j)$ including a normalization uncertainty,

$$\chi^2 = \sum_{i,j} (f(x_i) - y_i)\mathrm{V}(i,j)^{-1}(f(x_j) - y_j)\,, \tag{2.23}$$

will converge to a solution that is biased towards a lower value than expected due to the fact that smaller data values are assigned smaller normalization uncertainties. This D'Agostini bias was first observed in [268]. It becomes increasingly severe for large normalization uncertainties and/or a large number of data points, so precisely when there is a normalization uncertainty in an experiment that is 100% correlated among all data points. In addition, in a global fit of several experiments a bias that may occur in the combination needs to be avoided.

We follow the iterative fit strategy proposed by the NNPDF collaboration [269] to eliminate the bias, which is based on the observation that the normalization uncertainties should be proportional to the true value rather than the measurement. In this manner, the

modified iterative covariance matrix is given as

$$\mathrm{V}_{n+1}(i,j) = \mathrm{V}^{\mathrm{stat}}(i,j) + \frac{\mathrm{V}^{\mathrm{syst}}(i,j)}{y_i y_j} f_n(x_i) f_n(x_j)\,, \tag{2.24}$$

where $\mathrm{V}^{\mathrm{stat}}(i,j)$ is the statistical covariance matrix and the systematic covariance matrix $\mathrm{V}^{\mathrm{syst}}(i,j)$ is determined by multiplying the normalization factors with the fit function $f_n(x_i)$ in each iteration step rather than the data. The empirical covariance matrix can be chosen as the initial guess, with expected rapid convergence to the final solution.

In the fit to the data sets in Table 2.1 we only encounter either fully correlated or diagonal errors. We follow [269] and treat the uncorrelated systematic errors on the same footing as the statistical ones. For a single experiment one would therefore expect that the central values obtained in a fit with diagonal errors only should be close to the central values of the full fit,otherwise, one would need to understand better the role of the correlations. In the following, we will thus consider both diagonal and full fits to monitor whether significant differences arise.

2.3.2 Fits to SND

As the first set of fits we consider the SND data sets [249–252]. The results are summarized in Table 2.2, both for diagonal errors only and including correlations as described in the previous section. In each case we consider variants of the fits with $p_{\mathrm{conf}} = 2\ldots4$ free parameters in the conformal polynomial and at this stage display only the fit uncertainties, with systematic uncertainties of the dispersive representation to be added later.

The results in Table 2.2 show that the main effect of the correlations is an increase in the uncertainty, within the fit statistics the central values agree with the diagonal fit. However, we also note that the description of the data becomes worse, which can be remedied to some extent by increasing p_{conf}. While the diagonal fit proves very stable to variations of p_{conf}, we observe that when including the correlations the central value increases with p_{conf}, balancing the reduction in the central value compared to the diagonal fit in the variant with $p_{\mathrm{conf}} = 2$, the smallest for which a reasonable fit can be obtained.

We note that the treatment of the systematic uncertainties, closely following experiment as specified in Section 2.3.1, is critical to obtain consistent fits. If all systematic uncertainties were assumed to be fully correlated, the fit iteration would not even converge or, when restricted to a subset of the data, lead to a significant downward bias.

2.3.3 Fits to CMD-2 and BaBar

The CMD-2 data sets mainly cover the resonance regions, with [243] scattered around the ω peak and [253–255] around the ϕ. To be able to perform fits to the whole energy region up to 1.8 GeV and thus facilitate the comparison to the SND fits we combine the CMD-2 data with the BaBar data set [248], which starts directly above the ϕ and covers the remainder.

	diagonal			full		
p_{conf}	2	3	4	2	3	4
χ^2/dof	97.6/137	93.5/136	93.2/135	164.9/137	155.4/136	152.6/135
	= 0.71	= 0.69	= 0.69	= 1.20	= 1.14	= 1.13
p-value	0.996	0.998	0.998	0.052	0.12	0.14
M_ω [MeV]	782.62(4)	782.62(4)	782.62(4)	782.63(2)	782.63(2)	782.63(2)
Γ_ω [MeV]	8.68(6)	8.72(7)	8.73(7)	8.66(3)	8.68(3)	8.68(3)
M_ϕ [MeV]	1019.19(4)	1019.18(4)	1019.18(4)	1019.19(2)	1019.19(2)	1019.19(2)
Γ_ϕ [MeV]	4.16(8)	4.13(8)	4.13(8)	4.17(4)	4.16(4)	4.16(4)
c_ω [GeV^{-1}]	2.88(1)	2.89(1)	2.89(1)	2.87(3)	2.88(3)	2.90(3)
c_ϕ [GeV^{-1}]	−0.393(4)	−0.392(4)	−0.392(4)	−0.388(6)	−0.386(6)	−0.385(6)
$c_{\omega'}$ [GeV^{-1}]	−0.16(4)	−0.08(5)	−0.08(5)	−0.16(3)	−0.06(4)	−0.07(5)
$c_{\omega''}$ [GeV^{-1}]	−1.59(9)	−1.46(11)	−1.42(14)	−1.62(9)	−1.50(10)	−1.42(12)
c_1 [GeV^{-3}]	−0.43(11)	−0.33(13)	−0.32(13)	−0.37(11)	−0.18(12)	−0.06(15)
c_2 [GeV^{-3}]	−1.35(5)	−1.44(7)	−1.49(12)	−1.30(5)	−1.42(6)	−1.58(12)
c_3 [GeV^{-3}]	—	−0.45(9)	−0.41(12)	—	−0.48(8)	−0.41(10)
c_4 [GeV^{-3}]	—	—	1.40(10)	—	—	1.52(10)
$10^{10} \times a_\mu^{3\pi}\vert_{\leq 1.8\,\text{GeV}}$	47.28(25)	47.31(25)	47.34(25)	46.74(92)	46.97(93)	47.53(1.00)

Table 2.2: Fits to the combination of SND data sets [249–252], for diagonal errors and full covariance matrices. p_{conf} denotes the number of free parameters in the conformal polynomial. All errors refer to fit uncertainties only.

We do not find acceptable fits for the naive combination of all these data sets. To isolate the reason we perform two separate fits, first, to [243, 253, 254] and BaBar [248], as given in Table 2.3, as well as [243, 255] and BaBar [248], see Table 2.4. This strategy is motivated by the suspicion that inconsistencies among the CMD-2 data sets arise in the vicinity of the ϕ, which the separate consideration of the data sets covering this region should be able to corroborate.

In all cases we see that the diagonal and full fits are well compatible, so that the treatment of correlations becomes less of a concern than for the SND fits. However, we find that the fit quality is quite poor: while for the [253, 254] ϕ data sets the fits with $p_{\text{conf}} = 4$ might still be considered acceptable, this is certainly not the case for [255], even though also in this case higher orders in the conformal expansion do yield some improvement of the χ^2. The most relevant discrepancies in the fit results concern the ω coupling c_ω, which is significantly smaller in Table 2.4 despite being based on the same data set in the ω region, leading to the overall much lower HVP integral, as well as the ϕ mass. The fits in Table 2.3 prefer a value around $M_\phi = 1019.25(4)$ MeV, while the fits in Table 2.4 point to $M_\phi = 1019.09(3)$ MeV, suggesting that inconsistencies in the ϕ region are compensated elsewhere in the fit, thus the

	diagonal			full		
p_{conf}	2	3	4	2	3	4
χ^2/dof	83.9/62	83.5/61	77.4/60	91.9/62	91.6/61	84.3/60
	= 1.35	= 1.37	= 1.29	= 1.48	= 1.50	= 1.41
p-value	0.03	0.03	0.06	0.008	0.007	0.02
M_ω [MeV]	782.49(10)	782.49(10)	782.50(10)	782.49(9)	782.49(9)	782.50(9)
Γ_ω [MeV]	9.11(17)	9.13(16)	8.99(16)	9.11(15)	9.13(15)	9.00(15)
M_ϕ [MeV]	1019.25(4)	1019.25(4)	1019.22(4)	1019.28(4)	1019.27(4)	1019.25(4)
Γ_ϕ [MeV]	4.46(11)	4.45(11)	4.45(11)	4.46(10)	4.46(10)	4.46(10)
c_ω [GeV^{-1}]	2.91(4)	2.92(4)	2.88(4)	2.91(4)	2.92(4)	2.88(4)
c_ϕ [GeV^{-1}]	−0.406(8)	−0.406(8)	−0.407(8)	−0.405(8)	−0.404(8)	−0.405(8)
$c_{\omega'}$ [GeV^{-1}]	−0.25(11)	−0.21(13)	−0.19(14)	−0.24(11)	−0.21(12)	−0.18(13)
$c_{\omega''}$ [GeV^{-1}]	−2.03(32)	−1.97(31)	−2.69(37)	−2.01(31)	−1.98(30)	−2.73(35)
c_1 [GeV^{-3}]	0.12(43)	0.22(42)	0.20(30)	0.07(43)	0.17(43)	0.10(29)
c_2 [GeV^{-3}]	−1.14(12)	−1.19(14)	−0.31(40)	−1.16(11)	−1.19(13)	−0.24(39)
c_3 [GeV^{-3}]	—	−0.84(28)	−1.51(34)	—	−0.84(28)	−1.52(32)
c_4 [GeV^{-3}]	—	—	1.20(22)	—	—	1.19(21)
$10^{10} \times a_\mu^{3\pi}\vert_{\leq 1.8\,\text{GeV}}$	46.17(56)	46.19(55)	45.80(57)	46.23(74)	46.27(74)	45.83(75)

Table 2.3: Fits to the combination of the CMD-2 data sets [243, 253, 254] and BaBar [248].

change in c_ω.

From the mass shifts discussed in Appendix A.2, together with the PDG ϕ mass, we would expect a fit value $M_\phi = 1019.20\,\text{MeV}$, in perfect agreement with Table 2.2, largely consistent with Table 2.3, but clearly at odds with Table 2.4. Since within uncertainties the ω masses are consistent among the three fits, this suggests as a remedy to include energy-calibration uncertainties in the context of [255], in analogy to the energy rescalings found necessary in the case of the 2π channel [133]. In fact, [255] includes three different scans, and separate fits to each of them reveal that the first two yield ϕ masses in the expected range, while the third one differs, leading to the lower mass in Table 2.4. Accordingly, we apply a rescaling

$$\sqrt{s} \to \sqrt{s} + \xi(\sqrt{s} - 3M_\pi) \tag{2.25}$$

to the data of the third scan only. The fit prefers a rescaling around $\xi \sim 10^{-4}$, well in line with potential uncertainties of the energy calibration. Including ξ as an additional parameter in the fit indeed leads to a mild improvement in the χ^2.

However, removing this tension in M_ϕ by no means renders the resulting fits statistically acceptable. Inspection of the contribution to the χ^2 from each data point shows that a by far disproportionate amount originates from the last few points of each scan of [255] for

	diagonal			full		
p_{conf}	2	3	4	2	3	4
χ^2/dof	199.4/87	164.8/86	142.0/85	213.3/87	185.0/86	156.4/85
	= 2.29	= 1.91	= 1.67	= 2.45	= 2.15	= 1.84
p-value	8×10^{-11}	7×10^{-7}	1×10^{-4}	1×10^{-12}	3×10^{-9}	4×10^{-6}
M_ω [MeV]	782.53(10)	782.54(10)	782.56(10)	782.53(10)	782.54(9)	782.56(10)
Γ_ω [MeV]	8.74(12)	8.74(12)	8.48(13)	8.76(13)	8.80(12)	8.56(13)
M_ϕ [MeV]	1019.11(2)	1019.09(2)	1019.07(2)	1019.10(2)	1019.08(2)	1019.07(2)
Γ_ϕ [MeV]	4.40(6)	4.34(6)	4.34(6)	4.35(5)	4.30(5)	4.29(5)
c_ω [GeV^{-1}]	2.81(3)	2.81(3)	2.74(3)	2.80(3)	2.81(3)	2.74(3)
c_ϕ [GeV^{-1}]	−0.399(4)	−0.396(4)	−0.396(4)	−0.408(6)	−0.401(6)	−0.401(6)
$c_{\omega'}$ [GeV^{-1}]	−0.79(8)	−0.19(12)	−0.09(13)	−0.63(9)	−0.18(11)	−0.08(12)
$c_{\omega''}$ [GeV^{-1}]	−3.08(19)	−1.92(26)	−2.67(29)	−2.76(23)	−1.90(25)	−2.73(28)
c_1 [GeV^{-3}]	1.77(29)	1.43(27)	0.54(30)	1.38(32)	1.30(27)	0.37(29)
c_2 [GeV^{-3}]	−0.27(11)	−0.97(14)	0.25(32)	−0.47(11)	−0.99(13)	0.35(32)
c_3 [GeV^{-3}]	—	−0.60(23)	−1.35(27)	—	−0.60(22)	−1.40(25)
c_4 [GeV^{-3}]	—	—	1.34(21)	—	—	1.28(20)
$10^{10} \times a_\mu^{3\pi}\vert_{\leq 1.8\,\text{GeV}}$	44.36(48)	44.40(48)	43.87(49)	44.10(66)	44.32(66)	43.74(66)

Table 2.4: Fits to the combination of the CMD-2 data sets [243, 255] and BaBar [248].

which the cross section drops below 5 nb. In the end, we have to conclude that these points cannot be described in a statistically acceptable way with our dispersive representation. To demonstrate the huge impact on the fit, Table 2.5 gives the results when these critical points are removed. The fit is clearly still not perfect, but at least comparable in quality to Table 2.3. Accordingly, we believe that there is reason to suspect some additional systematic uncertainty in the off-peak cross sections from [255] and therefore will only consider the reduced data set as in Table 2.5 in the following (denoted by CMD-2′).

2.3.4 Combined fits

Our final preferred fit is shown in Table 2.6, including all data sets listed in Table 2.1 except for the DM2 data [257], which disagree with both the BaBar [248] and the SND [252] data especially in the vicinity of the $\omega''(1650)$. We also considered fits dropping the CMD-2 data set [255] altogether, see Table 2.7, but the overall effect is relatively minor, depending on the fit variant at most 0.2×10^{-10} in the final $(g-2)_\mu$ integral.

In all cases the χ^2 is significantly worse than in the separate fits discussed in the previous sections. Since there are now several experiments covering the same energy region, this is

	diagonal			full		
p_{conf}	2	3	4	2	3	4
χ^2/dof	117.9/76	111.8/75	97.7/74	133.9/76	129.1/75	112.2/74
	= 1.55	= 1.49	= 1.32	= 1.76	= 1.72	= 1.52
p-value	0.001	0.004	0.03	5×10^{-5}	1×10^{-4}	0.003
M_ω [MeV]	782.50(10)	782.50(10)	782.52(10)	782.51(10)	782.51(9)	782.53(10)
Γ_ω [MeV]	8.95(16)	9.01(14)	8.79(15)	8.96(15)	9.01(14)	8.82(14)
M_ϕ [MeV]	1019.19(3)	1019.18(3)	1019.15(3)	1019.17(2)	1019.16(2)	1019.14(3)
Γ_ϕ [MeV]	4.34(6)	4.31(6)	4.30(6)	4.31(5)	4.29(5)	4.28(5)
c_ω [GeV^{-1}]	2.87(4)	2.88(3)	2.83(3)	2.86(4)	2.88(3)	2.82(4)
c_ϕ [GeV^{-1}]	−0.393(4)	−0.392(4)	−0.392(4)	−0.397(6)	−0.395(6)	−0.394(6)
$c_{\omega'}$ [GeV^{-1}]	−0.37(12)	−0.19(13)	−0.13(14)	−0.34(11)	−0.18(12)	−0.12(12)
$c_{\omega''}$ [GeV^{-1}]	−2.20(35)	−1.94(29)	−2.73(32)	−2.17(34)	−1.94(27)	−2.80(31)
c_1 [GeV^{-3}]	0.41(48)	0.66(36)	0.28(29)	0.39(47)	0.60(35)	0.15(28)
c_2 [GeV^{-3}]	−0.95(13)	−1.14(14)	−0.03(35)	−0.98(12)	−1.14(14)	0.09(35)
c_3 [GeV^{-3}]	—	−0.75(25)	−1.51(30)	—	−0.76(25)	−1.54(28)
c_4 [GeV^{-3}]	—	—	1.26(22)	—	—	1.23(21)
$10^4 \times \xi$	1.4(7)	1.4(7)	1.4(7)	1.1(6)	1.0(6)	1.0(6)
$10^{10} \times a_\mu^{3\pi}\vert_{\leq 1.8\,\text{GeV}}$	45.35(54)	45.42(51)	44.89(52)	45.26(72)	45.38(70)	44.87(70)

Table 2.5: Fits to the combination of the CMD-2 data sets [243, 255] and BaBar [248], with modifications to [255] as described in the main text.

an indication of the degree of consistency among the various data sets. To account for these inconsistencies we follow the PDG prescription [22] and inflate the fit errors by the scale factor

$$S = \sqrt{\chi^2/\text{dof}}\,, \tag{2.26}$$

which increases uncertainties by about 20% compared to the fit errors given in Table 2.6. The systematic uncertainties are dominated by the degree of the conformal polynomial, while the uncertainties from $\pi\pi$ phase shifts and cutoff parameters are negligible in comparison. We adopt the full results for $p_{\text{conf}} = 3$ as our central value (as this gives the best fit), but keep the maximum differences to $p_{\text{conf}} = 2, 4$ as a source of systematic uncertainty. In addition, we perform fits in which the imaginary part of the conformal polynomial in (2.21) is constrained to behave as q^{-3} asymptotically, and include the observed variation as another source of systematics, see Table 2.8 for this last set of fits. As alluded to earlier, the fit quality deteriorates when imposing this additional constraint on the conformal polynomial, and therefore the full variation over all fit variants would likely be an overestimate of the systematic uncertainty. To gauge the impact, we take the average change for $p_{\text{conf}} = 2, 3, 4$

	diagonal			full		
p_{conf}	2	3	4	2	3	4
χ^2/dof	361.3/306	354.6/305	354.0/304	443.7/306	430.8/305	430.7/304
	= 1.18	= 1.16	= 1.16	= 1.45	= 1.41	= 1.42
p-value	0.02	0.03	0.03	4×10^{-7}	3×10^{-6}	2×10^{-6}
M_ω [MeV]	782.60(4)	782.60(4)	782.60(4)	782.63(2)	782.63(2)	782.63(2)
Γ_ω [MeV]	8.75(6)	8.79(6)	8.77(6)	8.69(3)	8.71(3)	8.71(3)
M_ϕ [MeV]	1019.23(2)	1019.22(2)	1019.22(2)	1019.20(1)	1019.20(1)	1019.20(1)
Γ_ϕ [MeV]	4.34(4)	4.32(4)	4.32(4)	4.24(3)	4.23(3)	4.23(3)
c_ω [GeV^{-1}]	2.87(1)	2.89(1)	2.88(1)	2.85(2)	2.86(2)	2.86(2)
c_ϕ [GeV^{-1}]	−0.395(3)	−0.394(3)	−0.394(3)	−0.388(3)	−0.386(3)	−0.386(3)
$c_{\omega'}$ [GeV^{-1}]	−0.18(3)	−0.09(5)	−0.08(5)	−0.17(3)	−0.07(4)	−0.06(4)
$c_{\omega''}$ [GeV^{-1}]	−1.65(8)	−1.52(10)	−1.55(10)	−1.65(8)	−1.52(8)	−1.53(10)
c_1 [GeV^{-3}]	−0.35(10)	−0.22(11)	−0.24(11)	−0.31(10)	−0.12(11)	−0.14(12)
c_2 [GeV^{-3}]	−1.28(4)	−1.39(6)	−1.33(9)	−1.24(4)	−1.36(5)	−1.34(9)
c_3 [GeV^{-3}]	—	−0.48(8)	−0.51(9)	—	−0.47(7)	−0.48(8)
c_4 [GeV^{-3}]	—	—	1.39(9)	—	—	1.41(9)
$10^4 \times \xi$	1.9(7)	1.8(7)	1.8(7)	1.3(5)	1.3(5)	1.3(5)
$10^{10} \times a_\mu^{3\pi}\vert_{\leq 1.8\,\text{GeV}}$	46.65(21)	46.70(21)	46.67(22)	45.87(47)	46.16(47)	46.10(50)

Table 2.6: Fits to the combination of SND [249–252], CMD-2′ [243, 253–255], BaBar [248], DM1 [256], and ND [258].

separately, and add the result in quadrature to the systematic error from the variation in p_{conf}.[5] The final fit is illustrated in Figure 2.1.

2.3.5 Extracting ω and ϕ masses

Our final result for the ω and ϕ parameters is

$$\begin{aligned} M_\omega &= 782.63(3)(1)\,\text{MeV} = 782.63(3)\,\text{MeV}\,, \\ \Gamma_\omega &= 8.71(4)(4)\,\text{MeV} = 8.71(6)\,\text{MeV}\,, \\ M_\phi &= 1019.20(2)(1)\,\text{MeV} = 1019.20(2)\,\text{MeV}\,, \\ \Gamma_\phi &= 4.23(4)(2)\,\text{MeV} = 4.23(4)\,\text{MeV}\,, \end{aligned} \tag{2.27}$$

[5] Note that the fits with $p_{\text{conf}} = 4$ from Table 2.8 already display signs of numerical instabilities, with large shifts in the fit parameters compared to $p_{\text{conf}} = 3$ and sizable cancellations among the terms in the conformal polynomial. We still include this fit in the estimate of the systematic uncertainties, otherwise, the systematic errors of the final results given in Sections 2.3.5 and 2.4 would decrease slightly.

	diagonal			full		
p_{conf}	2	3	4	2	3	4
χ^2/dof	286.5/263	283.3/262	283.3/261	368.0/263	358.9/262	358.6/261
	= 1.09	= 1.08	= 1.09	= 1.40	= 1.37	= 1.37
p-value	0.15	0.19	0.16	2×10^{-5}	6×10^{-5}	6×10^{-5}
M_ω [MeV]	782.60(4)	782.60(4)	782.60(4)	782.63(2)	782.63(2)	782.63(2)
Γ_ω [MeV]	8.77(6)	8.80(6)	8.80(6)	8.70(3)	8.71(3)	8.71(3)
M_ϕ [MeV]	1019.24(3)	1019.23(3)	1019.23(3)	1019.22(2)	1019.21(2)	1019.21(2)
Γ_ϕ [MeV]	4.28(6)	4.26(6)	4.26(6)	4.21(4)	4.20(4)	4.20(4)
c_ω [GeV^{-1}]	2.88(1)	2.89(1)	2.89(1)	2.85(2)	2.87(2)	2.87(2)
c_ϕ [GeV^{-1}]	−0.395(4)	−0.394(4)	−0.394(4)	−0.385(4)	−0.384(4)	−0.383(4)
$c_{\omega'}$ [GeV^{-1}]	−0.17(3)	−0.10(5)	−0.10(5)	−0.17(3)	−0.08(4)	−0.08(4)
$c_{\omega''}$ [GeV^{-1}]	−1.65(8)	−1.55(9)	−1.56(11)	−1.67(8)	−1.55(8)	−1.53(10)
c_1 [GeV^{-3}]	−0.36(10)	−0.27(11)	−0.27(12)	−0.30(10)	−0.14(11)	−0.11(12)
c_2 [GeV^{-3}]	−1.30(4)	−1.38(6)	−1.37(10)	−1.25(4)	−1.36(5)	−1.39(10)
c_3 [GeV^{-3}]	—	−0.51(8)	−0.51(9)	—	−0.51(7)	−0.49(8)
c_4 [GeV^{-3}]	—	—	1.34(9)	—	—	1.40(9)
$10^{10} \times a_\mu^{3\pi}\vert_{\leq 1.8\,\text{GeV}}$	46.81(22)	46.84(22)	46.84(22)	46.02(50)	46.21(50)	46.29(53)

Table 2.7: Fits to the combination of SND [249–252], CMD-2 [243, 253, 254], BaBar [248], DM1 [256], and ND [258].

with systematic errors derived as described in Section 2.3.4. In the comparison to the PDG parameters [22]

$$\begin{aligned} M_\omega &= 782.65(12)\,\text{MeV}\,, & \Gamma_\omega &= 8.49(8)\,\text{MeV}\,, \\ M_\phi &= 1019.461(16)\,\text{MeV}\,, & \Gamma_\phi &= 4.249(13)\,\text{MeV}\,, \end{aligned} \tag{2.28}$$

one needs to keep in mind that these parameters subsume radiative effects, where the expected corrections are worked out in Appendix A.2. For the ϕ, the expectation is that the fit of the bare parameters should produce a mass lower by 0.26 MeV with only small corrections in the width, in perfect agreement with (2.27) and (2.28). In contrast, the situation for the ω is more ambiguous: the number in (2.28) is dominated by the weighted average of extractions from $e^+e^- \to 3\pi$ ($M_\omega = 782.68(9)(4)$ MeV [243], $M_\omega = 782.79(8)(9)$ MeV [251]), $e^+e^- \to \pi^0\gamma$ ($M_\omega = 783.20(13)(16)$ MeV [270]), and $\bar{p}p \to \omega\pi^0\pi^0$ ($M_\omega = 781.96(13)(17)$ MeV [271]). In view of the expected downward shift of 0.13 MeV, our analysis thus supports the 3π number from [251], while the agreement with the PDG average is entirely coincidental. As argued in [133], the $\pi^0\gamma$ value is likely affected by an unphysical phase in the extraction, but our analysis shows that a similar effect does not occur in 3π. Therefore, our analysis

	diagonal			full		
p_{conf}	2	3	4	2	3	4
χ^2/dof	382.8/306 = 1.25	382.7/305 = 1.25	353.2/304 = 1.16	469.5/306 = 1.53	469.5/305 = 1.54	432.3/304 = 1.42
p-value	0.002	0.002	0.03	5×10^{-9}	4×10^{-9}	2×10^{-6}
M_ω [MeV]	782.59(4)	782.59(4)	782.60(4)	782.63(2)	782.63(2)	782.63(2)
Γ_ω [MeV]	8.70(6)	8.70(6)	8.68(6)	8.67(3)	8.67(3)	8.68(3)
M_ϕ [MeV]	1019.23(2)	1019.23(2)	1019.24(2)	1019.21(1)	1019.20(1)	1019.21(1)
Γ_ϕ [MeV]	4.35(4)	4.35(4)	4.36(4)	4.25(3)	4.25(3)	4.25(3)
c_ω [GeV^{-1}]	2.86(1)	2.86(1)	2.86(1)	2.82(2)	2.83(2)	2.82(2)
c_ϕ [GeV^{-1}]	−0.395(3)	−0.395(3)	−0.395(3)	−0.388(3)	−0.388(3)	−0.389(3)
$c_{\omega'}$ [GeV^{-1}]	−0.08(3)	−0.09(5)	0.10(5)	−0.07(3)	−0.07(4)	0.09(4)
$c_{\omega''}$ [GeV^{-1}]	−0.86(6)	−0.87(7)	3.48(8)	−0.85(6)	−0.85(6)	3.42(8)
c_1 [GeV^{-3}]	−1.45(6)	−1.45(7)	−2.07(5)	−1.42(6)	−1.42(6)	−2.02(6)
c_2 [GeV^{-3}]	−0.60(9)	−0.60(9)	−1.83(5)	−0.63(11)	−0.62(11)	−1.80(5)
c_3 [GeV^{-3}]	—	−0.08(6)	−0.60(5)	—	−0.03(6)	−0.55(5)
c_4 [GeV^{-3}]	—	—	2.90(11)	—	—	2.84(11)
$10^4 \times \xi$	1.9(7)	1.9(7)	1.9(7)	1.3(5)	1.3(5)	1.4(5)
$10^{10} \times a_\mu^{3\pi}\vert_{\leq 1.8\,\text{GeV}}$	46.59(22)	46.60(22)	46.55(21)	45.54(52)	45.54(52)	45.40(48)

Table 2.8: Same as Table 2.6, but with $\text{Im}\, C_p(q^2) \sim q^{-3}$ asymptotically.

compounds the tension with the VP-subtracted ω mass as extracted from the 2π channel, $M_\omega = 781.68(9)(3)$ MeV [133]. Including the expected upward shift of 0.06 MeV, the result for the width agrees with (2.28) at the level of $1.6\,\sigma$, again consistent with earlier extractions from the 3π channel ($\Gamma_\omega = 8.68(23)(10)$ MeV [243], $\Gamma_\omega = 8.68(4)(15)$ MeV [251]). The enlarged ω and ϕ resonance regions are depicted in Figure 2.2.

2.4 Consequences for the anomalous magnetic moment of the muon

Our central result for the 3π contribution to HVP is

$$a_\mu^{3\pi}|_{\leq 1.8\,\text{GeV}} = 46.2(6)(6) \times 10^{-10} = 46.2(8) \times 10^{-10}\,, \tag{2.29}$$

where the systematic errors are estimated as in Section 2.3.4. As a cross check we have also performed a fit to the data combination of [132] instead of the data directly, leading to

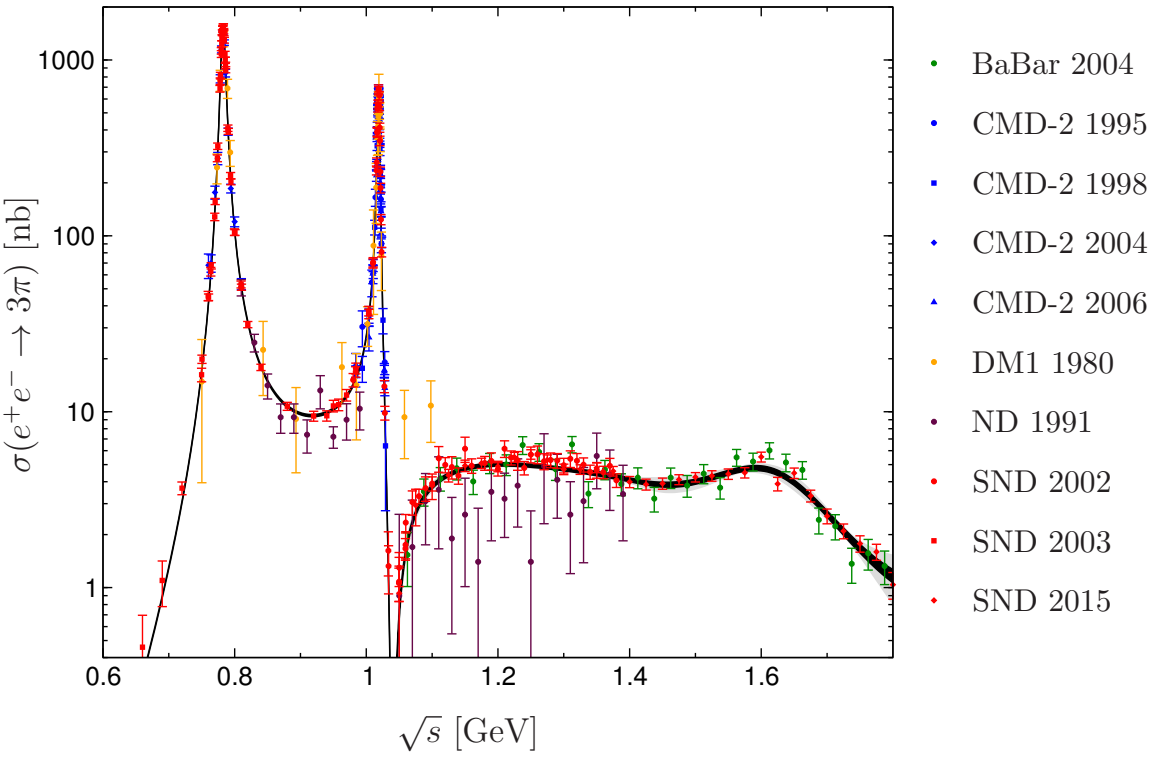

Figure 2.1: Fit to the $e^+e^- \to 3\pi$ data sets as listed in Table 2.1 (with VP removed everywhere). The black band includes the fit uncertainties only, while the gray band represents the total uncertainty, including the systematics of the dispersive representation. For most energies the two uncertainties are of similar size, so that the difference is hardly visible on the logarithmic scale.

almost the same central value

$$a_\mu^{3\pi}|_{\leq 1.8\,\text{GeV}} = 46.1(6)(8) \times 10^{-10} = 46.1(1.0) \times 10^{-10}\,, \tag{2.30}$$

with slightly larger uncertainties. The latter is likely related to the fact that although, as expected, we had to remove two bins (# 49 and # 52) corresponding to (nearly) vanishing cross sections to have the fit iteration converge, no further changes were applied to the combination, so that some of the potentially problematic points we identified in [255] could still impact the fit. The final result (2.29) agrees well with $a_\mu^{3\pi}|_{\leq 1.8\,\text{GeV}} = 46.2(1.5) \times 10^{-10}$ [131], besides a corroboration of the central value the QCD constraints also allow for a reduction of the uncertainty. The difference to $a_\mu^{3\pi}|_{\leq 1.8\,\text{GeV}} = 47.7(9) \times 10^{-10}$ [132] is mainly due to the interpolation applied to the data. We reproduce the central value with a linear interpolation of the bins of [132], while higher-order interpolations, as well as the dispersive fit (2.30), move the central value towards (2.29).[6] Our analysis does not support

[6] We thank B. Malaescu and D. Nomura for confirming that the choice of interpolation indeed explains the bulk of the difference between [131, 132].

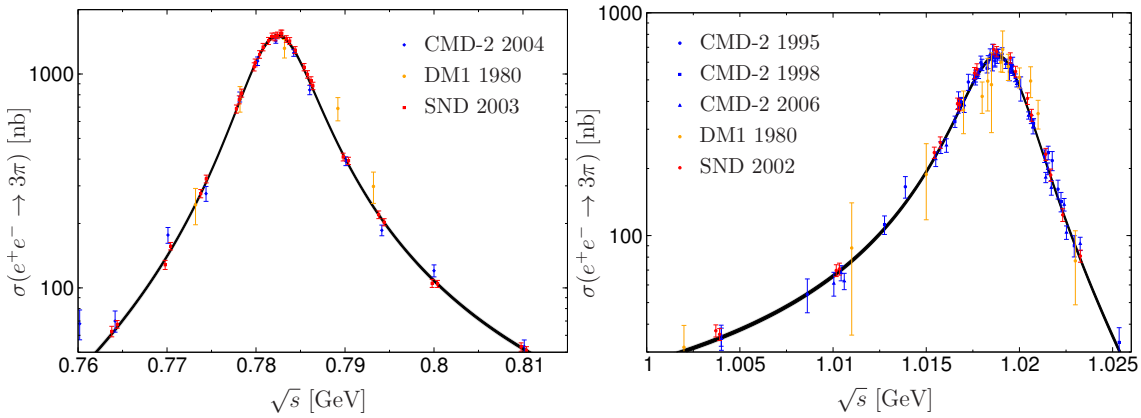

Figure 2.2: Fit to the $e^+e^- \to 3\pi$ data sets as listed in Table 2.1 (with VP removed everywhere) around the ω and ϕ resonance regions. The black band represents the fit uncertainties, and the gray band indicates the total uncertainty.

values as low as $a_\mu^{3\pi}|_{\leq 2.0\,\mathrm{GeV}} = 44.3(1.5) \times 10^{-10}$ [60], which is based on a Breit–Wigner description of ω and ϕ. Finally, we remark that for the threshold region we find a value $a_\mu^{3\pi}|_{\leq 0.66\,\mathrm{GeV}} = 0.019 \times 10^{-10}$ nearly twice as large as the estimate from [272] based upon a combination of the Wess–Zumino–Witten action and vector meson dominance (VMD) [273, 274]. Indeed, it was observed in [272] that this model underestimates the lowest-energy data points.

In combination with the 2π channel from [133] we obtain for the HVP contribution that has been evaluated imposing analyticity and unitarity constraints

$$a_\mu^{2\pi}|_{\leq 1.0\,\mathrm{GeV}} + a_\mu^{3\pi}|_{\leq 1.8\,\mathrm{GeV}} = [495.0(2.6) + 46.2(8)] \times 10^{-10} = 541.2(2.7) \times 10^{-10}\,, \quad (2.31)$$

which covers nearly 80% of the total HVP integral. Therefore, it comprises an important contribution to the data-driven approaches to HVP with constraints from analyticity, unitarity, and crossing symmetry entering the white paper [61].

2.5 Summary

We have presented a detailed analysis of the 3π contribution to HVP, including constraints from analyticity and unitarity as well as the low-energy theorem for the $\gamma^* \to 3\pi$ amplitude. Similarly to the 2π analysis of the pion vector form factor [133], the main motivations are, first, to see if a global fit subject to these constraints reveals inconsistencies in the data, and, second, derive the corresponding error estimate for the contribution to $(g-2)_\mu$. Given that this method is complementary to a direct integration of the data, where potential inconsistencies are addressed by a local error inflation, such global fits that incorporate general QCD constraints should increase the robustness of the SM prediction.

We find that most data sets can be fit satisfactorily with our dispersive representation, the exception being several points above the ϕ resonance from [255]. Fortunately, the impact

on the final HVP integral is minimal, due to the suppression of the cross section in this region, which could also enhance the relative importance of systematic effects in the data. Otherwise, in the 3π channel there is no tension between two high-statistics data sets, such as BaBar and KLOE in the 2π case, but the scale factor of the global fit, indicating overall consistency of the data base, is actually larger than in 2π. In addition, the main contribution, from the 3π cross section in the vicinity of the ω, is dominated by a single experiment [251]. For these reasons, a new high-statistics low-energy measurement in the 3π channel would be a highly welcome addition to the data base.

The central outcome of our study is (2.29)

$$a_\mu^{3\pi}|_{\leq 1.8\,\mathrm{GeV}} = 46.2(6)(6) \times 10^{-10} = 46.2(8) \times 10^{-10}\,. \tag{2.32}$$

Together with the 2π channel from [133], the two most important low-energy channels have now been scrutinized including analyticity and unitarity constraints, covering nearly 80% of the HVP integral. Thus, they comprise another crucial aspect of the data-driven evaluations of HVP in the white paper [61], in addition to the methods based on the direct integration of the data.

Finally, our analysis exacerbates a tension emerging between the 2π and 3π channels, that is, the extraction of the ω mass. In the 2π channel the ω only contributes via an isospin-violating effect, ρ–ω mixing, but due to the increased statistics the sensitivity is not much below that of the 3π channel. Yet, the ω mass extracted from the 2π channel is substantially lower than the one extracted from 3π. Currently, we are aware of neither a systematic effect in experiment nor an issue with the theoretical extraction that could resolve the tension. Besides improving the HVP contribution to $(g-2)_\mu$, new data could shed light on this puzzle as well.

Chapter 3

Hadronic vacuum polarization: $\pi^0\gamma$ [1]

3.1 Introduction

Following the spirit of Chapter 2, we commence to investigate the contribution of the $\pi^0\gamma$ channel to HVP in the muon $(g-2)_\mu$.

The vector mesons ω and ϕ are narrow states compared to other hadronic resonances in the low-energy QCD spectrum. In the case of the ω, this is because two-body decays are either forbidden by G-parity (2π) or require electromagnetic interactions ($\pi^0\gamma$, $\eta\gamma$), so that the dominant decay proceeds into 3π. In contrast, for the ϕ a G-parity conserving two-body decay into $\bar{K}K$ is possible, but suppressed by very small phase space, while the decay into 3π is small due to the Okubo–Zweig–Iizuka rule [276–278]. Accordingly, the most precise information on the mass of the ϕ comes from $e^+e^- \to \bar{K}K$ [243, 249, 279–281], which indeed dominates the PDG average [22]. For the determination of the ω mass, the reaction $e^+e^- \to 3\pi$ is the primary source of information [243, 251], but here the three-particle nature of the decay complicates a reliable extraction of the resonance parameters. In particular, there is a significant tension with the mass determination from $e^+e^- \to \pi^0\gamma$ [270], which together with $\bar{p}p \to \omega\pi^0\pi^0$ [271] leads to a scale factor $S = 1.9$ in the PDG average. In this work, we consider the reaction $e^+e^- \to \pi^0\gamma$ using a dispersive representation of the $\pi^0 \to \gamma\gamma^*$ TFF, which together with our previous work on the 3π channel in Chapter 2, allows us to present a combined determination of the ω and ϕ resonance parameters within the same framework consistent with the constraints from analyticity, unitarity, and crossing symmetry as well as low-energy theorems.

These constraints, as incorporated in the dispersive representation of the TFF [149, 150, 231], are not only valuable for a reliable extraction of resonance parameters, but also define a global fit function for the cross section that allows one to check the consistency of the data sets with these general principles. Applications to the $e^+e^- \to 2\pi$ [133, 135, 222, 282] and $e^+e^- \to 3\pi$ [134] channels have provided such analyses for the two dominant channels in the HVP contribution to the anomalous magnetic moment of the muon a_μ. Here, we will study the $e^+e^- \to \pi^0\gamma$ channel in the same spirit. Since the total contribution is about an order of magnitude smaller than the one of the 3π channel, very large relative

[1] This Chapter's contents have been published in [275].

changes would be required to notably influence the Standard Model prediction (1.64) and thus the tension with the BNL measurement (1.27). However, in view of recent results from lattice QCD [283] that suggest large modifications of the hadronic cross section at low energies [284–286], any further corroboration of the phenomenological HVP evaluation, especially for the channels relevant below 1 GeV such as $\pi^0\gamma$, is certainly worthwhile—in anticipation of improved measurements at Fermilab [70] and J-PARC [71].

The Chapter is organized as follows: in Section 3.2 we review the dispersive formalism for the pion TFF and the $e^+e^- \to \pi^0\gamma$ cross section, which is then applied in Section 3.3 to fit the available data sets. In Section 3.4 we discuss the consequences for the HVP contribution to a_μ, in Section 3.5 the combined analysis of the ω and ϕ resonance parameters from $e^+e^- \to 3\pi$ and $e^+e^- \to \pi^0\gamma$. We close with a summary in Section 3.6.

3.2 Time-like pion transition form factor and $e^+e^- \to \pi^0\gamma$ cross section

Based on the unitarity relation and its crucial building blocks, a once-subtracted dispersive representation for the time-like singly-virtual TFF $F_{\pi^0\gamma^*\gamma^*}(q^2,0)$ was constructed in [231],[2]

$$F_{\pi^0\gamma^*\gamma^*}(q^2,0) = F_{\pi\gamma\gamma} + \frac{1}{12\pi^2}\int_{4M_\pi^2}^{\infty} \mathrm{d}s' \frac{q_\pi^3(s')(F_\pi^V(s'))^*}{s'^{3/2}}\left\{f_1(s',q^2) - f_1(s',0) + \frac{q^2}{s'-q^2} f_1(s',0)\right\}, \tag{3.1}$$

where $q_\pi(s) = \sqrt{s/4 - M_\pi^2}$, $F_\pi^V(s)$ is the pion vector form factor, and $f_1(s,q^2)$ is the partial-wave amplitude for $\gamma^* \to 3\pi$ [197, 230–232], as a generalization of previous studies of the $\omega/\phi \to \pi^0\gamma^*$ TFFs [198, 229]. In particular, $F_{\pi^0\gamma^*\gamma^*}(q^2,0)$ was studied in [231] as a first step towards the doubly-virtual space-like TFF [149, 150], which determines the strength of the pion-pole contribution in a dispersive approach to hadronic light-by-light scattering [142–146], to demonstrate the consistency between 3π and $\pi^0\gamma$ data. Similarly, the ω and ϕ TFFs become relevant for the description of the left-hand cuts in the two-pion contributions [233–238].

$F_{\pi\gamma\gamma}$ denotes the normalization at $q^2 = 0$, as determined at leading order by the Wess–Zumino–Witten anomaly [139, 140]

$$F_{\pi\gamma\gamma} = \frac{1}{4\pi^2 F_\pi} = 0.2745(3)\,\mathrm{GeV}^{-1}\,. \tag{3.2}$$

This value, obtained from the pion decay constant $F_\pi = 92.28(10)\,\mathrm{MeV}$ [22], agrees with the recent PrimEx-II measurement of the neutral-pion life time [287], which implies

[2] See Section 4.3.1 for the detailed definition of the pion TFF.

$F_{\pi\gamma\gamma} = 0.2754(21)\,\text{GeV}^{-1}$. The relation between the $e^+e^- \to \pi^0\gamma$ cross section and the pion TFF, calculated from the dispersion relation (3.1), reads

$$\sigma^0_{e^+e^-\to\pi^0\gamma}(q^2) = \frac{2\pi^2\alpha^3}{3}\frac{(q^2 - M_{\pi^0}^2)^3}{q^6}|F_{\pi^0\gamma^*\gamma^*}(q^2, 0)|^2\,, \tag{3.3}$$

where $\alpha = e^2/(4\pi)$ and we neglected the mass of the electron. Strictly speaking, the dispersion relation (3.1) applies to the pure QCD process without further radiative correction, so that (3.3) describes the bare cross section $\sigma^0_{e^+e^-\to\pi^0\gamma}(q^2)$ excluding VP corrections. Accordingly, the mass parameters for ω and ϕ extracted from the fit do not include these VP corrections, in contrast to the PDG convention, see Section 3.5. We use the VP routine from [132] to remove VP from the experimental cross sections.

The isoscalar contribution, corresponding to $f_1(s', q^2) - f_1(s', 0)$ in the integrand of (3.1), was calculated in [231] using the previously determined partial wave $f_1(s, q^2)$, where the normalization function $a(q^2)$ was fixed from a fit to $e^+e^- \to 3\pi$ data; the isovector part, the last term in (3.1), was determined using a finite matching point of 1.2 GeV and a normalization at $q^2 = 0$ fixed to the chiral anomaly $F_{3\pi}$ for the $\gamma \to 3\pi$ amplitude [239–241]. We will implement the same constraint here, i.e., including quark-mass corrections [230, 267]

$$a(0) = \frac{F_{3\pi}}{3} \times 1.066(10)\,, \qquad F_{3\pi} = \frac{1}{4\pi^2 F_\pi^3}\,. \tag{3.4}$$

We stress again that in contrast to $F_{\pi\gamma\gamma}$, whose anomaly-constraint (3.2) has been confirmed by PrimEx-II at the level of 0.8%, the chiral prediction for $F_{3\pi}$, as already discussed in Section 2.2, has only been tested experimentally with 10% precision, from Primakoff measurements [261] and $\pi^-e^- \to \pi^-e^-\pi^0$ [262]. In the remainder of this Chapter, we assume that $F_{3\pi}$ follows the $F_{\pi\gamma\gamma}$ precedent, so that the remaining uncertainty in (3.4), from the quark-mass renormalization, becomes subleading compared to other sources of systematic uncertainty in the dispersive representation of the TFF. In view of open questions regarding the role of subleading terms in the chiral expansion of the $\pi^0 \to \gamma\gamma$ amplitude [160, 288–291], a more stringent test of $F_{3\pi}$ would be highly desirable, which could be achieved with data on $\gamma\pi^- \to \pi^-\pi^0$ taken in the COMPASS Primakoff program [263], using the dispersive framework proposed in [230, 232].

As already remarked in [231], the normalization function $a(q^2)$ could also be determined by a fit to $e^+e^- \to \pi^0\gamma$ instead of the 3π channel. We follow this approach in the present work and consider an update of this once-subtracted analysis based on the improved parameterization for $a(q^2)$ developed in [149, 150], including a conformal polynomial to be able to describe the inelastic effects that were found to be relevant in $e^+e^- \to 3\pi$ above the ϕ resonance [134]. For the details of the calculation of $f_1(s, q^2)$ we refer to [134, 149, 150] and Section 2.2, but reiterate the free parameters that enter the dispersive representation for the normalization function $a(q^2)$: apart from the ω and ϕ resonance parameters, these are their residues c_ω and c_ϕ, as well as, potentially, further free parameters

Experiment	Region of $\sqrt{s}$ [GeV]	# data points	Normalization uncertainty
SND 2000 [295]	[0.99, 1.03]	12	3.3%
SND 2003 [296]	[0.60, 0.97]	30	all systematics
SND 2016 [297]	[0.63, 1.35]	60	all systematics
SND 2018 [298]	[1.08, 1.35]	5	all systematics
CMD-2 2005 [270]	[0.60, 1.31]	46	6.0%

Table 3.1: Summary of the $e^+e^- \to \pi^0\gamma$ data sets. For [298] only data points for $\sqrt{s} < 1.4\,\text{GeV}$ are included, as the cross section in the region (1.4–2.0) GeV was found to be consistent with zero. In the last column we indicate the size of the systematic errors that we interpret as a normalization-type uncertainty and therefore assume to be 100% correlated.

in the conformal polynomial. For the evaluation of the final dispersion relation (3.1), we choose an integration cutoff s_{iv} above which an asymptotic behavior $\sim 1/s$ is assumed for both $F_\pi^V(s)$ and $f_1(s, q^2)$ [176, 177, 292–294]. The isovector part is updated as well in line with the isoscalar contribution.

The systematic uncertainties of the dispersive representation are taken into account as follows: the pion vector form factor $F_\pi^V(s)$ is calculated with different variations of the Omnès function [173] using different phase shifts [201, 202] as in [150]; in the meantime, the integration cutoffs $\Lambda_{3\pi}$ in the solution of the $\gamma^* \to 3\pi$ KT equations [195] and $\sqrt{s_{\text{iv}}}$ in the solution of the pion TFF (3.1) are varied in the range (1.8–2.5) GeV; lastly, the asymptotic behavior of the imaginary part of the conformal polynomial is varied as in Chapter 2. The central values of the cross sections are obtained by the best fits to the data sets scanning over the variations of these quantities. The systematic uncertainties are defined as the maximum deviations of all the variations from the central cross sections.

3.3 Fits to $e^+e^- \to \pi^0\gamma$ data

3.3.1 Data sets and normalization uncertainties

In addition to the $e^+e^- \to \pi^0\gamma$ cross section measurements [270, 295, 296] already included in [231], there are two new data sets, the most accurate new data determined from the whole data sample of the SND experiment [297] and another one that explored a new region between 1.4 and 2.0 GeV [298]. The full data sets that we consider in our analysis are listed in Table 3.1. These measurements were performed at the VEPP-2M collider with the SND [295–298] and CMD-2 [270] detectors.

As first observed in [268], a naive treatment of normalization-type systematic uncertainties

	diagonal	full
χ^2/dof	116.9/100	151.3/100
	= 1.17	= 1.51
p-value	0.12	7×10^{-4}
M_ω [MeV]	782.55(3)	782.58(3)
Γ_ω [MeV]	8.73(7)	8.68(6)
M_ϕ [MeV]	1019.18(5)	1019.18(6)
Γ_ϕ [MeV]	4.24(16)	4.27(17)
c_ω [GeV^{-1}]	2.95(2)	2.95(3)
c_ϕ [GeV^{-1}]	−0.378(11)	−0.382(13)
$10^4 \times \xi$	3.5(1.3)	4.0(1.0)
$10^{11} \times a_\mu^{\pi^0\gamma}\vert_{\leq 1.35\,\text{GeV}}$	44.05(24)	44.14(57)

Table 3.2: Fits to the combined SND data sets [295–298], for diagonal uncertainties and full covariance matrices. All errors refer to fit uncertainties only.

would lead to a bias in the fit. For the data sets in Table 3.1, the systematic uncertainties of [270, 295] are explicitly given in percentages and therefore interpreted as normalization uncertainties. Likewise, we assume that the systematic uncertainties of [296–298] can be attributed primarily to effects in the same category and thus treat all the systematics uncertainties as 100% correlated. Accordingly, we employ the iterative solution strategy introduced in [269] to treat the normalization uncertainties in a consistent manner and consider both fits with diagonal and full covariance matrices to better monitor the role of the correlations, in analogy to the strategy in Section 2.3.

3.3.2 Fits to SND

First, we perform fits to the SND data sets [295–298], with the results shown in Table 3.2. We display the best χ^2 results for both the diagonal fit and also the fully correlated one. Only the fit uncertainties are displayed in Table 3.2 at this step, as we will add the systematic uncertainties of our approach later. Fit errors are already inflated by the scale factor

$$S = \sqrt{\chi^2/\text{dof}}\,, \tag{3.5}$$

to account for potential inconsistencies between the data sets following the PDG prescription [22].

In contrast to Chapter 2, we do not include the $\omega'(1420)$ or other excited vector mesons in the fits since their residues come out consistent with zero, in such a way that their inclusion does not improve the quality of the fit. This strategy is consistent with the observation of a negligible cross section above 1.4 GeV in [298]. Similarly, the data points above the ϕ region are scarce, so that additional free parameters in the conformal polynomial in the parameterization of $a(q^2)$ also do not improve the fits. Therefore, we will use the conformal polynomial to implement the chiral low-energy theorem $F_{3\pi}$ (with S-wave singularities removed), but do not add additional free parameters.

The accuracy of the center-of-mass energy determination of the data set [296] is worse than the accuracy of the ω mass value. Therefore, an energy-scale bias ΔE was introduced in [296]. A separate fit to [296] indeed produces a smaller ω mass that is not compatible with the most precise measurement [297]. Therefore, we allow for an energy rescaling for [296],

$$\sqrt{s} \to \sqrt{s} + \xi(\sqrt{s} - M_{\pi^0}) \,. \tag{3.6}$$

The introduced scaling indeed leads to a considerable improvement of the fits, and its value around $\xi \sim 10^{-4}$ comes out in agreement with the energy-bias uncertainties. Similar rescalings within the quoted energy uncertainties were also found to improve the fit quality for the 2π [133] and 3π [134] channels. In the case of $\pi^0\gamma$, the data set from [296] is the only one for which we see a need for such a rescaling.

We observe that the correlated fit produces larger uncertainties for the parameters and the HVP contribution compared to the diagonal one. Otherwise, the central values of the parameters of both fits are in good agreement within uncertainties. Besides, we find that the correlated fit has a worse description than the diagonal fit, which is a general observation of the iterative fit strategy [269] concerning normalization uncertainties. In fact, this effect may be overestimated here because all systematic uncertainties of [296–298] were assumed to contribute in that category, so that the description could likely be improved if more details on the systematic uncertainties were available. At present, the relatively large χ^2 of the correlated fit is mainly driven by [298]: a fit to this data set alone gives a $\chi^2/\text{dof} = 88.7/54 = 1.64$ and a p-value of 0.2%. The fact that the p-value drops by another factor of 3 in the combined SND fit thus points to some minor tensions among [295–298].

3.3.3 Fits to CMD-2

Next, we turn to the fits to the CMD-2 data [270]. Although there is only a single data set, it covers almost the entire relevant energy region. The results are given in Table 3.3, in the same form as the SND fits, the only exception being the exclusion of the rescaling parameter. For comparison, the fit uncertainties are also inflated by the scale factor (3.5).

As for the SND fits, we again find internal consistency for the parameters of the diagonal and the correlated fits. A minor difference concerns the mass and width of the ω, which display relativity large upward shifts once the correlations are included.

Even once accounting for VP corrections, see Section 3.5, our result for the ω mass

	diagonal	full
χ^2/dof	42.50/40	57.39/40
	= 1.06	= 1.43
p-value	0.36	0.04
M_ω [MeV]	782.53(14)	782.68(9)
Γ_ω [MeV]	8.25(28)	8.41(19)
M_ϕ [MeV]	1019.18(7)	1019.18(6)
Γ_ϕ [MeV]	3.90(21)	3.90(17)
c_ω [GeV^{-1}]	2.91(7)	2.92(13)
c_ϕ [GeV^{-1}]	−0.342(13)	−0.341(17)
$10^{11} \times a_\mu^{\pi^0\gamma}\vert_{\leq 1.35\,\text{GeV}}$	44.88(99)	44.48(3.05)

Table 3.3: Fits to the CMD-2 data set [270].

is substantially smaller than in [270], which quotes $\bar{M}_\omega = 783.20(13)(16)\,\text{MeV}$. A key difference to our formalism is that the vector-meson-dominance ansatz from [270] (see also [299]) permits a complex phase between the ω and ρ contributions, which cannot be physical because it violates analyticity and unitarity, e.g., by introducing an imaginary part below the respective thresholds. In our fits, we do not see a conflict with the ω mass extracted from 3π cross sections, and thus conclude that the result from [270] is likely affected by the unphysical phase.

Compared to the SND fits, we observe that the width of the ϕ comes out appreciably smaller, albeit with rather large fit uncertainties. This observation will also be reflected in the determination of the width of the ϕ in the combined fit presented in the next section.

3.3.4 Combined fits

Finally, our combined SND and CMD-2 fit results are presented in Table 3.4, including all the data sets listed in Table 3.1. We take the correlated full fit as our central value, and define our systematic uncertainties as the maximum deviations from the different fit variations discussed in Section 3.2. In all cases, the uncertainties are statistics dominated, in part because a main source of systematic uncertainty from the 3π channel [134], the degree of the conformal polynomial, does not become relevant here given that the observed cross section becomes negligibly small around 1.4 GeV, with few data points above the ϕ resonance.

The combined fit, although dominated by the SND data, reflects some inconsistencies

	diagonal	full
χ^2/dof	173.3/146	238.6/146
	= 1.19	= 1.63
p-value	0.06	2×10^{-6}
M_ω [MeV]	782.55(3)	782.58(3)
Γ_ω [MeV]	8.71(7)	8.65(6)
M_ϕ [MeV]	1019.20(4)	1019.21(4)
Γ_ϕ [MeV]	4.08(13)	4.07(13)
c_ω [GeV^{-1}]	2.95(2)	2.93(3)
c_ϕ [GeV^{-1}]	−0.363(9)	−0.358(10)
$10^4 \times \xi$	3.5(1.3)	4.1(1.0)
$10^{11} \times a_\mu^{\pi^0\gamma}\vert_{\leq 1.35\,\text{GeV}}$	44.04(23)	43.82(58)

Table 3.4: Fits to the combined data sets as shown in Table 3.1.

between SND and CMD-2. Most prominently, the downward shift of the width of the ϕ in comparison to Table 3.2 is due to the CMD-2 data [270]. The coupling c_ϕ is also affected and shifted to a smaller value compared to the SND fits. Comparing the residues c_ω and c_ϕ to the 3π fit in Chapter 2, $c_\omega = 2.86(2)(4)$ and $c_\phi = -0.386(4)(2)$, we observe reasonable agreement, which indeed is better for c_ω than for c_ϕ. Taken together with the fact that also the ϕ width from the CMD-2 $\pi^0\gamma$ data drives the combined fit away from the 3π value, we conclude that indeed the interchannel consistency is better for the SND data sets. Figure 3.1 illustrates our final preferred fit.

The final result for the ω and ϕ parameters reads

$$\begin{aligned} M_\omega &= 782.58(3)(1)\,\text{MeV} = 782.58(3)\,\text{MeV}\,, \\ \Gamma_\omega &= 8.65(6)(1)\,\text{MeV} = 8.65(6)\,\text{MeV}\,, \\ M_\phi &= 1019.21(4)(3)\,\text{MeV} = 1019.21(5)\,\text{MeV}\,, \\ \Gamma_\phi &= 4.07(13)(1)\,\text{MeV} = 4.07(13)\,\text{MeV}\,, \end{aligned} \tag{3.7}$$

with systematic errors in the second brackets derived as described above. The close-up views of the ω and ϕ regions are shown in Figure 3.2. We stress that these resonance parameters do not include VP corrections, see Section 3.5 for a more detailed discussion.

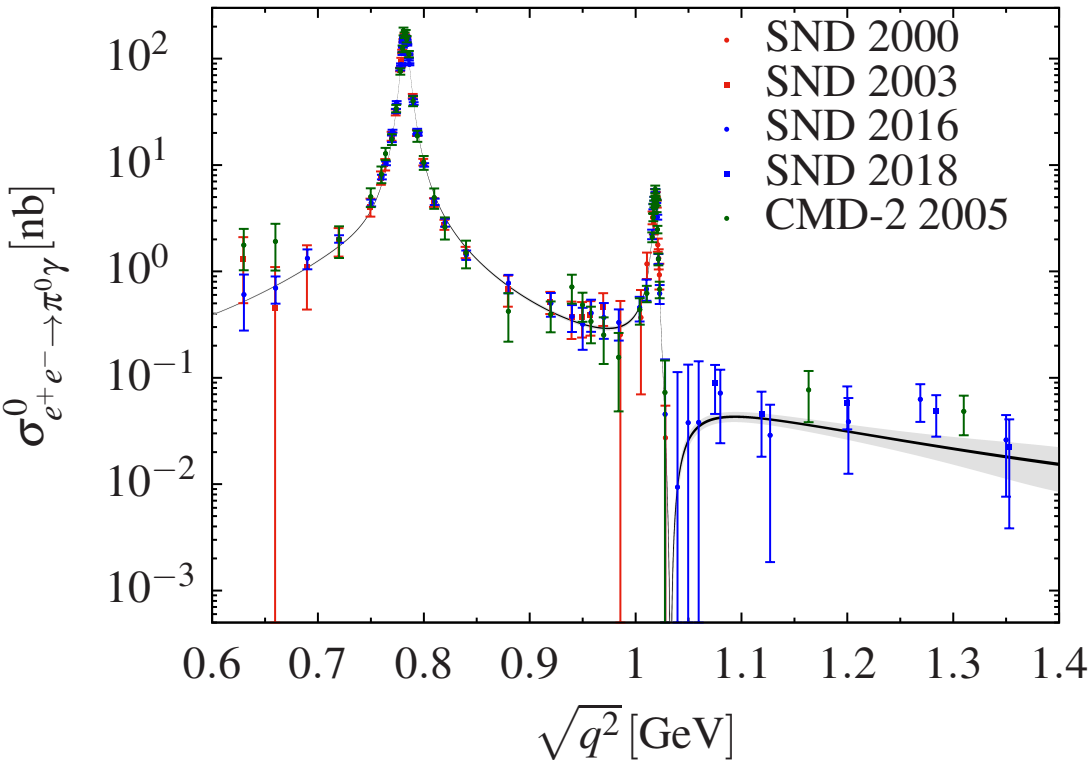

Figure 3.1: The final fit to the $e^+e^- \to \pi^0\gamma$ data sets as listed in Table 3.1 (with VP removed everywhere), where the gray band indicates the full uncertainty and the black band indicates the fit uncertainty.

3.4 Consequences for the anomalous magnetic moment of the muon

The key formula for the leading HVP contribution to $(g-2)_\mu$ is given in (1.55). Conventions need to be specified for the radiative corrections to the cross section in (1.55) so that higher-order insertions of HVP and HLbL scattering can be performed consistently [130, 162, 259]. In this regard, the "bare" cross section $\sigma^0(e^+e^- \to \text{hadrons})$ should be inclusive of FSR, but exempt from ISR and VP. As a consequence, s_{th} is no longer equal to the two-pion threshold, but $s_{\text{th}} = M^2_{\pi^0}$ due to the $\pi^0\gamma$ channel. Therefore, its HVP contribution to $(g-2)_\mu$ can be calculated using (1.55) in the same vain, but the kernel function should be analytically continued to the region $s < 4m_\mu^2$. In this region, it becomes [300]

$$\hat{K}(s < 4m_\mu^2) = \frac{3}{a^3}\left[16(a-2)\ln\frac{a}{4} - 2a(8-a) - 8\left(a^2-8a+8\right)\frac{\arctan\left(\sqrt{a-1}\right)}{\sqrt{a-1}}\right], \tag{3.8}$$

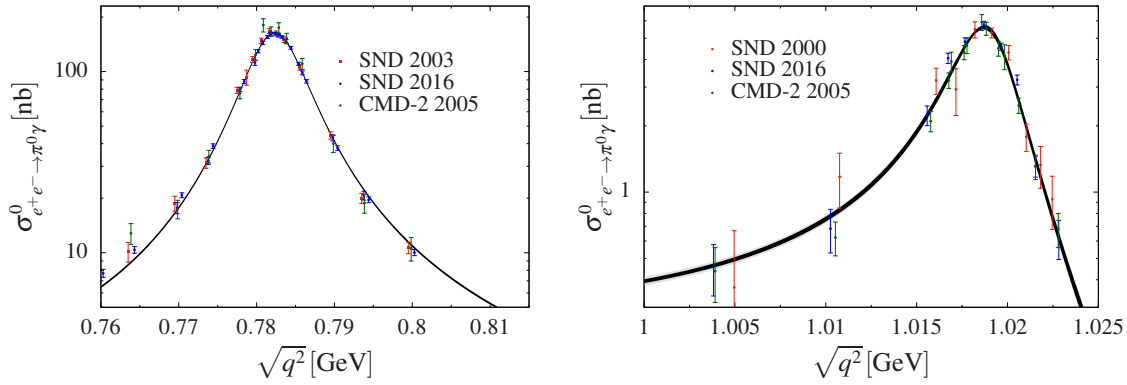

Figure 3.2: Fit around the ω and ϕ resonance regions. The black band represents the fit uncertainties, and the gray band indicates the total uncertainty.

where $a = 4m_\mu^2/s$. As illustrated in Figure 3.3, it monotonically increases from 0 at $s = 0$ to 1 for $s \to \infty$.

Based on the fits presented in the previous section our central result for the HVP contribution from the $\pi^0\gamma$ channel becomes

$$a_\mu^{\pi^0\gamma}|_{\leq 1.35\,\text{GeV}} = 43.8(6)(1) \times 10^{-11} = 43.8(6) \times 10^{-11}\,, \tag{3.9}$$

where the second uncertainty is systematic.[3] In comparison to the most recent direct-data-integration analyses, our result is in good agreement with $a_\mu^{\pi^0\gamma}|_{\leq 1.8\,\text{GeV}} = 44.1(1.0) \times 10^{-11}$ [135], with a slight improvement in the uncertainty thanks to the incorporation of the general QCD constraints. The small difference to $a_\mu^{\pi^0\gamma}|_{\leq 1.937\,\text{GeV}} = 45.8(1.0) \times 10^{-11}$ [136] partly originates from the application of the trapezoidal rule to scarce data in the tails of the ω resonance, similarly to the case of 3π. Higher-order interpolations to the data combination of [136] indeed move the HVP contribution towards (3.9). Our analysis does not support values as low as $a_\mu^{\pi^0\gamma}|_{\leq 2.0\,\text{GeV}} = 40.0(1.6) \times 10^{-11}$ [60], which is based on a Breit–Wigner description of ω and ϕ. The analysis [135] has updated [131] to account for the threshold contribution $a_\mu^{\pi^0\gamma}|_{\leq 0.6\,\text{GeV}} = 1.2 \times 10^{-11}$, which was already included in [132, 136]. It was determined in [272] based upon a combination of the chiral-anomaly term and ω-meson dominance [300]. This result is in line with our finding for the threshold region, $a_\mu^{\pi^0\gamma}|_{\leq 0.6\,\text{GeV}} = 1.3 \times 10^{-11}$. Indeed, the agreement between the prediction and the cross section of the first few data points was already observed in [272]. Although these small differences are negligible at the current level of accuracy required for HVP, it is reassuring

[3] We quote the HVP integral up to the last data point in [298] that shows a nonvanishing cross section, and in the comparison to other work indicate the energy up to which the sum of exclusive channels is considered. However, in practice the energy region above 1.35 GeV can simply be ignored in the $\pi^0\gamma$ channel, see [298]. An extrapolation of our results beyond 1.35 GeV suggests that this region contributes less than 0.1×10^{-11} to the HVP integral.

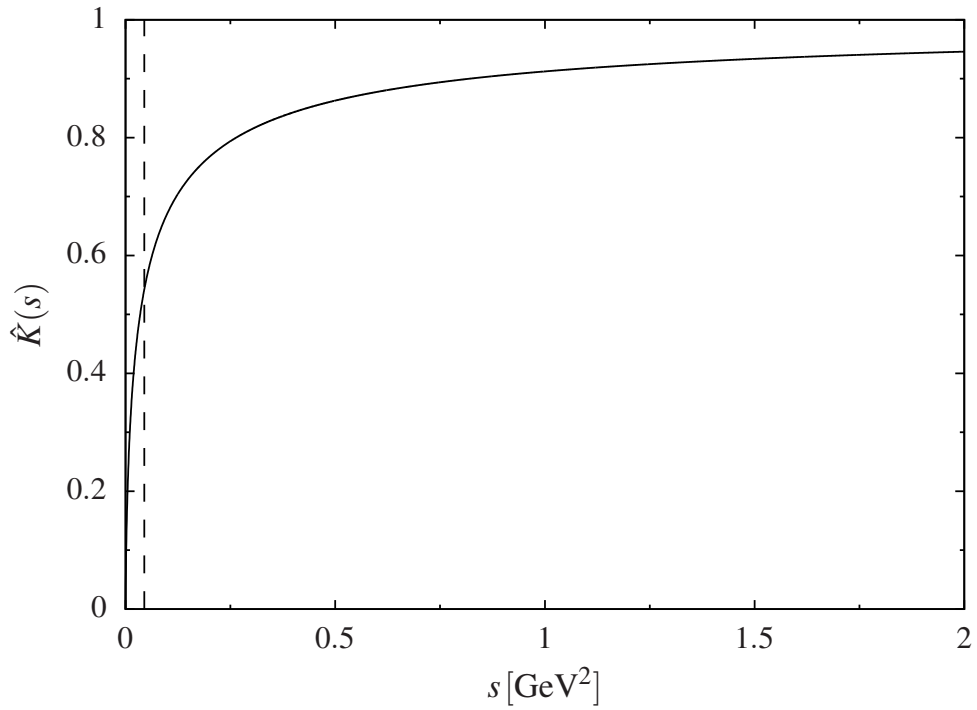

Figure 3.3: Kernel function $\hat{K}(s)$. The dashed line indicates $s = 4m_\mu^2$.

that the dispersive analysis also corroborates current estimates for the $\pi^0\gamma$ channel, making significant changes in HVP in the energy region up to 1 GeV increasingly unlikely. Other radiative effects beyond $\pi^0\gamma$, $\eta\gamma$, and the infrared-enhanced contributions in $\pi^+\pi^-\gamma$ are negligibly small compared to the current uncertainty of the full a_μ^{HVP}, see, e.g., [235].

3.5 ω and ϕ resonance parameters

Our final results for the ω and ϕ resonance parameters as determined from $e^+e^- \to \pi^0\gamma$ are contrasted to the results from $e^+e^- \to 3\pi$ of Chapter 2 in Table 3.5. There is good agreement throughout, leading to the combination in the last column. Since the $\pi^0\gamma$ channel is statistics-dominated for all quantities, see (3.7), the combination is straightforward despite the fact that the systematic errors related to the dispersive representation are correlated. Likewise, the statistical correlations among the resonance parameters (and with the residues) from the respective fits have a negligible impact on the combination. M_ω and Γ_ϕ require a small scale factor $S = 1.2$ (defined in accordance with the PDG conventions [22]). The slight tension for Γ_ϕ can be traced back to the CMD-2 data set [270], see Section 3.3.3. However, we conclude that within uncertainties the 3π and $\pi^0\gamma$ channels yield a consistent picture for the ω and ϕ resonance parameters.

To be able to compare our results to the PDG conventions, we need to restore the VP

	$e^+e^- \to 3\pi$	$e^+e^- \to \pi^0\gamma$	combination
M_ω [MeV]	782.631(28)	782.584(28)	782.607(23)
Γ_ω [MeV]	8.71(6)	8.65(6)	8.69(4)
M_ϕ [MeV]	1019.196(21)	1019.205(55)	1019.197(20)
Γ_ϕ [MeV]	4.23(4)	4.07(13)	4.22(5)

Table 3.5: ω and ϕ resonance parameters from $e^+e^- \to 3\pi$ (Chapter 2), $e^+e^- \to \pi^0\gamma$ (this work), and their combination. The final uncertainties for M_ω and Γ_ϕ include a scale factor $S = 1.2$. All parameters do not include VP corrections, see Table 3.6 for the comparison to the PDG parameters.

corrections that have been removed in the definition of the bare cross sections, which we will denote by a bar over the corresponding quantities. As argued in Appendix A, this leads to the shifts

$$\begin{aligned} \bar{M}_\omega &= \left(1 + \frac{e^2}{2g_{\omega\gamma}^2}\right) M_\omega = M_\omega + 0.128(3)\,\text{MeV}\,, \\ \bar{M}_\phi &= \left(1 + \frac{e^2}{2g_{\phi\gamma}^2}\right) M_\phi = M_\phi + 0.260(3)\,\text{MeV}\,, \end{aligned} \tag{3.10}$$

where the couplings are related to the respective e^+e^- widths, e.g., $\Gamma_{\omega\to e^+e^-} = e^4 M_\omega/(12\pi g_{\omega\gamma}^2)$, and the uncertainties have been propagated from the PDG values [22] (with potential differences to our determinations being higher-order effects). While otherwise shifts in the widths are negligible, there is an effect enhanced by ρ–ω mixing

$$\begin{aligned} \bar{\Gamma}_\omega &= \Gamma_\omega + \frac{e^2}{2g_{\omega\gamma}^2}\Gamma_\omega + \frac{M_\omega^2}{\Gamma_\rho - \Gamma_\omega}\frac{e^2}{g_{\rho\gamma}^2}\left(\frac{e^2}{g_{\omega\gamma}^2} - 2\epsilon_\omega\right) \\ &= \Gamma_\omega - 0.06(2)\,\text{MeV}\,, \end{aligned} \tag{3.11}$$

where we have assigned a generous uncertainty because the estimate relies on a narrow-resonance assumption for the ρ.

The resulting parameters, in comparison to the PDG values, are shown in Table 3.6. First, one sees that the ϕ mass agrees perfectly, with competitive uncertainties. This is an important observation because it demonstrates consistency between $e^+e^- \to 3\pi, \pi^0\gamma$ and $e^+e^- \to \bar{K}K$. The latter includes the BaBar measurements [279, 280], which, in contrast to all data sets for $e^+e^- \to \pi^0\gamma$ considered in this work as well as all the $e^+e^- \to 3\pi$ data sets relevant for the ω and ϕ parameters, have not been taken in energy-scan mode (at the VEPP-2M collider), but using initial-state radiation. The ϕ width also agrees within uncertainties, but not at the level of accuracy that can be achieved in the $\bar{K}K$ channel.

	$e^+e^- \to 3\pi, \pi^0\gamma$	PDG
$\bar{M}_\omega$ [MeV]	782.736(24)	782.65(12)
$\bar{\Gamma}_\omega$ [MeV]	8.63(5)	8.49(8)
$\bar{M}_\phi$ [MeV]	1019.457(20)	1019.461(16)
$\bar{\Gamma}_\phi$ [MeV]	4.22(5)	4.249(13)

Table 3.6: Comparison of ω and ϕ resonance parameters from $e^+e^- \to 3\pi, \pi^0\gamma$ to the PDG values, including VP corrections.

For the ω mass, its PDG value is dominated by the weighted average of determinations from $e^+e^- \to 3\pi$ ($\bar{M}_\omega = 782.68(9)(4)$ MeV [243], $\bar{M}_\omega = 782.79(8)(9)$ MeV [251]), $e^+e^- \to \pi^0\gamma$ ($\bar{M}_\omega = 783.20(13)(16)$ MeV [270]), and $\bar{p}p \to \omega\pi^0\pi^0$ ($\bar{M}_\omega = 781.96(13)(17)$ MeV [271]), where the spread among these determinations drives the scale factor $S = 1.9$ and thus an uncertainty much larger than we obtain from $e^+e^- \to 3\pi, \pi^0\gamma$.

As described in Section 3.3.3, we believe that the large value for the ω mass determined from $e^+e^- \to \pi^0\gamma$ in [270] originates from an unphysical phase in the vector-meson-dominance model used for the extraction. For the $\bar{p}p$ reaction, the uncertainties are more difficult to assess than in the e^+e^- processes because the shape of the background processes is unknown and because the width of the ω signal, $\Gamma = 38.1(3)$ MeV, is dominated by the experimental resolution and much larger than the intrinsic ω width. Energy scans in $e^+e^- \to 3\pi, \pi^0\gamma$, for which the entire amplitude can be reconstructed from general principles and whose energy resolution lies well below the ω width, should thus yield a much more reliable probe of the ω resonance parameters.

The ω mass can also be extracted via ρ–ω mixing in $e^+e^- \to 2\pi$, and it has been known for a while [224] that without further constraints such fits prefer significantly smaller values for M_ω than both the PDG average and our determination from $e^+e^- \to 3\pi, \pi^0\gamma$. This conclusion was recently confirmed in [133] within a dispersive approach, leading to $M_\omega = 781.68(10)$ MeV, in significant tension with Table 3.5. However, given the high accuracy required in the $e^+e^- \to 2\pi$ channel, additional imaginary parts from the radiative channels $\pi^0\gamma$, $\pi\pi\gamma$, etc. may actually become relevant [301]. Before their impact is better understood, we would thus consider the mass determination from $e^+e^- \to 3\pi, \pi^0\gamma$ to be more reliable.

As for the ω width, our value is consistent with earlier determinations from the 3π channel ($\bar{\Gamma}_\omega = 8.68(23)(10)$ MeV [243], $\bar{\Gamma}_\omega = 8.68(4)(15)$ MeV [251]), but lies above the PDG average by $1.5\,\sigma$. This tension is partly driven by an extraction from the reaction $pd \to {}^3\mathrm{He}\,\omega$ ($\bar{\Gamma}_\omega = 8.2(3)$ MeV [302]), but mostly due to an earlier measurement of $e^+e^- \to 3\pi$ by the ND collaboration ($\bar{\Gamma}_\omega = 8.4(1)$ MeV [303]). However, it should be noted that the error quoted in [303] is only statistical, while the modern data sets [243, 251] provide

a complete error estimate. Moreover, without access to the original data for $e^+e^- \to 3\pi$ from [303] it is impossible to assess its weight in global fits to the data base [134]. In such a situation we do not believe it is adequate to keep the ND measurement in the average for Γ_ω and would therefore consider our determination from modern $e^+e^- \to 3\pi, \pi^0\gamma$ data sets to be more reliable than the current PDG average.

3.6 Summary

We have studied the cross section for $e^+e^- \to \pi^0\gamma$ in a dispersive framework, which implements constraints from analyticity, unitarity, and crossing symmetry as well as low-energy theorems for the $\gamma \to 3\pi$ amplitude and the TFF for $\pi^0 \to \gamma\gamma^*$. The relation between this form factor and the $e^+e^- \to \pi^0\gamma$ cross section forms the basis for the subsequent data analysis.

As the next step, we considered the full data sets for $e^+e^- \to \pi^0\gamma$ from SND and CMD-2. An iterative fit algorithm was applied to eliminate the D'Agostini bias. Some tensions among different data sets exist and the resulting scale factor of the global fit turns out to be larger compared to those of similar analyses of the $e^+e^- \to 2\pi$ and $e^+e^- \to 3\pi$ reactions, which in part can be traced back to assumptions necessary for the details of the systematic uncertainties. However, we did not find any data set that needed to be excluded because of severe tensions nor did we identify problematic outliers in the data sets.

As a first application, we evaluated the $\pi^0\gamma$ contribution to HVP, with our central result given in (3.9). In general, the outcome is in good agreement with analyses using a direct integration of the data, with a slightly reduced uncertainty thanks to the global fit function defined by the dispersive representation. In combination with previous work on $e^+e^- \to 2\pi$ and $e^+e^- \to 3\pi$, the three largest channels below 1 GeV have now been subject to scrutiny using constraints from analyticity, unitarity, and low-energy theorems.

Finally, we studied the resulting ω and ϕ resonance parameters first from $e^+e^- \to \pi^0\gamma$ and then in combination with $e^+e^- \to 3\pi$. Contrary to previous analyses, we find good agreement between the two channels, suggesting that a previous tension could be due to unphysical complex phases in a vector-meson-dominance model employed for the $e^+e^- \to \pi^0\gamma$ channel. Comparing the combined determinations to the current PDG averages, see Table 3.6, we observe that for the ϕ mass, the value obtained from $e^+e^- \to 3\pi, \pi^0\gamma$ agrees perfectly at a similar level of precision, demonstrating consistency between extractions from $e^+e^- \to 3\pi, \pi^0\gamma$ and $e^+e^- \to \bar{K}K$, the latter dominating the PDG average. The width also comes out consistent, but with larger uncertainty than from the $\bar{K}K$ channel. For the ω, we find that the combination of $e^+e^- \to 3\pi$ and $e^+e^- \to \pi^0\gamma$ determines its mass at a level not far from the ϕ mass, and argue that the resulting values both for the ω mass and the width are more reliable than the current PDG averages. However, the tension with the ω mass determination from the 2π channel persists, suggesting that an improved understanding of isospin-breaking effects therein will become necessary.

Part II

Hadronic light-by-light scattering

Chapter 4

Hadronic light-by-light scattering: π^0 pole[1]

4.1 Introduction

For decades the anomalous magnetic moment of the muon, $a_\mu = (g-2)_\mu/2$, has been one of the prime physical quantities both to test the SM at quantum loop level and to monitor the signals coming from BSM physics. Its up-to-date value (1.27) reveals a tantalizing deviation of $3.7\,\sigma$ from the SM prediction (1.64). Potential BSM contributions to a_μ notwithstanding, the current theoretical uncertainties of the SM contributions are required to be controlled more precisely in order to synchronize with the upcoming experimental precision.

The dominant SM uncertainty arises from hadronic contributions [61]. The first leading category, HVP illustrated in diagram (a) of Figure 1.7, enters at $O(\alpha^2)$ in the expansion of the fine-structure constant, followed by the second HLbL scattering category shown in diagram (b) of Figure 1.7 at $O(\alpha^3)$. Despite the non-perturbative nature of these two contributions, it is possible to derive data-driven estimates based on dispersion relations. The HVP corrections can be related to the total cross section of $e^+e^- \to$ hadrons [86, 87]. Therefore, its evaluation benefits from improved experimental measurements, with most recent compilations [131, 132, 135, 136, 206, 207, 305] already providing uncertainties comparable to or less than HLbL. In contrast, current estimates of HLbL rely heavily on hadronic models [137, 138, 306–320], which despite being based on chiral symmetry or large-N_c arguments[2] and (partially) fulfilling constraints from pQCD involve model uncertainties that are difficult to control. In this regard, a dispersive framework for the evaluation of HLbL scattering based on the general principles of analyticity, unitarity, and crossing symmetry has been recently developed [142–146]. Such a framework thus provides an alternative model-independent determination of HLbL scattering complementary to lattice QCD calculations [160, 161, 203–205, 321–323], attributing the contributions to

[1] This Chapter's contents including Appendix B have been published in [149, 150, 304].

[2] To ensure anomaly cancellation in the SM subtleties arise in the large-N_c counting related to a rescaling of the quark charges. In consequence, the π^0- and η_8-pole contributions become suppressed by two orders in N_c compared to their naive scaling, which strongly challenges the viability of the large-N_c expansion as an organizing principle for HLbL scattering. This issue will be addressed below in Appendix B.1.

on-shell form factors and scattering amplitudes that are, at least in principle, accessible experimentally.

The single-meson poles constitute the simplest singularities of the HLbL tensor, whose residues are determined by the doubly-virtual TFFs. Therefore, the numerically dominant pion-pole contribution would be fully determined if the doubly-virtual pion TFF could be measured for all (relevant) space-like momenta. In the absence of such double-tag experiments for $e^+e^- \to e^+e^-\pi^0$, we dispersively reconstruct the pion TFF in light of the measurements of the $\pi^0 \to \gamma\gamma$ decay width, the $e^+e^- \to 3\pi$ cross section, and the space-like singly-virtual form factor from $e^+e^- \to e^+e^-\pi^0$ again owing to the constraints from analyticity and unitarity. The resulting form factor representation

$$F_{\pi^0\gamma^*\gamma^*} = F^{\text{disp}}_{\pi^0\gamma^*\gamma^*} + F^{\text{eff}}_{\pi^0\gamma^*\gamma^*} + F^{\text{asym}}_{\pi^0\gamma^*\gamma^*} \tag{4.1}$$

takes into account all low-energy intermediate states by the first dispersive part, incorporates the normalization and space-like high-energy data by the second (small) contribution from higher intermediate states, and implements the asymptotic constraints for arbitrary virtualities at $O(1/Q^2)$ via the last term. The pion-pole contribution is then evaluated based on this comprehensive dispersive determination of the pion TFF, completing previous efforts devoted to the data-driven determination of $a_\mu^{\pi^0\text{-pole}}$ [229–232] (see also [324–330]).

This Chapter is formatted as follows. The (unambiguous) definition of the pion-pole contribution to a_μ in the dispersive approach to HLbL scattering is recalled in Section 4.2, in terms of the on-shell pion TFF. Section 4.3 is devoted to the dispersive reconstruction of the TFF based on its isospin decomposition and unitarity relation, the fits to the $e^+e^- \to 3\pi$ cross section, and the double-spectral representation of the form factor. The decomposition (4.1) gives rise to various energy scales that are discussed in Section 4.4. The asymptotic constraints dictated by pQCD are discussed in Section 4.5. The numerical results for the form factor in both time-like and space-like regions as well as the pion-pole contribution to a_μ including a detailed discussion of its uncertainty estimates are presented in Section 4.6. Conclusions are drawn in Section 4.7 and additional supplementary material is collected in Appendix B .

4.2 Pion-pole contribution to a_μ

In order to evaluate the HLbL scattering contribution to the muon $(g-2)_\mu$, we define the full fourth-rank HLbL tensor $\Pi_{\mu\nu\lambda\sigma}$ following [146],

$$\Pi_{\mu\nu\lambda\sigma}(q_1,q_2,q_3) = -i\int \mathrm{d}^4x\,\mathrm{d}^4y\,\mathrm{d}^4z\,e^{-i(q_1\cdot x+q_2\cdot y+q_3\cdot z)}\langle 0|\,T\,\{j_\mu(x)j_\nu(y)j_\lambda(z)j_\sigma(0)\}|0\rangle\,, \tag{4.2}$$

where

$$j_\mu(x) = \frac{2}{3}(\bar{u}\gamma_\mu u)(x) - \frac{1}{3}(\bar{d}\gamma_\mu d)(x) - \frac{1}{3}(\bar{s}\gamma_\mu s)(x) \tag{4.3}$$

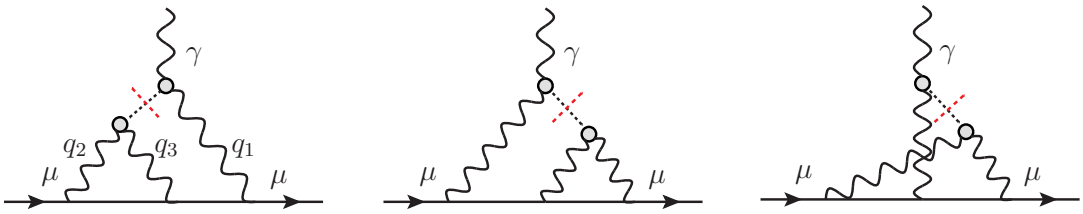

Figure 4.1: The pion-pole contribution to HLbL scattering of the muon $(g-2)_\mu$.

denotes the electromagnetic currents carried by the light quarks and q_i are the four-momenta of the photons. The LO HLbL contribution is then obtained by the projection technique [331]:

$$a_\mu^{\text{HLbL}} = -\frac{e^6}{48m_\mu}\int\frac{\mathrm{d}^4q_1}{(2\pi)^4}\int\frac{\mathrm{d}^4q_2}{(2\pi)^4}\frac{1}{q_1^2q_2^2(q_1+q_2)^2}\left[\frac{\partial}{\partial k^\rho}\Pi_{\mu\nu\lambda\sigma}(q_1,q_2,k-q_1-q_2)\right]_{k=0}$$
$$\times\,\mathrm{tr}\left\{(\not{p}+m_\mu)[\gamma^\rho,\gamma^\sigma](\not{p}+m_\mu)\gamma^\mu\frac{1}{\not{p}+\not{q}_1-m_\mu}\gamma^\lambda\frac{1}{\not{p}-\not{q}_2-m_\mu}\gamma^\nu\right\}, \tag{4.4}$$

where p is the four-momentum of the muon and $q_1+q_2+q_3=0$.

Diagrammatically, the pion-pole contribution can be attributed to the one-particle reducible piece of the HLbL tensor arising from a single pion propagator. There are three Feynman diagrams shown in Figure 4.1, where the momenta are indicated in the hadronic subgraph.

After projection onto the muon anomaly, we obtain the result [312]

$$a_\mu^{\pi^0\text{-pole}} = -e^6\int\frac{\mathrm{d}^4q_1}{(2\pi)^4}\int\frac{\mathrm{d}^4q_2}{(2\pi)^4}\frac{1}{q_1^2q_2^2(q_1+q_2)^2[(p+q_1)^2-m_\mu^2][(p-q_2)^2-m_\mu^2]}$$
$$\times\left[\frac{F_{\pi^0\gamma^*\gamma^*}(q_1^2,(q_1+q_2)^2)\,F_{\pi^0\gamma^*\gamma^*}(q_2^2,0)}{q_2^2-M_{\pi^0}^2}\hat{T}_1(q_1,q_2;p)\right.$$
$$\left.+\frac{F_{\pi^0\gamma^*\gamma^*}(q_1^2,q_2^2)\,F_{\pi^0\gamma^*\gamma^*}((q_1+q_2)^2,0)}{(q_1+q_2)^2-M_{\pi^0}^2}\hat{T}_2(q_1,q_2;p)\right], \tag{4.5}$$

where $p^2=m_\mu^2$, $F_{\pi^0\gamma^*\gamma^*}$ is the on-shell pion TFF, and the integral kernels $\hat{T}_1$ and $\hat{T}_2$ are shown in Appendix B.2. The first and second diagram give identical contributions collected in $\hat{T}_1$, while the third diagram leads to the term containing $\hat{T}_2$. Critically, this diagrammatic derivation happens to coincide with its dispersive definition, obtained by carefully isolating the respective residues in the HLbL tensor [143, 146].

After performing Wick rotations for the two-loop integrals, five out of six angular integrations can be carried out for arbitrary form factors resorting to Gegenbauer-polynomial techniques, which leads to a three-dimensional integral representation for the pion-pole

contribution [56],

$$\begin{aligned} a_\mu^{\pi^0\text{-pole}} &= \left(\frac{\alpha}{\pi}\right)^3 \int_0^\infty \mathrm{d}Q_1 \int_0^\infty \mathrm{d}Q_2 \int_{-1}^1 \mathrm{d}\tau \\ &\quad \times \Big[w_1(Q_1,Q_2,\tau)\, F_{\pi^0\gamma^*\gamma^*}(-Q_1^2,-Q_3^2)\, F_{\pi^0\gamma^*\gamma^*}(-Q_2^2,0) \\ &\quad + w_2(Q_1,Q_2,\tau)\, F_{\pi^0\gamma^*\gamma^*}(-Q_1^2,-Q_2^2)\, F_{\pi^0\gamma^*\gamma^*}(-Q_3^2,0) \Big] , \end{aligned} \tag{4.6}$$

where $Q_{1/2}^2 = -q_{1/2}^2$, $Q_3^2 = Q_1^2 + 2Q_1Q_2\tau + Q_2^2$, and $\tau = \cos\theta$, with θ the remaining angle between the Euclidean four-momenta Q_1 and Q_2. The weight functions appearing in (4.6) are given by

$$\begin{aligned} w_1(Q_1,Q_2,\tau) &= -\frac{2\pi}{3}\sqrt{1-\tau^2}\,\frac{Q_1^3Q_2^3}{Q_2^2+M_{\pi^0}^2}\,T_1(Q_1,Q_2,\tau)\,, \\ w_2(Q_1,Q_2,\tau) &= -\frac{2\pi}{3}\sqrt{1-\tau^2}\,\frac{Q_1^3Q_2^3}{Q_3^2+M_{\pi^0}^2}\,T_2(Q_1,Q_2,\tau)\,, \end{aligned} \tag{4.7}$$

where the kernel functions T_1 and T_2 are reproduced in Appendix B.2.

The relation (4.6) constitutes a special case of the master formula for the complete HLbL contribution to a_μ [146, 148], obtained by decomposing the HLbL tensor into scalar basis functions according to the general recipe established in [332, 333] that ensure the absence of kinematic singularities and zeros, critical for the applicability of a dispersive representation. In the end, twelve combinations of these scalar functions $\bar{\Pi}_i$ enter the master formula

$$a_\mu^{\text{HLbL}} = \frac{2\alpha^3}{3\pi^2}\int_0^\infty \mathrm{d}Q_1 \int_0^\infty \mathrm{d}Q_2 \int_{-1}^1 \mathrm{d}\tau \sqrt{1-\tau^2}\,Q_1^3Q_2^3 \sum_{i=1}^{12} \bar{T}_i(Q_1,Q_2,\tau)\bar{\Pi}_i(Q_1,Q_2,\tau)\,, \tag{4.8}$$

in which the pion pole only contributes to $\bar{\Pi}_1$ and $\bar{\Pi}_2$

$$\begin{aligned} \bar{\Pi}_1^{\pi^0\text{-pole}}(Q_1,Q_2,\tau) &= -\frac{F_{\pi^0\gamma^*\gamma^*}(-Q_1^2,-Q_2^2)F_{\pi^0\gamma^*\gamma^*}(-Q_3^2,0)}{Q_3^2+M_{\pi^0}^2}\,, \\ \bar{\Pi}_2^{\pi^0\text{-pole}}(Q_1,Q_2,\tau) &= -\frac{F_{\pi^0\gamma^*\gamma^*}(-Q_1^2,-Q_3^2)F_{\pi^0\gamma^*\gamma^*}(-Q_2^2,0)}{Q_2^2+M_{\pi^0}^2}\,, \end{aligned} \tag{4.9}$$

reproducing the equivalent representation (4.6) with $\bar{T}_1 = T_2$ and $\bar{T}_2 = T_1$.

If dispersion relations are not derived for the HLbL tensor but for the Pauli form factor directly [334], this equivalence has so far only been confirmed for a VMD form factor, and in general it is not guaranteed that dispersion relations for different quantities lead to the same notion of the pion pole. Moreover, in model calculations different definitions have been employed in the past, including off-shell pions [319, 335–344] and a variant introducing a

constant form factor at one vertex [138]. However, these ambiguities are specific to each particular model and do not occur in the dispersive approach to the HLbL tensor. Once an organizing principle in terms of its singularities is accepted, the pion-pole contribution as given by the master formula (4.6) and (4.8) follows unambiguously. In consequence, the recent phenomenological evaluations [141, 159, 345] and lattice QCD calculation [160, 346] of the pion-pole contribution have adopted this dispersive definition.

The properties of the weight functions w_1 and w_2 have been studied extensively in [141]. We briefly summarize their main features to gain some intuition for the evaluation of the multi-dimensional integral in the master formula (4.6). $w_1(Q_1, Q_2, \tau)$ and $w_2(Q_1, Q_2, \tau)$ are dimensionless, $w_2(Q_1, Q_2, \tau)$ is symmetric under $Q_1 \leftrightarrow Q_2$, and both tend to zero for $Q_i \to 0$ and $\tau \to \pm 1$. Asymptotically, they behave according to

$$\begin{aligned} &\lim_{Q_1\to\infty} w_1(Q_1, Q_2, \tau) \to \frac{1}{Q_1}\,, \qquad \lim_{Q_2\to\infty} w_1(Q_1, Q_2, \tau) \to \frac{1}{Q_2^2}\,, \\ &\lim_{Q_i\to\infty} w_2(Q_1, Q_2, \tau) \to \frac{1}{Q_i^3}\,, \end{aligned} \tag{4.10}$$

hence assuring the convergence of the three-dimensional integral (4.6) for a form factor approaching zero at large momenta. In fact, the contribution from w_2 even converges for a pointlike form factor. To better understand the divergence structure of the integral, it is instructive to consider the LO in ChPT. Since this corresponds to a pointlike form factor, the loop integral diverges, demanding a counter term that cannot be determined independently by other means but $a_\mu^{\pi^0\text{-pole}}$ itself. However, as pointed out in [311, 315], the chiral analysis does predict the logarithmically enhanced pieces, in a parameter-free way for the double logarithm and in terms of a low-energy constant (LEC) related to $P \to \ell^+\ell^-$ decays ($P = \pi^0, \eta$, $\ell = e, \mu$) for the single logarithm [347–350]. In the dispersive approach, this relation to pseudoscalar dilepton decays is accounted for automatically in terms of the TFFs, see Appendix B.3, as a matter of fact more accurately without any need to rely on the chiral expansion. This relation between the TFF and pseudoscalar decays is well-established in the literature [351–358], and indeed the representation for the TFF derived here for $(g-2)_\mu$ should prove valuable for an improved prediction for the $\pi^0 \to e^+e^-$ decay as well.

Finally, $w_1(Q_1, Q_2, \tau)$ and $w_2(Q_1, Q_2, \tau)$ are plotted as functions of Q_1 and Q_2 for $\tau = 0$ ($\theta = 90^\circ$) in Figure 4.2. It can been seen that the maximum peaks appear in the momenta range below 0.2 GeV for both $w_1(Q_1, Q_2, \tau)$ and $w_2(Q_1, Q_2, \tau)$. In line with the asymptotic behavior (4.10) we find that $w_2(Q_1, Q_2, \tau)$ is roughly an order of magnitude smaller than $w_1(Q_1, Q_2, \tau)$ for the same values of τ and falls off faster compared to $w_1(Q_1, Q_2, \tau)$ after reaching the maximum peak. In summary, the peaks of the weight functions $w_1(Q_1, Q_2, \tau)$ and $w_2(Q_1, Q_2, \tau)$ are concentrated in the momentum range $Q_i \leq 0.5\,\text{GeV}$ so that the most prevailing contribution in the master formula (4.6) arises from the low-energy region. Moreover, this is exactly the region where the pion TFF can be precisely determined in our dispersive framework, hence providing a possibility to model-independently evaluate the dominant pion-pole contribution with well-controlled uncertainties. Accordingly, we now

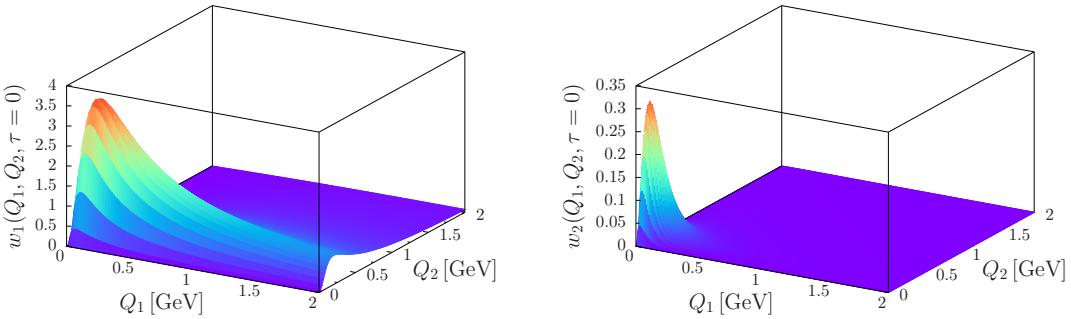

Figure 4.2: The weight functions $w_1(Q_1, Q_2, \tau)$ (left diagram) and $w_2(Q_1, Q_2, \tau)$ (right diagram) as functions of Q_1 and Q_2 for $\tau = 0$, $\theta = 90^\circ$.

turn to the dispersive determination of the pion TFF itself.

4.3 Dispersion relations for the pion transition form factor

4.3.1 Definition and low-energy properties

The pion TFF is defined by the QCD vertex function

$$i \int \mathrm{d}^4x\, e^{iq_1\cdot x} \langle 0|T\{j_\mu(x) j_\nu(0)\}|\pi^0(q_1+q_2)\rangle = \epsilon_{\mu\nu\alpha\beta}\, q_1^\alpha\, q_2^\beta\, F_{\pi^0\gamma^*\gamma^*}(q_1^2, q_2^2)\,, \tag{4.11}$$

where j_μ are the light quark currents defined in (4.3) and $\epsilon^{0123} = +1$.[3] It describes the interaction between an on-shell neutral pion ($(q_1+q_2)^2 = M_{\pi^0}^2$) and two off-shell photons with four-momenta q_1 and q_2. The normalization of the form factor for real photons is dictated by the Adler–Bell–Jackiw anomaly [111–113],

$$F_{\pi^0\gamma^*\gamma^*}(0,0) = \frac{1}{4\pi^2 F_\pi} \equiv F_{\pi\gamma\gamma}\,, \tag{4.12}$$

where $F_\pi = 92.28(10)$ MeV [22] is the pion decay constant. It is related to the neutral pion decay width into two photons by $F^2_{\pi^0\gamma^*\gamma^*}(0,0) = 4\,\Gamma(\pi^0 \to \gamma\gamma)/(\pi\alpha^2 M^3_{\pi^0})$, which has been tested up to 1.4% in a Primakoff measurement of the $\pi^0 \to \gamma\gamma$ decay width [359] (chiral and radiative corrections have been worked out in [288–291]). We used the chiral tree-level prediction (4.12) including the quark-mass renormalization of F_π, together with its 1.4% uncertainty, as the central value and uncertainty estimate for the normalization of the TFF

[3] Note that the definition of j_μ in [229–232] differs from (4.3) by a factor e. For $(g-2)_\mu$, however, the standard convention separates all factors of e upfront, which leads to the normalization given in (4.12).

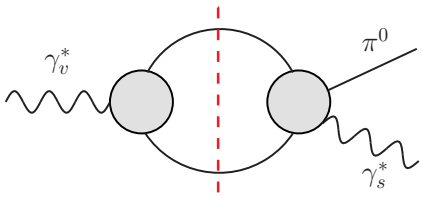

Figure 4.3: Two-body unitarity relation for $\gamma_v^* \to \gamma_s^* \pi^0$. The gray blobs represent the pion vector form factor and the $\gamma_s^* \to 3\pi$ amplitude, respectively, and the solid lines pion intermediate states.

in [149, 150]. Here, we update them to the final result of the PrimEx experiment in the final prediction of the pion-pole contribution (4.51), which achieved a precision of 0.75% [287, 360], so that, the dominant source of uncertainty is of systematic nature in understanding the emerging tension with the chiral two-loop prediction [291].

In a dispersive approach, the pion TFF is reconstructed from the most important lowest-lying singularities in the unitarity relation.[4] Assuming exact isospin symmetry, one of the photons in the $\pi^0\gamma^*\gamma^*$ vertex must be an isovector ($I = 1$) state and the other an isoscalar ($I = 0$). Therefore, the form factor can be decomposed into definite-isospin virtualities as

$$F_{\pi^0\gamma^*\gamma^*}(q_1^2, q_2^2) = F_{vs}(q_1^2, q_2^2) + F_{vs}(q_2^2, q_1^2)\,, \tag{4.13}$$

where the isovector and isoscalar virtualities are labeled by the indices v and s. At low energies, the unitarity relation for $\gamma_v^* \to \gamma_s^*\pi^0$ is dominated by the $\gamma_v^* \to \pi^+\pi^- \to \gamma_s^*\pi^0$ process as shown in Figure 4.3. Consequently, the building blocks in the sub-diagrams are the pion vector form factor and the $\gamma_s^* \to 3\pi$ amplitude.

The pion vector form factor is described by two differently subtracted variants of the Omnès representation [173]. First, it is parameterized by

$$F_\pi^V(s) = (1 + \alpha_V s)\Omega(s)\,, \qquad \Omega(s) = \exp\left\{\frac{s}{\pi}\int_{4M_\pi^2}^{\infty} \mathrm{d}s' \frac{\delta(s')}{s'(s'-s)}\right\}, \tag{4.14}$$

where $\Omega(s)$ is the Omnès function [173], and three different $\pi\pi$ P-wave phase-shift inputs are used for $\delta(s)$: Bern and Madrid phases [201, 202], respectively, are based on analyses of Roy- and Roy-like equations of $\pi\pi$ scattering. In addition, we consider an extension of [202] including the $\rho'(1450)$ and $\rho''(1700)$ resonances in an elastic approximation [229], fit to the pion vector form factor as measured in τ decays [361], in order to estimate the impact of inelasticities on the $\pi\pi$ input. The coefficient $\alpha_V \sim (1\text{–}10) \times 10^{-2}\,\mathrm{GeV}^{-2}$ is again obtained from a fit to [361] up to 1.0 GeV for Bern and Madrid phases and the full range for the third variant. The polynomial is set to a constant above 1.0 GeV (1.9 GeV for the

[4] In general, we restrict our attention to purely hadronic states, i.e. neglect radiative processes/corrections, which is justified by the smallness of the electromagnetic coupling constant. An exception is the energy range of the ω meson due to its eight-percent branching to $\pi^0\gamma$ [22]. This coupling of the three-pion states to $\pi^0\gamma$ is taken into account, see (2.19).

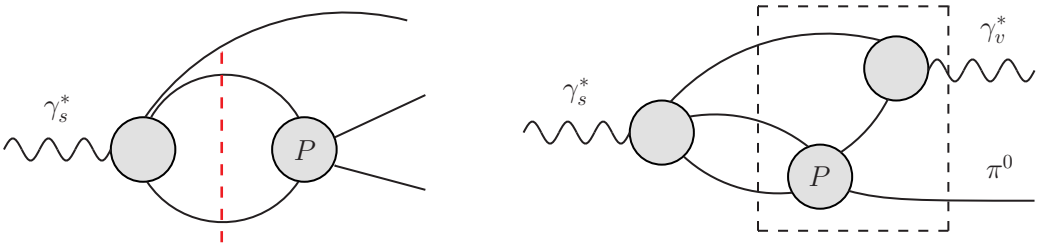

Figure 4.4: Two-body unitarity relation for the $\gamma_s^* \to 3\pi$ amplitude (left) and the approximation for three-body unitarity in $\gamma_s^* \to \gamma_v^*\pi^0$ that follows from the two-body rescattering (right). The part of the diagram in the dashed box can be viewed as a special case of the full $\pi^+\pi^-\pi^0 \to \gamma_v^*\pi^0$ amplitude. The gray blob labeled P refers to the P-wave $\pi\pi$ scattering amplitude.

third phase) to attain a better high-energy behavior. Second, a twice-subtracted version as in [231, 362] is used below 1.3 GeV (below 1.9 GeV for the third phase),

$$F_\pi^V(s) = \exp\left\{\frac{\langle r^2\rangle_\pi^V}{6}s + \frac{s^2}{\pi}\int_{4M_\pi^2}^{\infty} \mathrm{d}s' \frac{\delta(s')}{s'^2(s'-s)}\right\}, \tag{4.15}$$

with a fit radius $\langle r^2\rangle_\pi^V \sim 0.436\,\mathrm{fm}^2$ covering the data up to 1.0 GeV. It is smoothly guided to the once-subtracted representation at 1.9 GeV by adjusting the radius to the value that follows from the once-subtracted version by means of a sum rule, $\langle r^2_{\mathrm{sum}}\rangle_\pi^V \sim 0.420\,\mathrm{fm}^2$. The difference between both variants of F_π^V enters the dispersive uncertainty for subsequently calculated quantities.

Turning to the $\gamma_s^* \to 3\pi$ amplitude, its two-body unitarity relation is shown in the left diagram of Figure 4.4. It involves the final-state interactions between pion pairs, which can be resummed in terms of the P-wave phase shift in the dispersive framework. However, it possesses a more complex analytic structure as a three-body decay process, which will be discussed in detail in Section 4.3.2. While the full three-body unitarity $\gamma_s^* \to \pi^+\pi^-\pi^0 \to \gamma_v^*\pi^0$ governing the unitarity relation for $\gamma_s^* \to \gamma_v^*\pi^0$ cannot be implemented exactly in our approach, the $\pi\pi$ rescattering in the two-body unitarity relation for $\gamma_s^* \to 3\pi$ already generates the leading topologies containing three-pion cuts for $\gamma_s^* \to \gamma_v^*\pi^0$ as presented in the right diagram of Figure 4.4, approximating the left-hand cut structure in $3\pi \to \gamma_v^*\pi^0$ by pion-pole terms [231].

4.3.2 Parameterization of $e^+e^- \to 3\pi$

The $\gamma_s^* \to 3\pi$ formalism

The formalism of $\gamma_s^* \to 3\pi$ amplitude is essentially described in Section 2.2. Here, we solve (2.14) for $a(q^2) \to 1$ (and a finite cutoff $\Lambda_{3\pi}$ above which we assume the asymptotic behavior $\hat{\mathcal{F}}(s, q^2) \sim 1/s$) and restore the full overall-normalization dependence later. In

the present case, $a(q^2)$, as a function of q^2, contains the information about the coupling of the isoscalar photon to 3π states. Therefore, $a(q^2)$ was determined from $e^+e^- \to 3\pi$ cross section data in [231], assuming that three-body unitarity for $\gamma_s^* \to 3\pi$ is dominated by the narrow resonances ω and ϕ.

In this work, we take the improved parameterization of $a(q^2)$ (2.16), which introduces a conformal polynomial to account for the effects from inelastic channels. The degree p of the conformal polynomial is larger than the actual number of free parameters for the following reasons. First, the S-wave cusp must be eliminated because of the P-wave nature of the photon. Second, $a(q^2)$ is constructed in such a way that the sum rule for the subtraction constant α_A is exactly fulfilled, which induces another constraint on the coefficients c_i in (2.21). Third, the integration in (2.22) extends to infinity to fulfill the sum rule exactly, but in practice an isoscalar integration cutoff s_{is} needs to be introduced, both for the double-spectral representation of the TFF that we will derive below to satisfy the asymptotic constraints from pQCD and because the description of the $e^+e^- \to 3\pi$ data based on KT equations cannot be justified to arbitrarily high energies. In practice, we take $s_{\text{is}} = (1.8\,\text{GeV})^2$, so that, to ensure the validity of (2.22), the imaginary part of the conformal polynomial has to decrease sufficiently fast. For that reason, we constrain the c_i further to cancel the leading asymptotic behavior for $q^2 \to \infty$. For a degree p and n constraints on the asymptotic behavior the imaginary part behaves as $q^{-(2n+1)}$ and $p - n - 2$ free parameters remain. We find that the low-energy $e^+e^- \to 3\pi$ data can be well described with two free parameters for $n = 3$–5 and three free parameters for $n = 6$, with small deviations starting around 1.6 GeV. The representation for $a(q^2)$ constructed in this manner not only results in an improved description of the data, in particular above the ϕ resonance, but also guarantees the internal consistency of the different representations for the TFF when generalizing the single dispersion relation (4.19) to the double-spectral representation (4.22), see Section 4.3.3.

Fit results for $e^+e^- \to 3\pi$

We determine the normalization $a(q^2)$ by fitting the residues c_V and the coefficients of the conformal polynomial c_i to the $e^+e^- \to 3\pi$ data. The relation between the $e^+e^- \to 3\pi$ cross section (neglecting the electron mass) and the $\gamma_s^* \to \pi^+\pi^-\pi^0$ amplitude is given in Section 2.2.

As detailed in [231], the most comprehensive single data sets of the $e^+e^- \to 3\pi$ cross section at low and high energies are provided by SND [250, 251] and BaBar [248], respectively, so that the combined SND+BaBar data set yields the dominant constraint for the entire energy region below 1.8 GeV, with negligible differences when fitting to the full data base instead (see the fits in [231] to the data compilation from [363]). The uncertainty estimates for the fits are generated based on the following variations: $\mathcal{F}(s, q^2)$ is calculated using the three different $\pi\pi$ phase shifts introduced in Section 4.3.1 in the context of the pion vector form factor. Additionally, the cutoff $\Lambda_{3\pi}$ in the integral equation (2.14) above which the asymptotic behavior is assumed is varied from 1.8 to 2.5 GeV.

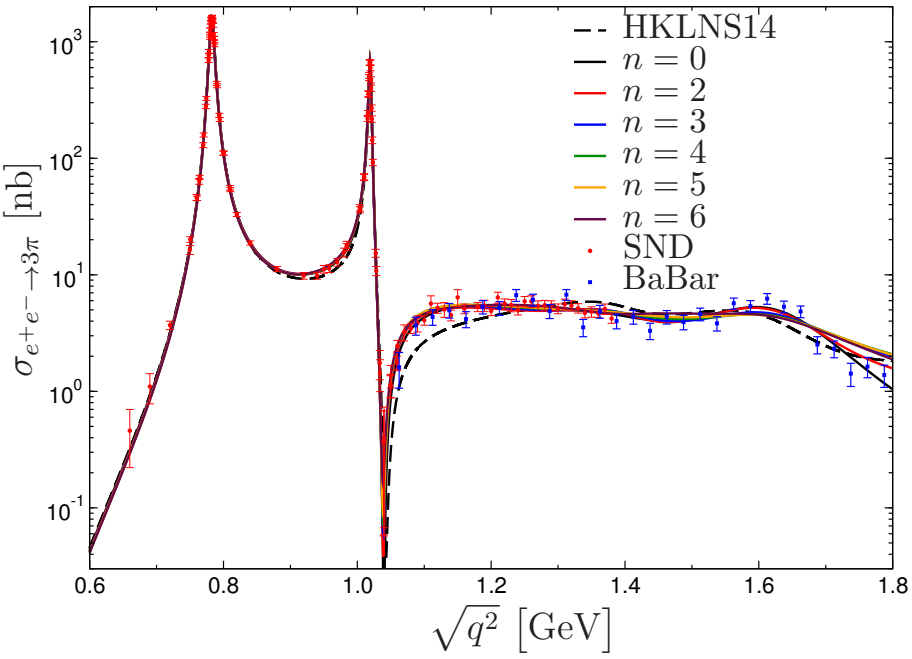

Figure 4.5: Fits to the $e^+e^- \to 3\pi$ cross section from SND [250, 251] and BaBar [248] with the different variants of the conformal polynomial labeled by n, the phase shift from [202], and $\Lambda_{3\pi} = 2.5\,\text{GeV}$, in comparison to [231] (HKLNS14).

The $e^+e^- \to 3\pi$ cross sections for different values of n fit to the SND+BaBar data sets below 1.8 GeV using the phase shift from [202] and a cutoff $\Lambda_{3\pi} = 2.5\,\text{GeV}$ are shown in Figure 4.5. It can be clearly seen that the fit results are substantially improved above the ϕ peak by introducing the conformal polynomial in comparison to the results obtained in [231]. The uncertainty bands for individual n are not included in the plot as the curves would be hard to distinguish otherwise especially below 1.6 GeV. The differences in the reduced χ^2, see Table 4.1 for the explicit fit results for the different phase shifts and cutoffs $\Lambda_{3\pi}$, are almost exclusively generated by the high-energy end of the fit range, thus indicating that indeed our KT description starts to break down around 1.8 GeV. The low-energy data, however, are described with a reduced $\chi^2/\text{dof} \sim 1$.

4.3.3 Double-spectral representation

The previous discussion of the isospin decomposition (4.13) and the crucial building blocks in the unitarity relation for the pion TFF, the pion vector form factor $F_\pi^V(s)$ and the $\gamma_s^* \to 3\pi$ P-wave amplitude $f_1(s, q^2)$, defines the quantities that enter a once-subtracted dispersion relation in the isovector virtuality (for fixed isoscalar virtuality) [230],

$$F_{vs}(q_1^2, q_2^2) = F_{vs}(0, q_2^2) + \frac{q_1^2}{12\pi^2} \int_{4M_\pi^2}^{\infty} \mathrm{d}x \frac{q_\pi^3(x)(F_\pi^V(x))^* f_1(x, q_2^2)}{x^{3/2}(x - q_1^2)}\,, \tag{4.16}$$

	$n = 3$	$n = 4$	$n = 5$	$n = 6$
c_ω [GeV^{-1}]	2.87 . . . 2.90	2.85 . . . 2.88	2.84 . . . 2.87	2.83 . . . 2.86
c_ϕ [GeV^{-1}]	−(0.400 . . . 0.412)	−(0.400 . . . 0.414)	−(0.400 . . . 0.414)	−(0.400 . . . 0.413)
$c_{\omega'}$ [GeV^{-1}]	−(0.24 . . . 0.52)	−(0.14 . . . 0.39)	−(0.040 . . . 0.33)	−0.15 . . . 0.14
$c_{\omega''}$ [GeV^{-1}]	−(0.80 . . . 1.16)	−(0.60 . . . 0.94)	−(0.49 . . . 0.90)	−(0.45 . . . 0.78)
c_1 [GeV^{-3}]	−(1.56 . . . 1.79)	−(1.75 . . . 1.96)	−(1.81 . . . 2.08)	−(2.00 . . . 2.24)
c_2 [GeV^{-3}]	−(1.05 . . . 1.16)	−(1.28 . . . 1.40)	−(1.44 . . . 1.50)	−(1.67 . . . 1.73)
c_3 [GeV^{-3}]	—	—	—	−0.05 . . . 0.12
χ^2/dof	1.37 . . . 1.70	1.58 . . . 2.03	1.68 . . . 2.15	1.71 . . . 2.16

Table 4.1: Fit parameters and reduced χ^2 for the $e^+e^- \to 3\pi$ fits to SND+BaBar [248, 250, 251] using different versions of the conformal polynomial with asymptotic behavior $q^{-(2n+1)}$. The ranges indicate the variation found for the different $\pi\pi$ phase shifts and values of $\Lambda_{3\pi}$.

with $q_\pi(s) = \sqrt{s/4 - M_\pi^2}$. For $q_2^2 = M_{\omega/\phi}^2$, the representation (4.16) has been used to describe the $\omega/\phi \to \pi^0\gamma^*$ TFFs, where the sum rule for the subtraction function

$$F_{vs}(0, q_2^2) = \frac{1}{12\pi^2} \int_{4M_\pi^2}^\infty \mathrm{d}x \frac{q_\pi^3(x)}{x^{3/2}} (F_\pi^V(x))^* f_1(x, q_2^2) \tag{4.17}$$

is related to the real-photon decays [229]. For $q_2^2 = 0$, (4.16) yields the isovector part of the singly-virtual pion TFF,

$$F_{vs}(q_1^2, 0) = F_{vs}(0, 0) + \frac{q_1^2}{12\pi^2} \int_{4M_\pi^2}^\infty \mathrm{d}x \frac{q_\pi^3(x)(F_\pi^V(x))^* f_1(x, 0)}{x^{3/2}(x - q_1^2)}, \tag{4.18}$$

where the sum rule $F_{vs}(0, 0) = F_{\pi\gamma\gamma}/2$ is typically saturated at the 90% level [230, 231].

For the $(g-2)_\mu$ application (4.6) we need a representation of the space-like doubly-virtual form factor that can be evaluated at arbitrarily high energies, matching smoothly onto the asymptotic behavior expected from pQCD, see Section 4.5. In this regard, the once-subtracted representation is disfavored because it approaches a constant for large virtualities, contradicting the pQCD scaling, unless the sum rule for the subtraction constant is fulfilled exactly. In practice, however, the uncertainties in the input always generate variants of the form factor that behave as a constant at high energies, and such a constant form factor does not lead to a convergent $(g-2)_\mu$ integral. Therefore, we start from an unsubtracted dispersion relation [231]

$$F_{vs}(q_1^2, q_2^2) = \frac{1}{12\pi^2} \int_{4M_\pi^2}^\infty \mathrm{d}x \frac{q_\pi^3(x)(F_\pi^V(x))^* f_1(x, q_2^2)}{x^{1/2}(x - q_1^2)}, \tag{4.19}$$

despite the expected 10% violation of the sum rule for the normalization $F_{\pi\gamma\gamma}/2$. To remedy this shortcoming, we introduce an isovector integration cutoff s_{iv} and add an effective pole collecting the contributions from higher intermediate states and high-energy contributions in the 2π and 3π channels, see Section 4.5 for details. In this manner, the representation (4.19), in principle, already determines the general doubly-virtual form factor. However, to find a representation that facilitates the evaluation in the entire space-like region we derive a more compact double-spectral representation that makes the analyticity of the form factor $F_{\pi^0\gamma^*\gamma^*}(q_1^2, q_2^2)$ in both of its arguments q_1^2 and q_2^2 explicit,

$$F_{\pi^0\gamma^*\gamma^*}(q_1^2, q_2^2) = \frac{1}{\pi^2}\int_0^\infty \mathrm{d}x \int_0^\infty \mathrm{d}y \frac{\rho(x,y)}{(x-q_1^2)(y-q_2^2)}\,, \tag{4.20}$$

where $\rho(x,y)$ is the double-spectral density that we aim to reconstruct from the low-lying hadronic intermediate states. Accordingly, the single dispersion relation (4.19) is elevated to the double-spectral form by performing yet another dispersion relation in the isoscalar variable,

$$F_{vs}(-Q_1^2, q_2^2) = \frac{1}{\pi}\int_{s_{\text{th}}}^{s_{\text{is}}} \mathrm{d}y \frac{\operatorname{Im} F_{vs}(-Q_1^2, y)}{y-q_2^2} = \frac{1}{12\pi^2}\int_{4M_\pi^2}^{s_{\text{iv}}} \mathrm{d}x \frac{q_\pi^3(x)(F_\pi^V(x))^* f_1(x, q_2^2)}{x^{1/2}(x+Q_1^2)}\,, \tag{4.21}$$

where s_{is} is the isoscalar integration cutoff and the threshold $s_{\text{th}} = M_{\pi^0}^2$ is the same as in (2.22). This leads to a double-spectral representation of the form factor,

$$\begin{aligned} F^{\text{disp}}_{\pi^0\gamma^*\gamma^*}(-Q_1^2, -Q_2^2) &= \frac{1}{\pi^2}\int_{4M_\pi^2}^{s_{\text{iv}}} \mathrm{d}x \int_{s_{\text{th}}}^{s_{\text{is}}} \mathrm{d}y \frac{\rho^{\text{disp}}(x,y)}{(x+Q_1^2)(y+Q_2^2)} + (Q_1 \leftrightarrow Q_2)\,, \\ \rho^{\text{disp}}(x,y) &= \frac{q_\pi^3(x)}{12\pi\sqrt{x}} \operatorname{Im}\left[(F_\pi^V(x))^* f_1(x,y)\right], \end{aligned} \tag{4.22}$$

to describe the low-energy properties, which can be applied to space-like doubly-virtual kinematics. The nonzero imaginary part of $F_{vs}(-Q_1^2, q^2)$ is attributed to three-body unitarity in the isoscalar virtuality, both the three-pion cuts which result in the deviation of the phase of $f_1(s, q^2)$ from the phase of $F_\pi^V(s)$ in the decay region $q^2 > 9M_\pi^2$ [229] and the complex nature of $a(q^2)$ as well. In fact, the complicated analytic structure of the partial wave $f_1(s, q^2)$ itself might make it seem surprising that the TFF fulfills a dispersive representation as simple as (4.20), see Appendix B.4 for a more detailed discussion.

Formally, the equivalence of the single dispersion relation (4.19) and the double-spectral representation (4.22) for $F_{vs}(q_1^2, q_2^2)$ implies a sum rule

$$(F_\pi^V(s))^* f_1(s, q_2^2) = \frac{1}{\pi}\int_{s_{\text{th}}}^{s_{\text{is}}} \mathrm{d}y \frac{\operatorname{Im}\left[(F_\pi^V(s))^* f_1(s,y)\right]}{y-q_2^2}\,, \tag{4.23}$$

which, once finite cutoffs are applied, requires that the singularities be concentrated in the low-energy region to ensure overall consistency, precisely the motivation for constraining

the high-energy behavior of the imaginary part of $a(q^2)$ accordingly. In this context, due to the pseudothreshold singularities located at $s = \left(\sqrt{q_2^2} - M_\pi\right)^2$ [229], it becomes more convenient to consider the integrated quantities instead, which is why we do not pursue the sum rule (4.23) itself any further.

4.4 Relevant scales for the transition between low and high energies

Having presented the construction of the dispersive representation of the low-energy properties of the pion TFF, we first wish to offer a qualitative understanding of the relevant *scales* that show up in its subsequent quantitative completion at higher energies. To this end, we will use phenomenologically successful models. The following reasoning is meant to be of qualitative use to help understanding the characteristic mass or energy scales that we find later in the model-independent final calculations.

For the calculation of the hadronic quantum fluctuations in the magnetic moment of the muon, the latter's mass provides a scale somewhat smaller than the masses of pions; hence it is clear that the low-energy sector of QCD plays the most important role for these quantum fluctuations. Yet, concerning the pion-pole contribution, it turns out that only a proper high-energy behavior of the pion TFF guarantees the convergence of the corresponding integrals. Thus, pure low-energy information is not enough for a quantitatively reliable determination of the pion-pole contribution. Fortunately, pQCD provides some input for the asymptotic behavior of the pion TFF [364–366]. Also from a practical point of view, an interpolation between the low-energy region and the asymptotic behavior is more constraining and therefore more accurate than a pure extrapolation. The question related to relevant scales is then: where is the effective onset s_m of the asymptotic region?

The central piece of our framework is the dispersive representation of the pion TFF: at low energies, the virtual photons couple dominantly to two- and three-pion states. Below about 1 GeV, these two- and three-pion states essentially behave elastically. Their rescattering is quantitatively under control by the dispersive framework developed in [197, 229–232]. We use the phrase "low-energy region" to characterize the regime dominated by elastic reactions. Above 1 GeV, new channels, i.e. inelasticities become important. For instance, in the isovector channel, the two-pion states (and the virtual photon) couple to four-pion states [197, 201, 202, 367–369]. Although the threshold for four pions lies significantly below 1 GeV, both the smallness of four-pion phase space near threshold and the derivative couplings of the pions demanded by chiral symmetry effectively delay the onset of the importance of the four-pion states to the $\pi\omega$ threshold. In the isoscalar channel, the three-pion states (and the virtual photon) couple to kaon pairs; this is particularly significant in the energy region of the ϕ meson, which has sizable branching fractions to kaon pairs and to three pions [22]. Of course, these are only examples: at higher energies, more and more channels come into play.

From a technical point of view, it is much more challenging to deal with the coupled-

channel dynamics above 1 GeV. On the other hand, it should be clear that for our purposes a less detailed knowledge of the regime beyond the low-energy region is acceptable. We have to expect an effective scale M_{eff} of the higher-lying inelasticities, i.e. the effective scale of the physics not covered by two- and three-pion states and their respective elastic rescattering, to reside at an energy larger than 1 GeV; but we shall argue now that it cannot be far away from it either.

The pion TFF is a part of the PVV three-point correlator, where P/V denotes a quark current with pseudoscalar/vector quantum numbers. With the standard Lehmann–Symanzik–Zimmermann procedure, one can map out the pion-pole contribution to the PVV correlator; see, e.g., [356]. The crucial point is that the whole PVV correlator would vanish if chiral symmetry were not broken [370]. On the other hand, chiral symmetry breaking is a long-distance, low-energy phenomenon. Quantitatively, it is characterized by the scale $4\pi F_\pi \approx 1\,\text{GeV}$ [371]. Thus, the pion TFF as part of the PVV correlator cannot be influenced too much from high-lying inelasticities, and we expect M_{eff} more or less close to 1 GeV.

This reasoning is not entirely independent of the question concerning the onset s_{m} of the asymptotic region; yet, it is not the same question. The asymptotic region concerns large *space-like* momenta where one can apply pQCD and the OPE, while the higher-lying inelasticities concern the *time-like* input for a dispersive representation. To relate the frameworks of OPE and dispersion theory, we use the QCD sum rule method [179, 372–375], to be more specific: the LCSRs [376–381]. The details of this analysis with the aim of an estimate for s_{m} are provided in Appendix B.5. In the QCD sum rule language, s_{m} coincides with the duality threshold. It enters as a free parameter that must be determined by comparison to data. For the case at hand, we compare to the singly-virtual pion TFF. By construction, the duality threshold must lie above the low-energy regime that is parameterized explicitly by hadronic resonances in the sum rule method, yet the analysis of Appendix B.5 reveals that the duality threshold cannot lie significantly higher either. Figure B.3 in Appendix B.5 shows that the best agreement with the data on the singly-virtual pion TFF is achieved by low values of s_{m}, again not much larger than $1\,\text{GeV}^2$.

4.5 Matching to the asymptotic behavior

The dispersive double-spectral density of (4.22) incorporates all the low-lying singularities in the 2π and 3π channels, but does not account for higher intermediate states nor the correct matching to pQCD. Therefore, we now develop the explicit form of the effective and asymptotic contributions in (4.1), considering both LO and NLO pQCD dynamics as well as an effective pole in order to impose the correct normalization $F_{\pi\gamma\gamma}$ and incorporate the constraints from space-like singly-virtual data.

4.5.1 Leading-order perturbative QCD

If both momenta q_1^2 and q_2^2 are large (and have the same sign), the T-product of the electromagnetic currents j_μ in (4.3) can be expanded along the light cone $x^2 = 0$. The lowest-order and leading-twist expansion of the TFF reads [364–366]

$$F_{\pi^0\gamma^*\gamma^*}(q_1^2, q_2^2) = -\frac{2F_\pi}{3}\int_0^1 \mathrm{d}u \frac{\phi_\pi(u)}{uq_1^2 + (1-u)q_2^2} + O(q_i^{-4}) \,, \tag{4.24}$$

where powers of asymptotic momenta are denoted by q_i. The twist-two pion distribution amplitude can be expanded in terms of Gegenbauer polynomials $C_{2n}^{3/2}$ as

$$\phi_\pi(u,\mu) = 6u(1-u)\left[1 + \sum_{n=1}^{\infty} a_{2n}(\mu) C_{2n}^{3/2}(2u-1)\right], \tag{4.25}$$

which provides a universal asymptotic distribution amplitude $\phi_\pi(u) = 6u(1-u)$ at large factorization scale $\mu \to \infty$ as the logarithmically μ-dependent coefficients a_{2n} tend to zero. Since at low scales the non-perturbative coefficients a_{2n} are largely unknown, we will use the asymptotic distribution amplitude $\phi_\pi(u)$ in the following analysis, ignoring the higher-order terms $n \geq 1$ as well as higher-twist corrections.

Introducing an asymmetry parameter $\omega = (q_1^2 - q_2^2)/(q_1^2 + q_2^2)$, the leading expression (4.24) can be changed into the form

$$F_{\pi^0\gamma^*\gamma^*}(q_1^2, q_2^2) = -\frac{4F_\pi}{3}\frac{f(\omega)}{q_1^2 + q_2^2} + O(q_i^{-4}) \,, \tag{4.26}$$

where

$$f(\omega) = \int_0^1 \mathrm{d}u \frac{\phi_\pi(u)}{u(1-\omega) + (1-u)(1+\omega)} \,. \tag{4.27}$$

Specifically, this implies the OPE limit [372, 382] for the diagonal form factor ($\omega = 0$),

$$F_{\pi^0\gamma^*\gamma^*}(-Q^2, -Q^2) = \frac{2F_\pi}{3Q^2} + O(Q^{-4}) \,. \tag{4.28}$$

In addition, formal evaluation at $\omega = \pm 1$ produces

$$F_{\pi^0\gamma^*\gamma^*}(-Q^2, 0) = F_{\pi^0\gamma^*\gamma^*}(0, -Q^2) = \frac{2F_\pi}{Q^2} + O(Q^{-4}) \,, \tag{4.29}$$

usually referred to as the Brodsky–Lepage (BL) limit of the singly-virtual form factor. However, the OPE expansion justifies (4.24) only for $|\omega| < 1/2$ [383, 384], otherwise its derivation cannot be considered rigorous. Apart from these two frequently studied conventional limits, (4.26) also predicts the asymptotic behavior for arbitrary virtualities q_1^2 and q_2^2 by (4.27). Hence, our representation will be matched to $f(\omega)$ to fully take

into account the entire domain of space-like virtualities, instead of just two particular limits (4.28) and (4.29). Beyond the leading expansion (4.24), calculations including α_s corrections [385, 386], higher terms in the Gegenbauer-polynomial expansion of $\phi_\pi(u)$ [376, 387] within QCD sum rules [377–379, 388], Dyson–Schwinger equations [389–392], and Regge theory [393–395] could be considered, but a consistent treatment of all subleading corrections becomes very complicated with little numerical impact on $(g-2)_\mu$. As an explicit example we will consider α_s corrections in Section 4.5.2.

At LO, we implement the pQCD constraints as follows. First, it has been observed that (4.24) can be transformed into a dispersion relation by a simple change of variables $u \to x/(x-q_2^2)$ for space-like virtuality q_2^2 [377],

$$F_{\pi^0\gamma^*\gamma^*}(q_1^2, q_2^2) = \frac{1}{\pi}\int_0^\infty \mathrm{d}x \frac{\operatorname{Im} F_{\pi^0\gamma^*\gamma^*}(x, q_2^2)}{x - q_1^2}\,, \tag{4.30}$$

with

$$\operatorname{Im} F_{\pi^0\gamma^*\gamma^*}(x, q_2^2) = \frac{2\pi F_\pi}{3(x-q_2^2)}\phi_\pi\left(\frac{x}{x-q_2^2}\right). \tag{4.31}$$

Furthermore, we find that identifying the discontinuities in the second variable q_2^2 leads to a new double-spectral representation for the asymptotic expression:

$$F_{\pi^0\gamma^*\gamma^*}(q_1^2, q_2^2) = \frac{1}{\pi^2}\int_0^\infty \mathrm{d}x \int_0^\infty \mathrm{d}y \frac{\rho^{\text{asym}}(x,y)}{(x-q_1^2)(y-q_2^2)}\,, \tag{4.32}$$

where

$$\rho^{\text{asym}}(x,y) = -2\pi^2 F_\pi x y \delta''(x-y) \tag{4.33}$$

is a double-spectral density proportional to xy and concentrated along the diagonal direction $x = y$ because of the second derivative of the delta function. Note that the singular nature of $\rho^{\text{asym}}(x,y)$ along the diagonal direction is a rather general feature not restricted to the asymptotic distribution amplitude $\phi_\pi(u)$. For instance, a constant pion distribution amplitude $\phi_\pi(u) = 1$ produces a double spectral density $(2\pi^2 F_\pi/3)\delta(x-y)$ proposed in the context of QCD sum rules [372].

The double-spectral form of the pQCD expression (4.32) then suggests to decompose the TFF in terms of the different integration regions

$$\begin{aligned} &F_{\pi^0\gamma^*\gamma^*}(q_1^2, q_2^2) \\ &\quad= \frac{1}{\pi^2}\int_0^{s_\mathrm{m}} \mathrm{d}x \int_0^{s_\mathrm{m}} \mathrm{d}y \frac{\rho(x,y)}{(x-q_1^2)(y-q_2^2)} + \frac{1}{\pi^2}\int_{s_\mathrm{m}}^\infty \mathrm{d}x \int_{s_\mathrm{m}}^\infty \mathrm{d}y \frac{\rho(x,y)}{(x-q_1^2)(y-q_2^2)} \\ &\quad+ \frac{1}{\pi^2}\int_0^{s_\mathrm{m}} \mathrm{d}x \int_{s_\mathrm{m}}^\infty \mathrm{d}y \frac{\rho(x,y)}{(x-q_1^2)(y-q_2^2)} + \frac{1}{\pi^2}\int_{s_\mathrm{m}}^\infty \mathrm{d}x \int_0^{s_\mathrm{m}} \mathrm{d}y \frac{\rho(x,y)}{(x-q_1^2)(y-q_2^2)}\,, \end{aligned} \tag{4.34}$$

where s_m is a continuum threshold introduced to separate the different regions, see the discussion in Section 4.4. On the one hand, the low-energy input to the double-spectral density has been derived in (4.22). On the other, the spectral density in the doubly-asymptotic region can be identified with $\rho^\mathrm{asym}(x,y)$ in (4.33). The spectral densities in the third and fourth mixed low- and high-energy regions are not well constrained, e.g. the asymptotic spectral density $\rho^\mathrm{asym}(x,y)$ applied in these regions simply vanishes. Given that the contribution from the doubly-asymptotic region alone can provide the correct asymptotic behavior and that both the BL limit as well as the available data can be described with a combination of the low-energy dispersive contribution and an effective pole, we will discard the contributions from the mixed regions altogether assuming that the effective pole sufficiently takes care of them. In the end, this defines the asymptotic contribution

$$\begin{aligned} F^\mathrm{asym}_{\pi^0\gamma^*\gamma^*}(q_1^2,q_2^2) &= 2F_\pi \int_{s_\mathrm{m}}^\infty \mathrm{d}x \frac{q_1^2 q_2^2}{(x-q_1^2)^2(x-q_2^2)^2} \\ &= \frac{2F_\pi q_1^2 q_2^2}{(q_1^2-q_2^2)^2}\left(\frac{1}{s_\mathrm{m}-q_1^2}+\frac{1}{s_\mathrm{m}-q_2^2}+\frac{2}{q_1^2-q_2^2}\ln\frac{s_\mathrm{m}-q_1^2}{s_\mathrm{m}-q_2^2}\right), \end{aligned} \tag{4.35}$$

which reproduces the limit defined by (4.24) for non-vanishing virtualities.

We remark that an asymptotic contribution of the form (4.35) could also be used to impose the correct asymptotic behavior on a hadronic model. For instance, for a VMD-inspired model one could write

$$\begin{aligned} F^\mathrm{VMD}_{\pi^0\gamma^*\gamma^*}(q_1^2,q_2^2) = F_{\pi\gamma\gamma}&\left[\frac{(1-\epsilon)\,M_1^4}{(M_1^2-q_1^2)(M_1^2-q_2^2)}+\frac{\epsilon\,M_2^4}{(M_2^2-q_1^2)(M_2^2-q_2^2)}\right] \\ &+ F^\mathrm{asym}_{\pi^0\gamma^*\gamma^*}(q_1^2,q_2^2)\,, \end{aligned} \tag{4.36}$$

which amounts to a simplified model for our full representation (4.1). By construction, all asymptotic limits for non-vanishing virtualities are correct, while the strict BL limit (4.29) emerges for $(1-\epsilon)M_1^2+\epsilon M_2^2 = 8\pi^2 F_\pi^2$. We tried to describe our full result using (4.36) as an approximation, treating either M_1, M_2, and ϵ, or, in addition, s_m as free fit parameters. Such an ansatz seems to work reasonably well, with systematic errors introduced at the level of a_μ around 0.5×10^{-11}, but of course cannot replace the full calculation.

4.5.2 Next-to-leading-order perturbative QCD

Higher orders in pQCD beyond the leading result [364–366] have been derived in [386]. Adapted to our notation, the corresponding correction can be expressed as

$$\begin{aligned}
F_{\pi^0\gamma^*\gamma^*}(q_1^2,q_2^2) &= -\frac{2F_\pi}{3}\int_0^1 \mathrm{d}u\,\frac{\phi_\pi(u)}{uq_1^2+(1-u)q_2^2}\left(1+\frac{C_F\alpha_s(\mu_s^2)}{2\pi}f(u,-q_1^2,-q_2^2,-\mu^2)\right),\\
f(u,q_1^2,q_2^2,\mu^2) &= -\frac{9}{2}+\frac{L_{12}(L_{12}-2)}{2}\left(1-\frac{q_1^2q_2^2}{(q_1^2-q_2^2)^2u(1-u)}\right)+\frac{3}{2}L_{12}\\
&\quad-\frac{q_1^2}{2(q_1^2-q_2^2)}\left(1-\frac{q_2^2}{(q_1^2-q_2^2)(1-u)}\right)L_1(L_1-2)+\frac{q_2^2}{2(q_1^2-q_2^2)u}(L_{12}-L_2)\\
&\quad+\frac{q_2^2}{2(q_1^2-q_2^2)}\left(1+\frac{q_1^2}{(q_1^2-q_2^2)u}\right)L_2(L_2-2)-\frac{q_1^2}{2(q_1^2-q_2^2)(1-u)}(L_{12}-L_1),\\
L_i &= \ln\frac{q_i^2}{\mu^2}, \qquad L_{12}=\ln\frac{uq_1^2+(1-u)q_2^2}{\mu^2}, \qquad C_F=\frac{N_c^2-1}{2N_c}=\frac{4}{3}.
\end{aligned} \tag{4.37}$$

In the singly-virtual limit we obtain

$$F_{\pi^0\gamma^*\gamma^*}(-Q^2,0)=\frac{2F_\pi}{Q^2}\left(1-\frac{5}{2}\frac{C_F\alpha_s(-Q^2)}{2\pi}\right)=\frac{2F_\pi}{Q^2}\left(1-\frac{5}{3}\frac{\alpha_s(-Q^2)}{\pi}\right), \tag{4.38}$$

in agreement with the result stated in [386]. Similarly, evaluation in the doubly-virtual limit produces

$$F_{\pi^0\gamma^*\gamma^*}(-Q^2,-Q^2)=\frac{2F_\pi}{3Q^2}\left(1-\frac{3}{2}\frac{C_F\alpha_s(-2Q^2)}{2\pi}\right)=\frac{2F_\pi}{3Q^2}\left(1-\frac{\alpha_s(-2Q^2)}{\pi}\right). \tag{4.39}$$

In each case, we have set $\mu_s^2=q_1^2+q_2^2$ [386]. As a powerful check on (4.37) the dependence on μ cancels also for general virtualities if the asymptotic form of the distribution amplitude is employed. Subleading terms in the Gegenbauer-polynomial expansion of the pion distribution amplitude again depend on μ, which compensates the μ dependence within the non-asymptotic α_s corrections.

For the asymptotic contribution to the pion TFF we seek corrections to

$$F^{\text{asym}}_{\pi^0\gamma^*\gamma^*}(q_1^2,q_2^2)=2F_\pi\int_{s_\text{m}}^\infty \mathrm{d}x\,\frac{q_1^2q_2^2}{(x-q_1^2)^2(x-q_2^2)^2}. \tag{4.40}$$

Since the corresponding double-spectral function is peaked at $x=y$, the canonical choice

of scale should be

$$F^{\text{asym}}_{\pi^0\gamma^*\gamma^*}(q_1^2,q_2^2) = 2F_\pi \int_{s_\text{m}}^\infty \mathrm{d}x \frac{q_1^2 q_2^2}{(x-q_1^2)^2(x-q_2^2)^2}\left(1+\frac{2}{3\pi}\alpha_s(-x)\delta(q_1^2,q_2^2,-x)\right),$$
$$\delta(q_1^2,q_2^2,\mu^2) = \frac{\int_0^1 \mathrm{d}u \frac{\phi_\pi(u)}{uq_1^2+(1-u)q_2^2} f(u,-q_1^2,-q_2^2,-\mu^2)}{\int_0^1 \mathrm{d}u \frac{\phi_\pi(u)}{uq_1^2+(1-u)q_2^2}}, \tag{4.41}$$

and we have checked that for Q^2 values of practical importance this estimate yields corrections close to the naive expectation $-\alpha_s(-2Q^2)/\pi \sim -10\%$ from the doubly-virtual limit. In the end, the uncertainty in the choice of matching scale s_m in the LO contribution safely encompasses such corrections.

4.5.3 Constraints from singly-virtual data

As the next step, we present the conceptual ideas how to incorporate high-energy TFF data in our representation (4.1). The final results of the corresponding fits will be provided in Section 4.6 together with all other results for the pion TFF in various kinematic regimes.

Despite the absence of doubly-virtual measurements of the TFF thus far, there is ample experimental information for space-like singly-virtual kinematics [396–399]. These data sets cover primarily large virtualities and thus provide the opportunity to probe the high-energy behavior of the singly-virtual form factor beyond the low-energy region $\lesssim 1\,\text{GeV}$, the latter being most relevant for a_μ. Most high-energy data in fact corroborate the BL limit $\lim_{Q^2\to\infty} Q^2 F_{\pi^0\gamma^*\gamma^*}(-Q^2,0) = 2F_\pi$ with $f(|\omega|=1)=3/2$ despite the questionable convergence at $|\omega|=1$, in contrast to a naive continuation of the OPE $f(|\omega|=1)=1$ or $f(|\omega|=1)=5/2$ obtained form the Chernyak–Zhitnitsky distribution amplitude [376, 387]. Potential deviations from the BL limit were suggested by the BaBar experiment [398], where the measured form factor exceeded the BL limit by as much as 50% at $Q^2 > 10\,\text{GeV}^2$, but the latest Belle measurement [399] did not find any evidence for such a rapid growth at high Q^2. We will assign sufficiently broad uncertainty bands that cover both scenarios, so that our final result for $a_\mu^{\pi^0\text{-pole}}$ will not depend on any prejudice either way.

Our representation evaluated for singly-virtual asymptotics receives contributions from the low-energy dispersive part (4.22), while the pQCD term (4.35) vanishes. In practice, the low-energy representation (4.22) already fulfills the BL limit at a level around 55%, so that only the remainder needs to be generated by higher intermediate states as well as high-energy contributions to the 2π and 3π channels. This can be conveniently achieved by an effective pole in the double-spectral density, which amounts to an extra term

$$F^{\text{eff}}_{\pi^0\gamma^*\gamma^*}(q_1^2,q_2^2) = \frac{g_\text{eff}}{4\pi^2 F_\pi}\frac{M_\text{eff}^4}{(M_\text{eff}^2-q_1^2)(M_\text{eff}^2-q_2^2)}, \tag{4.42}$$

where the coupling g_{eff} is determined by imposing the sum rule for $F_{\pi\gamma\gamma}$ and the mass parameter M_{eff} is fit to the space-like singly-virtual data [396–399]. The resulting parameters g_{eff} and M_{eff} are found to be around 10% and (1.5–2) GeV respectively, in agreement with the assumption that an effective pole subsumes the contributions from higher intermediate states. As pointed out in the discussions of the pion phase shift (2π states) and of the fit to the cross section for $e^+e^- \to 3\pi$ (3π states), our dispersive representation includes some part of the spectral strength of the energy region (1–2) GeV. Naively, one might then expect that the complementary part covered by the effective pole of (4.42) should lead to a value of M_{eff} significantly higher up in energy. However, as pointed out in Section 4.4, there cannot be much spectral strength at very high energies contributing to the pion TFF. Phrased differently, the range found for M_{eff} is completely reasonable and a better description of the region above 1 GeV would merely lead to a smaller value of g_{eff} instead of a higher value of M_{eff}.

In view of the tension of the BaBar data [398] both with the BL limit and the other data sets we need to specify how we treat the corresponding systematic uncertainty in our fits. First, we observe that, while otherwise the results are very stable with respect to the lower threshold Q^2_{min} above which data are fit, including the BaBar data induces a strong sensitivity on Q^2_{min}, and the χ^2 deteriorates appreciably if Q^2_{min} is increased. For this reason, we define the central value of our analysis by the fit to all data sets excluding BaBar, with $Q^2_{\text{min}} = 5\,\text{GeV}^2$, which leads to an asymptotic value almost exactly at the BL limit. To estimate the systematic uncertainties, we perform fits with $Q^2_{\text{min}} = (5\text{–}10)\,\text{GeV}^2$, with and without the BaBar data, and for each fit consider a $3\,\sigma$ error band. The envelope of all these fits corresponds to an uncertainty band $^{+20}_{-10}\%$ around the central value, where the asymmetric error reflects the fact that the BaBar data imply a systematic shift in the upward direction. In this way, we assign a very generous error band to the space-like fits, in such a way that the systematic uncertainties are safely covered by the corresponding error estimate in our final result. Moreover, since only data above $5\,\text{GeV}^2$ are included in the fit, the low-energy region remains a prediction, effectively improving the asymptotic behavior of the result from [231] by the matching to the pQCD constraints.

4.6 Numerical results

In this Section we present the numerical outcome of our analysis. First of all, in contrast to the fit strategy applied in Chapter 3, the singly-virtual pion TFF in the time-like region is *predicted* and the resulting $e^+e^- \to \pi^0\gamma$ cross section is compared to the corresponding experimental results. Second, the space-like doubly-virtual form factor is discussed, in particular along the singly-virtual and the diagonal direction, and the asymptotic behavior in the entire domain of space-like kinematics is further confronted with the predictions from pQCD. Last, the pion-pole contribution to a_μ is calculated along with comprehensive uncertainty estimates, each of which will be related to the various experimental input quantities.

4.6.1 Time-like form factor and $e^+e^- \to \pi^0\gamma$

According to (4.17) and (4.18), the time-like singly-virtual TFF obeys a once-subtracted dispersion relation:

$$F_{\pi^0\gamma^*\gamma^*}(q^2,0) = F_{\pi\gamma\gamma} + \frac{1}{12\pi^2}\int_{4M_\pi^2}^{\infty} \mathrm{d}x \frac{q_\pi^3(x)\left(F_\pi^V(x)\right)^*}{x^{3/2}}\left\{f_1(x,q^2) - f_1(x,0) + \frac{q^2}{x-q^2} f_1(x,0)\right\}, \tag{4.43}$$

where the normalization at the real photon point $q^2 = 0$ is fixed to the chiral anomaly using again the sum rule (4.17).[5] For the studies in [231], the isoscalar contribution corresponding to the first two terms in the integrand of (4.43) was calculated using the previously determined partial wave $f_1(s,q^2)$, where an asymptotic continuation $\sim 1/x$ was assumed above the isovector integration cutoff s_{iv}. The last term, the isovector piece, was determined using a finite matching point of 1.2 GeV [230]. Here, we will consider an update of this once-subtracted analysis based on the new parameterization for $a(q^2)$, including the conformal polynomial and the new isovector part, where s_{iv} is chosen as a strict integration cutoff for both isoscalar and isovector contributions in line with the dispersive representation (4.22). At the same time, the double-spectral representation (4.20) provides an unsubtracted form of the time-like TFF

$$F_{\pi^0\gamma^*\gamma^*}(q^2,0) = F^{\mathrm{disp}}_{\pi^0\gamma^*\gamma^*}(q^2,0) + F^{\mathrm{eff}}_{\pi^0\gamma^*\gamma^*}(q^2,0)\,, \tag{4.44}$$

where the determination of the parameters g_{eff} and M_{eff} in the effective pole is described in Section 4.5.3.

The relation between the $e^+e^- \to \pi^0\gamma$ cross section and the pion TFF reads (neglecting the mass of the electron for simplicity)

$$\sigma_{e^+e^-\to\pi^0\gamma}(q^2) = \frac{2\pi^2\alpha^3}{3}\frac{(q^2-M_{\pi^0}^2)^3}{q^6}\left|F_{\pi^0\gamma^*\gamma^*}(q^2,0)\right|^2. \tag{4.45}$$

We emphasize that our predictions of the time-like form factor and thus the cross section are entirely based on the dispersive framework with the input quantities described in the previous Sections: the anomalies $F_{\pi\gamma\gamma}$ and $F_{3\pi}$, the $\pi\pi$ P-wave phase shift, the pion vector form factor, and the $e^+e^- \to 3\pi$ cross section data.

The resulting $e^+e^- \to \pi^0\gamma$ cross section predicted from the once-subtracted and the unsubtracted TFFs based on the new parameterization of $a(q^2)$ are compared to the previous analysis [231] in Figure 4.6. In addition to the $e^+e^- \to \pi^0\gamma$ cross section measurements [270,

[5] This representation was first applied here to predict the $e^+e^- \to \pi^0\gamma$ cross section, and later promoted to the fit strategies presented in Chapter 3.

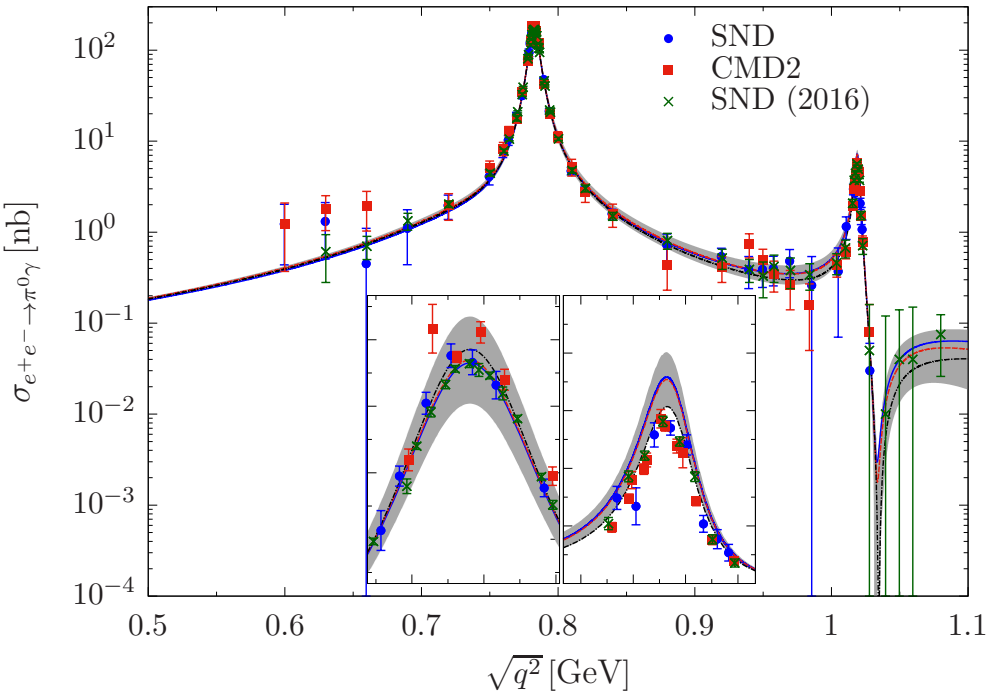

Figure 4.6: The $e^+e^- \to \pi^0\gamma$ cross section calculated from the once-subtracted TFF (blue solid line), the unsubtracted TFF (red dashed line), and [231] (black dot-dashed line), compared to the data of SND [295, 296], CMD2 [270], and SND (2016) [297]. The inserts show the same plot around the ω and ϕ peaks, respectively. The gray band indicates our uncertainty estimate for the unsubtracted TFF.

295, 296] already included in [231], we also take into account the most accurate new data determined from the full data sample of the SND experiment [297]. The mean values of our cross section are obtained averaging over the variations of the input quantities, n from 3–6 in the conformal polynomial of $a(q^2)$, and also the change of the integration cutoffs $\Lambda_{3\pi}$ and $\sqrt{s_{\text{iv}}}$ in the range (1.8–2.5) GeV. The band corresponding to the theoretical uncertainties σ_{th}, defined as the maximum deviations of all the variations from the average cross section, are only shown for the unsubtracted TFF in Figure 4.6, since otherwise the individual bands could hardly be differentiated. These results are fully consistent with [231], which is not immediately guaranteed for the unsubtracted version (4.44) given that the effective pole introduced to enforce the correct normalization implies a finite range of validity, the effects of which could potentially affect the low-energy region in particular for low masses M_{eff}.

We further calculate the reduced χ^2 corresponding to these results in the case of the different experimental data sets [270, 295–297] for a more quantitative assessment of our description. The reduced χ^2/dof calculated below 1 GeV and 1.1 GeV is shown in Table 4.2,

		SND	CMD2	SND (2016)
once-subtracted TFF	χ^2/dof	1.16 [2.76]	2.64 [12.7]	1.91 [4.73]
	$\tilde{\chi}^2$/dof	0.43 [0.73]	1.10 [1.85]	0.42 [0.68]
unsubtracted TFF	χ^2/dof	1.07 [2.51]	2.34 [11.5]	1.51 [4.04]
	$\tilde{\chi}^2$/dof	0.36 [0.62]	0.95 [1.45]	0.29 [0.50]
HKLNS14	χ^2/dof	0.90 [1.08]	1.82 [3.35]	2.15 [2.01]
	$\tilde{\chi}^2$/dof	0.54 [0.62]	1.18 [1.39]	0.68 [0.65]

Table 4.2: Reduced χ^2 and $\tilde{\chi}^2$ for the $e^+e^- \to \pi^0\gamma$ cross section determined from the once-subtracted and the unsubtracted TFFs and from [231] (HKLNS14), compared to SND [295, 296], CMD2 [270], and SND (2016) [297] below 1 GeV [below 1.1 GeV].

together with a modified variant

$$\tilde{\chi}^2 = \sum_{i=1}^{N} \frac{(y_i - y_{\text{th}}(q_i))^2}{\sigma_i^2 + \sigma_{\text{th}}^2(q_i)}\,, \tag{4.46}$$

where $q_i = \sqrt{q_i^2}$ and the difference between experiment and theory $y_i - y_{\text{th}}(q_i)$ is weighted by the combined uncertainty $\sqrt{\sigma_i^2 + \sigma_{\text{th}}^2(q_i)}$. We observe very good agreement between the once- and unsubtracted TFFs, while, as expected, differences to [231] arise from the new parameterization of $a(q^2)$. Below 1 GeV, the χ^2 deteriorates for the previously studied data sets from SND [295, 296] and CMD2 [270], but for the new SND data [297] the situation is reversed, here the new $a(q^2)$ leads to a better description. The difference can be traced back largely to the ω peak, see insert in Figure 4.6, where now the strength of the resonance is predicted almost perfectly, both for the subtracted and unsubtracted variants. In fact, the slight difference in the χ^2 originates almost exclusively from data outside the ω region.

Including the ϕ region, i.e. all data below 1.1 GeV, we find that the slight mismatch at the resonance peak already observed in [231] is compounded, and accordingly the χ^2 deteriorates appreciably when extending the energy region beyond 1 GeV. This indicates that, most likely, the inelastic effects in $a(q^2)$ fit to the 3π channel, including imaginary parts that open around the $K\bar{K}$ threshold, cannot describe the same energy region in the $e^+e^- \to \pi^0\gamma$ spectrum, reflecting the fact that these inelastic effects do not have to affect the 3π and $\pi^0\gamma$ channels in the same way. Accordingly, the marked improvement in the 3π channel just above the ϕ resonance comes at the expense of a mismatch in $\pi^0\gamma$. Phrased differently, the coefficients in the conformal polynomial if fit to $e^+e^- \to \pi^0\gamma$ instead of 3π would change as observed in Chapters 2 and 3, likely restoring agreement in the ϕ region.

In addition, a quantitative description above 1 GeV would at some point be distorted by the influence of the effective poles in the unsubtracted TFF (4.44), so that the once-subtracted variant would become more appropriate for that purpose. While it is therefore not unexpected that the χ^2 of the central values increases in the ϕ region, we remark that when including the uncertainty estimates, see $\tilde{\chi}^2$ in Table 4.2, the description hardly deteriorates and in the case of the new SND data and the unsubtracted TFF even slightly improves. This demonstrates that the gradual breakdown of the predictive power of our formalism in the time-like region around the ϕ resonance is largely captured by our uncertainty estimates.

In this work, we are most interested in the space-like TFF as it enters in $(g-2)_\mu$, and the improved description of 3π was constructed in such a way as to better control the analytic continuation to the space-like region. In principle, one could imagine fitting a similar representation of $a(q^2)$ to $e^+e^- \to \pi^0\gamma$ data alone (as in Chapter 3) and calculating the analytic continuation of the TFF based on the conformal parameters obtained in this fit. However, we conclude that the uncertainties in both the theoretical description and the data base are not competitive with a direct fit to $e^+e^- \to 3\pi$, which therefore provides the most reliable prediction of the space-like TFF. On the experimental side this conclusion is illustrated by the fact that the different data sets favor different theoretical predictions, see Table 4.2, while on the theory side the complications become most apparent in the analytic continuation. For the application in $(g-2)_\mu$ the asymptotic behavior requires an unsubtracted dispersion relation, but the effective pole would render precisely that variant unsuitable for a fit to the whole $e^+e^- \to \pi^0\gamma$ spectrum, as would be required for a reliable analytic continuation to the space-like region.

4.6.2 Space-like form factor

After the discussion of the time-like TFF, we start the analysis of the space-like doubly-virtual TFF

$$F_{\pi^0\gamma^*\gamma^*}(-Q_1^2,-Q_2^2) = F^{\text{disp}}_{\pi^0\gamma^*\gamma^*}(-Q_1^2,-Q_2^2) + F^{\text{eff}}_{\pi^0\gamma^*\gamma^*}(-Q_1^2,-Q_2^2) + F^{\text{asym}}_{\pi^0\gamma^*\gamma^*}(-Q_1^2,-Q_2^2) \tag{4.47}$$

by first comparing our result for the singly-virtual TFF with the once-subtracted dispersive representation employed in [231],

$$F_{\pi^0\gamma^*\gamma^*}(-Q^2,0) = F_{\pi\gamma\gamma} - \frac{Q^2}{\pi}\int_{s_{\text{th}}}^{\infty} \mathrm{d}s' \frac{\operatorname{Im} F_{\pi^0\gamma^*\gamma^*}(s',0)}{s'(s'+Q^2)}\,. \tag{4.48}$$

For this purpose, the singly-virtual form factor at low energies up to 3 GeV^2 is displayed in the form $Q^2 F_{\pi^0\gamma^*\gamma^*}(-Q^2,0)$ as a function of Q^2 in Figure 4.7, together with the experimental data from CELLO [396] and CLEO [397], where the total uncertainties are obtained by adding the statistical and systematic errors in quadrature.[6] Our theoretical uncertainty of the

[6] For the CELLO data, we directly take the uncertainties as given in [396] since systematic effects are not listed separately.

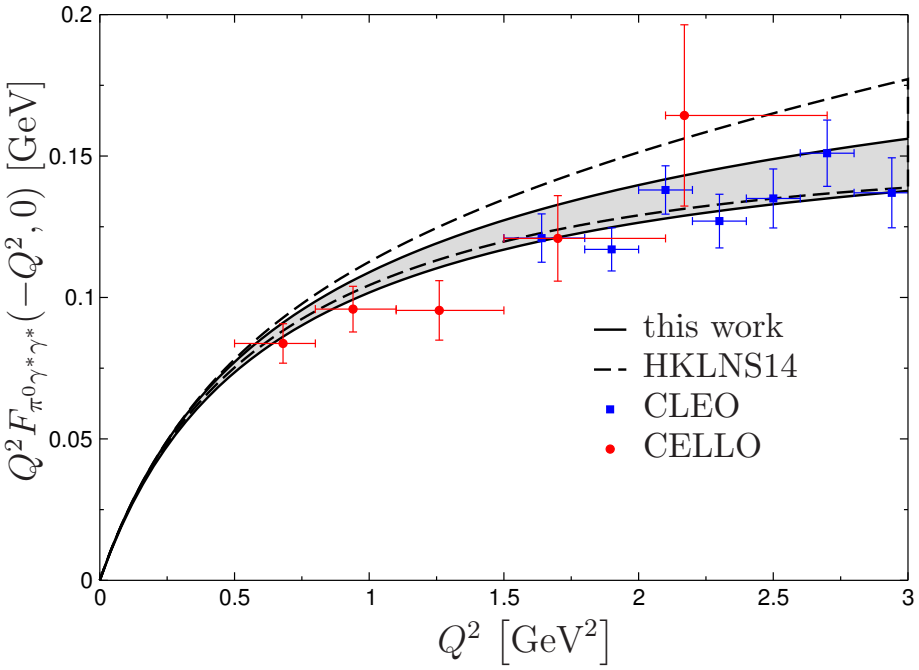

Figure 4.7: The singly-virtual form factors obtained in the current analysis (solid lines with gray uncertainty band) and from the once-subtracted representation [231] (HKLNS14, dashed lines) in the low-energy region, in comparison to CELLO [396] and CLEO [397] data.

singly-virtual form factor is estimated as the quadratic sum of the ±0.75% $F_{\pi\gamma\gamma}$ normalization uncertainty varying g_{eff}, the dispersive uncertainty, and the $^{+20}_{-10}$% BL uncertainty varying M_{eff}. Here, the dispersive error is defined as the maximum deviation from the central result found for different phase shifts and different pion vector form factors described in Section 4.3.1, n ranging from 3–6 in the fit of $a(q^2)$ to the $e^+e^- \to 3\pi$ cross section, and varying the integration cutoffs $\Lambda_{3\pi}$ and $\sqrt{s_{\text{iv}}}$ between (1.8–2.5) GeV. The resulting form factor depicted in solid lines is consistent with the available data and is close to the result obtained from the once-subtracted representation (4.48) in dashed lines at low energies below 1 GeV^2. At larger momenta the curves start to deviate, which is exactly expected from the matching of our representation to the correct high-energy behavior: the once-subtracted representation tends to show a linear behavior in the plot, whereas the unsubtracted form factor slowly converges to the BL limit.

Next, we update the low-energy parameters characterizing the singly-virtual TFF, most notably its radius

$$\begin{aligned} a_\pi &= \frac{M_{\pi^0}^2}{F_{\pi\gamma\gamma}} \frac{\partial}{\partial q^2} F_{\pi^0\gamma^*\gamma^*}(q^2, 0)\Big|_{q^2=0} \\ &= 31.5(2)_{F_{\pi\gamma\gamma}}(8)_{\text{disp}}(3)_{\text{BL}} \times 10^{-3} = 31.5(9) \times 10^{-3} \,. \end{aligned} \tag{4.49}$$

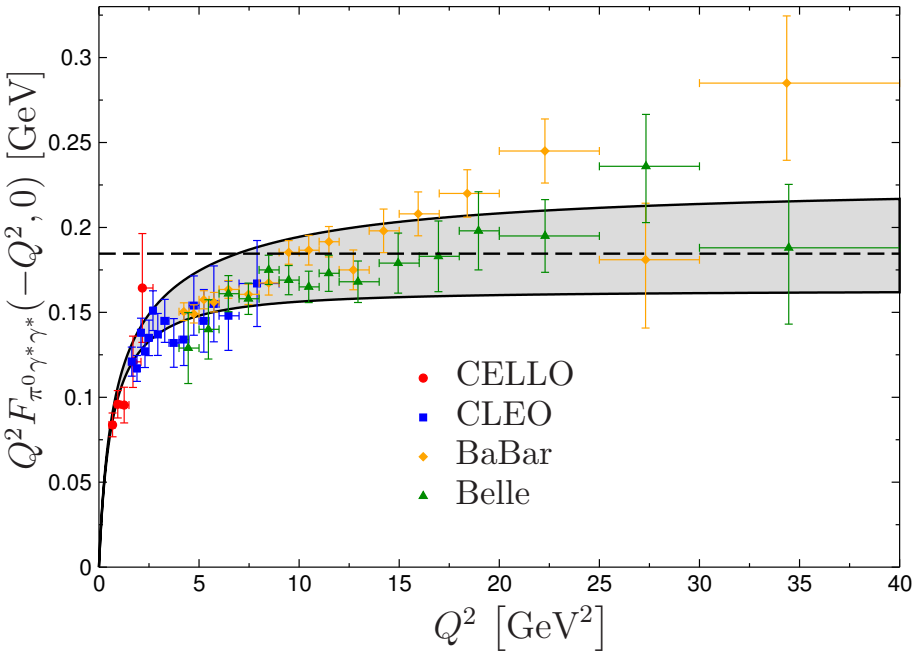

Figure 4.8: The singly-virtual form factor $Q^2 F_{\pi^0\gamma^*\gamma^*}(-Q^2,0)$ as a function of Q^2, in comparison to the experimental data [396–399]. The dashed horizontal line indicates the BL limit.

The increased value compared to $a_\pi = 30.7(6) \times 10^{-3}$ [231] traces back to the matching to the asymptotic behavior and corresponds to the fact that our form factor is slightly smaller than the once-subtracted TFF (4.48) as show in Figure 4.7. While fully consistent within uncertainties, the central value thus moves closer to the one derived from Padé approximants [317], $a_\pi = 32.4(2.2) \times 10^{-3}$, and also to the current experimental average $a_\pi^{\text{exp}} = 33.5(3.1) \times 10^{-3}$ [22], which is dominated by extractions from the Dalitz decay $\pi^0 \to e^+e^-\gamma$ [400] (compare also [401]) and the space-like CELLO data [396]. The dispersive approach continues to provide the most precise determination, due to the fact that other extractions are limited either by poor space-like data or the small kinematic region accessible in the Dalitz decay.

The next coefficient in the expansion around $q^2 = 0$ is evaluated as

$$\begin{aligned} b_\pi &= \frac{M_{\pi^0}^4}{F_{\pi\gamma\gamma}} \frac{1}{2} \frac{\partial^2}{\partial (q^2)^2} F_{\pi^0\gamma^*\gamma^*}(q^2,0)\Big|_{q^2=0} \\ &= 1.14(1)_{F_{\pi\gamma\gamma}}(4)_{\text{disp}}(1)_{\text{BL}} \times 10^{-3} = 1.14(4) \times 10^{-3}\,, \end{aligned} \tag{4.50}$$

where the overall uncertainty is entirely dominated by the dispersive one as expected for a low-energy parameter. The larger dispersive uncertainty compared to the result $1.10(2) \times 10^{-3}$ obtained in [231] partially originates from the fact that the uncertainty from the fits to the $e^+e^- \to 3\pi$ cross section using different variants of the conformal

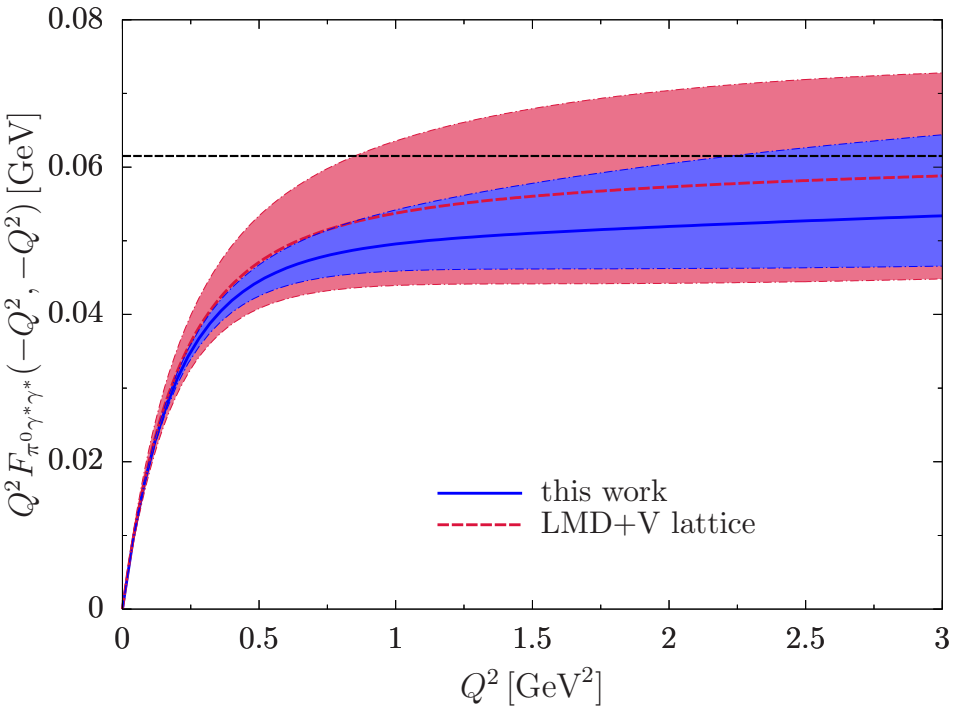

Figure 4.9: The diagonal form factor $Q^2 F_{\pi^0\gamma^*\gamma^*}(-Q^2,-Q^2)$ versus Q^2 at low energies (blue solid line with uncertainty band), compared to the LMD+V model fit to the lattice data [346] (red dashed line with uncertainty band). The black dashed line shows the OPE limit.

polynomials in the parameterization (2.16) is included in the dispersive one. However, the total uncertainty is still appreciably smaller e.g. compared to $1.06(26) \times 10^{-3}$ from [317].

The asymptotic behavior of the singly-virtual TFF $Q^2 F_{\pi^0\gamma^*\gamma^*}(-Q^2,0)$ at higher energies is shown in Figure 4.8, along with the BaBar and Belle measurements [398, 399] and the CELLO and CLEO data [396, 397] already included in Figure 4.7.[7] We find that the central value of our result almost matches the BL prediction, slowly approaching this limit from below. Although even fits including the BaBar data and using an energy threshold of $10\,\text{GeV}^2$ do not fully capture the rapid rise suggested by the BaBar data, our error band does cover all reasonably conceivable fit variants, see Section 4.5.3, which implies that the statistical significance of the last few BaBar data points does not suffice to drastically alter the fit results.

As the next step, we calculate the diagonal TFF $F_{\pi^0\gamma^*\gamma^*}(-Q^2,-Q^2)$ as another representative result for the doubly-virtual form factor. In the dispersive approach, the doubly-virtual diagonal form factor is completely determined by the singly-virtual inputs by virtue of its isospin structure. In particular, analyticity guarantees that the space-like form factor has

[7] We include the Q^2-independent error components of the systematic errors into the total uncertainties of BaBar and Belle [398, 399].

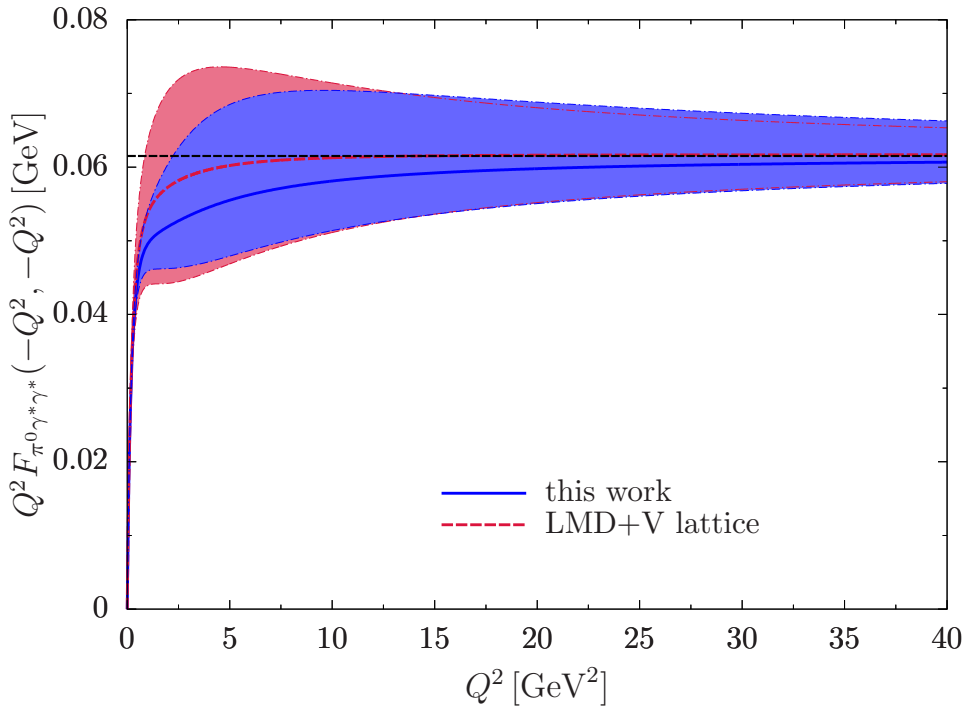

Figure 4.10: The diagonal form factor $Q^2 F_{\pi^0\gamma^*\gamma^*}(-Q^2,-Q^2)$ (blue solid line with uncertainty band), in comparison to the LMD+V model fit to the lattice data [346] (red dashed line with uncertainty band). The OPE limit of the form factor is indicated by the black dashed line.

to be a smooth function when matching to pQCD, even though it receives contributions from three different terms in (4.47), including the asymptotic contribution (4.35). The uncertainty in this asymptotic piece is estimated by varying the threshold parameter s_{m} in the range $(1.7 \pm 0.3)\,\mathrm{GeV}^2$, which ensures a smooth matching and coincides with the typical range found with LCSRs [376–379], see Section 4.4. It is then added quadratically to the other three sources of uncertainty already discussed in the context of the singly-virtual form factor.

The asymptotic behavior of the diagonal form factor is known rigorously from the OPE, see (4.28). In the absence of experimental measurements, our result given in the form $Q^2 F_{\pi^0\gamma^*\gamma^*}(-Q^2,-Q^2)$ in Figure 4.9 is compared to an LMD+V (lowest meson dominance + vector [370]) resonance model fit to lattice data extrapolated to the physical pion mass [346]. We find a slightly smaller diagonal form factor compared to the LMD+V model fit to lattice, otherwise observe consistency within the uncertainty bands. Similarly, the results for $Q^2 F_{\pi^0\gamma^*\gamma^*}(-Q^2,-Q^2)$ from our dispersive calculation and the lattice calculation of the TFF [346] at high energies up to $40\,\mathrm{GeV}^2$ are shown in Figure 4.10, again in agreement within uncertainties. Our central value approaches the OPE limit from below, which indicates a negative subleading $O(1/Q^4)$ contribution as obtained in [372]. The total

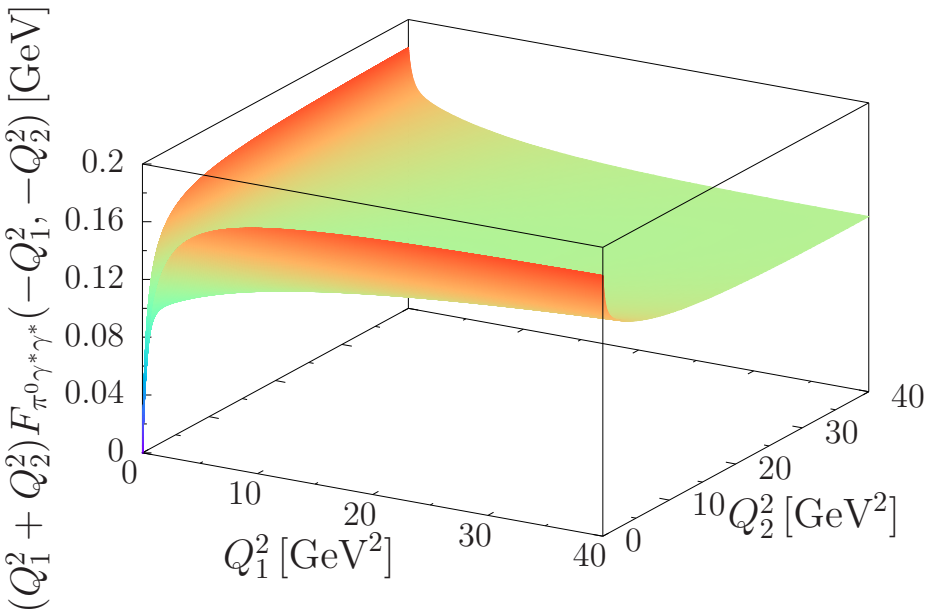

Figure 4.11: Three-dimensional representation of $(Q_1^2+Q_2^2)F_{\pi^0\gamma^*\gamma^*}(-Q_1^2,-Q_2^2)$ as a function of the photon virtualities.

uncertainty at low energy is largely dominated by the one from the normalization $F_{\pi\gamma\gamma}$, but the uncertainties from the BL limit and the asymptotic contribution start to compete at higher energies. Accordingly, the uncertainty bands of both analyses shrink to the central results at higher energies since they are suppressed as subleading terms in $O(1/Q^2)$ and both analyses are matched correctly to the leading OPE limit (4.28).

So far, we have shown the TFF for two special space-like kinematics to demonstrate consistency with experiment and lattice, respectively. However, the analysis is not complete since for $(g-2)_\mu$ we need the TFF as a function of two general photon virtualities. The full result, presented in the form $(Q_1^2+Q_2^2)F_{\pi^0\gamma^*\gamma^*}(-Q_1^2,-Q_2^2)$ as a function of Q_1^2 and Q_2^2, is depicted in Figure 4.11. The virtualities Q_1^2 and Q_2^2 cover broad ranges from low-energy to asymptotic regions of interest. The smooth transition and the correct high-energy behavior of the form factor in the entire kinematic domain are dictated by the analyticity of the form factor and the proper pQCD matching.

Finally, we compare the high-energy behavior of our dispersive representation (4.47) to the predictions of the asymptotic behavior from pQCD by analyzing the function $f(\omega)$ defined in (4.26) and (4.27). Its value encodes the asymptotic behavior of the TFF for arbitrary virtualities Q_1^2 and Q_2^2. $f(\omega)$ at the energy scale chosen as the highest accessible energy of the BaBar and Belle experiments [398, 399] is illustrated in the left diagram

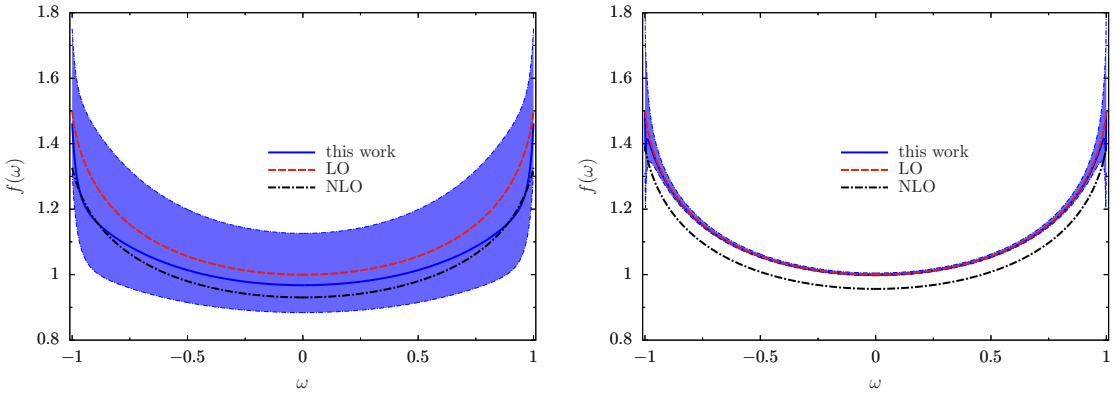

Figure 4.12: $f(\omega)$ obtained from the dispersive representation (4.47) (blue solid line with uncertainty band) calculated at $Q_1^2 + Q_2^2 = 35\,\text{GeV}^2$ (left) and at $Q_1^2 + Q_2^2 = 1.6 \times 10^3\,\text{GeV}^2$ (right), in comparison to $f(\omega)$ from the LO and NLO asymptotic pion distribution amplitudes $\phi_\pi(u) = 6u(1-u)$ (red dashed line) and (4.37) (black dot-dashed line).

of Figure 4.12. At these virtualities, our uncertainty band should safely cover most of the modifications to $f(\omega)$ from higher terms in the Gegenbauer-polynomial expansion as well as other proposed modifications of the pion distribution amplitude, as an example we show the α_s corrections (4.37). At very high energies, by construction, $f(\omega)$ obtained from the dispersive representation is nearly identical to the one obtained from the LO asymptotic pion distribution amplitude $\phi_\pi(u) = 6u(1-u)$, therefore ensuring the correct high-energy behavior of the form factor (see right diagram). In this case, since α_s vanishes only logarithmically, the NLO curve is not covered anymore by our uncertainty band, but such large virtualities are irrelevant for the $(g-2)_\mu$ integral. Moreover, a complete NLO matching would actually be disadvantageous, given that, by chance, for the relevant energy range our central curve, although matched to the LO amplitude asymptotically, comes out closer to the NLO prediction (see left diagram). We stress that Figure 4.12 merely demonstrates to which extent the TFF has approached the pQCD limit for a particular choice of photon virtualities, it does not provide additional insights into the pion distribution amplitude beyond its asymptotic form.

4.6.3 Consequences for a_μ

We now turn to the main application of the detailed analysis of the space-like doubly-virtual TFF presented in the preceding Section, the pion-pole contribution to a_μ. Evaluating the loop integrals in its definition (4.6) by means of the TFF representation (4.47), the final result reads

$$\begin{aligned} a_\mu^{\pi^0\text{-pole}} &= 63.0(0.9)_{F_{\pi\gamma\gamma}}(1.1)_{\text{disp}}\left(^{2.2}_{1.4}\right)_{\text{BL}}(0.6)_{\text{asym}} \times 10^{-11} \\ &= 63.0^{+2.7}_{-2.1} \times 10^{-11}\,. \end{aligned} \tag{4.51}$$

Here, the uncertainties from the numerical integration are negligible, in fact, we used both the standard variant (4.6) and a more symmetric parameterization of the integration region first suggested in [402] and subsequently implemented in [147, 148]. All uncertainties therefore derive from the TFF, with individual contributions estimated in close analogy to the previous Sections. First, the central value is defined by the average over all variants of the dispersive formalism, i.e. $\pi\pi$ phase shifts, cutoff parameters, parameterizations of the pion vector form factor, and the conformal polynomial, with the uncertainty defined as the maximum deviation from this average. The normalization uncertainty then reflects the final PrimEx result [287] for the π^0 decay width corresponding to an uncertainty of 0.75% in $F_{\pi\gamma\gamma}$, the BL error the uncertainty band from Figure 4.8, and the asymptotic error the impact of the variation of s_m in (4.35) according to $s_\mathrm{m} = (1.7 \pm 0.3)\,\mathrm{GeV}^2$. The quadratic sum of the four different sources of uncertainty defines our final estimate. Note that while this strategy is completely analogous to the corresponding error estimates discussed before for the time- and space-like TFF, due to the fact that the TFF enters squared in the integral it is critical to perform this error estimate for each source individually at the level of a_μ, using the total error band of the TFF instead would assume fully-correlated uncertainties and thereby overestimate the final error.

The decomposition (4.51) further suggests opportunities for future cross-checks and improvements. First, in comparison to the original published result, $a_\mu^{\pi^0\text{-pole}} = 62.6(1.7)_{F_{\pi\gamma\gamma}}(1.1)_\mathrm{disp}(^{2.2}_{1.4})_\mathrm{BL}(0.5)_\mathrm{asym} \times 10^{-11} = 62.6^{+3.0}_{-2.5} \times 10^{-11}$ [149, 150], the PrimEx-II measurement has already reduced the uncertainty in $F_{\pi\gamma\gamma}$ to 0.75% [287, 360], which translates to normalization and total uncertainties of 0.9 and $^{+2.7}_{-2.1} \times 10^{-11}$ in a_μ, respectively. Next, the dispersive uncertainties in particular in the low-energy space-like TFF could be cross-checked and potentially improved by upcoming data from BESIII [403], while the $F_{3\pi}$ low-energy theorem, used to normalize $a(q^2)$ in (2.17), is currently under study at COMPASS [404]. A conclusive measurement of the asymptotic singly-virtual TFF at Belle II [405, 406] would eliminate the systematic uncertainties from tensions between BaBar and Belle as well as the BL limit. In fact, simply taking the central fit to the full data base with $1\,\sigma$ uncertainties would formally reduce the BL error to 0.2×10^{-11} (with a central value of 63.1×10^{-11}), which emphasizes the fact that our result, at the level of accuracy quoted in (4.51), is insensitive to the tensions in the asymptotic behavior. Strictly speaking, all singly-virtual data on the space-like pion TFF [396–399] result from doubly-virtual measurements extrapolated to the point where one photon is on-shell. With our doubly-virtual TFF (4.47) at hand, agreement with data could be checked directly or our TFF could be used for the extrapolation. Also for this purpose, the values for radius (4.49) and curvature (4.50) might prove useful. Finally, absent doubly-virtual data it is not possible to reduce the pQCD uncertainties directly, but input from lattice QCD would allow one to further scrutinize this contribution.

Our central result (4.51) is compared to previous calculations in Table 4.3. For completeness, we have also provided references that consider an off-shell pion-exchange contribution, but emphasize that these results are model-dependent, corresponding to a particular choice

method	$a_\mu^{\pi^0\text{-pole}}$	$a_\mu^{\pi^0\text{-“exchange”}}$	$a_\mu^{\pi^0\text{-“const”}}$	reference
NJL model		81.8(16.5)		[335]
LMD+V		72(12)		[337]
holographic model		65.4(2.5)		[339]
Dyson–Schwinger equations		57.5(6.9)		[340]
nonlocal chiral quark model		50.1(3.7)		[341]
resonance chiral theory		65.8(1.2)		[342]
constituent chiral quark model		68(3)		[343]
resonance chiral theory		66.6(2.1)		[319]
LMD+V			78(10)	[138]
ENJL, VMD	59(9)			[307, 314]
VMD	57(6)			[310]
LMD+V	58(10)			[312]
lattice QCD, LMD+V fit	65.0(8.3)			[346]
rational approximants	63.6(2.7)			[159]
resonance chiral theory	58.1(9)			[345]
dispersion relations	$63.0^{+2.7}_{-2.1}$			this work

Table 4.3: Comparison to previous results for $a_\mu^{\pi^0\text{-pole}}$. The uncertainties are reproduced as given in the respective publication, see main text for further discussion. For completeness, we also list works that calculate contributions involving an off-shell pion instead (π^0-“exchange”) or put one of the form factors to a constant (π^0-“const”), but stress that these results either depend on the interpolator of the pion field or do not correspond to the dispersively defined pion pole, respectively, and therefore cannot be compared with the on-shell pion-pole contribution.

of the interpolating field. The wide spread among these results is therefore not surprising given that, in general, each model will represent a different such choice. Similarly, a model involving a constant TFF at the singly-virtual vertex in HLbL scattering [138] disagrees with the dispersive definition of the pion-pole contribution, so that the resulting number cannot be compared to ours either.

In the end, our central value is remarkably close to early estimates using hadronic models [307, 310, 312], either VMD, LMD+V, or the extended Nambu–Jona-Lasinio model, and falls within the quoted model errors that had been typically estimated at the level of 15%.

Recent updates in resonance chiral theory [345] find similar values, however, without an attempt to quantify the model uncertainty. Our central value is even closer to a calculation of the pion pole using a TFF constructed from rational approximants, with parameters determined from $\pi^0 \to \gamma\gamma$ and space-like singly-virtual data [159]. The quoted error contains the propagated uncertainties from the data input and estimates of the systematics of the approach by comparing different approximants and varying a parameter that describes doubly-virtual kinematics within a certain range. In this respect, the main advantages of the dispersive approach concern the fact that also data from the time-like region can be used, as illustrated by the key role of the $e^+e^- \to 3\pi$ data in our analysis; that the sensitivity to the space-like input is significantly reduced in comparison, removing the systematic uncertainty from the asymptotic behavior of the TFF; and that the doubly-virtual dependence is actually predicted within the formalism, eliminating the need for an extrapolation of the singly-virtual input to doubly-virtual kinematics. Further, we have provided an economical way to implement all short-distance constraints, which is not straightforward to achieve in hadronic models, e.g. the LMD+V model fails to produce the correct asymptotics for small but finite q_1^2 and $q_2^2 \to \infty$. Finally, our result also agrees with a calculation in lattice QCD [346]. Currently, an LMD+V ansatz is required to extend the lattice data to the full range of virtualities to perform the $(g-2)_\mu$ integral, but future updates at higher statistics are set to provide a sufficiently fine grid to enable a direct comparison to (4.51) in a fully model-independent way.

4.7 Conclusions and outlook

In this Chapter we presented a comprehensive dispersive reconstruction of the doubly-virtual pion TFF, which determines the residue of the pion-pole contribution to a_μ. As a first step, dispersion relations for the pion TFF were derived based on its isospin structure and unitarity relation, wherein the 2π and 3π intermediate states define the low-lying singularities in the isovector and isoscalar virtualities, respectively. As a consequence, the doubly-virtual pion TFF was reconstructed in light of the low-energy theorems for $F_{\pi\gamma\gamma}$ and $F_{3\pi}$, the $\pi\pi$ P-wave phase shifts from Roy- and Roy-like equations, and experimental input from $e^+e^- \to 2\pi, 3\pi$. Extending previous work, we achieved an improved description of the $e^+e^- \to 3\pi$ cross section data after introducing a conformal polynomial to take into account the inelastic effects in the 3π channel. Starting from the unsubtracted dispersion relation (4.19), the double-spectral representation (4.22) was derived afterwards as a convenient representation for the evaluation of the pion-pole $(g-2)_\mu$ loop integrals.

Another key advance in this Chapter concerns the consistent matching to constraints from pQCD. To this end, the LO leading-twist light-cone expansion (4.24) was reformulated in terms of an asymptotic double-spectral density, which leads to an asymptotic contribution (4.35) governing the correct high-energy behavior of the TFF for non-vanishing virtualities. We evaluated the known α_s corrections but found them to be negligible within uncertainties. As the final step, we introduced an effective pole term to remedy the normal-

ization of the form factor and account for constraints from space-like singly-virtual data measured in $e^+e^- \to e^+e^-\pi^0$. The validity of the dispersive approach was cross-checked by comparing the dispersive prediction for $e^+e^- \to \pi^0\gamma$ based on the time-like singly-virtual TFF to cross section data. We found good agreement up to 1 GeV, with deviations starting to appear in the vicinity of the ϕ resonance, right where the phase space for inelastic contributions in the $e^+e^- \to 3\pi$ fit was assumed to open. We studied the resulting space-like TFF (4.47) extensively both for singly- and doubly-virtual kinematics, in comparison to experimental data, lattice-QCD calculations, and theoretical predictions from pQCD.

This detailed study of the pion TFF, incorporating all the low-lying singularities and the correct high-energy behavior at $O(1/Q^2)$, culminates in the first dispersive determination of the pion-pole contribution to the muon $(g-2)_\mu$ (4.51), the lowest intermediate state in a dispersive approach to HLbL scattering. Most prominently, (4.51) determines the final number of the data-driven and dispersive evaluations of the pion-pole contribution to HLbL scattering in the white paper [61]. Our data-driven evaluation produces a central value in line with previous model-dependent estimates, but provides for the first time a determination that fully exploits the constraints from the fundamental principles of analyticity, unitarity, and crossing symmetry as well as the predictions from pQCD in deriving well-controlled uncertainty estimates. In fact, despite being already sufficient for a SM prediction of a_μ at the level of the upcoming experiments, these uncertainties can be reduced further by virtue of future more precise singly-virtual measurements both in low- and high-energy regimes.

As the largest individual piece, our determination of the pion-pole contribution to a_μ is a critical step towards a complete data-driven evaluation of HLbL scattering [142–146]. Moreover, the strategies developed here regarding the incorporation of high-energy constraints will facilitate similar studies of the η and η' TFFs [407–411], thus paving the way towards a fully data-driven determination of all light pseudoscalar-meson-pole contributions to HLbL scattering in $(g-2)_\mu$.

Part III

Decays of the neutral pion

Chapter 5

Neutral pion and its decay $\pi^0 \to e^+e^-$

5.1 Introduction

The neutral pion is the lightest hadron, with a mass of 134.9768(5) MeV [22]. This is in close relation to chiral symmetry breaking of QCD, where pions emerge as the (approximate) Goldstone bosons of the broken sector. Its mean life is $8.52(18) \times 10^{-17}$ s [22], which is a typical lifetime of particles that undergo electromagnetic decays. Most of the experiments measure the decay width of the neutral pion, which is then converted to the lifetime. But there are also direct measurements of its lifetime [412]. The quantum numbers of the π^0 are given as

$$I^G(J^{PC}) = 1^-(0^{-+}) \,. \tag{5.1}$$

As a consequence of the aforementioned properties, its main decay modes are all of electromagnetic nature [413–415]. Furthermore, these decays are closely related to the pion TFF that we have extensively discussed in Chapter 4. We list them in Table 5.1, which will be discussed in the following Sections.

5.1.1 $\pi^0 \to \gamma\gamma$

The largest decay channel $\pi^0 \to \gamma\gamma$ covers nearly 99% of the total width. It is induced by the famous chiral anomaly [111–113], which would otherwise be suppressed due to the Sutherland theorem [416]. The pertinent matrix element can be written as

$$\mathcal{M} = e^2 \varepsilon^{\mu\nu\rho\sigma} q_{1\mu} \epsilon^*_{1\nu} q_{2\rho} \epsilon^*_{2\sigma} F_{\pi^0\gamma^*\gamma^*}(0,0) \,, \tag{5.2}$$

where $F_{\pi^0\gamma^*\gamma^*}$ is the neutral pion TFF. The decay width reads

$$\begin{aligned} \Gamma(\pi^0 \to \gamma\gamma) &= \frac{1}{2} \frac{|\boldsymbol{q}_f|}{8\pi M^2_{\pi^0}} \sum_{\text{spins}} |\mathcal{M}|^2 = \frac{1}{32\pi M_{\pi^0}} \cdot \frac{e^4 M^4_{\pi^0}}{2} \left| F_{\pi^0\gamma^*\gamma^*}(0,0) \right|^2 \\ &= \frac{\pi\alpha^2 M^3_{\pi^0}}{4} \left| F_{\pi^0\gamma^*\gamma^*}(0,0) \right|^2 , \end{aligned} \tag{5.3}$$

Decay modes	$\pi^0 \to \gamma\gamma$	$\pi^0 \to e^+e^-\gamma$	$\pi^0 \to e^+e^-e^+e^-$	$\pi^0 \to e^+e^-$
Branching ratios	98.82%	1.17%	3.34×10^{-5}	6.46×10^{-8}

Table 5.1: Main decay channels and their fractions of the neutral pion.

where $\boldsymbol{q}_f$ is the final state momentum of the two photons. Using the lowest-order result of the pion TFF in ChPT ($O(q^4)$) given in (3.2) and (4.12) obtained from the Wess–Zumino–Witten effective Lagrangian (1.61), we find

$$\Gamma(\pi^0 \to \gamma\gamma) = \frac{\alpha^2 M_{\pi^0}^3}{64\pi^3 F_\pi^2} = 7.75(2)\,\text{eV}\,, \tag{5.4}$$

where the uncertainty stems solely from the pion decay constant $F_\pi = 92.28(10)$ MeV [22].

Equation (5.4) is exact in the chiral limit without any free parameters, where the pion decay constant at this order can be set to its physical value F_π. Nevertheless, chiral symmetry is explicitly broken by the masses of u and d quarks. In the framework of ChPT, one-loop corrections to (5.4) were performed later and found that there is no chiral logarithm [288, 417]; electromagnetic and higher-order chiral corrections were obtained more recently [289–291]. This leads to a common observation of about 4.5% enhancement with respect to the leading chiral decay width (5.4). A QCD sum rule approach [418] found a similar result. The achievement of the theoretical predictions at a level of 1% uncertainty makes it a hallmark process to test the firm QCD prediction in the anomaly sector.

On the experimental side, there are several different techniques to determine the lifetime. First of them is the already mentioned direct measurement, which utilizes highly boosted pion beams [412]. Indirect measurements can be performed firstly by measuring the cross section $e^+e^- \to e^+e^-\pi^0$ at colliders [419]. We can also connect the weak vector form factor of the charged pion to the lifetime of the neutral pion based on the conserved vector-current hypothesis and isospin symmetry [420]. At last, most precise measurements rely on the Primakoff effect, where high-energy photons interact with an atomic nucleus to produce neutral pions. The PrimEx measurement [359] has tested the $\pi^0 \to \gamma\gamma$ decay width up to 2.8%. In combination with the newest PrimEx-II experiment [287], the final result has reached an uncertainty of 1.5%.

The comparison of theory calculations and experimental measurements is shown in Figure 5.1. We find a systematic discrepancy between them, for which the potential reasons need to be identified. In particular, the cutting-edge measurement [287] reaffirms the tension with the higher-order corrections to the decay width.

5.1.2 $\pi^0 \to e^+e^-\gamma$

The $\pi^0 \to e^+e^-\gamma$ channel comprises again more than 99% of the remaining decay width after $\pi^0 \to \gamma\gamma$. This is the Dalitz decay mode named after Richard Dalitz [421], who first

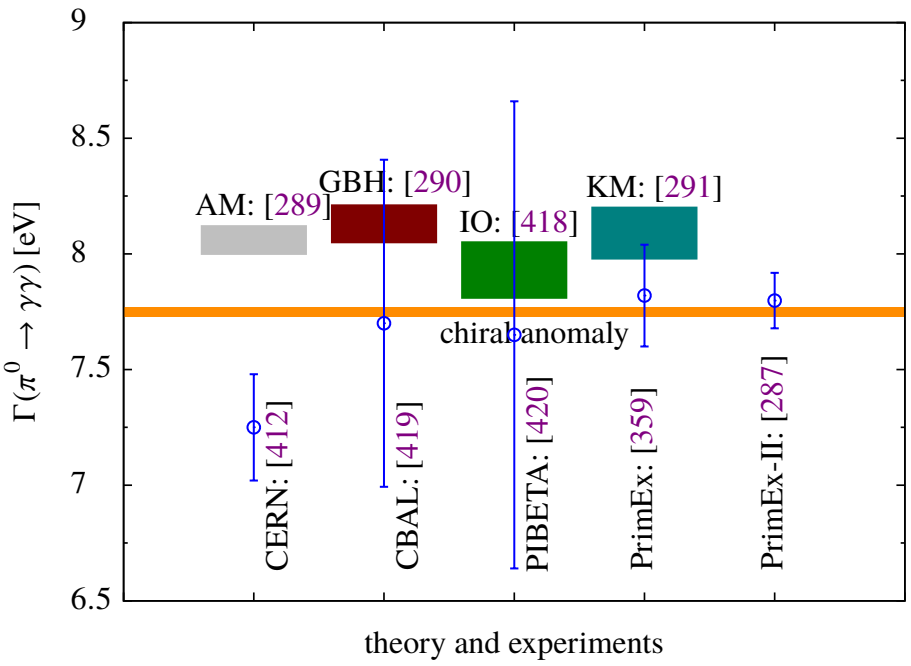

Figure 5.1: The comparison of theory and experiments.

established the connection of this decay to the two-photon decay. Its differential decay width normalized to the two-photon decay is given by

$$\frac{\mathrm{d}\Gamma(\pi^0 \to e^+e^-\gamma)}{\mathrm{d}q^2\Gamma(\pi^0 \to \gamma\gamma)} = \frac{2\alpha}{3\pi}\frac{1}{q^2}\sqrt{1-\frac{4m_e^2}{q^2}}\left(1+\frac{2m_e^2}{q^2}\right)\left(1-\frac{q^2}{M_{\pi^0}^2}\right)^3\left|\frac{F_{\pi^0\gamma^*\gamma^*}(q^2,0)}{F_{\pi^0\gamma^*\gamma^*}(0,0)}\right|^2 . \tag{5.5}$$

The kinematical accessible range of the electron–positron invariant mass squared q^2 varies between $4m_e^2 < q^2 < M_{\pi^0}^2$ so that the following approximation is valid for the pion TFF in this region,

$$\frac{F_{\pi^0\gamma^*\gamma^*}(q^2,0)}{F_{\pi^0\gamma^*\gamma^*}(0,0)} \approx 1 + a_\pi\frac{q^2}{M_{\pi^0}^2} + b_\pi\frac{q^4}{M_{\pi^0}^4} . \tag{5.6}$$

Using (4.49) and (4.50) from [150], we find the prediction[1]

$$\frac{\Gamma(\pi^0 \to e^+e^-\gamma)}{\Gamma(\pi^0 \to \gamma\gamma)} = 1.18760(8)\times 10^{-2} , \tag{5.7}$$

[1] This result is derived only from the form factor calculation without addressing the issue of radiative corrections [422].

which is in excellent agreement with the experimental value [22]

$$\left.\frac{\Gamma(\pi^0 \to e^+e^-\gamma)}{\Gamma(\pi^0 \to \gamma\gamma)}\right|_{\text{exp}} = 1.188(34) \times 10^{-2} \,. \tag{5.8}$$

5.1.3 $\pi^0 \to e^+e^-e^+e^-$

The four-electron decay $\pi^0 \to e^+e^-e^+e^-$ is called the double Dalitz decay, which involves the doubly-virtual pion TFF. However, the dependence of the decay rate on the pion TFF is very weak. Its matrix element is usually divided into a direct and an exchange term. Consequently, the interference between these two terms also needs to be considered when calculating the decay rate [414, 423–426].

The final-state photons should carry away the negative parity of the neutral pion in the decay $\pi^0 \to \gamma\gamma$. However, it is impossible to directly measure the polarization vectors of real photons to determine the neutral pion's parity. Therefore, its parity was only indirectly confirmed by slow negative pions captured in deuterium. But the double Dalitz decay $\pi^0 \to e^+e^-e^+e^-$ provides a direct measurement to confirm the parity of the π^0 [427].

The simplest wavefunctions that describe the two-photon system with even exchange symmetry can be constructed as [428]

$$\begin{aligned} \psi_1(2\gamma) &= A(\boldsymbol{\epsilon}_1 \cdot \boldsymbol{\epsilon}_2) \propto \cos\phi \,, \\ \psi_2(2\gamma) &= B(\boldsymbol{\epsilon}_1 \times \boldsymbol{\epsilon}_2) \cdot \boldsymbol{k} \propto \sin\phi \,, \end{aligned} \tag{5.9}$$

where $\boldsymbol{\epsilon}_1$ and $\boldsymbol{\epsilon}_2$ are the polarization vectors of two photons ($\boldsymbol{E}$-vectors) and $\boldsymbol{k}$ is the momentum of either photon in the pion rest frame. ϕ is the angle between the polarization planes. ψ_1 is a scalar quantity and therefore even under spatial inversion. On the other hand, ψ_2 is odd under spatial inversion, where the $\boldsymbol{E}$-vectors of the two photons are orthogonal. Since the plane of each electron pair is predominantly in that of the $\boldsymbol{E}$-vector, the measurement of the relative angle between the planes of pairs can infer the parity of π^0 [429, 430]. Apart from the confirmation of parity, this decay also sets constraints on CPT violation.

5.1.4 Rare π^0 decays

$\pi^0 \to e^+e^-$ is a loop- and helicity-suppressed decay, which we will discuss in Section 5.2. In addition to the main decay channels discussed above, there is also a fifth electromagnetic decay mode, $\pi^0 \to 4\gamma$, which is dominated by the electromagnetic "photon-photon splitting" mechanism. Its calculations in ChPT and other models were performed in [431–434]. Besides, there are also weak decays $\pi^0 \to \nu\bar{\nu}$ in the SM with extended massive neutrinos.

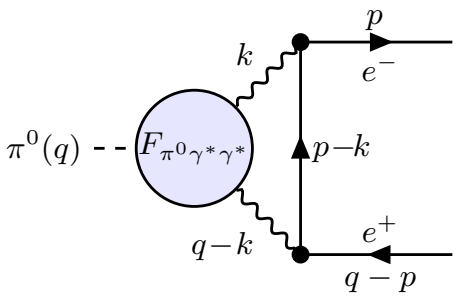

Figure 5.2: Decay $\pi^0 \to e^+e^-$.

5.2 Rare leptonic decay $\pi^0 \to e^+e^-$

The electromagnetic decay $\pi^0 \to e^+e^-$ plays an important role in the test of the long-distance dynamics of the strong interaction. The rareness of this decay because of the loop and the helicity suppression also raises the potential sensitivity to BSM physics. The very first calculation of it was performed already in 1959 [435]. Since then, plenty of developments have been made in the context of modeling of the vertex [436–439], models for the TFF [348, 440, 441], and ChPT and large-N_c QCD [347, 351].

Recently, this decay has drawn revived theoretical interests because of a precise determination of its branching ratio by the KTeV E799-II experiment at Fermilab [442],

$$B(\pi^0 \to e^+e^-(\gamma), x_D > 0.95) = 6.44(25)(22) \times 10^{-8}\,, \tag{5.10}$$

where

$$x_D = \frac{m^2_{e^+e^-}}{M^2_{\pi^0}} = 1 - 2\frac{E_\gamma}{M_{\pi^0}} \tag{5.11}$$

is the Dalitz variable. Recent theoretical predictions [352–356, 358] deviate from this measurement by around $3\,\sigma$.[2] On the other hand, the renewed analyses of radiative corrections [349, 350] suggest values closer to the experiment. With this background, we present here another formalism to revisit this rare decay by means of the double-spectral representation of the pion TFF applied in Chapter 4. To this end, the reduced amplitude of the decay is firstly derived in Section 5.2.1. Thereafter, the unitarity bound of this decay is shown in Section 5.2.2. The further expression of the reduced amplitude in terms of the double-spectral representation of the pion TFF is derived in 5.2.3, after which a short summary is drawn.

5.2.1 Derivation of the reduced amplitude

The lowest-order QED contribution to $\pi^0 \to e^+e^-$ as illustrated in Figure 5.2 involves the transition of the neutral pion to two virtual photons and, thus, it is determined by the

[2] See [443] for a recent lattice QCD calculation.

doubly-virtual TFF $F_{\pi^0\gamma^*\gamma^*}$ of the neutral pion. The relevant matrix element respecting Lorentz covariance, charge conjugation, and parity is given as [349, 444, 445]

$$i\mathcal{M} = P(m_e^2, m_e^2, q^2)\bar{u}(p, s_-)\gamma^5 v(q-p, s_+)\,, \tag{5.12}$$

where m_e is the electron mass, $q^2 = M_{\pi^0}^2$, and the projection

$$P(m_e^2, m_e^2, q^2) = -\lim_{\substack{p^2\to m_e^2\\(q-p)^2\to m_e^2}} \frac{1}{2q^2}\,\mathrm{tr}\left[(\not{p}+m_e)\Gamma_{\pi^0 e^+e^-}(\not{q}-\not{p}-m_e)\gamma^5\right]. \tag{5.13}$$

$\Gamma_{\pi^0 e^+e^-}$ is the one-particle irreducible $\pi^0 e^+e^-$ vertex. The decay width reads then

$$\begin{aligned}\Gamma(\pi^0\to e^+e^-) &= \frac{|\boldsymbol{p}_f|}{8\pi M_{\pi^0}^2}\sum_{\text{spins}}|\mathcal{M}|^2\\ &= \frac{|\boldsymbol{p}_f|}{8\pi M_{\pi^0}^2}\,\mathrm{tr}\left[-(\not{p}+m_e)\gamma^5(\not{q}-\not{p}-m_e)\gamma^5\right]\left|P(m_e^2,m_e^2,q^2)\right|^2\\ &= \frac{|\boldsymbol{p}_f|}{8\pi M_{\pi^0}^2}\cdot 2M_{\pi^0}^2\left|P(m_e^2,m_e^2,q^2)\right|^2 = \frac{M_{\pi^0}\beta}{8\pi}\left|P(m_e^2,m_e^2,q^2)\right|^2,\end{aligned} \tag{5.14}$$

where $\beta = \sqrt{1-4m_e^2/M_{\pi^0}^2}$ is the velocity of the outgoing electron–positron pair in the center-of-mass frame.

The vertex $\Gamma_{\pi^0 e^+e^-}$ reads at lowest order

$$i\Gamma_{\pi^0 e^+e^-} = -ie^4\varepsilon^{\mu\nu\rho\sigma}\int\frac{\mathrm{d}^4k}{(2\pi)^4}F_{\pi^0\gamma^*\gamma^*}(k^2,(q-k)^2)\frac{k_\rho(q-k)_\sigma\gamma_\mu(\not{p}-\not{k}+m_e)\gamma_\nu}{k^2(q-k)^2[(p-k)^2-m_e^2]}\,. \tag{5.15}$$

By virtue of the projection (5.13), we find

$$\begin{aligned}P(m_e^2,m_e^2,q^2) &= \frac{4im_e e^4}{q^2}\int\frac{\mathrm{d}^4k}{(2\pi)^4}\frac{q^2k^2-(q\cdot k)^2}{k^2(q-k)^2[(p-k)^2-m_e^2]}F_{\pi^0\gamma^*\gamma^*}(k^2,(q-k)^2)\\ &= 2m_e\alpha^2\frac{2i}{\pi^2q^2}\int\mathrm{d}^4k\frac{q^2k^2-(q\cdot k)^2}{k^2(q-k)^2[(p-k)^2-m_e^2]}F_{\pi^0\gamma^*\gamma^*}(k^2,(q-k)^2)\,.\end{aligned} \tag{5.16}$$

Using (5.3), the normalized branching ratio to the two-photon decay becomes

$$R = \frac{\Gamma(\pi^0\to e^+e^-)}{\Gamma(\pi^0\to\gamma\gamma)} = 2\left(\frac{\alpha m_e}{\pi M_{\pi^0}}\right)^2\beta\left|\mathcal{A}(q^2)\right|^2, \tag{5.17}$$

where the *reduced amplitude* is given by

$$\mathcal{A}(q^2) = \frac{2i}{\pi^2 q^2} \int \mathrm{d}^4k \frac{q^2k^2 - (q\cdot k)^2}{k^2(q-k)^2[(p-k)^2 - m_e^2]} \tilde{F}_{\pi^0\gamma^*\gamma^*}(k^2, (q-k)^2) \,. \tag{5.18}$$

$\tilde{F}_{\pi^0\gamma^*\gamma^*}(q_1^2, q_2^2) = F_{\pi^0\gamma^*\gamma^*}(q_1^2, q_2^2)/F_{\pi\gamma\gamma}$ in the expression of the reduced amplitude (5.18) is the normalized pion TFF.

5.2.2 Unitarity bound

Due to the smallness of the π^0 mass, no on-shell hadronic intermediate states contribute to the imaginary part of the reduced amplitude $\mathcal{A}(q^2)$ (this is not true any more for the dileptonic decays of η and η', where hadronic intermediate states contribute [357]). Therefore, the $\gamma\gamma$ intermediate-state cuts generate the only relevant imaginary part. The corresponding discontinuity of the reduced amplitude reads

$$\begin{aligned}\operatorname{disc}\mathcal{A}(q^2) =& \frac{2i}{\pi^2 q^2} \int \mathrm{d}^4k \frac{q^2k^2 - (q\cdot k)^2}{(p-k)^2 - m_e^2} \tilde{F}_{\pi\gamma^*\gamma^*}(k^2, (q-k)^2) \\ & \times (-2\pi i)\theta(k_0)\delta(k^2)(-2\pi i)\theta(q_0 - k_0)\delta[(q-k)^2] \\ =& \frac{\pi i}{\beta} \ln\left(\frac{1-\beta}{1+\beta}\right) \,. \end{aligned} \tag{5.19}$$

Therefore,

$$\operatorname{Im}\mathcal{A}(q^2) = \frac{\pi}{2\beta} \ln\left(\frac{1-\beta}{1+\beta}\right) \,, \tag{5.20}$$

which is a model-independent prediction. Using the property $\left|\mathcal{A}(q^2)\right| \geq \left|\operatorname{Im}\mathcal{A}(q^2)\right|$, we find the unitarity bound [436]

$$R \geq \frac{1}{2\beta} \left(\frac{\alpha m_e}{M_{\pi^0}}\right)^2 \ln^2\left(\frac{1-\beta}{1+\beta}\right) = 4.7 \times 10^{-8} \,. \tag{5.21}$$

Although the imaginary part dominates the decay width by comparison to the experiment, the real part also plays an indispensable role for an accurate theoretical prediction.

The reduced amplitude (5.18) is logarithmically divergent for a constant form factor $\tilde{F}_{\pi^0\gamma^*\gamma^*}$. In reality, the asymptotic behavior of the physical form factor renders the integral convergent. Some works [352, 437, 441] suggested to obtain the real part of the amplitude (5.18) dispersively from its imaginary one (5.20),

$$\begin{aligned}\operatorname{Re}\mathcal{A}(q^2) =& \mathcal{A}\left(q^2 = 0\right) + \frac{q^2}{\pi} \mathcal{P} \int_0^\infty \mathrm{d}s \frac{\operatorname{Im}\mathcal{A}(s)}{s(s-q^2)} \\ =& \mathcal{A}(q^2 = 0) + \frac{1}{\beta}\left[\frac{1}{4}\ln^2\left(\frac{1-\beta}{1+\beta}\right) + \frac{\pi^2}{12} + \mathrm{Li}_2\left(\frac{-1+\beta}{1+\beta}\right)\right], \end{aligned} \tag{5.22}$$

where the non-trivial dynamics is now absorbed in the subtraction constant $\mathcal{A}(q^2 = 0)$. This kind of approach is easily connected to the ChPT calculations [347, 351]. Nonetheless, a dispersion relation in terms of the pion mass squared q^2 would raise the potential issues of a not well-defined form factor in (5.18) for $q^2 \neq M_{\pi^0}^2$ and also additional disregarded contributions to the imaginary part (5.20) for large q^2.

5.2.3 Reduced amplitude with double-spectral representation

We have constructed a double-spectral representation for the pion TFF in Chapter 4, which is conveniently applied to the pion-pole contribution to HLbL scattering in the muon $(g-2)_\mu$. For the normalized pion TFF, it reads

$$\tilde{F}_{\pi^0\gamma^*\gamma^*}(q_1^2, q_2^2) = \frac{1}{\pi^2}\int_0^\infty \mathrm{d}x \int_0^\infty \mathrm{d}y \frac{\tilde{\rho}(x,y)}{(x-q_1^2)(y-q_2^2)}\,, \tag{5.23}$$

where $\tilde{\rho}(x,y)$ is the normalized double-spectral density. In the scenario for dileptonic decays, the evaluation of the loop integral (5.18) employing a Cauchy integral representation for the factorized TFF was initiated in [357]. In the same vein, we use the double dispersion relation for the TFF to express the reduced amplitude $\mathcal{A}(q^2)$ as [445]

$$\mathcal{A}(q^2) = \frac{1}{\pi^2}\int_0^\infty \mathrm{d}x \int_0^\infty \mathrm{d}y\, \tilde{\rho}(x,y) K(x,y)\,, \tag{5.24}$$

where

$$K(x,y) = \frac{2i}{\pi^2 q^2}\int \mathrm{d}^4k \frac{q^2k^2 - (q\cdot k)^2}{k^2(q-k)^2[(p-k)^2 - m_e^2](k^2-x)[(q-k)^2-y]} \tag{5.25}$$

represents the reduced amplitude $\mathcal{A}(q^2)$ for a VMD form factor with masses x and y, of which the contribution is then weighted by the double-spectral density $\tilde{\rho}(x,y)$ for two virtualities.

The calculation of the function $K(x,y)$ can be performed using the reduction technique [446] to express it in terms of the standard one-loop functions [447],

$$\begin{aligned}
K(x,y) = {} & \frac{1}{2q^2x}\left[B_0(m_e^2, m_e^2, x) - B_0(m_e^2, 0, m_e^2)\right] + (x \leftrightarrow y) \\
& + \frac{C_0(m_e^2, m_e^2, q^2, 0, m_e^2, y) - C_0(m_e^2, m_e^2, q^2, x, m_e^2, y)}{x} + (x \leftrightarrow y) \\
& + \frac{y\,C_0(m_e^2, m_e^2, q^2, x, m_e^2, y) - y\,C_0(m_e^2, m_e^2, q^2, 0, m_e^2, y)}{2q^2x} + (x \leftrightarrow y) \\
& - \frac{C_0(m_e^2, m_e^2, q^2, x, m_e^2, y)}{q^2} + \frac{q^2C_0(m_e^2, m_e^2, q^2, 0, m_e^2, 0)}{2xy} - \frac{q^2C_0(m_e^2, m_e^2, q^2, 0, m_e^2, x)}{2xy} \\
& - \frac{q^2C_0(m_e^2, m_e^2, q^2, 0, m_e^2, y)}{2xy} + \frac{q^2C_0(m_e^2, m_e^2, q^2, x, m_e^2, y)}{2xy}\,,
\end{aligned} \tag{5.26}$$

where

$$B_0(m_e^2, m_e^2, x) = \int \frac{\mathrm{d}^4k}{i\pi^2} \frac{1}{[(p-k)^2 - m_e^2](k^2 - x)} \tag{5.27}$$

with $p^2 = m_e^2$ and

$$C_0(m_e^2, m_e^2, q^2, x, m_e^2, y) = \int \frac{\mathrm{d}^4k}{i\pi^2} \frac{1}{[(p-k)^2 - m_e^2](k^2 - x)[(q-k)^2 - y]} \tag{5.28}$$

with $p^2 = (q-p)^2 = m_e^2$ are the standard Passarino–Veltman [446] scalar one-loop integrals. The reduction to these standard integrals should prove convenient for the numerical evaluation of the dispersive TFF with the double-spectral representation [445].

5.2.4 Summary and outlook

In this Section, we have presented a formalism to reexamine the rare leptonic decay $\pi^0 \to e^+e^-$ based on a double-spectral representation of the pion TFF.

First of all, the derivation of the reduced amplitude $\mathcal{A}(q^2)$ was reviewed. The unitarity bound for the decay stemming from the two-photon cut was then calculated and the corresponding limit was determined. At last, the loop integral of the reduced amplitude corresponding to the TFF that fulfills a double-spectral representation was expressed in terms of the standard one-loop functions.

One may ask why not directly evaluate the integral of the reduced amplitude (5.18) using the available space-like TFF that was already applied to the pion-pole contribution in Chapter 4? Unfortunately, the TFF entering the reduced amplitude not only concerns the space-like, but also the time-like region. Therefore, the form factor has to be analytically continued to complex variables if we would first perform a Wick rotation. Apart from the strategies for the double-spectral representation already developed in Chapter 4, the numerical treatment of (5.24) suggested in Section 5.2.3 poses additional challenges as the pseudothreshold singularities in the dispersive double-spectral density of (4.22) must be properly treated to obtain a stable numerical result. Besides, we should also correctly deal with the singular double-spectral density (4.33) of the pion TFF arising from the asymptotic region.

To conclude, our approach facilitates a suitable numerical treatment for the dispersively constructed TFF, for which future work is still in progress.

Chapter 6

Conclusion

In this thesis, we have investigated the hadronic effects at the precision frontier of the Standard Model in two different fields—the hadronic contributions to the anomalous magnetic moment of the muon $(g-2)_\mu$ and the rare dilepton decay $\pi^0 \to e^+e^-$. We aimed to describe the contributing hadronic interactions and effects model-independently and precisely by combining fundamental principles of the S-matrix, dispersion relations, low-energy theorems of quantum chromodynamics (QCD), and perturbative QCD.

Our studies of both hadronic-vacuum-polarization (HVP) and hadronic-light-by-light-scattering (HLbL) corrections to the muon $(g-2)_\mu$ have been largely acknowledged by the "Muon $g-2$ Theory Initiative" white paper [61]. For the 3π channel, our analysis enabled us to provide another independent check for the 3π HVP contribution with a global fit function fulfilling QCD constraints, complementary to strategies based on direct integration of the data. Meanwhile, the comparison between different approaches helped to resolve the persistent tension among [131] and [132]. Together with [131–133, 135, 136], our result was adopted by the merging of model-independent HVP results in the white paper [61], culminated in the final HVP number (1.59).

Following the same spirit, we studied the contribution of the $\pi^0\gamma$ channel to HVP in the muon $(g-2)_\mu$ based on a dispersive representation of the underlying $\pi^0 \to \gamma\gamma^*$ transition form factor (TFF), which proves convenient to describe the cross section of the reaction $e^+e^- \to \pi^0\gamma$. Thus, in combination with the 2π [133] and 3π [134] channels, the HVP contributions of three largest exclusive channels below 1 GeV have been scrutinized in a dispersive framework. These determinations of the low-multiplicity-channel contributions have become more critical in view of the recent lattice HVP result by BMW collaboration [283] differing from phenomenology, where the tension is likely to originate from the low-energy region. A potential shift of the total HVP contributions as in [283] would also impact the global electroweak fits [284–286], such as the running of the fine structure constant α. Besides, we found the good agreement when combining the ω and ϕ resonance parameters obtained from $e^+e^- \to 3\pi$ and $e^+e^- \to \pi^0\gamma$, which was then compared to the PDG average [22]. The tension of the ω mass with the 2π channel persists, calling for a more detailed analysis of isospin-breaking effects in the latter.

In the second part of the thesis, we reported on the first dispersive calculation of the pion-pole contribution to HLbL scattering in the muon $(g-2)_\mu$. We performed a dispersive

treatment of the doubly-virtual pion TFF that determines the pion-pole contribution: the low-lying 2π and 3π singularities in the isovector and isoscalar virtualities were considered first; we have found the leading-order, leading-twist light-cone expansion can be reformulated in terms of an asymptotic double-spectral density; finally, an effective pole term was introduced to remedy the normalization of the form factor and account for constraints from space-like singly-virtual data. Our data-driven evaluation provides for the first time a determination that fulfills the constraints from analyticity, unitarity, low-energy theorems, and perturbative QCD. Therefore, it entered the compilation of the total HLbL contributions (1.63) in the white paper [61] as the determination of the largest individual piece in the HLbL corrections to the muon $(g-2)_\mu$.

In the last part of the thesis, our discussion started with the main decay patterns of the neutral pion and focused on the rare decay $\pi^0 \to e^+e^-$. As the leading-order contribution to this decay is determined by the pion TFF, we developed a framework suitable to evaluate it using the dispersively constructed pion TFF.

What headway and outlook can we make on the presented topics? First of all, more precise determinations of hadronic cross sections from larger data samples obtained by either scan (SND and CMD-3) or initial-state-radiation (BESIII and BelleII) experiments will always improve the prediction of the HVP contributions. Therefore, both for 3π and $\pi^0\gamma$, further improvements in the precision of HVP contributions are expected in light of new data inputs. Besides, in comparison to the 2π final-state radiation carried out with a scalar QED approximation, there are no similar calculations of it for 3π. Therefore, a detailed analysis of final-state radiation in the 3π channel will not only fill out the vacancy of theoretical studies, but also provide a more rigorous evaluation of its HVP contribution.

Secondly, the completion of the HLbL contributions from η and η' poles in a dispersive approach is highly appreciated towards a 10% uncertainty goal for the HLbL contributions to the muon $(g-2)_\mu$. In this regard, the conceptual development of the pion-pole contribution, the largest individual piece in a dispersive approach to HLbL scattering, will shed light on the similar studies for the η and η' poles [407–410] to determine the complete light pseudoscalar-meson-pole contributions. In the context of the two-pion contributions to HLbL scattering, the mesonic TFFs $\omega, \phi \to \pi^0\gamma^*$ become relevant for the description of the left-hand cuts beyond the Born terms in $\gamma^*\gamma^* \to \pi\pi$ [233–238]. As the evaluation of the $g-2$ integral concerns the entire space-like region, correct implementations of mesonic form factors respecting their asymptotic behaviors dictated by perturbative QCD will be essential for a data-driven evaluation of the two-pion contributions including higher resonances, such as $f_2(1270)$.

Finally, the ongoing numerical treatment of the decay $\pi^0 \to e^+e^-$ with the dispersive pion TFF will make our estimate available to compare with the experiment [442] and other theoretical calculations. Besides an extension to the decays $\eta, \eta' \to \ell^+\ell^-$, the generalization of our approach to the rare kaon decays $K_L, K_S \to \ell^+\ell^-$ is also very promising. These rare kaon decays play a key role in flavor physics, where the corrections from new physics motivated by the B anomalies or the ε'/ε tension could be probed too. A dispersive analysis

of the long-distance effects plus an effective-field-theory treatment of the short-distance contributions in these decays will pave the way towards disentangling the imprints of physics beyond the Standard Model, e.g., the scenario of minimal flavor violation.

The work of this thesis, together with other theoretical advances in the evaluation of the anomalous magnetic moment of the muon since the older "Glasgow consensus" [448], is contained in a nutshell in the final muon $(g-2)_\mu$ Standard Model prediction (1.64). We conclude assertively that precision calculations of hadronic contributions at the low-energy frontier is not only indispensable for comprehending QCD thoroughly at non-perturbative regime, but also invaluable for making firmer Standard Model predictions to pin down the signals from physics beyond the Standard Model.

Appendix A

Hadronic vacuum polarization

A.1 Estimate of the F-wave contribution

For $q^2 = 0$ [232] and $q^2 = M_\omega^2$ [197] the impact of F-waves on the $\gamma^* \to 3\pi$ amplitude was shown to be completely negligible below the $\rho_3(1690)$ resonance, but since we consider virtualities up to $\sqrt{q^2} = 1.8\,\text{GeV}$ for our HVP study, one may ask the question whether the impact of these resonant F-waves can still be ignored. There is little phenomenological information on the $\rho_3\pi\gamma^*$ coupling besides the $\rho_3 \to \pi\omega$ branching ratio. However, the fact that the corresponding ω-dominance estimate from [232] is in line with preliminary results from COMPASS [263] suggests that at least within $[0, M_\omega^2]$ the q^2-dependence should be approximately described by $a(q^2)$. Here, we estimate a potential F-wave contribution by assuming that this approximation remains meaningful up to $\sqrt{q^2} = 1.8\,\text{GeV}$.

The decomposition of the amplitude including F-waves becomes [197]

$$\begin{aligned}\mathcal{F}(s,t,u;q^2) &= \mathcal{F}(s;q^2) + \mathcal{F}(t;q^2) + \mathcal{F}(u;q^2) \\ &\quad + P_3'(z_s)G(s;q^2) + P_3'(z_t)G(t;q^2) + P_3'(z_u)G(u;q^2)\,, \end{aligned} \tag{A.1}$$

where the scattering angles follow by permuting the Mandelstam variables in (2.6) accordingly. To estimate the ρ_3 contribution, we first establish the connection to a narrow-resonance approximation of the P-wave

$$\mathcal{F}_\rho(s;q^2) = a(q^2)\frac{M_\rho^2}{M_\rho^2 - s}\,, \tag{A.2}$$

with $M_\rho^2 \to M_\rho^2 - iM_\rho\Gamma_\rho$ in the decay region. We can then estimate the ρ_3 contribution as

$$\begin{aligned} G_{\rho_3}(s;q^2) &= a(q^2)\frac{M_{\rho_3}^2}{M_{\rho_3}^2 - s}C_{\rho_3}\frac{\sigma_\pi^2(s)\lambda(q^2,M_\pi^2,s)}{M_\omega^4}\,, \\ C_{\rho_3} &= \frac{\pi^2 g_{\rho_3\pi\pi}g_{\rho_3\pi\omega}M_\omega^4}{5g_{\omega\gamma}M_{\rho_3}^2}\,, \qquad |C_{\rho_3}| \sim 1\times 10^{-3}\,, \end{aligned} \tag{A.3}$$

where the coupling constants are set to the values from [232]. Numerically, we find that the interference between P- and F-waves gives a correction around 1% at $\sqrt{q^2} = 1.8\,\text{GeV}$, while the pure F-wave contribution is suppressed by another two orders of magnitude. These results confirm the expectation that the $\rho_3(1690)$ should not become relevant until well above the threshold $M_{\rho_3} + M_\pi \sim 1.83\,\text{GeV}$ where the decay becomes possible.

A.2 Electromagnetic mass shifts

The separation of VP from the full cross section affects the ω and ϕ pole parameters because the VP function itself involves the corresponding poles, only suppressed by e^2. The size of the expected shifts can be analyzed analytically in a Bethe–Salpeter multi-channel approach [449, 450]. For instance, the ω contribution to the VP function $\Pi(s)$ becomes

$$\Pi_\omega(s) = \frac{e^2 s}{g_{\omega\gamma}^2} \frac{1}{s - M_\omega^2 + i M_\omega \Gamma_\omega}\,, \tag{A.4}$$

where the coupling is related to the two-electron width $\Gamma_{\omega\to e^+e^-} = e^4 M_\omega/(12\pi g_{\omega\gamma}^2)$, i.e. $g_{\omega\gamma} = 16.7(2)$ [22]. Expanding around the shifted pole parameters, one finds the relation

$$\bar{M}_\omega = \left(1 + \frac{e^2}{2g_{\omega\gamma}^2}\right) M_\omega + O(e^4)\,, \qquad \bar{\Gamma}_\omega = \left(1 + \frac{e^2}{2g_{\omega\gamma}^2}\right) \Gamma_\omega + O(e^4)\,, \tag{A.5}$$

where $\bar{M}_\omega$ and $\bar{\Gamma}_\omega$ include the effects of VP, while M_ω and Γ_ω should be identified with the fit parameters in (2.27). Numerically, (A.5) implies

$$\Delta M_\omega = \bar{M}_\omega - M_\omega = 0.13\,\text{MeV}\,, \qquad \Delta\Gamma_\omega = \bar{\Gamma}_\omega - \Gamma_\omega = 1.4\,\text{keV}\,. \tag{A.6}$$

M_ω is thus expected to be about 0.13 MeV lower than in PDG conventions, while the effect on the width due to Π_ω is negligible. The same argument for the ϕ produces a mass shift

$$\Delta M_\phi = \bar{M}_\phi - M_\phi = \frac{e^2}{2g_{\phi\gamma}^2} M_\phi = 0.26\,\text{MeV}\,. \tag{A.7}$$

Finally, for the ω width there is an additional effect due to ρ–ω mixing, i.e., a higher-order effect enhanced by the small mass difference between ω and ρ. In a vector-meson-dominance approximation for the ρ we find the relation

$$\Delta\Gamma_\omega = \frac{e^2}{2g_{\omega\gamma}^2}\Gamma_\omega + \frac{M_\omega^2}{\Gamma_\rho - \Gamma_\omega} \frac{e^2}{g_{\rho\gamma}^2} \left(\frac{e^2}{g_{\omega\gamma}^2} - 2\epsilon_\omega\right) = -0.06\,\text{MeV}\,, \tag{A.8}$$

with mixing parameter $\epsilon_\omega \sim 2 \times 10^{-3}$ [133], and by comparing fits with and without VP we verified that this indeed describes well the observed shift in the ω width.

Appendix B

Hadronic light-by-light scattering

B.1 Large-N_c scaling

If the chiral anomaly $F_{\pi\gamma\gamma}$ were to scale with N_c, the ChPT expression for the pion pole would acquire on overall factor N_c^2 [311, 315], and together with the scaling $F_\pi^2 \sim N_c$ this would reproduce the overall N_c scaling of the quark-loop contribution to HLbL scattering, see e.g. [137, 138].

However, as pointed out in [451–453] this argument is not consistent because to ensure anomaly cancellation in the SM the quark charges need to be rescaled as well. We consider directly the $SU(3)$ case, where

$$Q_u = \frac{1}{2}\left(1 + \frac{1}{N_c}\right), \qquad Q_d = Q_s = -\frac{1}{2}\left(1 - \frac{1}{N_c}\right). \tag{B.1}$$

For the decay of $\pi^0 \to \gamma\gamma$ as well as the octet and singlet decays of the η, η' system, $\eta_8, \eta_0 \to \gamma\gamma$, one finds that the charge factors

$$\begin{aligned} (Q_u^2 - Q_d^2)N_c &= 1\,, \\ \frac{1}{\sqrt{3}}(Q_u^2 + Q_d^2 - 2Q_s^2)N_c &= \frac{1}{\sqrt{3}}\,, \\ \sqrt{\frac{2}{3}}(Q_u^2 + Q_d^2 + Q_s^2)N_c &= \sqrt{\frac{3}{8}}N_c - \frac{1}{\sqrt{6}} + \sqrt{\frac{3}{8}}\frac{1}{N_c}\,, \end{aligned} \tag{B.2}$$

actually cancel the N_c scaling except for in the singlet component. Accordingly, a test of $N_c = 3$ either has to rely on η, η' decays, where the mixing adds further complications [454], or more complicated decays such as $\eta \to \pi\pi\gamma$ [453, 455]. Note that for such a test the implicit dependence of F_π on N_c is irrelevant since F_π would simply be taken from experiment.

For the HLbL tensor we consider the corresponding flavor decomposition of the current

$$j^\mu = (Q_u - Q_d)j_3^\mu + \frac{1}{\sqrt{3}}(Q_u + Q_d - 2Q_s)j_8^\mu + \sqrt{\frac{2}{3}}(Q_u + Q_d + Q_s)j_0^\mu\,, \tag{B.3}$$

where

$$j_3^\mu = \frac{1}{2}(\bar{u}\gamma^\mu u - \bar{d}\gamma^\mu d)\,, \qquad j_8^\mu = \frac{1}{2\sqrt{3}}(\bar{u}\gamma^\mu u + \bar{d}\gamma^\mu d - 2\bar{s}\gamma^\mu s)\,,$$
$$j_0^\mu = \frac{1}{\sqrt{6}}(\bar{u}\gamma^\mu u + \bar{d}\gamma^\mu d + \bar{s}\gamma^\mu s)\,. \tag{B.4}$$

Collecting terms at different orders in N_c this produces

$$j^\mu = j_3^\mu + \frac{1}{\sqrt{3}} j_8^\mu - \frac{1}{\sqrt{6}} j_0^\mu + \sqrt{\frac{3}{2}}\frac{1}{N_c} j_0^\mu \equiv j_{\text{LO}}^\mu + j_{\text{NLO}}^\mu\,, \tag{B.5}$$

where we have named the two currents according to their N_c scaling,

$$j_{\text{LO}}^\mu = \frac{1}{2}(\bar{u}\gamma^\mu u - \bar{d}\gamma^\mu d - \bar{s}\gamma^\mu s)\,, \qquad j_{\text{NLO}}^\mu = \frac{1}{2N_c}(\bar{u}\gamma^\mu u + \bar{d}\gamma^\mu d + \bar{s}\gamma^\mu s)\,. \tag{B.6}$$

Restricted onto $SU(2)$, these currents correspond to the isovector and isoscalar component, respectively.

The leading N_c behavior of the quark loop can therefore only occur when each current receives a contribution from j_{LO}^μ. However, since the currents (B.6) correspond to charges $Q_{\text{LO}} = \text{diag}(1,-1,-1)$ and $Q_{\text{NLO}} = \mathbb{1}$, both of which fulfill $Q^2 = \mathbb{1}$, this implies that π^0 and η_8 have to couple to exactly one of them each—otherwise the charge factor $\text{Tr}\big(Q^2\lambda_a\big)$, with Gell-Mann matrices λ_a, $a = 3, 8$, vanishes—and therefore cannot contribute at LO in N_c, completely in line with the cancellation observed in (B.2). For the π^0, this result simply follows from isospin conservation, see (4.13), which forces exactly one of the currents to be isoscalar.

We are thus led to the prediction that the π^0 and η_8 poles should be suppressed by $1/N_c^2$ compared to the singlet component η_0, in clear contradiction to phenomenology. To obtain a more realistic estimate one needs to include both the chiral scaling and, potentially, η–η' mixing. Since the mixing disappears in the chiral limit, the effect should scale with m_s, in such a way that the overlap of the η with the singlet η_0 should be suppressed by M_K^2/Λ_χ^2. For a typical choice of Λ_χ this N_c-leading but quark-mass-suppressed contribution to the η from the η_0 is therefore not that different from the N_c-suppressed η_8 itself. Taking everything together, the η and η' poles should be suppressed by

$$\frac{M_\eta^2}{M_{\pi^0}^2}\left\{1, \frac{1}{N_c}\frac{\Lambda_\chi^2}{M_K^2}, \frac{1}{N_c^2}\frac{\Lambda_\chi^4}{M_K^4}\right\} \gtrsim 10, \qquad \frac{M_{\eta'}^2}{M_{\pi^0}^2}\frac{1}{N_c^2} \sim 6\,, \tag{B.7}$$

relative to the π^0 pole, respectively. While the η' contribution comes out correctly, the one from the η pole is predicted to be too small by about a factor 3 (depending on the exact choice of Λ_χ), and accordingly the hierarchy between η and η' is reversed. Worse, the

$1/N_c$ suppression of the π^0 pole compounds the mismatch with the pion loop, which has often been considered as leading in a chiral counting but subleading in N_c, see e.g. [56], but with the corrected N_c assignments in the charges its contribution would be expected to be enhanced by one power in N_c and two in the chiral scaling compared to the π^0 pole, in spectacular disagreement with phenomenology. From our perspective, this casts doubt on the viability of the large-N_c expansion as an organizing principle for HLbL scattering.

A potential way around these conclusions would require considering QCD on its own, not as part of the SM gauge theories. This is essentially done in the original literature [187, 188, 456], where it was shown that planar diagrams dominate in the limit $N_c \to \infty$, $\alpha_s N_c$ fixed. One could then argue that the factors of N_c that originate in the quark charges due to anomaly cancellation do not correspond to this topological expansion and should therefore not be counted in this notion of the large-N_c limit [457]. On the other hand, the large-N_c scaling of (B.6) does provide an explanation for the suppression of the isoscalar current in electromagnetic reactions, which raises the question why the implied hierarchy fails in the context of HLbL scattering.

B.2 Integral kernels

The integral kernels $\hat{T}_1(q_1, q_2; p)$ and $\hat{T}_2(q_1, q_2; p)$ for (4.5) read:

$$\begin{aligned}
\hat{T}_1(q_1, q_2; p) &= -\frac{16}{3}\left((q_1 \cdot q_2)^2 - q_1^2 q_2^2\right) m_\mu^2 - \frac{16}{3} q_1^2 (p \cdot q_2)^2 \\
&\quad + p \cdot q_1 \left(\frac{16}{3} p \cdot q_2 q_1 \cdot q_2 - \frac{8}{3} q_2^2 q_1 \cdot q_2\right) + p \cdot q_2 \left(8 q_1^2 q_2^2 - \frac{16}{3}(q_1 \cdot q_2)^2\right), \\
\hat{T}_2(q_1, q_2; p) &= -\frac{8}{3}\left((q_1 \cdot q_2)^2 - q_1^2 q_2^2\right) m_\mu^2 - \frac{8}{3} q_2^2 (p \cdot q_1)^2 - \frac{8}{3} q_1^2 (p \cdot q_2)^2 \\
&\quad - \frac{4}{3} q_1^2 p \cdot q_2 \left(q_2^2 + q_1 \cdot q_2\right) + p \cdot q_1 \left(\frac{4}{3}\left(q_1^2 + q_1 \cdot q_2\right) q_2^2 + \frac{16}{3} p \cdot q_2 q_1 \cdot q_2\right).
\end{aligned} \tag{B.8}$$

The kernel functions $T_1(Q_1, Q_2, \tau)$ and $T_2(Q_1, Q_2, \tau)$ in (4.7) are given as

$$\begin{aligned}
T_1(Q_1, Q_2, \tau) &= \frac{Q_1\left(\sigma_1^E - 1\right)\left(Q_1\tau\left(\sigma_1^E + 1\right) + 4Q_2\left(\tau^2 - 1\right)\right) - 4\tau m_\mu^2}{Q_1 Q_2 Q_3^2 m_\mu^2} \\
&\quad + X\frac{8\left(\tau^2 - 1\right)\left(2m_\mu^2 - Q_2^2\right)}{Q_3^2 m_\mu^2}\,, \\
T_2(Q_1, Q_2, \tau) &= \frac{1}{2Q_1 Q_2 Q_3^2 m_\mu^2}\Big[Q_1^2\tau\left(\sigma_1^E - 1\right)\left(\sigma_1^E + 5\right) + Q_2^2\tau\left(\sigma_2^E - 1\right)\left(\sigma_2^E + 5\right) \\
&\quad + 4Q_1 Q_2\left(\sigma_1^E + \sigma_2^E - 2\right) - 8\tau m_\mu^2\Big] + X\left(\frac{8\left(\tau^2 - 1\right)}{Q_3^2} - \frac{4}{m_\mu^2}\right),
\end{aligned} \tag{B.9}$$

where

$$\begin{aligned}
X &= \frac{1}{Q_1 Q_2 x}\arctan\left(\frac{zx}{1 - z\tau}\right), & x &= \sqrt{1 - \tau^2}\,, \\
z &= \frac{Q_1 Q_2}{4m_\mu^2}(1 - \sigma_1^E)(1 - \sigma_2^E)\,, & \sigma_i^E &= \sqrt{1 + \frac{4m_\mu^2}{Q_i^2}}\,, \\
Q_3^2 &= Q_1^2 + 2Q_1 Q_2\tau + Q_2^2\,.
\end{aligned} \tag{B.10}$$

B.3 The pion pole in chiral perturbation theory

An analysis of HLbL scattering at LO in ChPT coupled to lepton fields produces the following representation [311, 315][1]

$$a_\mu^{\pi^0\text{-pole, ChPT}} = 3\left(\frac{\alpha}{\pi}\right)^3\left(\frac{m_\mu}{F_\pi}\right)^2\left(\frac{1}{4\pi}\right)^2\left\{\ln^2\frac{\Lambda}{\mu} + \left[\frac{1}{6}\chi(\Lambda) - f(r) + \frac{1}{2}\right]\ln\frac{\Lambda}{\mu} + C(\Lambda)\right\}, \tag{B.11}$$

where

$$f(r) = \ln\frac{m_\mu^2}{\mu^2} + \frac{1}{6}r^2\ln r - \frac{1}{6}(2r + 13) + \frac{1}{3}(2 + r)\sqrt{r(4 - r)}\arccos\frac{\sqrt{r}}{2}\,. \tag{B.12}$$

Here, $r = M_{\pi^0}^2/m_\mu^2$, Λ is a UV cutoff, in ChPT to be identified with the scale of chiral symmetry breaking $\Lambda_\chi \sim 4\pi F_\pi$, the IR scale μ should be identified with M_{π^0} [448], $\chi(\Lambda)$ is a LEC that renormalizes the 1-loop ChPT expression for $\pi^0 \to e^+e^-$, and $C(\Lambda)$ subsumes all terms not enhanced by a logarithm.

[1] For the reasons explained in Appendix B.1, $a_\mu^{\pi^0\text{-pole}}$ does not actually scale with N_c^2. In the following, we therefore set $N_c = 3$ from the start.

The precise definition of $\chi(\Lambda)$ depends on the scheme, which in (B.11) is chosen in accordance with [347]. Explicitly, conventions can be specified using the reduced amplitude for $P \to \ell^+\ell^-$ discussed in Section 5.2.1,

$$A_\ell(q^2) = \frac{2i}{\pi^2 q^2} \int \mathrm{d}^4k \frac{k^2 q^2 - (q\cdot k)^2}{k^2(q-k)^2((p-k)^2 - m_\ell^2)} \tilde{F}(k^2, (q-k)^2)\,, \tag{B.13}$$

where $q^2 = M_P^2$ denotes the mass of the pseudoscalar, $p^2 = m_\ell^2$ the lepton mass, and $\tilde{F}(q_1^2, q_2^2)$ the TFF for $P \to \gamma^*\gamma^*$ normalized by the chiral anomaly

$$\tilde{F}(q_1^2, q_2^2) = \frac{F(q_1^2, q_2^2)}{F_{\pi\gamma\gamma}}\,. \tag{B.14}$$

For the decay kinematics one has, in addition, $(p-q)^2 = m_\ell^2$, and thus $2p\cdot q = M_P^2$.

At LO in ChPT $\tilde{F}(q_1^2, q_2^2) = 1$ and the integral in (B.13) diverges. This divergence is cured by introducing counterterms based on the Lagrangian [347]

$$\mathcal{L} = \frac{3i\alpha^2}{32\pi^2}(\bar{\ell}\gamma^\mu\gamma_5\ell)\left\{\chi_1 \,\mathrm{tr}\,(Q^2\{U^\dagger, \partial_\mu U\}) + \chi_2 \,\mathrm{tr}\,(QU^\dagger Q\partial_\mu U - Q\partial_\mu U^\dagger QU)\right\}, \tag{B.15}$$

where Q is the charge matrix and U contains the meson fields. Altogether, this leads to [347]

$$\mathrm{Re}\, A_\ell^{\mathrm{ChPT}}(q^2) = 3\ln\frac{m_\ell}{\Lambda} - \frac{\chi(\Lambda)}{4} - \frac{7}{2} + \frac{1}{\beta_\ell}\left[\frac{\pi^2}{12} + \frac{1}{4}\ln^2\frac{1-\beta_\ell}{1+\beta_\ell} + \mathrm{Li}_2\left(\frac{\beta_\ell - 1}{\beta_\ell + 1}\right)\right], \tag{B.16}$$

where

$$\mathrm{Li}_2(x) = -\int_0^x \mathrm{d}t \frac{\ln(1-t)}{t}, \qquad \beta_\ell = \sqrt{1 - \frac{4m_\ell^2}{q^2}}\,, \tag{B.17}$$

and $\chi(\Lambda) = \chi_1^{\mathrm{r}}(\Lambda) + \chi_2^{\mathrm{r}}(\Lambda)$. Note, however, that the choice of scheme is not unique in the literature: another popular choice [348] is related by $\chi(\Lambda) = \chi^{[347]}(\Lambda) = \chi^{[348]}(\Lambda) - 4$.

Since the pion pole as defined in dispersion theory [143, 146] coincides with the diagrammatic expression (4.5), we can start from this expression to analyze how the ChPT constraints emerge within dispersion relations. First, we expand the kernel functions in terms of muon propagators as far as possible, using relations of the form

$$\int \frac{\mathrm{d}^4q_2}{(2\pi)^4} \frac{F(q_1^2, q_2^2)F((q_1+q_2)^2, 0)}{(q_2^2 - M_{\pi^0}^2)q_2^2(q_1+q_2)^2} q_2^\mu = \int \frac{\mathrm{d}^4q_2}{(2\pi)^4} \frac{F(q_1^2, q_2^2)F((q_1+q_2)^2, 0)}{(q_2^2 - M_{\pi^0}^2)q_2^2(q_1+q_2)^2} \frac{q_1\cdot q_2}{q_1^2} q_1^\mu\,, \tag{B.18}$$

which follow from a standard tensor decomposition. This produces

$$
\begin{aligned}
a_{\mu,T_1}^{\pi^0\text{-pole, disp}} &= -\frac{32\pi^2}{3F_\pi^2}\left(\frac{\alpha}{\pi}\right)^3 \int \frac{\mathrm{d}^4 q_2}{(2\pi)^4} \frac{\tilde{F}(q_2^2,0)}{q_2^2(q_2^2-M_{\pi^0}^2)} \left(\frac{2m_\mu^2+q_2^2}{(p-q_2)^2-m_\mu^2}-1\right) \\
&\quad \times \int \frac{\mathrm{d}^4 q_1}{(2\pi)^4} \frac{q_1^2 q_2^2-(q_1\cdot q_2)^2}{q_1^2(q_1+q_2)^2((p+q_1)^2-m_\mu^2)} \tilde{F}(q_1^2,(q_1+q_2)^2)\,, \\
a_{\mu,T_2}^{\pi^0\text{-pole, disp}} &= -\frac{16\pi^2}{3F_\pi^2}\left(\frac{\alpha}{\pi}\right)^3 \int \frac{\mathrm{d}^4 q_1}{(2\pi)^4} \int \frac{\mathrm{d}^4 q_2}{(2\pi)^4} \frac{\tilde{F}(q_1^2,q_2^2)\tilde{F}((q_1+q_2)^2,0)}{q_1^2 q_2^2 (q_1+q_2)^2((q_1+q_2)^2-M_{\pi^0}^2)} \\
&\quad \times \left[\frac{(q_1^2+q_1\cdot q_2)q_2^2}{(p-q_2)^2-m_\mu^2}+\frac{(q_2^2+q_1\cdot q_2)q_1^2}{(p+q_1)^2-m_\mu^2}\right. \\
&\qquad \left. +\frac{2m_\mu^2(q_1^2q_2^2-(q_1\cdot q_2)^2)-q_1^2q_2^2(q_1+q_2)^2}{((p+q_1)^2-m_\mu^2)((p-q_2)^2-m_\mu^2)}\right]. \qquad \text{(B.19)}
\end{aligned}
$$

Accordingly, the representation for the T_1 term can be expressed as

$$
a_{\mu,T_1}^{\pi^0\text{-pole, disp}} = -\left(\frac{\alpha}{\pi}\right)^3 \frac{1}{3F_\pi^2}\frac{1}{i}\int \frac{\mathrm{d}^4 q_2}{(2\pi)^4} \frac{\tilde{F}(q_2^2,0)}{q_2^2-M_{\pi^0}^2}\left(\frac{2m_\mu^2+q_2^2}{(p-q_2)^2-m_\mu^2}-1\right) I_\mu(q_2^2)\,, \qquad \text{(B.20)}
$$

where

$$
I_\ell(q^2) = \frac{2i}{\pi^2 q^2}\int \mathrm{d}^4 k \frac{k^2q^2-(q\cdot k)^2}{k^2(q-k)^2((p-k)^2-m_\ell^2)} \tilde{F}(k^2,(q-k)^2) \qquad \text{(B.21)}
$$

has been defined in close analogy to $A_\ell(q^2)$, the difference being that q^2 is not restricted to $M_{\pi^0}^2$. We checked numerically for a VMD form factor that the representation (B.19) reproduces the known result.

In [312] it was established that the T_2 term remains finite even for a pointlike form factor, so that the corresponding integral cannot contribute to any singularities. The logarithmically enhanced terms in (B.11) all originate from the approximation where the form factors are put equal to unity, at this order in the chiral expansion their structure is not resolved. Matching the dispersive representation (B.20) onto (B.11) therefore requires taking the pointlike limit in the appropriate fashion. First, we note that for $I_\mu(q_2^2)$ we cannot use the form (B.16), since this relies on the specific kinematics for the pseudoscalar decay. Explicit calculation with Feynman parameters shows that in addition to the logarithmically divergent piece there is a contribution involving $\ln\left(-q_2^2\right)$, whose coefficient is related to the $\ln\Lambda$ term. The corresponding structure is therefore

$$
I_\mu(q_2^2) = -3\ln\frac{\Lambda}{\mu} - \frac{\chi(\Lambda)}{4} + \frac{3}{2}\ln\left(-\frac{q_2^2}{\mu^2}\right) + C_\mu\,, \qquad \text{(B.22)}
$$

with some constant piece C_μ. The chiral LEC still regulates the divergence since its specific form does not depend on the kinematics. Once the form factor is replaced by its pointlike limit, the same LEC therefore describes the renormalization of the $\pi^0 \to \ell^+\ell^-$ vertex (assuming lepton flavor universality). This argument already shows that for the dispersive formalism to be consistent with the chiral constraints derived in [311, 315] it suffices that the form factor used be consistent with the LEC $\chi(\Lambda)$, as extracted from $\pi^0 \to e^+e^-$ or $\eta \to \ell^+\ell^-$.

The individual terms in (B.11) can then be understood as follows: for the second loop integral we have

$$\begin{aligned}
&\frac{1}{i}\int \frac{\mathrm{d}^4 q_2}{(2\pi)^4}\frac{1}{q_2^2 - M_{\pi^0}^2}\left(\frac{2m_\mu^2 + q_2^2}{(p-q_2)^2 - m_\mu^2} - 1\right)\\
&= \frac{1}{16\pi^2}\left(3m_\mu^2 \ln\frac{\Lambda^2}{\mu^2} - 2m_\mu^2 \int_0^1 \mathrm{d}x\,(1+x)\ln\frac{x^2 m_\mu^2 + (1-x)M_{\pi^0}^2}{\mu^2}\right)\\
&= \frac{3m_\mu^2}{16\pi^2}\left(\ln\frac{\Lambda^2}{\mu^2} - f(r) - \frac{1}{2}\right),
\end{aligned} \tag{B.23}$$

with $f(r)$ as given in (B.12). Next, the $\ln(-q_2^2)$ piece leads to a term

$$\begin{aligned}
\frac{1}{16\pi^4}\left[2m_\mu^2 \int_0^1 \mathrm{d}x\,(1+x)\frac{1}{i}\int \frac{\mathrm{d}^4 q_2}{q_2^4}\frac{3}{2}\ln\left(-\frac{q_2^2}{\mu^2}\right)\right] &= \frac{3m_\mu^2}{16\pi^4}\frac{3}{2}2\pi^2 \int^{\frac{\Lambda}{\mu}} \frac{\mathrm{d}x\,x^3}{x^4}\ln x^2\\
&= \frac{3m_\mu^2}{16\pi^2}3\ln^2\frac{\Lambda}{\mu}\,.
\end{aligned} \tag{B.24}$$

Adding the individual contributions we find

$$\begin{aligned}
a_{\mu,T_1,\,\mathrm{div}}^{\pi^0\text{-pole, disp}} &= -\left(\frac{\alpha}{\pi}\right)^3 \frac{1}{3F_\pi^2}\frac{3m_\mu^2}{16\pi^2}\\
&\quad\times\left[\left(-3\ln\frac{\Lambda}{\mu} - \frac{\chi(\Lambda)}{4} + C_\mu\right)\left(2\ln\frac{\Lambda}{\mu} - f(r) - \frac{1}{2}\right) + 3\ln^2\frac{\Lambda}{\mu}\right]\\
&= 3\left(\frac{\alpha}{\pi}\right)^3\left(\frac{m_\mu}{F_\pi}\right)^2\left(\frac{1}{4\pi}\right)^2\left\{\ln^2\frac{\Lambda}{\mu} + \left[\frac{1}{6}\chi(\Lambda) - f(r) + \tilde{C}_\mu\right]\ln\frac{\Lambda}{\mu} + \ldots\right\}.
\end{aligned} \tag{B.25}$$

Taking the pointlike limit of (B.20) in this way therefore reproduces the basic features of the direct ChPT result (B.11), in particular the coefficient of the double logarithm, the contribution from $\chi(\Lambda)$, and the part of the coefficient of the single logarithm that is non-analytic in the quark mass. The analytic contribution, $\tilde{C}_\mu = 1/2$, requires a more careful treatment of the renormalization schemes [311, 315] and certainly cannot be expected to emerge from a naive cutoff regularization of the loop integrals.

In conclusion, the above discussion demonstrates that dispersion relations for HLbL scattering in the form of [143, 146] fulfill the low-energy constraints from ChPT. Most aspects of (B.11) can already be derived from a pointlike form factor alone, so that the corresponding constraints are automatically maintained due to the structure of the loop integrals, which become identical to ChPT once the form factor is set to unity. The only information about the pion TFF beyond its pointlike limit is contained in the LEC $\chi(\Lambda)$, which is needed to renormalize the $\pi^0 \to \mu^+\mu^-$ vertex due to the missing form-factor suppression for high momenta. Such a contribution therefore does not arise in a dispersive approach where the full form factor enters, but consistency with the chiral constraint is automatic as long as the employed form factor agrees with experimental constraints from $\pi^0 \to e^+e^-$ and/or $\eta \to \ell^+\ell^-$ (the latter if $SU(3)$ symmetry is assumed). This comparison can indeed proceed in terms of $\chi(\Lambda)$: a given representation for the pion TFF can be turned into a prediction for this LEC, which can then be compared to the experimental value as extracted from the decay width. Equivalently, the decay width calculated from the form factor could be directly compared to the experimental result, with the chiral LEC one particular choice how to present the relation between HLbL scattering and the rare meson decays. We stress, however, that the comparison in terms of the TFF directly is actually preferable since it dispenses with the need for the chiral expansion.

B.4 Anomalous thresholds and analyticity

The presence of two electromagnetic currents in the $\pi^0 \to \gamma^*\gamma^*$ transition together with light pion intermediate states makes it appear likely that anomalous thresholds [458] require a modification of the integration contours in (4.20), and indeed for similar quantities in the context of HLbL scattering, e.g. the partial waves for $\gamma^*\gamma^* \to \pi\pi$, such complications do arise for time-like virtualities [142, 146]. For the pion TFF the crucial analytic properties can be derived from the triangle diagram C_0 shown in Figure B.1, depending on the mass m_1 [459].

The key assumption in the derivation of the dispersion relation for $F_{vs}(q_1^2, q_2^2)$ is that the dependence on the isovector virtuality permits a standard dispersive reconstruction. The corresponding imaginary part reads ($s = q_1^2$)

$$\operatorname{Im} C_0(s) = \frac{\theta(s - 4M_\pi^2)}{\sqrt{\lambda(s, M_\pi^2, q_2^2)}} \ln \frac{s - 3M_\pi^2 - q_2^2 + 2m_1^2 - \sigma_\pi(s)\sqrt{\lambda(s, M_\pi^2, q_2^2)}}{s - 3M_\pi^2 - q_2^2 + 2m_1^2 + \sigma_\pi(s)\sqrt{\lambda(s, M_\pi^2, q_2^2)}}, \tag{B.26}$$

which defines the critical points

$$s_\pm(q_2^2) = \frac{1}{2}\left\{3M_\pi^2 + q_2^2 - m_1^2 \pm \sigma_\pi(m_1^2)\sqrt{\lambda(m_1^2, M_\pi^2, q_2^2)}\right\}. \tag{B.27}$$

Anomalous thresholds arise if either point, as a function of q_2^2, crosses the unitarity cut and moves onto the first sheet. The trajectory of $s_-(q_2^2)$ indeed comes close at $q_2^2 = M_\pi^2 + 2m_1^2$,

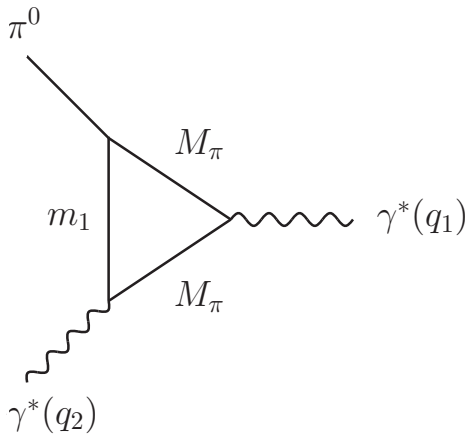

Figure B.1: Triangle topology in the $\pi^0 \to \gamma^*\gamma^*$ transition. For the physical case $m_1 \geq 2M_\pi$ no anomalous thresholds occur.

but since the KT equations are solved for $q_2^2 \to q_2^2 + i\epsilon$, the intersection with the real axis occurs at

$$s_c = 4M_\pi^2\left(1 - \frac{\epsilon^2}{4m_1^2(m_1^2 - 4M_\pi^2)}\right). \tag{B.28}$$

In the KT solution the mass m_1^2 is replaced by a spectral function whose support starts at $s' = 4M_\pi^2$, so that the intersection with the unitarity cut is narrowly avoided. However, this derivation shows that if there were a lighter state with mass below $2M_\pi$, the trajectory would indeed move onto the first sheet and require a modification of the integration contour.

In general, the occurrence of anomalous thresholds in a dispersion relation in the photon virtuality q_1^2 depends crucially on the form of the $\gamma^* \to 3\pi$ amplitude. The preceding discussion applies if that amplitude may be described by a dispersion relation in the crossed channel with threshold above $2M_\pi$, in particular the first diagram in Figure B.2. Even at two-loop order (in $\gamma^* \to 3\pi$, see second diagram in Figure B.2, corresponding to three loops for the TFF) such a representation exists, and even more so a representation free of anomalous thresholds [460]. Indeed, an anomalous threshold in the $\gamma^* \to 3\pi$ amplitude would likely trigger an anomalous threshold in the pion TFF itself. In this way, the first problematic diagram occurs at three-loop order for the $\gamma^* \to 3\pi$ amplitude (third diagram in Figure B.2, corresponding to four loops in the TFF): the 3π triangle should give rise to anomalous thresholds. However, this diagram involves an additional cut, implying that the corresponding $\gamma^* \to 3\pi$ amplitude cannot be decomposed in terms of single-variable functions anymore. Such contributions involving 4π cuts cannot be fully accounted for in our dispersive analysis of the $\gamma^* \to 3\pi$ amplitude, and thus appear within the estimates for higher intermediate states, but not in the dispersive part of the decomposition.

Apart from anomalous thresholds, it is surprising that a simple dispersion relation for the TFF arises despite the complicated analytic structure of the partial wave $f_1(s, q_2^2)$. To test this assumption numerically, we separated the normalization according to $f_1(s, q^2) =$

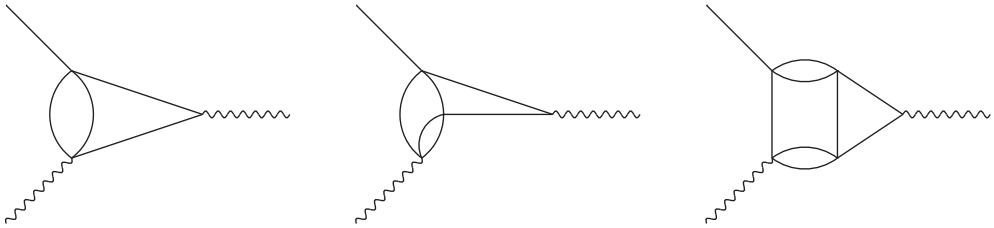

Figure B.2: Topologies for $\pi^0 \to \gamma^*\gamma^*$. The solid lines all refer to pion states, but the analytic properties of these Feynman diagrams are again indicative of the general analytic structure.

$a(q^2)\bar{f}_1(s,q^2)$ and expressed the form factor in terms of

$$F_{vs}(q_1^2,q_2^2) = a(q_2^2)g(q_1^2,q_2^2)\,, \qquad g(q_1^2,q_2^2) = \frac{1}{12\pi^2}\int_{4M_\pi^2}^{\infty}\mathrm{d}x\frac{q_\pi^3(x)(F_\pi^V(x))^*\bar{f}_1(x,q_2^2)}{x^{1/2}(x-q_1^2)}\,. \tag{B.29}$$

The requirement that the single and double dispersion relations be equivalent then implies that

$$a(q_2^2)g(q_1^2,q_2^2) = \frac{1}{\pi}\int_{s_\mathrm{th}}^{\infty}\mathrm{d}y\frac{\mathrm{Im}\,[a(y)g(q_1^2,y)]}{y-q_2^2}\,, \tag{B.30}$$

and since, by construction, $a(q_2^2)$ is analytic the same is true for $F_{vs}(q_1^2,q_2^2)$ as soon as $g(q_1^2,q_2^2)$ is analytic. Taking q_1^2 space-like, this statement follows from

$$\begin{aligned}
\frac{1}{\pi}\int\mathrm{d}y\frac{\mathrm{Im}\,F_{vs}(q_1^2,y)}{y-q_2^2-i\epsilon} &= \frac{1}{\pi^2}\int\mathrm{d}y\frac{\mathrm{Im}\,a(y)}{y-q_2^2-i\epsilon}\int\mathrm{d}y'\frac{\mathrm{Im}\,g(q_1^2,y')}{y'-y+i\epsilon}\\
&\quad+\frac{1}{\pi^2}\int\mathrm{d}y'\frac{\mathrm{Im}\,g(q_1^2,y')}{y'-q_2^2-i\epsilon}\int\mathrm{d}y\frac{\mathrm{Im}\,a(y)}{y-y'-i\epsilon}\\
&= \frac{1}{\pi^2}\int\mathrm{d}y\,\mathrm{Im}\,a(y)\int\mathrm{d}y'\,\mathrm{Im}\,g(q_1^2,y')\\
&\quad\times\frac{1}{y'-y+i\epsilon}\left(\frac{1}{y-q_2^2-i\epsilon}-\frac{1}{y'-q_2^2-i\epsilon}\right)\\
&= \frac{1}{\pi^2}\int\mathrm{d}y\frac{\mathrm{Im}\,a(y)}{y-q_2^2-i\epsilon}\int\mathrm{d}y'\frac{\mathrm{Im}\,g(q_1^2,y')}{y'-q_2^2-i\epsilon}\\
&= a(q_2^2)g(q_1^2,q_2^2) = F_{vs}(q_1^2,q_2^2)\,,
\end{aligned} \tag{B.31}$$

and the general case follows by analytic continuation in q_1^2. From the KT solution we do not have access to $g(q_1^2,q_2^2)$ above $q_2^2 = (1.8\,\mathrm{GeV})^2$, but we can still check if, with a reasonable high-energy completion of the imaginary part, the resulting function $g(q_1^2,q_2^2)$ fulfills a dispersion relation. Empirically, we observe that with a continuation according to $1/y^2$ a once-subtracted dispersion relation does reproduce the KT result, providing another check on the consistency of our dispersive formalism for the pion TFF.

B.5 Scale estimate from light-cone QCD sum rules

We start with a dispersive representation of the doubly-virtual pion TFF for space-like momenta

$$F_{\pi^0\gamma^*\gamma^*}(q_1^2, q_2^2) = \frac{1}{\pi}\int_0^\infty \mathrm{d}s \frac{\operatorname{Im} F_{\pi^0\gamma^*\gamma^*}(s, q_2^2)}{s - q_1^2} \tag{B.32}$$

and split the spectral information into high and low energies [377, 378]:

$$F_{\pi^0\gamma^*\gamma^*}(q_1^2, q_2^2) = \frac{G_V(q_2^2)}{M_V^2 - q_1^2} + \frac{1}{\pi}\int_{s_\mathrm{m}}^\infty \mathrm{d}s \, \frac{\operatorname{Im} F_{\pi^0\gamma^*\gamma^*}(s, q_2^2)}{s - q_1^2} \,. \tag{B.33}$$

For the low-energy part we use a VMD model [461]:

$$\operatorname{Im} F_{\pi^0\gamma^*\gamma^*}(s, q_2^2) \approx G_V(q_2^2)\, \pi\, \delta(s - M_V^2) \quad \text{for} \quad s < s_\mathrm{m} \,, \tag{B.34}$$

with a vector-meson mass M_V and a quantity G_V proportional to the electromagnetic form factor for the transition of the vector meson to the pion.

Duality between hadronic and quark–gluon ("OPE") degrees of freedom suggests that at high energies, properly energy-averaged quantities should agree for both representations [377, 378]. Therefore one demands

$$\frac{1}{\pi}\int_{s_\mathrm{m}}^\infty \mathrm{d}s \, \frac{\operatorname{Im} F_{\pi^0\gamma^*\gamma^*}(s, q_2^2)}{s - q_1^2} \approx \frac{1}{\pi}\int_{s_\mathrm{m}}^\infty \mathrm{d}s \, \frac{\operatorname{Im} F^{\mathrm{OPE}}_{\pi^0\gamma^*\gamma^*}(s, q_2^2)}{s - q_1^2} \tag{B.35}$$

for any value of q_1^2 (and sufficiently large s_m) and

$$\frac{1}{\pi}\int_0^\infty \mathrm{d}s \, \frac{\operatorname{Im} F_{\pi^0\gamma^*\gamma^*}(s, q_2^2)}{s - q_1^2} \approx \frac{1}{\pi}\int_0^\infty \mathrm{d}s \, \frac{\operatorname{Im} F^{\mathrm{OPE}}_{\pi^0\gamma^*\gamma^*}(s, q_2^2)}{s - q_1^2} \tag{B.36}$$

for asymptotically large q_1^2. Taken together, these relations allow one to determine [377, 378] both parts on the right-hand side of (B.33), leading to

$$G_V(q^2) \approx \frac{1}{\pi}\int_0^{s_\mathrm{m}} \mathrm{d}s \operatorname{Im} F^{\mathrm{OPE}}_{\pi^0\gamma^*\gamma^*}(s, q^2) \tag{B.37}$$

and

$$F_{\pi^0\gamma^*\gamma^*}(q_1^2, q_2^2) \approx \frac{1}{M_V^2 - q_1^2}\frac{1}{\pi}\int_0^{s_\mathrm{m}} \mathrm{d}s \operatorname{Im} F^{\mathrm{OPE}}_{\pi^0\gamma^*\gamma^*}(s, q_2^2) + \frac{1}{\pi}\int_{s_\mathrm{m}}^\infty \mathrm{d}s \, \frac{\operatorname{Im} F^{\mathrm{OPE}}_{\pi^0\gamma^*\gamma^*}(s, q_2^2)}{s - q_1^2} \,. \tag{B.38}$$

The pion TFF is symmetric in its two virtualities whereas the right-hand side of (B.38) is not. We symmetrize the expression by hand and obtain

$$\begin{aligned} &F_{\pi^0\gamma^*\gamma^*}(q_1^2, q_2^2) \\ &\quad\approx \frac{1}{2}\Bigg[\frac{1}{M_V^2 - q_1^2}\frac{1}{\pi}\int_0^{s_\mathrm{m}} \mathrm{d}s\, \mathrm{Im}\, F^{\mathrm{OPE}}_{\pi^0\gamma^*\gamma^*}(s, q_2^2) + \frac{1}{\pi}\int_{s_\mathrm{m}}^{\infty} \mathrm{d}s\, \frac{\mathrm{Im}\, F^{\mathrm{OPE}}_{\pi^0\gamma^*\gamma^*}(s, q_2^2)}{s - q_1^2} \\ &\quad + \frac{1}{M_V^2 - q_2^2}\frac{1}{\pi}\int_0^{s_\mathrm{m}} \mathrm{d}s\, \mathrm{Im}\, F^{\mathrm{OPE}}_{\pi^0\gamma^*\gamma^*}(q_1^2, s) + \frac{1}{\pi}\int_{s_\mathrm{m}}^{\infty} \mathrm{d}s\, \frac{\mathrm{Im}\, F^{\mathrm{OPE}}_{\pi^0\gamma^*\gamma^*}(q_1^2, s)}{s - q_2^2}\Bigg]\,. \end{aligned} \tag{B.39}$$

In [377, 378], a Borel transformation has been applied to (B.36) and a Borelized version of (B.38) is used for the singly-virtual pion TFF. In the following, we use the symmetrized finite-energy sum rule (B.39) as it is. It has the advantage that it contains only two non-perturbative parameters, the vector-meson mass M_V and the "continuum threshold" s_m, i.e. the onset of the asymptotic regime.

Finally, we need the OPE expression for the spectral information. To this end, we use the asymptotic LO leading-twist expression (4.24) that relates the pion TFF to the pion distribution amplitude [364–366]. The final expression for this LCSR VMD approach (LV) is

$$\begin{aligned} F^{\mathrm{LV}}_{\pi^0\gamma^*\gamma^*}(q_1^2, q_2^2) &:= \frac{F_\pi}{3}\int_0^{x_1} \mathrm{d}x\, \frac{\phi_\pi(x)}{(1-x)(M_V^2 - q_2^2)} - \frac{F_\pi}{3}\int_{x_1}^{1} \mathrm{d}x\, \frac{\phi_\pi(x)}{x q_1^2 + (1-x) q_2^2} \\ &+ \frac{F_\pi}{3}\int_0^{x_2} \mathrm{d}x\, \frac{\phi_\pi(x)}{(1-x)(M_V^2 - q_1^2)} - \frac{F_\pi}{3}\int_{x_2}^{1} \mathrm{d}x\, \frac{\phi_\pi(x)}{x q_2^2 + (1-x) q_1^2}\,, \end{aligned} \tag{B.40}$$

where

$$x_i := \frac{s_\mathrm{m}}{s_\mathrm{m} - q_i^2}\,. \tag{B.41}$$

Expression (B.40) shows very satisfying high- and low-energy limits provided one chooses $M_V^2 = 8\pi^2 F_\pi^2$ [462–464]. In line with the chiral anomaly one obtains

$$F^{\mathrm{LV}}_{\pi^0\gamma^*\gamma^*}(0,0) = \frac{2F_\pi}{3M_V^2}\int_0^1 \frac{\phi_\pi(x)}{1-x} = \frac{2F_\pi}{M_V^2} = \frac{1}{4\pi^2 F_\pi}\,. \tag{B.42}$$

The BL limit [364–366] is recovered:

$$\begin{aligned} F^{\mathrm{LV}}_{\pi^0\gamma^*\gamma^*}(-Q^2, 0) &= \frac{F_\pi}{3}\int_0^{x_Q} \mathrm{d}x\, \frac{\phi_\pi(x)}{(1-x)M_V^2} + \frac{F_\pi}{3}\int_{x_Q}^{1} \mathrm{d}x\, \frac{\phi_\pi(x)}{xQ^2} \\ &+ \frac{F_\pi}{3}\int_0^1 \mathrm{d}x\, \frac{\phi_\pi(x)}{(1-x)(M_V^2 + Q^2)} \\ &= \frac{1}{Q^2}\frac{2F_\pi}{3}\int_0^1 \mathrm{d}x\, \frac{\phi_\pi(x)}{x} + O(1/Q^4) = \frac{2F_\pi}{Q^2} + O(1/Q^4)\,. \end{aligned} \tag{B.43}$$

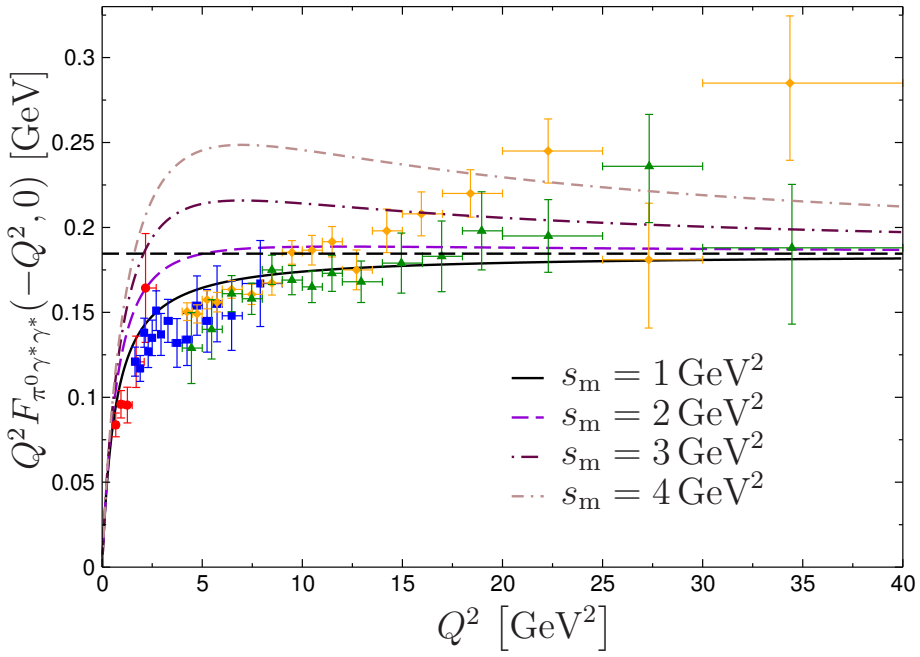

Figure B.3: Comparison of (B.40) to singly-virtual pion TFF data [396–399]. Color coding for the experimental points as in Figure 4.8.

Finally, for large Q_1^2, Q_2^2 one finds the relation

$$F^{\mathrm{LV}}_{\pi^0\gamma^*\gamma^*}(-Q_1^2, -Q_2^2) = \frac{2F_\pi}{3}\int_0^1 \mathrm{d}x\,\frac{\phi_\pi(x)}{xQ_1^2 + (1-x)Q_2^2} + O(1/Q_i^4)\,, \tag{B.44}$$

which is in line with the OPE prediction [364–366, 384]. More generally, if both virtualities are space-like, (B.40) vanishes as soon as one of the two virtualities becomes infinitely large, irrespective of the value of the other virtuality. This property is not so easy to achieve for hadronic resonance saturation models.

Before we show the results, we stress again that the QCD sum rule formula (B.40) containing in particular the VMD model for the low-energy part is not meant for a full-fledged quantitative calculation of the pion TFF, but for understanding the size of s_m. Figure B.3 shows a comparison of formula (B.40) to the data on the singly-virtual pion TFF for different values of s_m. Obviously, large values of s_m do not agree with the data while a value of $s_m = 1\,\mathrm{GeV}^2$ provides a consistent picture.

Bibliography

[1] H. Weyl, *Eine Neue Erweiterung der Relativitätstheorie*, Annalen Phys. **59** (1919) 101 (cit. on p. 1).

[2] C.-N. Yang and R. L. Mills, *Conservation of Isotopic Spin and Isotopic Gauge Invariance*, Phys. Rev. **96** (1954) 191 (cit. on p. 1).

[3] S. Weinberg, *The Making of the Standard Model*, Eur. Phys. J. C **34** (2004) 5, ed. by G. 't Hooft, arXiv: hep-ph/0401010 (cit. on p. 1).

[4] Y. Nambu, *Axial Vector Current Conservation in Weak Interactions*, Phys. Rev. Lett. **4** (1960) 380, ed. by T. Eguchi (cit. on p. 1).

[5] J. Goldstone, *Field Theories with Superconductor Solutions*, Nuovo Cim. **19** (1961) 154 (cit. on p. 1).

[6] Y. Nambu and G. Jona-Lasinio, *Dynamical Model of Elementary Particles Based on an Analogy with Superconductivity. I*, Phys. Rev. **122** (1961) 345, ed. by T. Eguchi (cit. on p. 1).

[7] Y. Nambu and G. Jona-Lasinio, *Dynamical Model of Elementary Particles Based on an Analogy with Superconductivity. II*, Phys. Rev. **124** (1961) 246, ed. by T. Eguchi (cit. on p. 1).

[8] J. Goldstone, A. Salam and S. Weinberg, *Broken Symmetries*, Phys. Rev. **127** (1962) 965 (cit. on p. 1).

[9] F. Englert and R. Brout, *Broken Symmetry and the Mass of Gauge Vector Mesons*, Phys. Rev. Lett. **13** (1964) 321, ed. by J. Taylor (cit. on p. 1).

[10] P. W. Higgs, *Broken Symmetries, Massless Particles and Gauge Fields*, Phys. Lett. **12** (1964) 132 (cit. on p. 1).

[11] P. W. Higgs, *Broken Symmetries and the Masses of Gauge Bosons*, Phys. Rev. Lett. **13** (1964) 508, ed. by J. Taylor (cit. on p. 1).

[12] P. W. Higgs, *Spontaneous Symmetry Breakdown without Massless Bosons*, Phys. Rev. **145** (1966) 1156 (cit. on p. 1).

[13] S. L. Glashow, *Partial Symmetries of Weak Interactions*, Nucl. Phys. **22** (1961) 579 (cit. on p. 1).

[14] S. Weinberg, *A Model of Leptons*, Phys. Rev. Lett. **19** (1967) 1264 (cit. on p. 1).

[15] A. Salam, *Weak and Electromagnetic Interactions*, Conf. Proc. C **680519** (1968) 367 (cit. on p. 1).

[16] D. Gross and F. Wilczek, *Asymptotically Free Gauge Theories. I*, Phys. Rev. D **8** (1973) 3633 (cit. on p. 1).

[17] H. Fritzsch, M. Gell-Mann and H. Leutwyler, *Advantages of the Color Octet Gluon Picture*, Phys. Lett. B **47** (1973) 365 (cit. on p. 1).

[18] M. Gell-Mann and F. Low, *Quantum Electrodynamics at Small Distances*, Phys. Rev. **95** (1954) 1300 (cit. on p. 1).

[19] M. Tanabashi et al., *Review of Particle Physics*, Phys. Rev. D **98** (2018) 030001 (cit. on p. 2).

[20] D. J. Gross and F. Wilczek, *Ultraviolet Behavior of Non-Abelian Gauge Theories*, Phys. Rev. Lett. **30** (1973) 1343, ed. by J. Taylor (cit. on p. 2).

[21] H. Politzer, *Reliable Perturbative Results for Strong Interactions?*, Phys. Rev. Lett. **30** (1973) 1346, ed. by J. Taylor (cit. on p. 2).

[22] P. Zyla et al., *Review of Particle Physics*, PTEP **2020** (2020) 083C01 (cit. on pp. 2, 54, 57, 63, 65, 71, 72, 75, 81, 82, 92, 93, 99, 112, 123, 124, 126, 133, 138).

[23] K. G. Wilson, *Confinement of Quarks*, Phys. Rev. D **10** (1974) 2445, ed. by J. Taylor (cit. on p. 3).

[24] C. Vafa and E. Witten, *Restrictions on Symmetry Breaking in Vector-like Gauge Theories*, Nucl. Phys. B **234** (1984) 173 (cit. on p. 3).

[25] S. Weinberg, *Phenomenological Lagrangians*, Physica A **96** (1979) 327, ed. by S. Deser (cit. on p. 3).

[26] J. Gasser and H. Leutwyler, *Chiral Perturbation Theory to One Loop*, Annals Phys. **158** (1984) 142 (cit. on p. 3).

[27] J. Gasser and H. Leutwyler, *Chiral Perturbation Theory: Expansions in the Mass of the Strange Quark*, Nucl. Phys. B **250** (1985) 465 (cit. on p. 3).

[28] G. Arnison et al., *Experimental Observation of Isolated Large Transverse Energy Electrons with Associated Missing Energy at* $\sqrt{s} = 540\,\text{GeV}$, Phys. Lett. B **122** (1983) 103 (cit. on p. 3).

[29] G. Arnison et al., *Experimental Observation of Lepton Pairs of Invariant Mass Around* $95\,\text{GeV}/c^2$ *at the CERN SPS Collider*, Phys. Lett. B **126** (1983) 398 (cit. on p. 3).

[30] F. Abe et al., *Observation of Top Quark Production in $\bar{p}p$ Collisions with the Collider Detector at Fermilab*, Phys. Rev. Lett. **74** (1995) 2626, arXiv: hep-ex/9503002 (cit. on p. 3).

[31] S. Abachi et al., *Observation of the Top Quark*, Phys. Rev. Lett. **74** (1995) 2632, arXiv: hep-ex/9503003 (cit. on p. 3).

[32] G. Aad et al., *Observation of a New Particle in the Search for the Standard Model Higgs Boson with the ATLAS Detector at the LHC*, Phys. Lett. B **716** (2012) 1, arXiv: 1207.7214 [hep-ex] (cit. on p. 3).

[33] S. Chatrchyan et al., *Observation of a New Boson at a Mass of* 125 GeV *with the CMS Experiment at the LHC*, Phys. Lett. B **716** (2012) 30, arXiv: 1207.7235 [hep-ex] (cit. on p. 3).

[34] W. E. Lamb and R. C. Retherford, *Fine Structure of the Hydrogen Atom by a Microwave Method*, Phys. Rev. **72** (1947) 241 (cit. on p. 3).

[35] H. Bethe, *The Electromagnetic Shift of Energy Levels*, Phys. Rev. **72** (1947) 339 (cit. on pp. 3, 9).

[36] I. Khriplovich and M. Pospelov, *Electric Dipole Moment of the W-boson and the Electron in the Kobayashi–Maskawa Model*, Sov. J. Nucl. Phys. **53** (1991) 638 (cit. on p. 5).

[37] M. Kobayashi and T. Maskawa, *CP-Violation in the Renormalizable Theory of Weak Interaction*, Prog. Theor. Phys. **49** (1973) 652 (cit. on p. 5).

[38] P. A. Dirac, *The Quantum Theory of the Electron*, Proc. Roy. Soc. Lond. A **A117** (1928) 610 (cit. on p. 5).

[39] P. A. Dirac, *The Quantum Theory of the Electron. Part II*, Proc. Roy. Soc. Lond. A **A118** (1928) 351 (cit. on p. 5).

[40] W. Gordon, *Der Strom der Diracschen Elektronentheorie*, Z. Physik **50** (1928) 630 (cit. on p. 5).

[41] V. B. Berestetskii, O. N. Krokhin and A. X. Klebnikov, *Concerning the Radiative Correction to the μ-meson Magnetic Moment*, Zh. Eksp. Teor. Fiz. **30** (1956) 788 (cit. on p. 6).

[42] W. Cowland, *On Schwinger's Theory of the Muon*, Nucl. Phys. **8** (1958) 397 (cit. on p. 6).

[43] A. Czarnecki and W. J. Marciano, *Muon Anomalous Magnetic Moment: A Harbinger for "New Physics"*, Phys. Rev. D **64** (2001) 013014, arXiv: hep-ph/0102122 (cit. on p. 6).

[44] G. Giudice, P. Paradisi and M. Passera, *Testing New Physics with the Electron $g-2$*, JHEP **11** (2012) 113, arXiv: 1208.6583 [hep-ph] (cit. on p. 6).

[45] H. Davoudiasl and W. J. Marciano, *Tale of Two Anomalies*, Phys. Rev. D **98** (2018) 075011, arXiv: 1806.10252 [hep-ph] (cit. on p. 6).

[46] A. Crivellin, M. Hoferichter and P. Schmidt-Wellenburg, *Combined Explanations of $(g-2)_{\mu,e}$ and Implications for a Large Muon EDM*, Phys. Rev. **D98** (2018) 113002, arXiv: 1807.11484 [hep-ph] (cit. on p. 6).

[47] A. Crivellin, D. Mueller and F. Saturnino, *Correlating $h \to \mu^+\mu^-$ to the Anomalous Magnetic Moment of the Muon via Leptoquarks*, (2020), arXiv: 2008.02643 [hep-ph] (cit. on p. 6).

[48] D. Hanneke, S. Fogwell and G. Gabrielse, *New Measurement of the Electron Magnetic Moment and the Fine Structure Constant*, Phys. Rev. Lett. **100** (2008) 120801, arXiv: 0801.1134 [physics.atom-ph] (cit. on p. 6).

[49] D. Hanneke, S. Hoogerheide and G. Gabrielse, *Cavity Control of a Single-Electron Quantum Cyclotron: Measuring the Electron Magnetic Moment*, Phys. Rev. A **83** (2011) 052122, arXiv: 1009.4831 [physics.atom-ph] (cit. on p. 6).

[50] R. H. Parker et al., *Measurement of the Fine-Structure Constant as a Test of the Standard Model*, Science **360** (2018) 191, arXiv: 1812.04130 [physics.atom-ph] (cit. on pp. 6, 9).

[51] M. Endo and W. Yin, *Explaining Electron and Muon $g-2$ Anomaly in SUSY without Lepton-Flavor Mixings*, JHEP **08** (2019) 122, arXiv: 1906.08768 [hep-ph] (cit. on p. 6).

[52] C. Hati et al., *Anomalies in ^{8}Be Nuclear Transitions and $(g-2)_{e,\mu}$: Towards a Minimal Combined Explanation*, JHEP **07** (2020) 235, arXiv: 2005.00028 [hep-ph] (cit. on p. 6).

[53] K. Melnikov and A. Vainshtein, *Theory of the Muon Anomalous Magnetic Moment*, Springer Tracts Mod. Phys. **216** (2006) 1 (cit. on p. 6).

[54] J. P. Miller, E. de Rafael and B. Roberts, *Muon $(g-2)$: Experiment and Theory*, Rept. Prog. Phys. **70** (2007) 795, arXiv: hep-ph/0703049 (cit. on p. 6).

[55] F. Jegerlehner, *The Anomalous Magnetic Moment of the Muon*, Springer Tracts Mod. Phys. **226** (2008) (cit. on pp. 6, 19).

[56] F. Jegerlehner and A. Nyffeler, *The Muon $g-2$*, Phys. Rept. **477** (2009) 1, arXiv: 0902.3360 [hep-ph] (cit. on pp. 6, 90, 141).

[57] J. P. Miller et al., *Muon $(g-2)$: Experiment and Theory*, Ann. Rev. Nucl. Part. Sci. **62** (2012) 237 (cit. on p. 6).

[58] T. Blum et al., *The Muon* $(g-2)$ *Theory Value: Present and Future*, (2013), arXiv: 1311.2198 [hep-ph] (cit. on p. 6).

[59] M. Lindner, M. Platscher and F. S. Queiroz, *A Call for New Physics: The Muon Anomalous Magnetic Moment and Lepton Flavor Violation*, Phys. Rept. **731** (2018) 1, arXiv: 1610.06587 [hep-ph] (cit. on p. 6).

[60] F. Jegerlehner, *The Anomalous Magnetic Moment of the Muon*, Springer Tracts Mod. Phys. **274** (2017) (cit. on pp. 6, 68, 80).

[61] T. Aoyama et al., *The Anomalous Magnetic Moment of the Muon in the Standard Model*, Phys. Rept. **887** (2020) 1, arXiv: 2006.04822 [hep-ph] (cit. on pp. 6, 9, 13, 17, 19, 68, 69, 87, 120, 133, 134).

[62] W. H. Louisell, R. W. Pidd and H. R. Crane, *An Experimental Measurement of the Gyromagnetic Ratio of the Free Electron*, Phys. Rev. **94** (1954) 7 (cit. on p. 7).

[63] A. Schupp, R. Pidd and H. Crane, *Measurement of the g Factor of Free, High-Energy Electrons*, Phys. Rev. **121** (1961) 1 (cit. on p. 7).

[64] V. Bargmann, L. Michel and V. Telegdi, *Precession of the Polarization of Particles Moving in a Homogeneous Electromagnetic Field*, Phys. Rev. Lett. **2** (1959) 435, ed. by T. Damour, I. Todorov and B. Zhilinskii (cit. on p. 7).

[65] G. Bennett et al., *Improved Limit on the Muon Electric Dipole Moment*, Phys. Rev. D **80** (2009) 052008, arXiv: 0811.1207 [hep-ex] (cit. on p. 8).

[66] W. Liu et al., *High Precision Measurements of the Ground State Hyperfine Structure Interval of Muonium and of the Muon Magnetic Moment*, Phys. Rev. Lett. **82** (1999) 711 (cit. on p. 8).

[67] G. Bennett et al., *Final Report of the Muon E821 Anomalous Magnetic Moment Measurement at BNL*, Phys. Rev. D **73** (2006) 072003, arXiv: hep-ex/0602035 (cit. on p. 8).

[68] P. J. Mohr, D. B. Newell and B. N. Taylor, *CODATA Recommended Values of the Fundamental Physical Constants: 2014*, Rev. Mod. Phys. **88** (2016) 035009, arXiv: 1507.07956 [physics.atom-ph] (cit. on p. 8).

[69] J. Bailey et al., *Final Report on the CERN Muon Storage Ring Including the Anomalous Magnetic Moment and the Electric Dipole Moment of the Muon, and a Direct Test of Relativistic Time Dilation*, Nucl. Phys. B **150** (1979) 1 (cit. on p. 8).

[70] J. Grange et al., *Muon* $(g-2)$ *Technical Design Report*, (2015), arXiv: 1501.06858 [physics.ins-det] (cit. on pp. 8, 51, 72).

[71] M. Abe et al., *A New Approach for Measuring the Muon Anomalous Magnetic Moment and Electric Dipole Moment*, PTEP **2019** (2019) 053C02, arXiv: 1901.03047 [physics.ins-det] (cit. on pp. 8, 51, 72).

[72] J. S. Schwinger, *On Quantum-Electrodynamics and the Magnetic Moment of the Electron*, Phys. Rev. **73** (1948) 416 (cit. on p. 9).

[73] T. Aoyama et al., *Complete Tenth-Order QED Contribution to the Muon $g-2$*, Phys. Rev. Lett. **109** (2012) 111808, arXiv: 1205.5370 [hep-ph] (cit. on pp. 9, 13).

[74] T. Aoyama, T. Kinoshita and M. Nio, *Theory of the Anomalous Magnetic Moment of the Electron*, Atoms **7** (2019) 28 (cit. on pp. 9, 13).

[75] H. Foley and P. Kusch, *On the Intrinsic Moment of the Electron*, Phys. Rev. **73** (1948) 412 (cit. on p. 9).

[76] P. Kusch and H. Foley, *The Magnetic Moment of the Electron*, Phys. Rev. **74** (1948) 250 (cit. on p. 9).

[77] C. Itzykson and J. Zuber, *Quantum Field Theory*, International Series in Pure and Applied Physics, McGraw-Hill, 1980, ISBN: 978-0-486-44568-7 (cit. on p. 9).

[78] M. E. Peskin and D. V. Schroeder, *An Introduction to Quantum Field Theory*, Addison-Wesley, 1995, ISBN: 978-0-201-50397-5 (cit. on pp. 9, 30, 45).

[79] A. Zee, *Quantum Field Theory in a Nutshell*, 2003, ISBN: 978-0-691-14034-6 (cit. on pp. 9, 22).

[80] H. Suura and E. H. Wichmann, *Magnetic Moment of the Mu Meson*, Phys. Rev. **105** (1957) 1930 (cit. on pp. 9, 11).

[81] A. Petermann, *Magnetic moment of the μ Meson*, Phys. Rev. **105** (1957) 1931 (cit. on pp. 9, 11).

[82] C. M. Sommerfield, *Magnetic Dipole Moment of the Electron*, Phys. Rev. **107** (1957) 328 (cit. on pp. 9, 10).

[83] A. Petermann, *Fourth Order Magnetic Moment of the Electron*, Helv. Phys. Acta **30** (1957) 407 (cit. on pp. 9, 10).

[84] A. Petermann, *Fourth Order Magnetic Moment of the Electron*, Nucl. Phys. **5** (1958) 677 (cit. on pp. 9, 10).

[85] C. M. Sommerfield, *The Magnetic Moment of the Electron*, Annals Phys. **5** (1958) 26 (cit. on pp. 9, 10).

[86] Bouchiat, Claude and Michel, Louis, *La Résonance dans la Diffusion Méson π-Méson π et le Moment Magnétique Anormal du Méson μ*, J. Phys. Radium **22** (1961) 121 (cit. on pp. 11, 16, 51, 87).

[87] S. J. Brodsky and E. de Rafael, *Suggested Boson-Lepton Pair Couplings and the Anomalous Magnetic Moment of the Muon*, Phys. Rev. **168** (1968) 1620 (cit. on pp. 11, 16, 51, 87).

[88] H. Elend, *On the Anomalous Magnetic Moment of the Muon*, Phys. Lett. **20** (1966) 682 (cit. on p. 11).

[89] M. Passera, *The Standard Model Prediction of the Muon Anomalous Magnetic Moment*, J. Phys. G **31** (2005) R75, arXiv: hep-ph/0411168 (cit. on p. 11).

[90] T. Kinoshita, *Sixth-Order Radiative Corrections to the Muon Magnetic Moment.*, Nuovo Cim. B **51** (1967) 140 (cit. on p. 12).

[91] S. Laporta and E. Remiddi, *The Analytical Value of the Electron* $(g-2)$ *at Order* α^3 *in QED*, Phys. Lett. B **379** (1996) 283, arXiv: hep-ph/9602417 (cit. on p. 13).

[92] S. Laporta and E. Remiddi, *The Analytical Value of the Electron Light-Light Graphs Contribution to the Muon* $(g-2)$ *in QED*, Phys. Lett. B **301** (1993) 440 (cit. on p. 13).

[93] S. Laporta, *The Analytical Contribution of the Sixth Order Graphs with Vacuum Polarization Insertions to the Muon* $(g-2)$ *in QED*, Nuovo Cim. A **106** (1993) 675 (cit. on p. 13).

[94] A. Czarnecki and M. Skrzypek, *The Muon Anomalous Magnetic Moment in QED: Three-Loop Electron and Tau Contributions*, Phys. Lett. B **449** (1999) 354, arXiv: hep-ph/9812394 (cit. on p. 13).

[95] S. Laporta, *High-Precision Calculation of the 4-Loop Contribution to the Electron* $g-2$ *in QED*, Phys. Lett. B **772** (2017) 232, arXiv: 1704.06996 [hep-ph] (cit. on p. 13).

[96] S. Laporta, *Analytical and Numerical Contributions of Some Tenth Order Graphs Containing Vacuum Polarization Insertions to the Muon* $(g-2)$ *in QED*, Phys. Lett. B **328** (1994) 522, arXiv: hep-ph/9404204 (cit. on p. 13).

[97] A. Kurz et al., *Light-by-Light-Type Corrections to the Muon Anomalous Magnetic Moment at Four-Loop Order*, Phys. Rev. D **92** (2015) 073019, arXiv: 1508.00901 [hep-ph] (cit. on p. 13).

[98] A. Kurz et al., *Electron Contribution to the Muon Anomalous Magnetic Moment at Four Loops*, Phys. Rev. D **93** (2016) 053017, arXiv: 1602.02785 [hep-ph] (cit. on p. 13).

[99] T. Aoyama et al., *Tenth-Order Electron Anomalous Magnetic Moment: Contribution of Diagrams without Closed Lepton Loops*, Phys. Rev. D **91** (2015) 033006, [Erratum: Phys. Rev. D 96 (2017) 019901], arXiv: 1412.8284 [hep-ph] (cit. on p. 13).

[100] T. Aoyama, T. Kinoshita and M. Nio, *Revised and Improved Value of the QED Tenth-Order Electron Anomalous Magnetic Moment*, Phys. Rev. D **97** (2018) 036001, arXiv: 1712.06060 [hep-ph] (cit. on p. 13).

[101] A. Czarnecki, W. J. Marciano and A. Vainshtein, *Refinements in Electroweak Contributions to the Muon Anomalous Magnetic Moment*, Phys. Rev. D **67** (2003) 073006, [Erratum: Phys. Rev. D 73 (2006) 119901], arXiv: hep-ph/0212229 (cit. on pp. 13–15).

[102] C. Gnendiger, D. Stöckinger and H. Stöckinger-Kim, *The Electroweak Contributions to $(g-2)_\mu$ after the Higgs Boson Mass Measurement*, Phys. Rev. D **88** (2013) 053005, arXiv: 1306.5546 [hep-ph] (cit. on pp. 13, 14).

[103] R. Jackiw and S. Weinberg, *Weak-Interaction Corrections to the Muon Magnetic Moment and to Muonic-Atom Energy Levels*, Phys. Rev. D **5** (1972) 2396 (cit. on p. 13).

[104] I. Bars and M. Yoshimura, *Muon Magnetic Moment in a Finite Theory of Weak and Electromagnetic Interactions*, Phys. Rev. D **6** (1972) 374 (cit. on p. 13).

[105] G. Altarelli, N. Cabibbo and L. Maiani, *The Drell–Hearn Sum Rule and the Lepton Magnetic Moment in the Weinberg Model of Weak and Electromagnetic Interactions*, Phys. Lett. B **40** (1972) 415 (cit. on p. 13).

[106] W. A. Bardeen, R. Gastmans and B. Lautrup, *Static Quantities in Weinberg's Model of Weak and Electromagnetic Interactions*, Nucl. Phys. B **46** (1972) 319 (cit. on p. 13).

[107] K. Fujikawa, B. Lee and A. Sanda, *Generalized Renormalizable Gauge Formulation of Spontaneously Broken Gauge Theories*, Phys. Rev. D **6** (1972) 2923 (cit. on p. 13).

[108] G. 't Hooft, *Renormalization of Massless Yang–Mills Fields*, Nucl. Phys. B **33** (1971) 173 (cit. on p. 14).

[109] G. 't Hooft, *Renormalizable Lagrangians for Massive Yang–Mills Fields*, Nucl. Phys. B **35** (1971) 167, ed. by J. Taylor (cit. on p. 14).

[110] G. 't Hooft and M. Veltman, *Combinatorics of Gauge Fields*, Nucl. Phys. B **50** (1972) 318 (cit. on p. 14).

[111] S. L. Adler, *Axial-Vector Vertex in Spinor Electrodynamics*, Phys. Rev. **177** (1969) 2426 (cit. on pp. 15, 44, 92, 123).

[112] J. Bell and R. Jackiw, *A PCAC Puzzle: $\pi^0 \to \gamma\gamma$ in the σ-Model*, Nuovo Cim. A **60** (1969) 47 (cit. on pp. 15, 44, 92, 123).

[113] W. A. Bardeen, *Anomalous Ward identities in Spinor Field Theories*, Phys. Rev. **184** (1969) 1848 (cit. on pp. 15, 44, 92, 123).

[114] T. Kukhto et al., *The Dominant Two-Loop Electroweak Contributions to the Anomalous Magnetic Moment of the Muon*, Nucl. Phys. B **371** (1992) 567 (cit. on p. 15).

[115] C. Bouchiat, J. Iliopoulos and P. Meyer, *An Anomaly-Free Version of Weinberg's Model*, Phys. Lett. B **38** (1972) 519 (cit. on p. 15).

[116] C. Korthals Altes and M. Perrottet, *Anomalous Ward-Identities, Gauge-Variance and Appearance of Ghosts in Higgs–Kibble Type Theories*, Phys. Lett. B **39** (1972) 546 (cit. on p. 15).

[117] D. J. Gross and R. Jackiw, *Effect of Anomalies on Quasi-Renormalizable Theories*, Phys. Rev. D **6** (1972) 477 (cit. on p. 15).

[118] S. Peris, M. Perrottet and E. de Rafael, *Two-Loop Electroweak Corrections to the Muon $g-2$: A New Class of Hadronic Contributions*, Phys. Lett. B **355** (1995) 523, arXiv: hep-ph/9505405 (cit. on p. 15).

[119] A. Czarnecki, B. Krause and W. J. Marciano, *Electroweak Fermion-Loop Contributions to the Muon Anomalous Magnetic Moment*, Phys. Rev. D **52** (1995) 2619, arXiv: hep-ph/9506256 (cit. on p. 15).

[120] A. Czarnecki, B. Krause and W. J. Marciano, *Electroweak Corrections to the Muon Anomalous Magnetic Moment*, Phys. Rev. Lett. **76** (1996) 3267, arXiv: hep-ph/9512369 (cit. on p. 15).

[121] G. Degrassi and G. Giudice, *QED Logarithms in the Electroweak Corrections to the Muon Anomalous Magnetic Moment*, Phys. Rev. D **58** (1998) 053007, arXiv: hep-ph/9803384 (cit. on p. 15).

[122] M. Knecht et al., *Electroweak Hadronic Contributions to the Muon $(g-2)$*, JHEP **11** (2002) 003, arXiv: hep-ph/0205102 (cit. on p. 15).

[123] G. 't Hooft et al., eds., *Recent Developments in Gauge Theories. Proceedings, Nato Advanced Study Institute*, vol. 59, 1980 1 (cit. on p. 15).

[124] A. Vainshtein, *Perturbative and Nonperturbative Renormalization of Anomalous Quark Triangles*, Phys. Lett. B **569** (2003) 187, arXiv: hep-ph/0212231 (cit. on p. 15).

[125] S. Heinemeyer, D. Stöckinger and G. Weiglein, *Electroweak and Supersymmetric Two-Loop Corrections to $(g-2)_\mu$*, Nucl. Phys. B **699** (2004) 103, arXiv: hep-ph/0405255 (cit. on p. 15).

[126] T. Gribouk and A. Czarnecki,
Electroweak Interactions and the Muon $g-2$: Bosonic Two-Loop Effects,
Phys. Rev. D **72** (2005) 053016, arXiv: hep-ph/0509205 (cit. on p. 15).

[127] R. Alemany, M. Davier and A. Höcker,
Improved Determination of the Hadronic Contribution to the Muon $(g-2)$ and to $\alpha(M_Z^2)$ Using New Data from Hadronic τ Decays, Eur. Phys. J. C **2** (1998) 123,
arXiv: hep-ph/9703220 (cit. on p. 17).

[128] R. Barbieri and E. Remiddi, *Sixth Order Electron and Muon $(g-2)/2$ from Second Order Vacuum Polarization Insertion*, Phys. Lett. B **49** (1974) 468 (cit. on p. 17).

[129] R. Barbieri and E. Remiddi,
Electron and Muon $\frac{1}{2}(g-2)$ from Vacuum Polarization Insertions,
Nucl. Phys. B **90** (1975) 233 (cit. on p. 17).

[130] A. Kurz et al., *Hadronic Contribution to the Muon Anomalous Magnetic Moment to Next-to-Next-to-Leading Order*, Phys. Lett. B **734** (2014) 144,
arXiv: 1403.6400 [hep-ph] (cit. on pp. 17, 53, 79).

[131] M. Davier et al., *Reevaluation of the Hadronic Vacuum Polarisation Contributions to the Standard Model Predictions of the Muon $g-2$ and $\alpha(m_Z^2)$ Using Newest Hadronic Cross-Section Data*, Eur. Phys. J. C **77** (2017) 827,
arXiv: 1706.09436 [hep-ph] (cit. on pp. 17, 51, 67, 80, 87, 133).

[132] A. Keshavarzi, D. Nomura and T. Teubner,
Muon $g-2$ and $\alpha(M_Z^2)$: A New Data-Based Analysis,
Phys. Rev. D **97** (2018) 114025, arXiv: 1802.02995 [hep-ph]
(cit. on pp. 17, 51, 53, 66, 67, 73, 80, 87, 133).

[133] G. Colangelo, M. Hoferichter and P. Stoffer,
Two-Pion Contribution to Hadronic Vacuum Polarization, JHEP **02** (2019) 006,
arXiv: 1810.00007 [hep-ph]
(cit. on pp. 17, 52, 53, 55, 61, 65, 66, 68, 69, 71, 76, 83, 133, 138).

[134] M. Hoferichter, B.-L. Hoid and B. Kubis,
Three-Pion Contribution to Hadronic Vacuum Polarization, JHEP **08** (2019) 137,
arXiv: 1907.01556 [hep-ph] (cit. on pp. 17, 51, 71, 73, 76, 77, 84, 133).

[135] M. Davier et al., *A New Evaluation of the Hadronic Vacuum Polarisation Contributions to the Muon Anomalous Magnetic Moment and to $\alpha(m_Z^2)$*,
Eur. Phys. J. C **80** (2020) 241, [Erratum: Eur. Phys. J. C 80 (2020) 410],
arXiv: 1908.00921 [hep-ph] (cit. on pp. 17, 51, 71, 80, 87, 133).

[136] A. Keshavarzi, D. Nomura and T. Teubner,
$g-2$ of Charged Leptons, $\alpha(M_Z^2)$, and the Hyperfine Splitting of Muonium,
Phys. Rev. D **101** (2020) 014029, arXiv: 1911.00367 [hep-ph]
(cit. on pp. 17, 51, 80, 87, 133).

[137] E. de Rafael, *Hadronic Contributions to the Muon $g-2$ and Low-Energy QCD*, Phys. Lett. B **322** (1994) 239, arXiv: hep-ph/9311316 (cit. on pp. 18, 87, 139).

[138] K. Melnikov and A. Vainshtein, *Hadronic Light-by-Light Scattering Contribution to the Muon Anomalous Magnetic Moment Reexamined*, Phys. Rev. D **70** (2004) 113006, arXiv: hep-ph/0312226 (cit. on pp. 18, 19, 87, 91, 118, 139).

[139] J. Wess and B. Zumino, *Consequences of Anomalous Ward Identities*, Phys. Lett. B **37** (1971) 95 (cit. on pp. 18, 47, 52, 54, 72).

[140] E. Witten, *Global Aspects of Current Algebra*, Nucl. Phys. B **223** (1983) 422 (cit. on pp. 18, 47, 52, 54, 72).

[141] A. Nyffeler, *Precision of a Data-Driven Estimate of Hadronic Light-by-Light Scattering in the Muon $g-2$: Pseudoscalar-Pole Contribution*, Phys. Rev. D **94** (2016) 053006, arXiv: 1602.03398 [hep-ph] (cit. on pp. 19, 91).

[142] M. Hoferichter et al., *Virtual Photon-Photon Scattering*, Int. J. Mod. Phys. Conf. Ser. **35** (2014) 1460400, ed. by P. Gauzzi and G. Venanzoni, arXiv: 1309.6877 [hep-ph] (cit. on pp. 19, 51, 72, 87, 120, 146).

[143] G. Colangelo et al., *Dispersive Approach to Hadronic Light-by-Light Scattering*, JHEP **09** (2014) 091, arXiv: 1402.7081 [hep-ph] (cit. on pp. 19, 51, 72, 87, 89, 120, 143, 146).

[144] P. Stoffer, *Dispersive Treatments of $K_{\ell 4}$ Decays and Hadronic Light-by-Light Scattering*, PhD thesis, 2014, arXiv: 1412.5171 [hep-ph] (cit. on pp. 19, 51, 72, 87, 120).

[145] G. Colangelo et al., *Towards a Data-Driven Analysis of Hadronic Light-by-Light Scattering*, Phys. Lett. B **738** (2014) 6, arXiv: 1408.2517 [hep-ph] (cit. on pp. 19, 51, 72, 87, 120).

[146] G. Colangelo et al., *Dispersion Relation for Hadronic Light-by-Light Scattering: Theoretical Foundations*, JHEP **09** (2015) 074, arXiv: 1506.01386 [hep-ph] (cit. on pp. 19, 51, 72, 87–90, 120, 143, 146).

[147] G. Colangelo et al., *Rescattering Effects in the Hadronic-Light-by-Light Contribution to the Anomalous Magnetic Moment of the Muon*, Phys. Rev. Lett. **118** (2017) 232001, arXiv: 1701.06554 [hep-ph] (cit. on pp. 19, 51, 117).

[148] G. Colangelo et al., *Dispersion Relation for Hadronic Light-by-Light Scattering: Two-Pion Contributions*, JHEP **04** (2017) 161, arXiv: 1702.07347 [hep-ph] (cit. on pp. 19, 51, 90, 117).

[149] M. Hoferichter et al., *Pion-Pole Contribution to Hadronic Light-by-Light Scattering in the Anomalous Magnetic Moment of the Muon*, Phys. Rev. Lett. **121** (2018) 112002, arXiv: 1805.01471 [hep-ph] (cit. on pp. 19, 51, 52, 56, 57, 71–73, 87, 93, 117).

[150] M. Hoferichter et al., *Dispersion Relation for Hadronic Light-by-Light Scattering: Pion Pole*, JHEP **10** (2018) 141, arXiv: 1808.04823 [hep-ph] (cit. on pp. 19, 51, 52, 56, 57, 71–74, 87, 93, 117, 125).

[151] G. Colangelo et al., *Short-Distance Constraints on Hadronic Light-by-Light Scattering in the Anomalous Magnetic Moment of the Muon*, Phys. Rev. D **101** (2020) 051501, arXiv: 1910.11881 [hep-ph] (cit. on pp. 19, 51).

[152] G. Colangelo et al., *Longitudinal Short-Distance Constraints for the Hadronic Light-by-Light Contribution to $(g-2)_\mu$ with Large-N_c Regge Models*, JHEP **03** (2020) 101, arXiv: 1910.13432 [hep-ph] (cit. on pp. 19, 51).

[153] J. Bijnens, N. Hermansson-Truedsson and A. Rodríguez-Sánchez, *Short-Distance Constraints for the HLbL Contribution to the Muon Anomalous Magnetic Moment*, Phys. Lett. B **798** (2019) 134994, arXiv: 1908.03331 [hep-ph] (cit. on p. 19).

[154] L. Cappiello et al., *Axial-Vector and Pseudoscalar Mesons in the Hadronic Light-by-Light Contribution to the Muon $(g-2)$*, Phys. Rev. D **102** (2020) 016009, arXiv: 1912.02779 [hep-ph] (cit. on p. 19).

[155] M. Knecht, *On Some Short-Distance Properties of the Fourth-Rank Hadronic Vacuum Polarization Tensor and the Anomalous Magnetic Moment of the Muon*, JHEP **08** (2020) 056, arXiv: 2005.09929 [hep-ph] (cit. on p. 19).

[156] P. Masjuan, P. Roig and P. Sanchez-Puertas, *A Different Viewpoint on the Hadronic Light-by-Light Tensor Short-Distance Constraints*, (2020), arXiv: 2005.11761 [hep-ph] (cit. on p. 19).

[157] J. Lüdtke and M. Procura, *Effects of Longitudinal Short-Distance Constraints on the Hadronic Light-by-Light Contribution to the Muon $g-2$*, (2020), arXiv: 2006.00007 [hep-ph] (cit. on p. 19).

[158] J. Bijnens et al., *Short-Distance HLbL Contributions to the Muon Anomalous Magnetic Moment beyond Perturbation Theory*, (2020), arXiv: 2008.13487 [hep-ph] (cit. on p. 19).

[159] P. Masjuan and P. Sanchez-Puertas, *Pseudoscalar-Pole Contribution to the $(g_\mu-2)$: A Rational Approach*, Phys. Rev. D **95** (2017) 054026, arXiv: 1701.05829 [hep-ph] (cit. on pp. 19, 91, 118, 119).

[160] A. Gérardin, H. B. Meyer and A. Nyffeler, *Lattice Calculation of the Pion Transition Form Factor with $N_f = 2 + 1$ Wilson Quarks*, Phys. Rev. D **100** (2019) 034520, arXiv: 1903.09471 [hep-lat] (cit. on pp. 19, 51, 73, 87, 91).

[161] T. Blum et al., *Hadronic Light-by-Light Scattering Contribution to the Muon Anomalous Magnetic Moment from Lattice QCD*, Phys. Rev. Lett. **124** (2020) 132002, arXiv: 1911.08123 [hep-lat] (cit. on pp. 19, 51, 87).

[162] G. Colangelo et al., *Remarks on Higher-Order Hadronic Corrections to the Muon $g - 2$*, Phys. Lett. B **735** (2014) 90, arXiv: 1403.7512 [hep-ph] (cit. on pp. 19, 53, 79).

[163] J. Wess and B. Zumino, *Supergauge Transformations in Four Dimensions*, Nucl. Phys. B **70** (1974) 39, ed. by A. Salam and E. Sezgin (cit. on p. 20).

[164] S. Ferrara and E. Remiddi, *Absence of the Anomalous Magnetic Moment in a Supersymmetric Abelian Gauge Theory*, Phys. Lett. B **53** (1974) 347 (cit. on p. 20).

[165] T. Moroi, *The Muon Anomalous Magnetic Dipole Moment in the Minimal Supersymmetric Standard Model*, Phys. Rev. D **53** (1996) 6565, [Erratum: Phys. Rev. D 56 (1997) 4424], arXiv: hep-ph/9512396 (cit. on p. 20).

[166] M. J. Dugan, H. Georgi and D. B. Kaplan, *Anatomy of a Composite Higgs Model*, Nucl. Phys. B **254** (1985) 299 (cit. on p. 21).

[167] A. D. Martin and T. D. Spearman, *Elementary Particle Theory*, North-Holland, 1970 (cit. on p. 21).

[168] R. J. Eden et al., *The Analytic S-Matrix*, Cambridge University Press, 1966 (cit. on p. 25).

[169] D. I. Olive, *Unitarity and the Evaluation of Discontinuities*, Nuovo Cim. **26** (1962) 73 (cit. on p. 27).

[170] M. Sugawara and A. Kanazawa, *Subtractions in Dispersion Relations*, Phys. Rev. **123** (1961) 1895 (cit. on p. 34).

[171] R. Cutkosky, *Singularities and Discontinuities of Feynman Amplitudes*, J. Math. Phys. **1** (1960) 429 (cit. on p. 36).

[172] K. M. Watson, *Some General Relations between the Photoproduction and Scattering of π Mesons*, Phys. Rev. **95** (1954) 228 (cit. on p. 37).

[173] R. Omnès, *On the Solution of Certain Singular Integral Equations of Quantum Field Theory*, Nuovo Cim. **8** (1958) 316 (cit. on pp. 38, 55, 74, 93).

[174] S. Mandelstam, *Determination of the Pion-Nucleon Scattering Amplitude from Dispersion Relations and Unitarity. General Theory*, Phys. Rev. **112** (1958) 1344 (cit. on p. 39).

[175] T. Regge, *Introduction to Complex Orbital Momenta*, Nuovo Cim. **14** (1959) 951 (cit. on p. 39).

[176] M. Froissart, *Asymptotic Behavior and Subtractions in the Mandelstam Representation*, Phys. Rev. **123** (1961) 1053 (cit. on pp. 40, 74).

[177] A. Martin, *Unitarity and High-Energy Behavior of Scattering Amplitudes*, Phys. Rev. **129** (1963) 1432 (cit. on pp. 40, 74).

[178] K. G. Wilson, *Non-Lagrangian Models of Current Algebra*, Phys. Rev. **179** (1969) 1499 (cit. on p. 40).

[179] M. A. Shifman, A. Vainshtein and V. I. Zakharov, *QCD and Resonance Physics. Applications*, Nucl. Phys. B **147** (1979) 448 (cit. on pp. 41, 100).

[180] E. Poggio, H. R. Quinn and S. Weinberg, *Smearing Method in the Quark Model*, Phys. Rev. D **13** (1976) 1958 (cit. on p. 41).

[181] J. Donoghue, E. Golowich and B. R. Holstein, *Dynamics of the Standard Model*, **2** (2014) (cit. on p. 41).

[182] P. Colangelo and A. Khodjamirian, *QCD Sum Rules, a Modern Perspective*, (2000) 1495, ed. by M. Shifman and B. Ioffe, arXiv: hep-ph/0010175 (cit. on pp. 41, 42).

[183] I. Balitsky, V. M. Braun and A. Kolesnichenko, *Radiative Decay $\Sigma^+ \to p\gamma$ in Quantum Chromodynamics*, Nucl. Phys. B **312** (1989) 509 (cit. on p. 42).

[184] V. M. Braun and I. Filyanov, *QCD Sum Rules in Exclusive Kinematics and Pion Wave Function*, Sov. J. Nucl. Phys. **50** (1989) 511 (cit. on p. 42).

[185] V. Chernyak and I. Zhitnitsky, *B-Meson Exclusive Decays into Baryons*, Nucl. Phys. B **345** (1990) 137 (cit. on p. 42).

[186] A. Khodjamirian, "Quantum Chromodynamics and Hadrons: An Elementary Introduction", *European School on High-Energy Physics*, 2004 173, arXiv: hep-ph/0403145 (cit. on p. 42).

[187] G. 't Hooft, *A Planar Diagram Theory for Strong Interactions*, Nucl. Phys. B **72** (1974) 461, ed. by J. Taylor (cit. on pp. 43, 141).

[188] G. 't Hooft, *A Two-Dimensional Model for Mesons*, Nucl. Phys. B **75** (1974) 461 (cit. on pp. 43, 141).

[189] S. Coleman, *Aspects of Symmetry: Selected Erice Lectures*, Cambridge University Press, 1985, ISBN: 978-0-521-31827-3 (cit. on p. 44).

[190] A. V. Manohar, "Large N QCD", *Les Houches Summer School in Theoretical Physics, Session 68: Probing the Standard Model of Particle Interactions*, 1998 1091, arXiv: hep-ph/9802419 (cit. on p. 44).

[191] R. F. Lebed, *Phenomenology of Large N_c QCD*, Czech. J. Phys. **49** (1999) 1273, ed. by J. Adam, P. Bydzovsky and J. Mares, arXiv: nucl-th/9810080 (cit. on p. 44).

[192] K. Fujikawa, *Path-Integral Measure for Gauge-Invariant Fermion Theories*, Phys. Rev. Lett. **42** (1979) 1195 (cit. on p. 45).

[193] G. 't Hooft, *Naturalness, Chiral Symmetry, and Spontaneous Chiral Symmetry Breaking*, NATO Sci. Ser. B **59** (1980) 135, ed. by G. 't Hooft et al. (cit. on p. 47).

[194] B.-L. Hoid, M. Hoferichter and B. Kubis, *Hadronic Vacuum Polarization: Three-Pion Channel*, EPJ Web Conf. **234** (2020) 01006, ed. by G. D'Ambrosio et al. (cit. on p. 51).

[195] N. Khuri and S. Treiman, *Pion-Pion Scattering and $K^{\pm} \to 3\pi$ Decay*, Phys. Rev. **119** (1960) 1115 (cit. on pp. 51, 74).

[196] I. Aitchison and R. Golding, *Relativistic Three-Pion Dynamics in the ω Channel*, J. Phys. G **4** (1978) 43 (cit. on p. 51).

[197] F. Niecknig, B. Kubis and S. P. Schneider, *Dispersive Analysis of $\omega \to 3\pi$ and $\phi \to 3\pi$ Decays*, Eur. Phys. J. C **72** (2012) 2014, arXiv: 1203.2501 [hep-ph] (cit. on pp. 51, 55, 56, 72, 99, 137).

[198] I. Danilkin et al., *Dispersive Analysis of $\omega/\phi \to 3\pi$, $\pi\gamma^*$*, Phys. Rev. D **91** (2015) 094029, arXiv: 1409.7708 [hep-ph] (cit. on pp. 51, 72).

[199] M. Dax, T. Isken and B. Kubis, *Quark-Mass Dependence in $\omega \to 3\pi$ Decays*, Eur. Phys. J. C **78** (2018) 859, arXiv: 1808.08957 [hep-ph] (cit. on p. 51).

[200] M. Albaladejo et al., *$\omega \to 3\pi$ and $\omega\pi^0$ Transition Form Factor Revisited*, (2020), arXiv: 2006.01058 [hep-ph] (cit. on p. 51).

[201] R. García-Martín et al., *Pion-Pion Scattering Amplitude. IV. Improved Analysis with Once Subtracted Roy-Like Equations up to* 1100 MeV, Phys. Rev. D **83** (2011) 074004, arXiv: 1102.2183 [hep-ph] (cit. on pp. 51, 74, 93, 99).

[202] I. Caprini, G. Colangelo and H. Leutwyler,
Regge Analysis of the $\pi\pi$ Scattering Amplitude, Eur. Phys. J. C **72** (2012) 1860,
arXiv: 1111.7160 [hep-ph] (cit. on pp. 51, 74, 93, 96, 99).

[203] T. Blum et al., *Connected and Leading Disconnected Hadronic Light-by-Light Contribution to the Muon Anomalous Magnetic Moment with a Physical Pion Mass*,
Phys. Rev. Lett. **118** (2017) 022005, arXiv: 1610.04603 [hep-lat]
(cit. on pp. 51, 87).

[204] T. Blum et al., *Using Infinite Volume, Continuum QED and Lattice QCD for the Hadronic Light-by-Light Contribution to the Muon Anomalous Magnetic Moment*,
Phys. Rev. D **96** (2017) 034515, arXiv: 1705.01067 [hep-lat]
(cit. on pp. 51, 87).

[205] E.-H. Chao et al., *Hadronic Light-by-Light Contribution to $(g-2)_\mu$ from Lattice QCD with $SU(3)$ Flavor Symmetry*, Eur. Phys. J. C **80** (2020) 869,
arXiv: 2006.16224 [hep-lat] (cit. on pp. 51, 87).

[206] F. Jegerlehner, *The Role of Mesons in Muon $g-2$*,
EPJ Web Conf. **199** (2019) 01010, ed. by N. Wrońska, A. Magiera and W. Przygoda,
arXiv: 1809.07413 [hep-ph] (cit. on pp. 51, 52, 87).

[207] M. Benayoun, L. Delbuono and F. Jegerlehner,
$BHLS_2$, a New Breaking of the HLS Model and its Phenomenology,
Eur. Phys. J. C **80** (2020) 81, [Erratum: Eur. Phys. J. C 80 (2020) 244],
arXiv: 1903.11034 [hep-ph] (cit. on pp. 51, 52, 87).

[208] B. Chakraborty et al., *Strong-Isospin-Breaking Correction to the Muon Anomalous Magnetic Moment from Lattice QCD at the Physical Point*,
Phys. Rev. Lett. **120** (2018) 152001, arXiv: 1710.11212 [hep-lat]
(cit. on p. 51).

[209] S. Borsanyi et al., *Hadronic Vacuum Polarization Contribution to the Anomalous Magnetic Moments of Leptons from First Principles*,
Phys. Rev. Lett. **121** (2018) 022002, arXiv: 1711.04980 [hep-lat]
(cit. on p. 51).

[210] T. Blum et al., *Calculation of the Hadronic Vacuum Polarization Contribution to the Muon Anomalous Magnetic Moment*, Phys. Rev. Lett. **121** (2018) 022003,
arXiv: 1801.07224 [hep-lat] (cit. on p. 51).

[211] D. Giusti, F. Sanfilippo and S. Simula,
Light-Quark Contribution to the Leading Hadronic Vacuum Polarization Term of the Muon $g-2$ from Twisted-Mass Fermions, Phys. Rev. D **98** (2018) 114504,
arXiv: 1808.00887 [hep-lat] (cit. on p. 51).

[212] E. Shintani and Y. Kuramashi,
Hadronic Vacuum Polarization Contribution to the Muon $g-2$ with $2+1$ Flavor Lattice QCD on a Larger than $(10\,\mathrm{fm})^4$ Lattice at the Physical Point,
Phys. Rev. D **100** (2019) 034517, arXiv: 1902.00885 [hep-lat] (cit. on p. 51).

[213] C. Davies et al., *Hadronic-Vacuum-Polarization Contribution to the Muon's Anomalous Magnetic Moment from Four-Flavor Lattice QCD*,
Phys. Rev. D **101** (2020) 034512, arXiv: 1902.04223 [hep-lat] (cit. on p. 51).

[214] A. Gérardin et al., *The Leading Hadronic Contribution to $(g-2)_\mu$ from Lattice QCD with $N_f = 2+1$ Flavours of $O(a)$ Improved Wilson Quarks*,
Phys. Rev. D **100** (2019) 014510, arXiv: 1904.03120 [hep-lat] (cit. on p. 51).

[215] C. Aubin et al., *Light Quark Vacuum Polarization at the Physical Point and Contribution to the Muon $g-2$*, Phys. Rev. D **101** (2020) 014503,
arXiv: 1905.09307 [hep-lat] (cit. on p. 51).

[216] D. Giusti and S. Simula,
Lepton Anomalous Magnetic Moments in Lattice QCD+QED,
PoS **LATTICE2019** (2019) 104, arXiv: 1910.03874 [hep-lat] (cit. on p. 51).

[217] G. Abbiendi et al.,
Measuring the Leading Hadronic Contribution to the Muon $g-2$ via μe Scattering,
Eur. Phys. J. C **77** (2017) 139, arXiv: 1609.08987 [hep-ex] (cit. on p. 51).

[218] J. de Trocóniz and F. Ynduráin, *Precision Determination of the Pion Form Factor and Calculation of the Muon $g-2$*, Phys. Rev. D **65** (2002) 093001,
arXiv: hep-ph/0106025 (cit. on p. 52).

[219] H. Leutwyler, "Electromagnetic Form Factor of the Pion",
Continuous Advances in QCD 2002 / ARKADYFEST (honoring the 60th birthday of Prof. Arkady Vainshtein), 2002 23, arXiv: hep-ph/0212324 (cit. on p. 52).

[220] G. Colangelo, *Hadronic Contributions to a_μ below One* GeV,
Nucl. Phys. B Proc. Suppl. **131** (2004) 185, ed. by M. Incagli and G. Venanzoni,
arXiv: hep-ph/0312017 (cit. on p. 52).

[221] J. de Trocóniz and F. Ynduráin,
Hadronic Contributions to the Anomalous Magnetic Moment of the Muon,
Phys. Rev. D **71** (2005) 073008, arXiv: hep-ph/0402285 (cit. on p. 52).

[222] B. Ananthanarayan, I. Caprini and D. Das, *Pion Electromagnetic Form Factor at High Precision with Implications to $a_\mu^{\pi\pi}$ and the Onset of Perturbative QCD*,
Phys. Rev. D **98** (2018) 114015, arXiv: 1810.09265 [hep-ph] (cit. on pp. 52, 71).

[223] B. Aubert et al., *Precise Measurement of the $e^+e^- \to \pi^+\pi^-(\gamma)$ Cross Section with the Initial State Radiation Method at BABAR*, Phys. Rev. Lett. **103** (2009) 231801,
arXiv: 0908.3589 [hep-ex] (cit. on p. 52).

[224] J. Lees et al., *Precise Measurement of the $e^+e^- \to \pi^+\pi^-(\gamma)$ Cross Section with the Initial-State Radiation Method at BABAR*, Phys. Rev. D **86** (2012) 032013, arXiv: 1205.2228 [hep-ex] (cit. on pp. 52, 83).

[225] F. Ambrosino et al., *Measurement of $\sigma(e^+e^- \to \pi^+\pi^-\gamma(\gamma)$ and the Dipion Contribution to the Muon Anomaly with the KLOE Detector*, Phys. Lett. B **670** (2009) 285, arXiv: 0809.3950 [hep-ex] (cit. on p. 52).

[226] F. Ambrosino et al., *Measurement of $\sigma(e^+e^- \to \pi^+\pi^-)$ from Threshold to $0.85\,\text{GeV}^2$ using Initial State Radiation with the KLOE Detector*, Phys. Lett. B **700** (2011) 102, arXiv: 1006.5313 [hep-ex] (cit. on p. 52).

[227] D. Babusci et al., *Precision Measurement of $\sigma(e^+e^- \to \pi^+\pi^-\gamma)/\sigma(e^+e^- \to \mu^+\mu^-\gamma)$ and Determination of the $\pi^+\pi^-$ Contribution to the Muon Anomaly with the KLOE Detector*, Phys. Lett. B **720** (2013) 336, arXiv: 1212.4524 [hep-ex] (cit. on p. 52).

[228] A. Anastasi et al., *Combination of KLOE $\sigma(e^+e^- \to \pi^+\pi^-\gamma(\gamma))$ Measurements and Determination of $a_\mu^{\pi^+\pi^-}$ in the Energy Range $0.10 < s < 0.95\,\text{GeV}^2$*, JHEP **03** (2018) 173, arXiv: 1711.03085 [hep-ex] (cit. on p. 52).

[229] S. P. Schneider, B. Kubis and F. Niecknig, *$\omega \to \pi^0\gamma^*$ and $\phi \to \pi^0\gamma^*$ Transition Form Factors in Dispersion Theory*, Phys. Rev. D **86** (2012) 054013, arXiv: 1206.3098 [hep-ph] (cit. on pp. 52, 72, 88, 92, 93, 97–99).

[230] M. Hoferichter, B. Kubis and D. Sakkas, *Extracting the Chiral Anomaly from $\gamma\pi \to \pi\pi$*, Phys. Rev. D **86** (2012) 116009, arXiv: 1210.6793 [hep-ph] (cit. on pp. 52, 54, 56, 72, 73, 88, 92, 96, 97, 99, 107).

[231] M. Hoferichter et al., *Dispersive Analysis of the Pion Transition Form Factor*, Eur. Phys. J. C **74** (2014) 3180, arXiv: 1410.4691 [hep-ph] (cit. on pp. 52, 71–74, 88, 92, 94–97, 99, 106–112).

[232] M. Hoferichter, B. Kubis and M. Zanke, *Radiative Resonance Couplings in $\gamma\pi \to \pi\pi$*, Phys. Rev. D **96** (2017) 114016, arXiv: 1710.00824 [hep-ph] (cit. on pp. 52, 54, 55, 72, 73, 88, 92, 99, 137, 138).

[233] R. García-Martín and B. Moussallam, *MO Analysis of the High Statistics Belle Results on $\gamma\gamma \to \pi^+\pi^-, \pi^0\pi^0$ with Chiral Constraints*, Eur. Phys. J. C **70** (2010) 155, arXiv: 1006.5373 [hep-ph] (cit. on pp. 52, 72, 134).

[234] M. Hoferichter, D. R. Phillips and C. Schat, *Roy–Steiner Equations for $\gamma\gamma \to \pi\pi$*, Eur. Phys. J. C **71** (2011) 1743, arXiv: 1106.4147 [hep-ph] (cit. on pp. 52, 72, 134).

[235] B. Moussallam, *Unified Dispersive Approach to Real and Virtual Photon-Photon Scattering at Low Energy*, Eur. Phys. J. C **73** (2013) 2539, arXiv: 1305.3143 [hep-ph] (cit. on pp. 52, 72, 81, 134).

[236] I. Danilkin and M. Vanderhaeghen, *Dispersive Analysis of the $\gamma\gamma^* \to \pi\pi$ process*, Phys. Lett. B **789** (2019) 366, arXiv: 1810.03669 [hep-ph] (cit. on pp. 52, 72, 134).

[237] M. Hoferichter and P. Stoffer, *Dispersion Relations for $\gamma^*\gamma^* \to \pi\pi$: Helicity Amplitudes, Subtractions, and Anomalous Thresholds*, JHEP **07** (2019) 073, arXiv: 1905.13198 [hep-ph] (cit. on pp. 52, 72, 134).

[238] I. Danilkin, O. Deineka and M. Vanderhaeghen, *Dispersive Analysis of the $\gamma^*\gamma^* \to \pi\pi$ Process*, Phys. Rev. D **101** (2020) 054008, arXiv: 1909.04158 [hep-ph] (cit. on pp. 52, 72, 134).

[239] S. L. Adler et al., *Low-Energy Theorem for $\gamma + \gamma \to \pi + \pi + \pi$*, Phys. Rev. D **4** (1971) 3497 (cit. on pp. 52, 54, 73).

[240] M. Terent'ev, *Process $\pi^\pm \to \pi^0\pi^\pm$ in Coulomb Field and Anomalous Divergence of Neutral Axial-Vector Current*, Phys. Lett. B **38** (1972) 419 (cit. on pp. 52, 54, 73).

[241] R. Aviv and A. Zee, *Low-Energy Theorem for $\gamma \to 3\pi$*, Phys. Rev. D **5** (1972) 2372 (cit. on pp. 52, 54, 73).

[242] R. Akhmetshin et al., *Measurement of $e^+e^- \to \pi^+\pi^-$ Cross-Section with CMD-2 around ρ-Meson*, Phys. Lett. B **527** (2002) 161, arXiv: hep-ex/0112031 (cit. on p. 52).

[243] R. Akhmetshin et al., *Update: A Reanalysis of Hadronic Cross Section Measurements at CMD-2*, Phys. Lett. B **578** (2004) 285, arXiv: hep-ex/0308008 (cit. on pp. 52, 58–66, 71, 83).

[244] M. Achasov et al., *Study of the Process $e^+e^- \to \pi^+\pi^-$ in the Energy Region $400 < \sqrt{s} < 1000$ MeV*, J. Exp. Theor. Phys. **101** (2005) 1053, arXiv: hep-ex/0506076 (cit. on p. 52).

[245] M. Achasov et al., *Update of the $e^+e^- \to \pi^+\pi^-$ Cross-Section Measured by the Spherical Neutral Detector in the Energy Region $400 < \sqrt{s} < 1000$ MeV*, J. Exp. Theor. Phys. **103** (2006) 380, arXiv: hep-ex/0605013 (cit. on p. 52).

[246] V. Aul'chenko et al., *Measurement of the $e^+e^- \to \pi^+\pi^-$ Cross Section with the CMD-2 Detector in the* 370–520-MeV *Energy Range*, JETP Lett. **84** (2006) 413, arXiv: hep-ex/0610016 (cit. on p. 52).

[247] R. Akhmetshin et al., *High-Statistics Measurement of the Pion Form Factor in the ρ-Meson Energy Range with the CMD-2 Detector*, Phys. Lett. B **648** (2007) 28, arXiv: hep-ex/0610021 (cit. on p. 52).

[248] B. Aubert et al.,
Study of the $e^+e^- \to \pi^+\pi^-\pi^0$ Process Using Initial State Radiation with BaBar,
Phys. Rev. D **70** (2004) 072004, arXiv: hep-ex/0408078
(cit. on pp. 52, 57–65, 95–97).

[249] M. Achasov et al., *Measurements of the Parameters of the $\phi(1020)$ Resonance through Studies of the Processes $e^+e^- \to K^+K^-$, K_SK_L, and $\pi^+\pi^-\pi^0$*,
Phys. Rev. D **63** (2001) 072002, arXiv: hep-ex/0009036
(cit. on pp. 52, 58–60, 64, 65, 71).

[250] M. Achasov et al., *Study of the Process $e^+e^- \to \pi^+\pi^-\pi^0$ in the Energy Region $\sqrt{s}$ from* 0.98 *to* 1.38 GeV, Phys. Rev. D **66** (2002) 032001, arXiv: hep-ex/0201040
(cit. on pp. 52, 58–60, 64, 65, 95–97).

[251] M. Achasov et al.,
Study of the Process $e^+e^- \to \pi^+\pi^-\pi^0$ in the Energy Region $\sqrt{s}$ below 0.98 GeV,
Phys. Rev. D **68** (2003) 052006, arXiv: hep-ex/0305049
(cit. on pp. 52, 58–60, 64–66, 69, 71, 83, 95–97).

[252] V. Aul'chenko et al.,
Study of the $e^+e^- \to \pi^+\pi^-\pi^0$ Process in the Energy Range 1.05–2.00 GeV,
J. Exp. Theor. Phys. **121** (2015) 27 (cit. on pp. 52, 58–60, 62, 64, 65).

[253] R. Akhmetshin et al.,
Measurement of ϕ Meson Parameters with CMD-2 Detector at VEPP-2M Collider,
Phys. Lett. B **364** (1995) 199 (cit. on pp. 52, 58–61, 64, 65).

[254] R. Akhmetshin et al.,
Study of Dynamics of $\phi \to \pi^+\pi^-\pi^0$ Decay with CMD-2 Detector,
Phys. Lett. B **434** (1998) 426 (cit. on pp. 52, 58–61, 64, 65).

[255] R. Akhmetshin et al., *Study of $\phi \to \pi^+\pi^-\pi^0$ with CMD-2 Detector*,
Phys. Lett. B **642** (2006) 203 (cit. on pp. 52, 58–64, 67, 68).

[256] A. Cordier et al., *Cross Section of the Reaction $e^+e^- \to \pi^+\pi^-\pi^0$ for C.M. Energies From* 750 *to* 1100 MeV, Nucl. Phys. B **172** (1980) 13 (cit. on pp. 52, 58, 64, 65).

[257] A. Antonelli et al., *Measurement of the $e^+e^- \to \pi^+\pi^-\pi^0$ and $e^+e^- \to \omega\pi^+\pi^-$ Reactions in the Energy Interval* 1350–2400 MeV, Z. Phys. C **56** (1992) 15
(cit. on pp. 52, 58, 62).

[258] S. Dolinsky et al., *Summary of Experiments with the Neutral Detector at the e^+e^- Storage Ring VEPP-2M*, Phys. Rept. **202** (1991) 99 (cit. on pp. 52, 58, 64, 65).

[259] J. Calmet et al., *Higher Order Hadronic Corrections to the Anomalous Magnetic Moment of the Muon*, Phys. Lett. B **61** (1976) 283 (cit. on pp. 53, 79).

[260] F. Campanario et al., *Standard Model Radiative Corrections in the Pion Form Factor Measurements Do Not Explain the a_μ Anomaly*,
Phys. Rev. D **100** (2019) 076004, arXiv: 1903.10197 [hep-ph] (cit. on p. 53).

[261] Y. M. Antipov et al., *Investigation of the Chiral Anomaly $\gamma \to 3\pi$ in Pion Pair Production by Pion in the Nuclear Coulomb Field*, Phys. Rev. D **36** (1987) 21 (cit. on pp. 54, 73).

[262] I. Giller et al., *A New Determination of the $\gamma\pi \to \pi\pi$ Anomalous Amplitude via $\pi^- e^- \to \pi^- e^- \pi^0$ Data*, Eur. Phys. J. A **25** (2005) 229, arXiv: hep-ph/0503207 (cit. on pp. 54, 73).

[263] J. A. Seyfried, *Determination of the Chiral Anomaly and Studies on the Pion Polarizability in Pion–Nickel Reactions from COMPASS at CERN*, MA thesis: TU, München, 2017 (cit. on pp. 54, 73, 137).

[264] M. Jacob and G. Wick, *On the General Theory of Collisions for Particles with Spin*, Annals Phys. **7** (1959) 404 (cit. on p. 54).

[265] J. Stern, H. Sazdjian and N. Fuchs, *What π-π Scattering Tells Us about Chiral Perturbation Theory*, Phys. Rev. D **47** (1993) 3814, arXiv: hep-ph/9301244 (cit. on p. 55).

[266] M. Knecht et al., *The Low Energy $\pi\pi$ Amplitude to One and Two Loops*, Nucl. Phys. B **457** (1995) 513, arXiv: hep-ph/9507319 (cit. on p. 55).

[267] J. Bijnens, A. Bramon and F. Cornet, *Three-Pseudoscalar Photon Interactions in Chiral Perturbation Theory*, Phys. Lett. B **237** (1990) 488 (cit. on pp. 56, 73).

[268] G. D'Agostini, *On the Use of the Covariance Matrix to Fit Correlated Data*, Nucl. Instrum. Meth. A **346** (1994) 306 (cit. on pp. 58, 74).

[269] R. D. Ball et al., *Fitting Parton Distribution Data with Multiplicative Normalization Uncertainties*, JHEP **05** (2010) 075, arXiv: 0912.2276 [hep-ph] (cit. on pp. 58, 59, 75, 76).

[270] R. Akhmetshin et al., *Study of the Processes $e^+e^- \to \eta\gamma$, $\pi^0\gamma \to 3\gamma$ in the C.M. Energy Range* 600–1380 MeV *at CMD-2*, Phys. Lett. B **605** (2005) 26, arXiv: hep-ex/0409030 (cit. on pp. 65, 71, 74–78, 81, 83, 107–109).

[271] C. Amsler et al., *Antiproton–Proton Annihilation at Rest into $\omega\pi^0\pi^0$*, Phys. Lett. B **311** (1993) 362 (cit. on pp. 65, 71, 83).

[272] K. Hagiwara et al., *Predictions for $g-2$ of the Muon and $\alpha_{QED}(M_Z^2)$*, Phys. Rev. D **69** (2004) 093003, arXiv: hep-ph/0312250 (cit. on pp. 68, 80).

[273] E. Kuraev and Z. Silagadze, *Once more about the $\omega \to 3\pi$ Contact Term*, Phys. Atom. Nucl. **58** (1995) 1589, arXiv: hep-ph/9502406 (cit. on p. 68).

[274] A. Ahmedov et al., *Near-Threshold Radiative 3π Production in e^+e^- Annihilation*, JHEP **09** (2002) 008, arXiv: hep-ph/0201157 (cit. on p. 68).

[275] B.-L. Hoid, M. Hoferichter and B. Kubis, *Hadronic Vacuum Polarization and Vector-Meson Resonance Parameters from $e^+e^- \to \pi^0\gamma$*, Eur. Phys. J. C **80** (2020) 988, arXiv: 2007.12696 [hep-ph] (cit. on p. 71).

[276] S. Okubo, *φ-Meson and Unitary Symmetry Model*, Phys. Lett. **5** (1963) 165 (cit. on p. 71).

[277] G. Zweig, "An $SU(3)$ Model for Strong Interaction Symmetry and Its Breaking. Version 2", *Developments in the Quark Theory of Hadrons*, ed. by D. Lichtenberg and S. P. Rosen, vol. 1, 1964 22 (cit. on p. 71).

[278] J. Iizuka, *A Systematics and Phenomenology of Meson Family*, Prog. Theor. Phys. Suppl. **37** (1966) 21 (cit. on p. 71).

[279] J. Lees et al., *Precision Measurement of the $e^+e^- \to K^+K^-(\gamma)$ Cross Section with the Initial-State Radiation Method at BABAR*, Phys. Rev. D **88** (2013) 032013, arXiv: 1306.3600 [hep-ex] (cit. on pp. 71, 82).

[280] J. Lees et al., *Cross Sections for the Reactions $e^+e^- \to K^0_S K^0_L$, $K^0_S K^0_L \pi^+\pi^-$, $K^0_S K^0_S \pi^+\pi^-$, and $K^0_S K^0_S K^+K^-$ from Events with Initial-State Radiation*, Phys. Rev. D **89** (2014) 092002, arXiv: 1403.7593 [hep-ex] (cit. on pp. 71, 82).

[281] E. Kozyrev et al., *Study of the Process $e^+e^- \to K^+K^-$ in the Center-of-Mass Energy Range* 1010–1060 MeV *with the CMD-3 Detector*, Phys. Lett. B **779** (2018) 64, arXiv: 1710.02989 [hep-ex] (cit. on p. 71).

[282] G. Colangelo, M. Hoferichter and P. Stoffer, *Constraints on the Two-Pion Contribution to Hadronic Vacuum Polarization*, (2020), arXiv: 2010.07943 [hep-ph] (cit. on p. 71).

[283] S. Borsanyi et al., *Leading-Order Hadronic Vacuum Polarization Contribution to the Muon Magnetic Moment from Lattice QCD*, (2020), arXiv: 2002.12347 [hep-lat] (cit. on pp. 72, 133).

[284] A. Crivellin et al., *Hadronic Vacuum Polarization: $(g-2)_\mu$ versus Global Electroweak Fits*, Phys. Rev. Lett. **125** (2020) 091801, arXiv: 2003.04886 [hep-ph] (cit. on pp. 72, 133).

[285] A. Keshavarzi et al., *Muon $g-2$ and $\Delta\alpha$ Connection*, Phys. Rev. D **102** (2020) 033002, arXiv: 2006.12666 [hep-ph] (cit. on pp. 72, 133).

[286] B. Malaescu and M. Schott, *Impact of Correlations between a_μ and α_{QED} on the EW Fit*, (2020), arXiv: 2008.08107 [hep-ph] (cit. on pp. 72, 133).

[287] I. Larin et al., *Precision Measurement of the Neutral Pion Lifetime*, Science **368** (2020) 506 (cit. on pp. 72, 93, 117, 124, 125).

[288] J. Bijnens, A. Bramon and F. Cornet, *Pseudoscalar Decays into Two Photons in Chiral Perturbation Theory*, Phys. Rev. Lett. **61** (1988) 1453 (cit. on pp. 73, 92, 124).

[289] B. Ananthanarayan and B. Moussallam,
Electromagnetic Corrections in the Anomaly Sector, JHEP **05** (2002) 052,
arXiv: hep-ph/0205232 (cit. on pp. 73, 92, 124, 125).

[290] J. Goity, A. Bernstein and B. Holstein,
Decay $\pi^0 \to \gamma\gamma$ to Next to Leading Order in Chiral Perturbation Theory,
Phys. Rev. D **66** (2002) 076014, arXiv: hep-ph/0206007
(cit. on pp. 73, 92, 124, 125).

[291] K. Kampf and B. Moussallam, *Chiral Expansions of the π^0 Lifetime*,
Phys. Rev. D **79** (2009) 076005, arXiv: 0901.4688 [hep-ph]
(cit. on pp. 73, 92, 93, 124, 125).

[292] G. R. Farrar and D. R. Jackson, *Pion Form Factor*, Phys. Rev. Lett. **43** (1979) 246
(cit. on p. 74).

[293] A. Duncan and A. H. Mueller, *Asymptotic Behavior of Composite-Particle Form Factors and the Renormalization Group*, Phys. Rev. D **21** (1980) 1636
(cit. on p. 74).

[294] A. Efremov and A. Radyushkin,
Factorization and Asymptotic Behavior of Pion Form Factor in QCD,
Phys. Lett. B **94** (1980) 245 (cit. on p. 74).

[295] M. Achasov et al.,
Experimental Study of the Processes $e^+e^- \to \phi \to \eta\gamma, \pi^0\gamma$ at VEPP-2M,
Eur. Phys. J. C **12** (2000) 25 (cit. on pp. 74–76, 107–109).

[296] M. Achasov et al., *Experimental Study of the $e^+e^- \to \pi^0\gamma$ Process in the Energy Region $\sqrt{s} = 0.60$–0.97 GeV*, Phys. Lett. B **559** (2003) 171,
arXiv: hep-ex/0302004 (cit. on pp. 74–76, 108, 109).

[297] M. Achasov et al.,
Study of the Reaction $e^+e^- \to \pi^0\gamma$ with the SND Detector at the VEPP-2M Collider,
Phys. Rev. D **93** (2016) 092001, arXiv: 1601.08061 [hep-ex]
(cit. on pp. 74–76, 108, 109).

[298] M. Achasov et al., *Measurement of the $e^+e^- \to \pi^0\gamma$ Cross Section in the Energy Range* 1.075–2 GeV *at SND*, Phys. Rev. D **98** (2018) 112001,
arXiv: 1809.07631 [hep-ex] (cit. on pp. 74–76, 80).

[299] N. Achasov et al., *A Fresh Look at $\phi - \omega$ Mixing*, Sov. J. Nucl. Phys. **54** (1991) 664
(cit. on p. 77).

[300] N. Achasov and A. Kiselev, *Contribution to Muon $g-2$ from $\pi^0\gamma$ and $\eta\gamma$ Intermediate States in the Vacuum Polarization*, Phys. Rev. D **65** (2002) 097302,
arXiv: hep-ph/0202047 (cit. on pp. 79, 80).

[301] B. Kubis et al., In Preparation (cit. on p. 83).

[302] R. Wurzinger et al.,
Near-Threshold Production of ω Mesons in the $pd \to {}^3He\omega$ Reaction,
Phys. Rev. C **51** (1995) 443 (cit. on p. 83).

[303] V. Aulchenko et al., *The Width of the ω-Meson*, Phys. Lett. B **186** (1987) 432 (cit. on pp. 83, 84).

[304] B.-L. Hoid et al., *Pion-Pole Contribution to Hadronic Light-by-Light Scattering*, PoS **CD2018** (2019) 052 (cit. on p. 87).

[305] F. Jegerlehner, *Muon $g-2$ Theory: The Hadronic Part*,
EPJ Web Conf. **166** (2018) 00022, ed. by A. Di Domenico,
arXiv: 1705.00263 [hep-ph] (cit. on p. 87).

[306] J. Bijnens, E. Pallante and J. Prades,
Hadronic Light-by-Light Contribution to the Muon $g-2$,
Phys. Rev. Lett. **75** (1995) 1447, [Erratum: Phys. Rev. Lett. 75 (1995) 3781],
arXiv: hep-ph/9505251 (cit. on p. 87).

[307] J. Bijnens, E. Pallante and J. Prades,
Analysis of the Hadronic Light-by-Light Contributions to the Muon $g-2$,
Nucl. Phys. B **474** (1996) 379, arXiv: hep-ph/9511388 (cit. on pp. 87, 118).

[308] M. Hayakawa, T. Kinoshita and A. Sanda,
Hadronic Light-by-Light Scattering Effect on Muon $g-2$,
Phys. Rev. Lett. **75** (1995) 790, arXiv: hep-ph/9503463 (cit. on p. 87).

[309] M. Hayakawa, T. Kinoshita and A. Sanda,
Hadronic Light-by-Light Scattering Contribution to Muon $g-2$,
Phys. Rev. D **54** (1996) 3137, arXiv: hep-ph/9601310 (cit. on p. 87).

[310] M. Hayakawa and T. Kinoshita, *Pseudoscalar Pole Terms in the Hadronic Light-by-Light Scattering Contribution to Muon $g-2$*,
Phys. Rev. D **57** (1998) 465, [Erratum: Phys. Rev. D 66 (2002) 019902],
arXiv: hep-ph/9708227 (cit. on pp. 87, 118).

[311] M. Knecht et al., *Hadronic Light-By-Light Scattering Contribution to the Muon $g-2$: An Effective Field Theory Approach*, Phys. Rev. Lett. **88** (2002) 071802,
arXiv: hep-ph/0111059 (cit. on pp. 87, 91, 139, 142, 145).

[312] M. Knecht and A. Nyffeler, *Hadronic Light-by-Light Corrections to the Muon $g-2$: The Pion-Pole Contribution*, Phys. Rev. D **65** (2002) 073034,
arXiv: hep-ph/0111058 (cit. on pp. 87, 89, 118, 144).

[313] I. R. Blokland, A. Czarnecki and K. Melnikov, *Pion Pole Contribution to Hadronic Light-By-Light Scattering and Muon Anomalous Magnetic Moment*,
Phys. Rev. Lett. **88** (2002) 071803, arXiv: hep-ph/0112117 (cit. on p. 87).

[314] J. Bijnens, E. Pallante and J. Prades, *Comment on the Pion Pole Part of the Light-by-Light Contribution to the Muon $g-2$*, Nucl. Phys. B **626** (2002) 410, arXiv: hep-ph/0112255 (cit. on pp. 87, 118).

[315] M. Ramsey-Musolf and M. B. Wise, *Hadronic Light-by-Light Contribution to Muon $g-2$ in Chiral Perturbation Theory*, Phys. Rev. Lett. **89** (2002) 041601, arXiv: hep-ph/0201297 (cit. on pp. 87, 91, 139, 142, 145).

[316] K. T. Engel, H. H. Patel and M. J. Ramsey-Musolf, *Hadronic Light-by-Light Scattering and the Pion Polarizability*, Phys. Rev. D **86** (2012) 037502, arXiv: 1201.0809 [hep-ph] (cit. on p. 87).

[317] P. Masjuan, *$\gamma^*\gamma \to \pi^0$ Transition Form Factor at Low Energies from a Model-Independent Approach*, Phys. Rev. D **86** (2012) 094021, arXiv: 1206.2549 [hep-ph] (cit. on pp. 87, 112, 113).

[318] K. T. Engel and M. J. Ramsey-Musolf, *The Muon Anomalous Magnetic Moment and the Pion Polarizability*, Phys. Lett. B **738** (2014) 123, arXiv: 1309.2225 [hep-ph] (cit. on p. 87).

[319] P. Roig, A. Guevara and G. López Castro, *$VV'P$ Form Factors in Resonance Chiral Theory and the $\pi-\eta-\eta'$ Light-by-Light Contribution to the Muon $g-2$*, Phys. Rev. D **89** (2014) 073016, arXiv: 1401.4099 [hep-ph] (cit. on pp. 87, 90, 118).

[320] J. Bijnens and J. Relefors, *Pion Light-by-Light Contributions to the Muon $g-2$*, JHEP **09** (2016) 113, arXiv: 1608.01454 [hep-ph] (cit. on p. 87).

[321] T. Blum et al., *Hadronic Light-by-Light Scattering Contribution to the Muon Anomalous Magnetic Moment from Lattice QCD*, Phys. Rev. Lett. **114** (2015) 012001, arXiv: 1407.2923 [hep-lat] (cit. on p. 87).

[322] J. Green et al., *Lattice QCD Calculation of Hadronic Light-by-Light Scattering*, Phys. Rev. Lett. **115** (2015) 222003, arXiv: 1507.01577 [hep-lat] (cit. on p. 87).

[323] T. Blum et al., *Lattice Calculation of Hadronic Light-by-Light Contribution to the Muon Anomalous Magnetic Moment*, Phys. Rev. D **93** (2016) 014503, arXiv: 1510.07100 [hep-lat] (cit. on p. 87).

[324] *Proceedings of the Second International PrimeNet Workshop*, 2012, arXiv: 1204.5509 [nucl-ex] (cit. on p. 88).

[325] *MesonNet Workshop on Meson Transition Form Factors*, 2012, arXiv: 1207.6556 [hep-ph] (cit. on p. 88).

[326] K. Kampf, A. Kupsc and P. Masjuan, eds., *MesonNet 2013 International Workshop. Mini-Proceedings*, 2013, arXiv: 1308.2575 [hep-ph] (cit. on p. 88).

[327] W. Gradl et al., eds., *Light Meson Dynamics Workshop. Mini Proceedings*, 2014, arXiv: 1403.6380 [hep-ph] (cit. on p. 88).

[328] T. Blum, ed., *Hadronic Contributions to the Muon Anomalous Magnetic Moment Workshop. $(g-2)_\mu$: Quo Vadis? Workshop. Mini Proceedings*, 2014, arXiv: 1407.4021 [hep-ph] (cit. on p. 88).

[329] *MesonNet 2014 International Workshop. Mini-Proceedings*, 2014, arXiv: 1412.5451 [nucl-ex] (cit. on p. 88).

[330] S. Leupold et al., *Towards a Dispersive Determination of the Pion Transition Form Factor*, EPJ Web Conf. **166** (2018) 00013, ed. by A. Di Domenico (cit. on p. 88).

[331] S. J. Brodsky and J. D. Sullivan, *W-Boson Contribution to the Anomalous Magnetic Moment of the Muon*, Phys. Rev. **156** (1967) 1644 (cit. on p. 89).

[332] W. A. Bardeen and W. Tung, *Invariant Amplitudes for Photon Processes*, Phys. Rev. **173** (1968) 1423, [Erratum: Phys. Rev. D 4 (1971) 3229] (cit. on p. 90).

[333] R. Tarrach, *Invariant Amplitudes for Virtual Compton Scattering Off Polarized Nucleons Free from Kinematical Singularities, Zeros and Constraints*, Nuovo Cim. A **28** (1975) 409 (cit. on p. 90).

[334] V. Pauk and M. Vanderhaeghen, *Anomalous Magnetic Moment of the Muon in a Dispersive Approach*, Phys. Rev. D **90** (2014) 113012, arXiv: 1409.0819 [hep-ph] (cit. on p. 90).

[335] E. Bartos et al., *Scalar and Pseudoscalar Meson Pole Terms in the Hadronic Light-by-Light Contributions to a_μ^{had}*, Nucl. Phys. B **632** (2002) 330, arXiv: hep-ph/0106084 (cit. on pp. 90, 118).

[336] A. E. Dorokhov and W. Broniowski, *Pion Pole Light-by-Light Contribution to $g-2$ of the Muon in a Nonlocal Chiral Quark Model*, Phys. Rev. D **78** (2008) 073011, arXiv: 0805.0760 [hep-ph] (cit. on p. 90).

[337] A. Nyffeler, *Hadronic Light-by-Light Scattering in the Muon $g-2$: A New Short-Distance Constraint on Pion Exchange*, Phys. Rev. D **79** (2009) 073012, arXiv: 0901.1172 [hep-ph] (cit. on pp. 90, 118).

[338] D. K. Hong and D. Kim, *Pseudo Scalar Contributions to Light-by-Light Correction of Muon $g-2$ in AdS/QCD*, Phys. Lett. B **680** (2009) 480, arXiv: 0904.4042 [hep-ph] (cit. on p. 90).

[339] L. Cappiello, O. Catà and G. D'Ambrosio, *Hadronic Light by Light Contribution to the $(g-2)_\mu$ with Holographic Models of QCD*, Phys. Rev. D **83** (2011) 093006, arXiv: 1009.1161 [hep-ph] (cit. on pp. 90, 118).

[340] T. Goecke, C. S. Fischer and R. Williams, *Hadronic Light-by-Light Scattering in the Muon $g-2$: A Dyson–Schwinger Equation Approach*, Phys. Rev. D **83** (2011) 094006, [Erratum: Phys. Rev. D 86 (2012) 099901], arXiv: 1012.3886 [hep-ph] (cit. on pp. 90, 118).

[341] A. E. Dorokhov, A. E. Radzhabov and A. S. Zhevlakov, *The Pseudoscalar Hadronic Channel Contribution of the Light-by-Light Process to the Muon $(g-2)_\mu$ within the Nonlocal Chiral Quark Model*, Eur. Phys. J. C **71** (2011) 1702, arXiv: 1103.2042 [hep-ph] (cit. on pp. 90, 118).

[342] K. Kampf and J. Novotný, *Resonance Saturation in the Odd-Intrinsic Parity Sector of Low-Energy QCD*, Phys. Rev. D **84** (2011) 014036, arXiv: 1104.3137 [hep-ph] (cit. on pp. 90, 118).

[343] D. Greynat and E. de Rafael, *Hadronic Contributions to the Muon Anomaly in the Constituent Chiral Quark Model*, JHEP **07** (2012) 020, arXiv: 1204.3029 [hep-ph] (cit. on pp. 90, 118).

[344] A. E. Dorokhov, A. E. Radzhabov and A. S. Zhevlakov, *The Light-by-Light Contribution to the Muon $(g-2)$ from Lightest Pseudoscalar and Scalar Mesons within Nonlocal Chiral Quark Model*, Eur. Phys. J. C **72** (2012) 2227, arXiv: 1204.3729 [hep-ph] (cit. on p. 90).

[345] A. Guevara, P. Roig and J. Sanz-Cillero, *Pseudoscalar Pole Light-by-Light Contributions to the Muon $(g-2)$ in Resonance Chiral Theory*, JHEP **06** (2018) 160, arXiv: 1803.08099 [hep-ph] (cit. on pp. 91, 118, 119).

[346] A. Gérardin, H. B. Meyer and A. Nyffeler, *Lattice Calculation of the Pion Transition Form Factor $\pi^0 \to \gamma^*\gamma^*$*, Phys. Rev. D **94** (2016) 074507, arXiv: 1607.08174 [hep-lat] (cit. on pp. 91, 113, 114, 118, 119).

[347] M. J. Savage, M. Luke and M. B. Wise, *The Rare Decays $\pi^0 \to e^+e^-$, $\eta \to e^+e^-$ and $\eta \to \mu^+\mu^-$ in Chiral Perturbation Theory*, Phys. Lett. B **291** (1992) 481, arXiv: hep-ph/9207233 (cit. on pp. 91, 127, 130, 143).

[348] L. Ametller, A. Bramon and E. Massó, *$\pi^0 \to e^+e^-$ and $\eta \to \mu^+\mu^-$ Decays Reexamined*, Phys. Rev. D **48** (1993) 3388, arXiv: hep-ph/9302304 (cit. on pp. 91, 127, 143).

[349] P. Vasko and J. Novotný, *Two-Loop QED Radiative Corrections to the Decay $\pi^0 \to e^+e^-$: The Virtual Corrections and Soft-Photon Bremsstrahlung*, JHEP **10** (2011) 122, arXiv: 1106.5956 [hep-ph] (cit. on pp. 91, 127, 128).

[350] T. Husek, K. Kampf and J. Novotný, *Rare Decay $\pi^0 \to e^+e^-$: On Corrections beyond the Leading Order*, Eur. Phys. J. C **74** (2014) 3010, arXiv: 1405.6927 [hep-ph] (cit. on pp. 91, 127).

[351] M. Knecht et al., *Decay of Pseudoscalars into Lepton Pairs and Large-N_c QCD*, Phys. Rev. Lett. **83** (1999) 5230, arXiv: hep-ph/9908283 (cit. on pp. 91, 127, 130).

[352] A. E. Dorokhov and M. A. Ivanov, *Rare Decay $\pi^0 \to e^+e^-$: Theory Confronts KTeV Data*, Phys. Rev. D **75** (2007) 114007, arXiv: 0704.3498 [hep-ph] (cit. on pp. 91, 127, 129).

[353] A. E. Dorokhov and M. A. Ivanov, *On Mass Corrections to the Decays $P \to l^+l^-$*, JETP Lett. **87** (2008) 531, arXiv: 0803.4493 [hep-ph] (cit. on pp. 91, 127).

[354] A. E. Dorokhov, M. A. Ivanov and S. G. Kovalenko, *Complete Structure-Dependent Analysis of the Decay $P \to l^+l^-$*, Phys. Lett. B **677** (2009) 145, arXiv: 0903.4249 [hep-ph] (cit. on pp. 91, 127).

[355] P. Masjuan and P. Sanchez-Puertas, *Phenomenology of Bivariate Approximants: The $\pi^0 \to e^+e^-$ Case and Its Impact on the Electron and Muon $g-2$*, (2015), arXiv: 1504.07001 [hep-ph] (cit. on pp. 91, 127).

[356] T. Husek and S. Leupold, *Two-Hadron Saturation for the Pseudoscalar–Vector–Vector Correlator and Phenomenological Applications*, Eur. Phys. J. C **75** (2015) 586, arXiv: 1507.00478 [hep-ph] (cit. on pp. 91, 100, 127).

[357] P. Masjuan and P. Sanchez-Puertas, *η and η' Decays into Lepton Pairs*, JHEP **08** (2016) 108, arXiv: 1512.09292 [hep-ph] (cit. on pp. 91, 129, 130).

[358] E. Weil et al., *Electromagnetic Decays of the Neutral Pion*, Phys. Rev. D **96** (2017) 014021, arXiv: 1704.06046 [hep-ph] (cit. on pp. 91, 127).

[359] I. Larin et al., *New Measurement of the π^0 Radiative Decay Width*, Phys. Rev. Lett. **106** (2011) 162303, arXiv: 1009.1681 [nucl-ex] (cit. on pp. 92, 124, 125).

[360] A. H. Gasparian, *Preliminary Results from the PrimEx-II Experiment at Jefferson Lab*, PoS **CD15** (2016) 048 (cit. on pp. 93, 117).

[361] M. Fujikawa et al., *High-Statistics Study of the $\tau^- \to \pi^-\pi^0\nu_\tau$ Decay*, Phys. Rev. D **78** (2008) 072006, arXiv: 0805.3773 [hep-ex] (cit. on p. 93).

[362] F.-K. Guo et al., *Quark Mass Dependence of the Pion Vector Form Factor*, Phys. Lett. B **678** (2009) 90, arXiv: 0812.3270 [hep-ph] (cit. on p. 94).

[363] K. Hagiwara et al., *$(g-2)_\mu$ and $\alpha(M_Z^2)$ Re-evaluated Using New Precise Data*, J. Phys. G **38** (2011) 085003, arXiv: 1105.3149 [hep-ph] (cit. on p. 95).

[364] G. Lepage and S. J. Brodsky, *Exclusive Processes in Quantum Chromodynamics: Evolution Equations for Hadronic Wavefunctions and the Form Factors of Mesons*, Phys. Lett. B **87** (1979) 359 (cit. on pp. 99, 101, 104, 150, 151).

[365] G. Lepage and S. J. Brodsky, *Exclusive Processes in Perturbative Quantum Chromodynamics*, Phys. Rev. D **22** (1980) 2157 (cit. on pp. 99, 101, 104, 150, 151).

[366] S. J. Brodsky and G. Lepage, *Large-Angle Two-Photon Exclusive Channels in Quantum Chromodynamics*, Phys. Rev. D **24** (1981) 1808 (cit. on pp. 99, 101, 104, 150, 151).

[367] G. Colangelo, J. Gasser and H. Leutwyler, *$\pi\pi$ Scattering*, Nucl. Phys. B **603** (2001) 125, arXiv: hep-ph/0103088 (cit. on p. 99).

[368] G. Ecker and R. Unterdorfer, *Four-Pion Production in e^+e^- Annihilation*, Eur. Phys. J. C **24** (2002) 535, arXiv: hep-ph/0203075 (cit. on p. 99).

[369] J. Lees et al., *Measurement of the $e^+e^-\to\pi^+\pi^-\pi^0\pi^0$ Cross Section Using Initial-State Radiation at BABAR*, Phys. Rev. D **96** (2017) 092009, arXiv: 1709.01171 [hep-ex] (cit. on p. 99).

[370] M. Knecht and A. Nyffeler, *Resonance Estimates of $O(p^6)$ Low-Energy Constants and QCD Short-Distance Constraints*, Eur. Phys. J. C **21** (2001) 659, arXiv: hep-ph/0106034 (cit. on pp. 100, 114).

[371] A. Manohar and H. Georgi, *Chiral-Quarks and the Non-Relativistic Quark Model*, Nucl. Phys. B **234** (1984) 189 (cit. on p. 100).

[372] V. Novikov et al., *Use and Misuse of QCD Sum Rules, Factorization and Related Topics*, Nucl. Phys. B **237** (1984) 525 (cit. on pp. 100–102, 114).

[373] L. Reinders, H. Rubinstein and S. Yazaki, *Hadron Properties from QCD Sum Rules*, Phys. Rept. **127** (1985) 1 (cit. on p. 100).

[374] S. Narison, *QCD Spectral Sum Rules*, vol. 26, 1989 (cit. on p. 100).

[375] D. B. Leinweber, *QCD Sum Rules for Skeptics*, Annals Phys. **254** (1997) 328, arXiv: nucl-th/9510051 (cit. on p. 100).

[376] V. Chernyak and A. Zhitnitsky, *Asymptotic Behavior of Exclusive Processes in QCD*, Phys. Rept. **112** (1984) 173 (cit. on pp. 100, 102, 105, 114).

[377] A. Khodjamirian, *Form-Factors of $\gamma^*\rho\to\pi$ and $\gamma^*\gamma\to\pi^0$ Transitions and Light-Cone Sum Rules*, Eur. Phys. J. C **6** (1999) 477, arXiv: hep-ph/9712451 (cit. on pp. 100, 102, 114, 149, 150).

[378] S. Agaev et al., *Light Cone Sum Rules for the $\pi^0\gamma^*\gamma$ Form Factor Revisited*, Phys. Rev. D **83** (2011) 054020, arXiv: 1012.4671 [hep-ph] (cit. on pp. 100, 102, 114, 149, 150).

[379] S. Mikhailov, A. Pimikov and N. Stefanis, *Systematic Estimation of Theoretical Uncertainties in the Calculation of the Pion-Photon Transition Form Factor Using Light-Cone Sum Rules*, Phys. Rev. D **93** (2016) 114018, arXiv: 1604.06391 [hep-ph] (cit. on pp. 100, 102, 114).

[380] Y.-L. Shen et al., *Power Corrections to the Pion Transition Form Factor from Higher-Twist Distribution Amplitudes of a Photon*, Phys. Rev. D **99** (2019) 096013, arXiv: 1901.10259 [hep-ph] (cit. on p. 100).

[381] N. Stefanis, *Pion-Photon Transition Form Factor in Light Cone Sum Rules and Tests of Asymptotics*, Phys. Rev. D **102** (2020) 034022, arXiv: 2006.10576 [hep-ph] (cit. on p. 100).

[382] V. Nesterenko and A. Radyushkin, *Comparison of the QCD Sum Rule Approach and Perturbative QCD Analysis for $\gamma^*\gamma^* \to \pi^0$ Process*, Sov. J. Nucl. Phys. **38** (1983) 284 (cit. on p. 101).

[383] A. Gorsky, *The $\pi^0\gamma\gamma$ Form factor at Different Photon Virtualities in the Sum-Rule Method and in Perturbative QCD. (In Russian)*, Yad. Fiz. **46** (1987) 938 (cit. on p. 101).

[384] A. V. Manohar, *The Decays $Z \to W\pi$, $Z \to \gamma\pi$ and the Pion Form Factor*, Phys. Lett. B **244** (1990) 101 (cit. on pp. 101, 151).

[385] F. del Aguila and M. Chase, *Higher Order QCD Corrections to an Exclusive Two-Photon Process*, Nucl. Phys. B **193** (1981) 517 (cit. on p. 102).

[386] E. Braaten, *Quantum-Chromodynamic Corrections to Meson-Photon Transition Form Factors*, Phys. Rev. D **28** (1983) 524 (cit. on pp. 102, 104).

[387] V. Chernyak and A. Zhitnitsky, *Exclusive Decays of Heavy Mesons*, Nucl. Phys. B **201** (1982) 492, [Erratum: Nucl. Phys. B 214 (1983) 547] (cit. on pp. 102, 105).

[388] A. Radyushkin and R. Ruskov, *Transition Form Factor $\gamma\gamma^* \to \pi^0$ and QCD Sum Rules*, Nucl. Phys. B **481** (1996) 625, arXiv: hep-ph/9603408 (cit. on p. 102).

[389] K. Raya et al., *Structure of the Neutral Pion and Its Electromagnetic Transition Form Factor*, Phys. Rev. D **93** (2016) 074017, arXiv: 1510.02799 [nucl-th] (cit. on p. 102).

[390] G. Eichmann et al., *On the Large-Q^2 Behavior of the Pion Transition Form Factor*, Phys. Lett. B **774** (2017) 425, arXiv: 1704.05774 [hep-ph] (cit. on p. 102).

[391] G. Eichmann et al., *Single Pseudoscalar Meson Pole and Pion Box Contributions to the Anomalous Magnetic Moment of the Muon*, Phys. Lett. B **797** (2019) 134855, [Erratum: Phys. Lett. B 799 135029 (2019)], arXiv: 1903.10844 [hep-ph] (cit. on p. 102).

[392] K. Raya, A. Bashir and P. Roig, *Contribution of Neutral Pseudoscalar Mesons to a_μ^{HLbL} within a Schwinger–Dyson Equations Approach to QCD*, Phys. Rev. D **101** (2020) 074021, arXiv: 1910.05960 [hep-ph] (cit. on p. 102).

[393] E. Ruiz Arriola and W. Broniowski, *Pion Transition Form Factor and Distribution Amplitudes in Large-N_c Regge Models*, Phys. Rev. D **74** (2006) 034008, arXiv: hep-ph/0605318 (cit. on p. 102).

[394] E. Ruiz Arriola and W. Broniowski, *Pion Transition Form Factor in the Regge Approach and Incomplete Vector-Meson Dominance*, Phys. Rev. D **81** (2010) 094021, arXiv: 1004.0837 [hep-ph] (cit. on p. 102).

[395] M. Gorchtein, P. Guo and A. P. Szczepaniak, *Form Factors of Pseudoscalar Mesons*, Phys. Rev. C **86** (2012) 015205, arXiv: 1102.5558 [nucl-th] (cit. on p. 102).

[396] H. Behrend et al., *A Measurement of the π^0, η and η' Electromagnetic Form Factors*, Z. Phys. C **49** (1991) 401 (cit. on pp. 105, 106, 110–113, 117, 151).

[397] J. Gronberg et al., *Measurements of the Meson-Photon Transition Form Factors of Light Pseudoscalar Mesons at Large Momentum Transfer*, Phys. Rev. D **57** (1998) 33, arXiv: hep-ex/9707031 (cit. on pp. 105, 106, 110–113, 117, 151).

[398] B. Aubert et al., *Measurement of the $\gamma\gamma^* \to \pi^0$ Transition Form Factor*, Phys. Rev. D **80** (2009) 052002, arXiv: 0905.4778 [hep-ex] (cit. on pp. 105, 106, 112, 113, 115, 117, 151).

[399] S. Uehara et al., *Measurement of $\gamma\gamma^* \to \pi^0$ Transition Form Factor at Belle*, Phys. Rev. D **86** (2012) 092007, arXiv: 1205.3249 [hep-ex] (cit. on pp. 105, 106, 112, 113, 115, 117, 151).

[400] C. Lazzeroni et al., *Measurement of the π^0 Electromagnetic Transition Form Factor Slope*, Phys. Lett. B **768** (2017) 38, arXiv: 1612.08162 [hep-ex] (cit. on p. 112).

[401] P. Adlarson et al., *Measurement of the $\pi^0 \to e^+e^-\gamma$ Dalitz Decay at the Mainz Microtron*, Phys. Rev. C **95** (2017) 025202, arXiv: 1611.04739 [hep-ex] (cit. on p. 112).

[402] G. Eichmann, C. S. Fischer and W. Heupel,
Four-Point Functions and the Permutation Group S_4,
Phys. Rev. D **92** (2015) 056006, arXiv: 1505.06336 [hep-ph] (cit. on p. 117).

[403] C. Redmer, *The $\gamma\gamma$ Physics Program at BESIII*,
EPJ Web Conf. **166** (2018) 00017, ed. by A. Di Domenico (cit. on p. 117).

[404] D. Steffen, *COMPASS Status*, in $g-2$ workshop (18-22, June 2018) (cit. on p. 117).

[405] T. Abe et al., *Belle II Technical Design Report*, (2010),
arXiv: 1011.0352 [physics.ins-det] (cit. on p. 117).

[406] W. Altmannshofer et al., *The Belle II Physics Book*, PTEP **2019** (2019) 123C01,
ed. by E. Kou and P. Urquijo, [Erratum: PTEP 2020 (2020) 029201],
arXiv: 1808.10567 [hep-ex] (cit. on p. 117).

[407] F. Stollenwerk et al.,
Model-Independent Approach to $\eta \to \pi^+\pi^-\gamma$ and $\eta' \to \pi^+\pi^-\gamma$,
Phys. Lett. B **707** (2012) 184, arXiv: 1108.2419 [nucl-th]
(cit. on pp. 120, 134).

[408] C. Hanhart et al., *Dispersive Analysis for $\eta \to \gamma\gamma^*$*,
Eur. Phys. J. C **73** (2013) 2668, [Erratum: Eur. Phys. J. C 75 (2015) 242],
arXiv: 1307.5654 [hep-ph] (cit. on pp. 120, 134).

[409] B. Kubis and J. Plenter,
Anomalous Decay and Scattering Processes of the η Meson,
Eur. Phys. J. C **75** (2015) 283, arXiv: 1504.02588 [hep-ph]
(cit. on pp. 120, 134).

[410] C. Xiao et al., *Towards an Improved Understanding of $\eta \to \gamma^*\gamma^*$*, (2015),
arXiv: 1509.02194 [hep-ph] (cit. on pp. 120, 134).

[411] B. Kubis,
Towards a Dispersive Determination of the η and η' Transition Form Factors,
EPJ Web Conf. **166** (2018) 00012, ed. by A. Di Domenico (cit. on p. 120).

[412] H. Atherton et al., *Direct Measurement of the Lifetime of the Neutral Pion*,
Phys. Lett. B **158** (1985) 81 (cit. on pp. 123–125).

[413] L. Landsberg, *Electromagnetic Decays of Light Mesons*,
Phys. Rept. **128** (1985) 301 (cit. on p. 123).

[414] T. Petri, *Anomalous Decays of Pseudoscalar Mesons*, MA thesis, 2010,
arXiv: 1010.2378 [nucl-th] (cit. on pp. 123, 126).

[415] K. Kampf, "On Decays of Light Unflavoured Pseudoscalar Mesons",
Proceedings, 2nd International Workshop on Physics of fundamental Symmetries and Interactions at low energies and the precision frontier (PSI2010): PSI, Villigen, Switzerland, October 11-14, 2010, 2011, arXiv: 1109.4370 [hep-ph]
(cit. on p. 123).

[416] D. Sutherland, *Current Algebra and Some Non-Strong Mesonic Decays*, Nucl. Phys. B **2** (1967) 433 (cit. on p. 123).

[417] J. Donoghue, B. R. Holstein and Y. Lin, *Chiral Loops in $\pi^0, \eta^0 \to \gamma\gamma$ and η-η' Mixing*, Phys. Rev. Lett. **55** (1985) 2766, [Erratum: Phys. Rev. Lett. 61 (1988) 1527] (cit. on p. 124).

[418] B. Ioffe and A. Oganesian, *Axial Anomaly and the Precise Value of the $\pi^0 \to 2\gamma$ Decay Width*, Phys. Lett. B **647** (2007) 389, arXiv: hep-ph/0701077 (cit. on pp. 124, 125).

[419] D. Williams et al., *Formation of the Pseudoscalars π^0, η and η' in the Reaction $\gamma\gamma \to \gamma\gamma$*, Phys. Rev. D **38** (1988) 1365 (cit. on pp. 124, 125).

[420] M. Bychkov et al., *New Precise Measurement of the Pion Weak Form Factors in $\pi^+ \to e^+\nu\gamma$ Decay*, Phys. Rev. Lett. **103** (2009) 051802, arXiv: 0804.1815 [hep-ex] (cit. on pp. 124, 125).

[421] R. Dalitz, *On an Alternative Decay Process for the Neutral π-Meson*, Proc. Phys. Soc. A **64** (1951) 667 (cit. on p. 124).

[422] K. Kampf, M. Knecht and J. Novotný, *The Dalitz Decay $\pi^0 \to e^+e^-\gamma$ Revisited*, Eur. Phys. J. C **46** (2006) 191, arXiv: hep-ph/0510021 (cit. on p. 125).

[423] C. Terschlüsen et al., *Reactions with Pions and Vector Mesons in the Sector of Odd Intrinsic Parity*, Eur. Phys. J. A **49** (2013) 116, arXiv: 1305.1181 [hep-ph] (cit. on p. 126).

[424] R. Escribano and S. Gonzàlez-Solís, *A Data-Driven Approach to π^0, η and η' Single and Double Dalitz Decays*, Chin. Phys. C **42** (2018) 023109, arXiv: 1511.04916 [hep-ph] (cit. on p. 126).

[425] K. Kampf, J. Novotný and P. Sanchez-Puertas, *Radiative Corrections to Double-Dalitz Decays Revisited*, Phys. Rev. D **97** (2018) 056010, arXiv: 1801.06067 [hep-ph] (cit. on p. 126).

[426] L. Gan et al., *Precision Tests of Fundamental Physics with η and η' Mesons*, (2020), arXiv: 2007.00664 [hep-ph] (cit. on p. 126).

[427] N. M. Kroll and W. Wada, *Internal Pair Production Associated with the Emission of High-Energy Gamma Rays*, Phys. Rev. **98** (1955) 1355 (cit. on p. 126).

[428] D. Perkins, *Introduction to High Energy Physics*, 1982, ISBN: 978-0-521-62196-0 (cit. on p. 126).

[429] R. Plano et al., *Parity of the Neutral Pion*, Phys. Rev. Lett. **3** (1959) 525 (cit. on p. 126).

[430] E. Abouzaid et al.,
Determination of the Parity of the Neutral Pion via Its Four-Electron Decay,
Phys. Rev. Lett. **100** (2008) 182001, arXiv: 0802.2064 [hep-ex] (cit. on p. 126).

[431] E. Bratkovskaya, E. Kuraev and Z. Silagadze,
On the Four-Photon Decay of the Neutral Pion, Phys. Lett. B **359** (1995) 217,
arXiv: hep-ph/9506310 (cit. on p. 126).

[432] Y. Liao, *Rare Decay $\pi^0 \to 4\gamma$ in Chiral Perturbation Theory*,
Phys. Rev. D **57** (1998) 1573 (cit. on p. 126).

[433] E. Kuraev, V. Bytev and Y. Bystritsky, *Quark Loop Contribution to $\pi^0 \to 4\gamma$*,
Phys. Rev. D **73** (2006) 054021, arXiv: hep-ph/0311086 (cit. on p. 126).

[434] Z. Silagadze, *Vector-Meson-Dominance Model Contribution to $\pi^0 \to 4\gamma$*,
Phys. Scripta **70** (2004) 280, arXiv: hep-ph/0311089 (cit. on p. 126).

[435] S. Drell, *Direct Decay $\pi^0 \to e^+e^-$*, Nuovo Cim. **11** (1959) 693 (cit. on p. 127).

[436] S. Berman and D. Geffen,
The Electromagnetic Structure and Alternative Decay Modes of the π^0,
Nuovo Cim. **18** (1960) 1192 (cit. on pp. 127, 129).

[437] M. Pratap and J. Smith, *η and Pion Decays into Lepton Pairs*,
Phys. Rev. D **5** (1972) 2020 (cit. on pp. 127, 129).

[438] L. Bergström, *Rare Decay of a Pseudoscalar Meson into a Lepton Pair – A Way to Detect New Interactions?*, Z. Phys. C **14** (1982) 129 (cit. on p. 127).

[439] L. Ametller et al., *The Quark Triangle: Application to Pion and Eta Decays*,
Nucl. Phys. B **228** (1983) 301 (cit. on p. 127).

[440] C. Quigg and J. Jackson, *Decays of Neutral Pseudoscalar Mesons into Lepton Pairs*,
(1968) (cit. on p. 127).

[441] L. Bergström et al., *Q^2 Duality and Rare Pion Decays*,
Phys. Lett. B **126** (1983) 117 (cit. on pp. 127, 129).

[442] E. Abouzaid et al., *Measurement of the Rare Decay $\pi^0 \to e^+e^-$*,
Phys. Rev. D **75** (2007) 012004, arXiv: hep-ex/0610072 (cit. on pp. 127, 134).

[443] N. H. Christ et al.,
Calculating the Two-photon Contribution to $\pi^0 \to e^+e^-$ Decay Amplitude,
PoS **LATTICE2019** (2020) 097, arXiv: 2001.05642 [hep-lat] (cit. on p. 127).

[444] H. Ghaderi, *The Rare Decay of the Neutral Pion into a Dielectron*,
MA thesis: Uppsala University, Nuclear Physics, 2013 (cit. on p. 128).

[445] J. Lüdtke, *Zerfall Leichter Pseudoskalare in Zwei Leptonen*,
BA Thesis: Bonn University, 2016 (cit. on pp. 128, 130, 131).

[446] G. Passarino and M. Veltman,
One-Loop Corrections for e^+e^- Annihilation into $\mu^+\mu^-$ in the Weinberg Model,
Nucl. Phys. B **160** (1979) 151 (cit. on pp. 130, 131).

[447] G. 't Hooft and M. Veltman, *Scalar One-Loop Integrals*,
Nucl. Phys. B **153** (1979) 365 (cit. on p. 130).

[448] J. Prades, E. de Rafael and A. Vainshtein, "The Hadronic Light-by-Light Scattering Contribution to the Muon and Electron Anomalous Magnetic Moments",
Adv. Ser. Direct. High Energy Phys. Vol. 20, 2009 303,
arXiv: 0901.0306 [hep-ph] (cit. on pp. 135, 142).

[449] C. Hanhart, *A New Parameterization for the Pion Vector Form Factor*,
Phys. Lett. B **715** (2012) 170, arXiv: 1203.6839 [hep-ph] (cit. on p. 138).

[450] C. Hanhart et al., In Preparation (cit. on p. 138).

[451] A. Abbas, *Anomalies and Charge Quantization in the Standard Model with Arbitrary Number of Colors*, Phys. Lett. B **238** (1990) 344 (cit. on p. 139).

[452] J. Gerard and T. Lahna, *The Asymptotic Behavior of the $\pi^0\gamma^*\gamma^*$ Vertex*,
Phys. Lett. B **356** (1995) 381, arXiv: hep-ph/9506255 (cit. on p. 139).

[453] O. Bär and U. Wiese, *Can One See the Number of Colors?*,
Nucl. Phys. B **609** (2001) 225, arXiv: hep-ph/0105258 (cit. on p. 139).

[454] B. Borasoy, *The Number of Colors in the Decays $\pi^0, \eta, \eta' \to \gamma\gamma$*,
Eur. Phys. J. C **34** (2004) 317, arXiv: hep-ph/0402294 (cit. on p. 139).

[455] B. Borasoy and E. Lipartia, *Can One See the Number of Colors in $\eta, \eta' \to \pi^+\pi^-\gamma$?*,
Phys. Rev. D **71** (2005) 014027, arXiv: hep-ph/0410141 (cit. on p. 139).

[456] E. Witten, *Baryons in the $1/N$ Expansion*, Nucl. Phys. B **160** (1979) 57
(cit. on p. 141).

[457] E. de Rafael, *Analytic Approaches to Kaon Physics*, Nucl. Phys. B Proc. Suppl. **119** (2003) 71, ed. by R. Edwards, J. W. Negele and D. Richards,
arXiv: hep-ph/0210317 (cit. on p. 141).

[458] S. Mandelstam, *Unitarity Condition Below Physical Thresholds in the Normal and Anomalous Cases*, Phys. Rev. Lett. **4** (1960) 84 (cit. on p. 146).

[459] W. Lucha, D. Melikhov and S. Simula,
Dispersion Representations and Anomalous Singularities of the Triangle Diagram,
Phys. Rev. D **75** (2007) 016001, [Erratum: Phys. Rev. D 92 (2015) 019901],
arXiv: hep-ph/0610330 (cit. on p. 146).

[460] J. Gasser, B. Kubis and A. Rusetsky,
Cusps in $K \to 3\pi$ Decays: A Theoretical Framework, Nucl. Phys. B **850** (2011) 96,
arXiv: 1103.4273 [hep-ph] (cit. on p. 147).

[461] J. J. Sakurai, *Currents and Mesons*, The University of Chicago Press, 1969 (cit. on p. 149).

[462] U.-G. Meißner, *Low-Energy Hadron Physics from Effective Chiral Lagrangians with Vector Mesons*, Phys. Rept. **161** (1988) 213 (cit. on p. 150).

[463] E. Marco and W. Weise, *QCD Spectral Sum Rules and Spontaneously Broken Chiral Symmetry*, Phys. Lett. B **482** (2000) 87, arXiv: hep-ph/9911287 (cit. on p. 150).

[464] S. Leupold, *Rho Meson Properties from Combining QCD-Based Models*, Nucl. Phys. A **743** (2004) 283, arXiv: hep-ph/0303020 (cit. on p. 150).

Acknowledgements

First of all, I would like to express my immense gratitude to my supervisor, Bastian Kubis, for his enormous support and encouragement during my entire study in Bonn. Both his tolerance and guidance shed light on the dark alley when I was staying in the phase of "to forgive yourself for wasting time." I am strongly inspired and learned much from his deep insights and right instincts in physics. I am also influenced a lot by his gentle, thoughtful personality.

I acknowledge Ulf-G. Meißner for being the second advisor of my PhD thesis. The acknowledgment also extends to his instant approvals to support all the conferences and workshops I have attended.

I am very grateful to the collaborators of my research projects, Martin Hoferichter, Stefan Leupold, and Peter Stoffer, for their enlightening ideas, creative opinions, and thorough discussions in person or via email, from which I gained invaluable experience for my own research. In particular, I would like to mention the excellent collaboration with Martin Hoferichter. I am deeply impressed by his great efficiency—whatever proposals he has made will very likely get implemented in the next hour. This "Sachdev-type" working style of him often encouraged and pushed me forward. Also, I would like to thank him for providing me the opportunity for future research.

I enjoyed the cheerful environment created with my office mates Simon Holz, Tobias Isken, and Jonahtan Lozano de la Parra. I will certainly miss our regular tea–coffee breaks and random dinner hang-outs. I also cherish the friendship with Meng-Lin Du, Janak Prabhu, Stefan Ropertz, and other colleagues from the group and the institute.

I appreciated the opportunities and the intercultural atmosphere brought by the Sino–German CRC 110 project. It reminds me of the fruitful discussions with Meng-Lin Du, Feng-Kun Guo, Zhi-Hui Guo, Simon Holz, Tobias Isken, Yu Lu, Malwin Niehus, and Stefan Ropertz. Sincere thanks to Christa Börsch, Lu Cao, Ting Chen, Yun-Hua Chen, Christian Jost, Barbara Kraus, Liuming Liu, Li Ma, Bernard Metsch, Jin-Yi Pang, Martin Ueding, Guang-Juan Wang, Qian Wang, Markus Werner, Jia-Jun Wu, Zhi Yang, ... , for their help and the events organized.

I am thankful for the encouragements from my friends Mören and Orgaa in the remote Alxa League, and Haixin Qiu at the neighboring institute. Besides, I wish we could resume the "Tichu" or "Di-Zhu" events with Peter Stoffer, Serena Grädel, Johanna and Franz Niecknig.

At last, I am indebted to my family for their supports; especially, to Tula Hoid, for her smiles, company, and devotion in every realm of life.